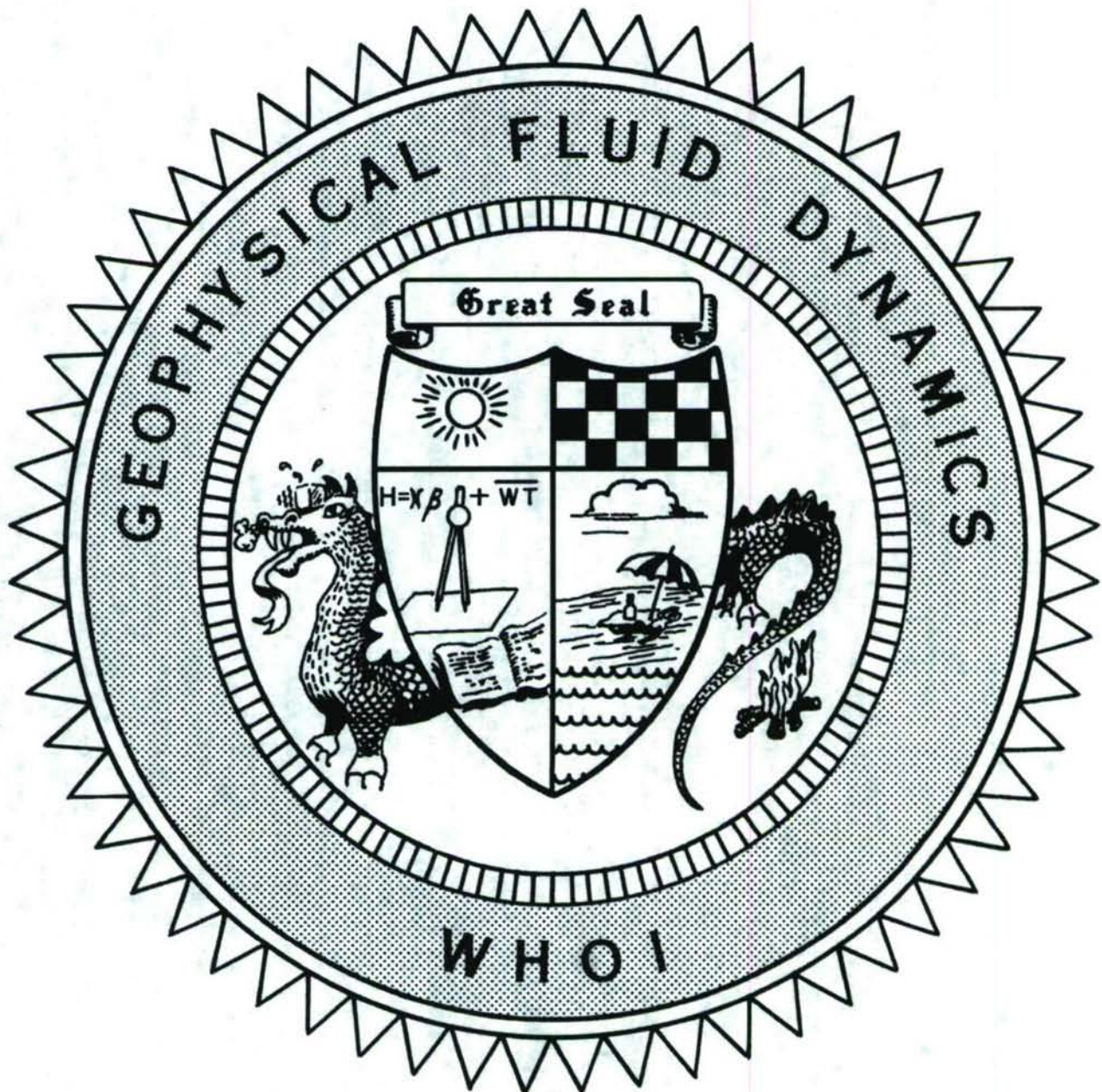


2006 Program of Study: Ice



20071016410

Course Lectures
Fellows Project Reports

This page intentionally left blank

2007-02

2006 Program of Studies: Ice

by

Neil Balmforth and John Wettlaufer, Co-Directors; Grae Worster, Principal Lecturer

March 2007


Technical Report

Funding was provided by the National Science Foundation under Grant No. OCE 03-25296.

Reproduction in whole or in part is permitted for any purpose of the United States Government. This report should be cited as Woods Hole Oceanog. Inst. Tech. Rept., 2007-02.

Approved for public release; distribution unlimited.

Approved for Distribution:



Robert A. Weller, Chair

Department of Physical Oceanography

Abstract

N. J. Balmforth and J. S. Wettlaufer
October 2006

Ice was the topic under discussion at Walsh Cottage during the 2006 Geophysical Fluid Dynamics Summer Study Program. Professor Grae Worster (University of Cambridge) was the principal lecturer, and navigated our path through the fluid dynamics of icy processes in GFD.

Towards the end of Grae's lectures, we also held the 2006 GFD Public Lecture. This was given by Greg Dash of the University of Washington, on matters of ice physics and a well-known popularization: "Nine Ices, Cloud Seeding and a Brother's Farewell; how Kurt Vonnegut learned the science for Cat's Cradle (but conveniently left some out)." We again held the talk at Redfield Auditorium, and relaxed in the evening sunshine at the reception afterwards.

As usual, the principal lectures were followed by a variety of seminars on topics icy and otherwise. We had focused sessions on sea ice, the impact of ice on climate, and glaciology.

This year was a good summer for softball, with the Fellows enjoying some notable successes on the field (against both the other WHOI teams and the staff team at the summer's close).

Some important acknowledgements: Young-Jin Kim helped out with the computers during the first few weeks, and Keith Bradley worked his usual magic in the Lab throughout the summer. The program continues to be indebted to W.H.O.I. Academic Programs, who once more provided a perfect atmosphere. Most unlike the '65 Dodge, Jeanne Fleming, Penny Foster and Janet Fields all contributed importantly to the smooth running of the program.

TABLE OF CONTENTS

ABSTRACT	i
TABLE OF CONTENTS	ii
PARTICIPANTS	iv
LECTURE SCHEDULE	viii
PRINCIPAL LECTURES	
Grae Worster, Cambridge University	
Lecture 1	
<i>Introduction to Ice</i>	
Grae Worster	1
Lecture 2:	
<i>Diffusion-controlled solidification</i>	
Grae Worster	12
Lecture 3:	
<i>Interfacial instability in super-cooled fluid</i>	
Grae Worster	20
Lecture 4:	
<i>Interfacial instability in two-component melts</i>	
Grae Worster	31
Lecture 5:	
<i>Formation of mushy layers</i>	
Grae Worster	44
Lecture 6:	
<i>Idealized mushy layers</i>	
Grae Worster	55
Lecture 7:	
<i>Convection in mushy layers</i>	
Grae Worster	67
Lecture 8:	
<i>Interfacial pre-melting</i>	
Grae Worster	72

Lecture 9: <i>Thermomolecular flow, thermal regelation and frost heave</i> Grae Worster	81
Lecture - John Wettlaufer, Yale University <i>Some useful statistical thermodynamics</i>	92
FELLOW'S REPORTS	
<i>Glancing interactions of internal solitary waves</i> Daniel Goldberg, New York University	97
<i>Mush-liquid interfaces with cross flow</i> Devin Conroy, University of California, San Diego	117
<i>Arctic catastrophes in an idealized sea ice model</i> Ian Eisenman, Harvard University	133
<i>Breaking moraine dams by catastrophic erosional incision</i> Rachel Zammett, University of Oxford	162
<i>Patterns of convection in a mushy layer</i> Shane Keating, University of California, San Diego	189
<i>The evaporation of a salty film</i> Robert Style, Cambridge University	204
<i>A particle-simulation method to study mixing efficiencies</i> Takahide Okabe, University of Texas, Austin	227
<i>On thin ice: the mechanics of failure in sea ice</i> Dominic Vella, Cambridge University	248
<i>The formation of star patterns on lake ice</i> Victor Tsai, Harvard University	272

2006 GFD FELLOWS, STAFF AND VISITORS

Fellows

Devin Conroy	University of California, San Diego
Ian Eisenmann	Harvard University
Daniel Goldberg	New York University
Shane Keating	University of California, San Diego
Takahide Okabe	University of Texas, Austin
Robert Style	University of Cambridge, U.K.
Victor Tsai	Harvard University
Dominic Vella	University of Cambridge, U.K.
Rachel Zammett	University of Oxford

Staff and Visitors

Sridhar Anandakrishnan	Penn State University
James Anderson	Stevens Institute of Technology
Neil J. Balmforth	University of British Columbia
Andrew Belmonte	Penn State University
Robert Bindschadler	NASA Goddard Space Flight Center
Goran Bjork	Goteborg University
Tim Boyd	Oregon State University
Kelly Brunt	University of Chicago
Eliza Calder	University of Buffalo
Mac Cathles	University of Chicago
Colm-cille Caufield	University of Cambridge
Claudia Cenedese	WHOI
Gregory Dash	University of Washington
Charles Doering	University of Michigan
Predrag Cvitanovic	Georgia Institute of Technology
Paul Dellar	Imperial College
Petri Fast	Lawrence Livermore National Laboratory
Daniel Feltham	University College, London
Andrew Fowler	University of Oxford
Karl Helfrich	WHOI
Richard Hindmarsh	British Antarctic Survey
Louis Howard	Massachusetts Institute of Technology
Lam Hui	Columbia University
Bror Johnson	Boston University
Joseph B. Keller	Stanford University
Young-Jin Kim	University of Chicago
Norman R. Lebovitz	University of Chicago
Doug MacAyeal	University of Chicago
Amala Mahadevan	Boston University
Lakshminarayanan Mahadevan	Harvard University

Willem V.R. Malkus	Massachusetts Institute of Technology
Shreyas Mandre	University of British Columbia
Doug Martinson	Lamont Doherty Earth Observatory
James MacElwaine	University of Cambridge
Miles McPhee	McPhee Research Corporation
Keith Moffatt	University of Cambridge
Jamie Morison	University of Washington
Richard Moritz	University of Washington
Philip J. Morrison	University of Texas at Austin
Jerome Neufeld	Yale University
Thomas Neumann	University of Vermont
Sophie Nowicki	University of Oxford
Marcel Oliver	International University, Bremen
Michael Patterson	Yale University
Don Perovich	Cold Regions Research and Engineering Laboratory
Antonello Provenzale	Istituto di Scienze Dell'Atmosfera
Charles Raymond	University of Washington
Alan Rempel	University of Oregon
Claes G. Rooth	University of Miami
Bert Rudels	Finnish Institute of Marine Research
Roiy Sayag	Harvard University
Peter Schlosser	Columbia University
Christian Schoof	University of British Columbia
Tiffany Shaw	University of Toronto
Edward Spiegel	Columbia University
Mary-Louise Timmermanns	WHOI
Martin Truffer	University of Alaska, Fairbanks
Norbert Untersteiner	University of Washington
George Veronis	Yale University
John Walsh	University of Alaska, Fairbanks
Andrew Wells	University of Cambridge
Matthew Wells	University of Toronto
John Wettlaufer	Yale University
John Whitehead	WHOI
Dale Winebrenner	University of Washington
Grae Worster	University of Cambridge
Jun Zhang	New York University

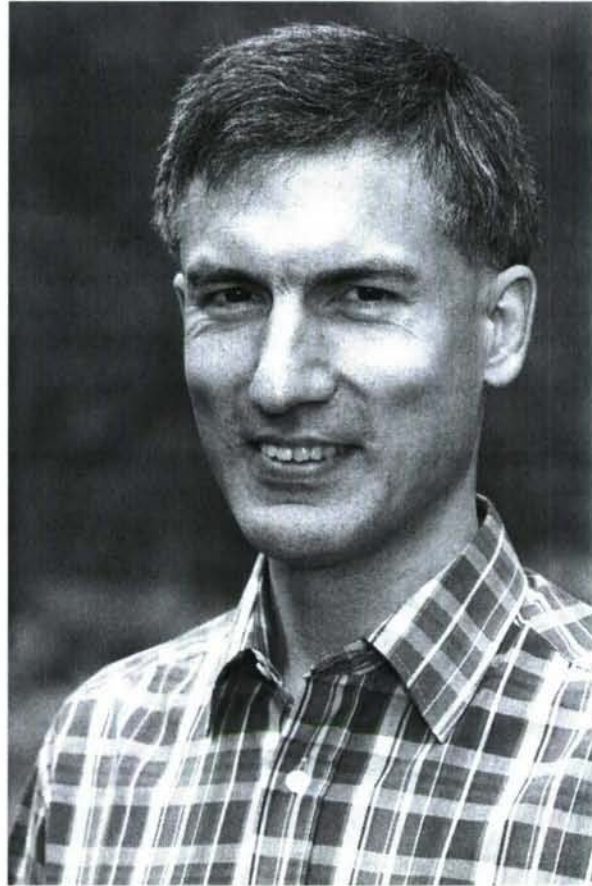


2006 Participants

Front row: Ed Spiegel (standing); Penny Foster; Paul Dellar; Charles Doering; Takahide Okabe; Daniel Goldberg; Joe Keller; George Veronis; Devin Conroy; Dominic Vella; Rachel Zammett; Shane Keating; Sridhar Anandakrishnan; Tom Neumann; Phil Morrison (standing); Ian Eisenman (standing)

Back row: Andrew Fowler; Neil Balmforth; Keith Moffatt; Sophie Nowicki; Robert Style; Alan Rempel; Herb Keller; Grae Worster; Victor Tsai; Andrew Wells; John Wettlaufer; Lou Howard; Dale Winebrenner; Jim Rice; Christian Schoof

**2006 Principal Lecturer
Grae Worster**



2006 GFD Lecture Schedule

June 19 - June 30

Principal Lecturer — Grae Worster, University of Cambridge

Monday, June 19

10:00 AM

Grae Worster

Introduction to Ice

Tuesday, June 20

10:00 AM

Grae Worster

Diffusion-controlled solidification

Wednesday, June 21

10:00 AM

Grae Worster

Interfacial instability in super-cooled fluid

Thursday, June 22

10:00 AM

Grae Worster

Interfacial instability in two-component melts

Friday, June 23

10:00 AM

Grae Worster

Formation of mushy layers

Monday, June 26

10:00 AM

Grae Worster

Idealized mushy layers

Tuesday, June 27

10:00 AM

Grae Worster

Convection in mushy layers

Wednesday, June 28

10:00 AM

Grae Worster

Interfacial pre-melting

Thursday, June 29

10:00 AM

Grae Worster

Thermomolecular flow, thermal regelation and frost heave

Friday, June 30

10:00 AM

John Wettlaufer, Yale University

Some useful statistical thermodynamics

July 3 - July 7

Monday, July 3

10:30 AM

Norbert Untersteiner, University of Washington

Large scale heat and mass balance of sea ice in the Arctic

Monday, July 3 (continued)

2:30 PM

Norbert Untersteiner, University of Washington

Glacier mass balance, lithotripsy and porters in the Karakorum

Tuesday, July 4

HOLIDAY

Wednesday, July 5

10:30 AM

John Walsh, University of Alaska

Global climate modeling: simulations of the Polar regions

2:30 PM

Andrey Proshutinsky, WHOI, Physical Oceanography Department

Arctic Ocean circulation, structure and freshwater balance

Thursday, July 6

10:30 AM

Doug Martinson, Columbia University

Ice/Ocean interaction from the ocean side: teleconnections

Friday, July 7

10:30 AM

Charles Doering, University of Michigan

Twist and shout! Maximal enstrophy generation in the 3-D Navier-Stokes equation

July 10 - July 14

Monday, July 10

10:30 AM

Lam Hui, Columbia University

Strings, ice and cosmology

Tuesday, July 11

10:00 AM

Smith Conference Room - Steinbach Scholar/P.O. Dept. Seminar

Miles McPhee, McPhee Research Corporation

Momentum heat and mass transfer through a sea-ice/ocean boundary

2:30 PM

Jamie Morison, University of Washington

Vehicular ice/ocean interactions

Wednesday, July 12

10:30 AM

Richard Moritz, University of Washington

Thickness distribution of sea ice: theory and observation

3:00 PM

Carriage House, Quissett Campus, Steinbach Scholar lecture

Miles McPhee, McPhee Research Corporation

Turbulence, scales, eddy viscosity/diffusivity, and simple models for the ocean boundary layers

Thursday, July 13

10:30 AM

Daniel Feltham, University College of London

Sea ice dynamics

Thursday, July 13 (continued)

3:00 PM **Clark 201, Quissett Campus, Special P.O. Dept. Seminar**
Richard Moritz, University of Washington
*Variability of sea ice draft at the North Pole Environmental
Observatory, 2001-2005*

Friday, July 14

10:00 AM **P.O. Dept. and GFD students only seminar, Clark 201**
Miles McPhee, McPhee Research Corporation
*Sea ice as a superb rotating laboratory: why freeze your butt
when you could be sipping Mai Tais in Lahina*

2:30 PM Mary-Louise Timmermans, WHOI, P.O. Dept.
Mixing in the deep Canada basin of the Arctic Ocean

July 17 - July 21

Monday, July 17

10:30 AM Bert Rudels, Finnish Institute of Marine Research
Convection in the Arctic

Tuesday, July 18

10:30 AM Colm-cille Caulfield, University of Cambridge
Internal waves

Wednesday, July 19

10:30 AM Hajo Eicken, University of Alaska
Biota in sea ice

2:30 PM Don Perovich, Cold Regions Research and Engineering Lab
Sea ice optics

Thursday, July 20

10:30 AM Richard Hindmarsh, British Antarctic Survey
Influence of horizontal stress gradients on ice-sheet stability

Friday, July 21

10:30 am Joseph Keller, Stanford University
Ponytail motion, Hill's equation and body weight

July 24 - July 28

Monday, July 24

10:30 AM Michael Patterson, Yale University
Shaken not stirred: mixing in stratified flows

Tuesday, July 25

10:30 AM

Goran Bjork, Goteborg University

Thermodynamic response of sea ice with a thickness distribution

Wednesday, July 26

10:30 AM

Christian Schoof, University of British Columbia

Glaciers rubbed the wrong way

2:30 PM

Norm Lebovitz, University of Chicago

Low-dimensional models of subcritical instability in shear flows

Thursday, July 27

10:30 AM

Robert Bindshadler, NASA Goddard Space Flight Center

The new view of ice sheet dynamics

2:30 PM

Petri Fast, Lawrence Livermore National Laboratory

Simulating moving boundaries in thin liquid layers

Friday, July 28

10:30 AM

Keith Moffatt, University of Cambridge

Time-periodic flow in a corner at low Re

July 31 - August 4

Monday, July 31

2:30 PM

Andrew Fowler, Oxford University

Dynamical problems in glaciology

Tuesday, August 1

10:30 AM

Dale Winebrenner, University of Washington

Do martian ice caps flow

Wednesday, August 2

10:30 AM

Sridhar Anandakrishnan, Pennsylvania State University

Peeling back the ice layers by listening to what lies beneath

2:30 PM

Paul Dellar, Imperial College

Derivation of macroscopic equations for rarified gases by elimination of fast variables

Thursday, August 3

10:30 AM

Doug MacAyeal, University of Chicago

H-Bombs, icebergs and other GFD problems

2:30 PM

Tom Neumann, University of Vermont

Wind Pumping, porous media and the fate of ice sheets

Friday, August 4

10:30 AM

Sophie Nowicki, University College of London

Transition zones in ice sheets

August 7 - August 11

Monday, August 7

10:30 AM

Andrew Belmonte, Pennsylvania State University

Cavity ripples in water

Tuesday, August 8

10:30 AM

Herb Keller, CalTech

Orbital calculations and mission design

Wednesday, August 9

10:30 AM

James McElwaine, University of Cambridge

Avalanches

2:30 PM

Keith Moffatt, University of Cambridge

Rattleback diversions & the geodynamo

Thursday, August 10

10:30 AM

Alan Rempel, University of Oregon

The stress of it all...the entire glacier

2:30 PM

Jun Zhang, New York University

Experimental attempts to simulate continental drift

Friday, August 11

10:30 AM

Predrag Cvitanovic, Georgia Tech

The demise of Spiegel's periodic orbits in turbulence relativity for cyclists

6:00 PM

Ed Spiegel, Columbia University

On the bifurcation of species

August 14-15

Monday, August 14

2:30 PM

Eliza Calder, S.U.N.Y. at Buffalo

Of things Strombolian

Tuesday, August 15

10:30 AM

Louis Howard, M.I.T./Florida State University

What good is a tetrakaidecahedron

August 22 - August 25

FELLOWS' PRESENTATIONS

Monday, August 22

10:30 AM

Robert Style, Cambridge University

Salty droplets: solidification and instabilities

Tuesday, August 22 (continued)

1:30 PM Rachel Zammett, Oxford University
Dambusters: Catastrophic incisions in natural dams

2:45 PM Dominic Vella, Cambridge University
On thin ice

Wednesday, August 23

10:00 AM Shane Keating, University of California, San Diego
Mush! Convective patterns in mushy layers

11:15 AM Devin Conroy, University of California, San Diego
Growth of a mushy layer in a corner flow

2:15 PM Daniel Goldberg, New York University
Glancing interactions of large internal waves

3:30 PM Victor Tsai, Harvard University
Ice stars

Thursday, August 24

10:00 AM Take Okabe University of Texas
Mixing efficiency

11:15 AM Ian Eisenman, Harvard University
Arctic catastrophes in an idealized sea ice model

GFD 2006 Lecture 1: Introduction to Ice

Grae Worster; notes by Rachel Zammett and Devin Conroy

March 15, 2007

1 Introduction

Our aim in this course is to understand some of the processes associated with ice in the natural environment. Figure 1 shows the location of some of Earth's ice during the northern winter. These ice deposits may be categorized as sea ice, ice sheets and shelves, and permafrost.

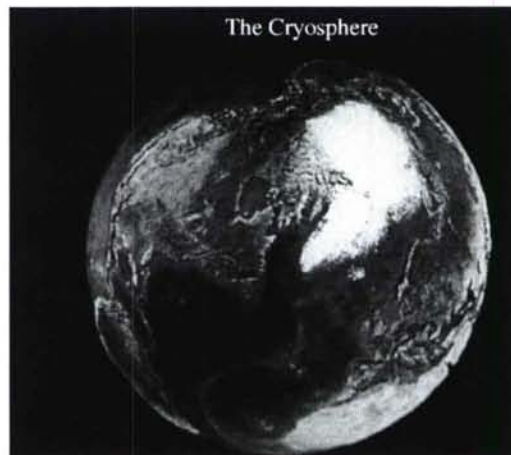


Figure 1: Satellite image showing the ice cover in the northern hemisphere during northern winter, showing sea ice lying in the Arctic basin, the permanent ice sheet over Greenland and permafrost in the exposed land surface.

2 Ice sheets

Firstly, figure 1 shows the ice sheet that covers approximately 80% of Greenland. This is about 10^5 years old and reaches depths of 2–3 kilometers. On large scales, ice can be treated as a highly viscous, non-Newtonian fluid that can flow because it is a polycrystalline solid and contains a percentage of unfrozen water (figure 2). Looking on a scale of about $100\mu m$,

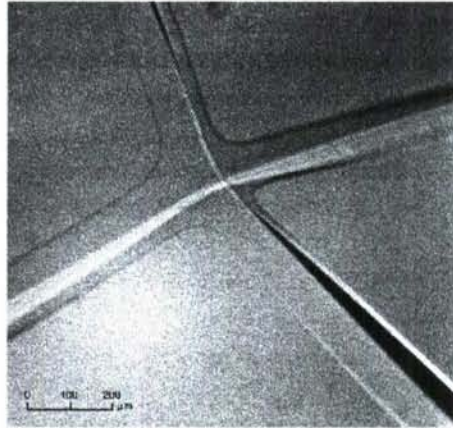


Figure 2: Image of the intersection of four ice grains. Between these grains lie the veins containing liquid water and dissolved impurities. The scale bar on this picture is $100\ \mu\text{m}$.

we can see the ice grain junctions and the veins which lie between them. The liquid water contained in the veins between the ice crystals lubricates the flow, allowing the ice to flow more easily. This water can also transport dissolved impurities, which will therefore move relative to the ice crystals; this is important when analyzing ice cores, for example.

Figure 2 also shows that there is a curvature to the solid–liquid interface which is associated with the surface energy of the phase boundary. We will see later that this surface energy sets the scales for morphological instabilities of the solid–liquid interface, such as those seen in snowflakes (figure 4).

The grounded ice cap flows slowly towards the coast, sometimes flowing into floating ice shelves, which ultimately break up to form icebergs. Projects such as the Greenland Ice Core Project (GRIP) have obtained deep ice cores from near Greenland’s summit. Analyzing the properties of the ice cores, such as oxygen isotope ratios, allow inferences about the ancient climate to be drawn.

In figure 3 we see the flow from the grounded ice sheet to a floating ice shelf (Larsen B) in Antarctica. At the edge of the ice shelf we see the calving of icebergs; this is responsible for approximately 80% of the mass lost from Antarctica. The icebergs are composed predominantly of freshwater ice, as the ice which comprises the ice sheets first fell as snow. Owing to the density difference between water and ice, approximately 90% of the volume of an iceberg is below the surface of the ocean.

When these icebergs come into contact with the warm, salty ocean they ablate, providing a freshwater flux to the ocean. This is important as the production of deep ocean waters is sensitive to changes in the freshwater budget.

3 Sea ice

Secondly, there is the sea ice which fills the Arctic basin and is formed by direct freezing of the ocean. It is typically 1–3 m thick and less than 10 years old; in its first year, sea

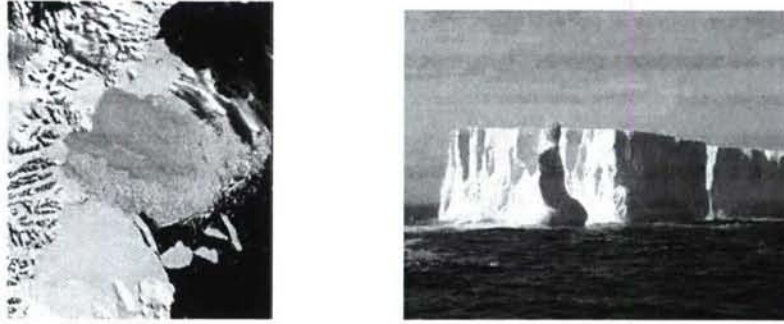


Figure 3: (left) Satellite image of the Larsen B ice shelf on the coast of Antarctica. Near the edge of the ice shelf, it is possible to see the icebergs formed by calving. (right) An example of an iceberg formed by calving at the edge of an ice sheet or ice shelf. Here the vertical face is 30 m above the surface of the ocean, meaning that approximately 300 m of ice lie below the surface.

ice typically grows to a depth of 1 m. This relative youth (in comparison to ice sheets or glaciers, for example) is caused by the movement of sea ice by polar winds and ocean currents to warmer waters, where it melts.

Many of the structures and processes observed in sea ice develop because the thermal diffusivity of heat is much larger than the diffusivity of salt. In this course we shall see that sea ice can be considered as an inhomogeneous porous medium. While sheet ice only contains water in the veins between ice crystals, sea ice has a much higher porosity (approximately 10 % in old ice and up to 40 % in new ice). The porous nature of sea ice means that it can also be modified by internal convection.

We shall consider sea ice to be a mushy layer, which is a two-phase reactive porous medium. We see in figure 4 that it is not macroscopically solid; instead, it is composed of ice platelets with salty brine between them. The platelets which form are composed of pure ice crystals, as the crystals reject the salt contained in the ocean water. Some of this rejected salt convects into the ocean below the sea ice, and the rest remains between the crystals.

This convection is also seen in the laboratory. Figure 5 shows shadowgraph pictures of sea ice growing in a laboratory. In figure 5 (left) when the sea ice is only 3 cm thick, it is possible to see some convection occurring in the salt water below it, but it is small scale and has no obvious structure. However, when the ice has grown to a thickness of about 13 cm (figure 5), it is possible to see strong convective plumes in the water below. These have a high salt content and therefore deliver a large flux of salt to the water below. We shall see that there is a critical ice thickness at which such plumes occur; this criterion for the onset of convection is determined by a form of Rayleigh number.

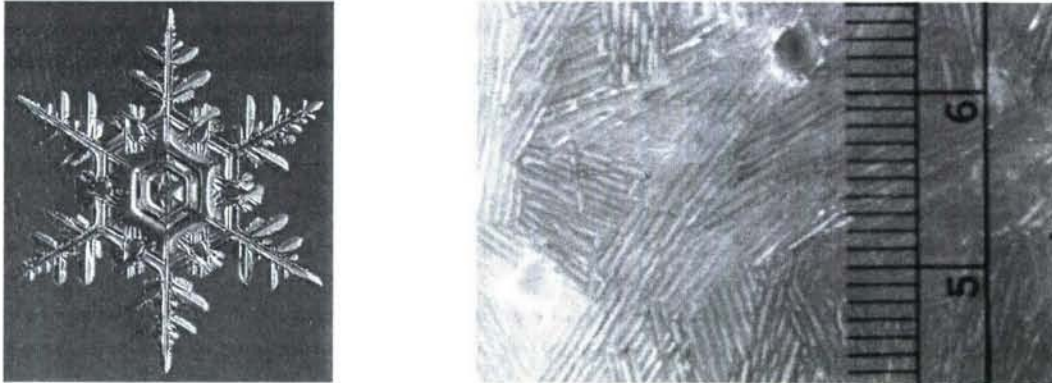


Figure 4: (left) Picture of a snowflake. Here the smallest scale at which instabilities occur is comparable to the radius of the tip of one of the needles. (right) Horizontal cross section of sea ice, showing both ice platelets and brine channels. The ice platelets are typically less than 1 mm wide and form a porous matrix, which allows convection and the erosion of such channels by the rejection of salt. These channels have a diameter of a few millimetres.

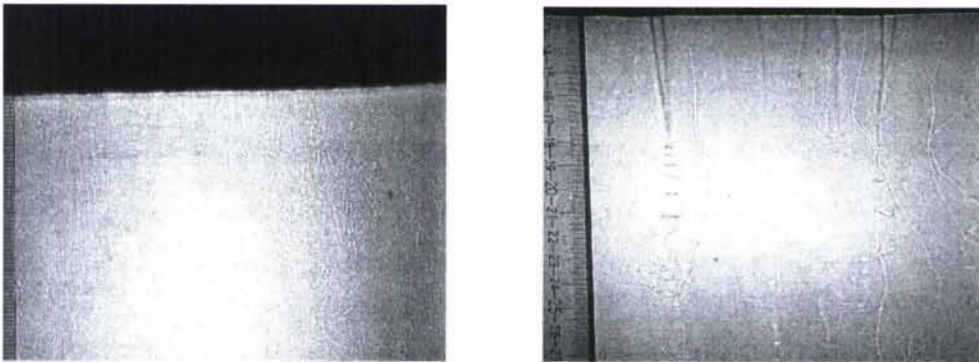


Figure 5: (left) Image of sea ice growing in the laboratory. At this time, the layer of ice (the dark upper region) is 3 cm thick, and it is possible to see some convection occurring below it. (right) Image of sea ice growing in the laboratory where the layer of ice is now 13 cm thick, and it is possible to see the salty convective plumes below it. It is also possible to see the 'pinching' instability at the base of these plumes. Note that the scales of the images are different.



Figure 6: (left) An example of erosion caused to a rockery by winter frost. (right) Stone circles as an example of differential frost heave.

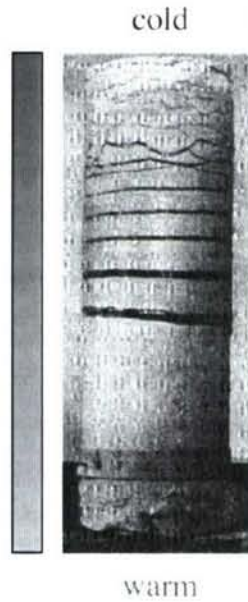


Figure 7: (left) Ice needles protruding from soil. (right) Photograph of a column of water-saturated soil cooled at the top (Taber, 1929). The black regions are ice lenses, which contain no soil; between these are regions of partially frozen soil. There may also be ice between the soil particles below the lowest lens.

4 Permafrost

The final type of ice we shall consider is permafrost, or permanently frozen ground (defined as remaining below 0°C for more than two years). It occurs both on land and beneath offshore Arctic continental shelves, and its thickness ranges from less than one meter to greater than 1 kilometer. Permafrost underlies about 15% of the exposed land surface in the Northern Hemisphere and causes deformation of the ground; we shall be looking at this and the associated flows.

Figure 6 shows the effects of ice damage to rocks and buildings if they are eroded by winter frost. The ground may also ‘heave’, i. e. rise upwards due to water being pulled up from the unfrozen ground below. Differential frost heave may form patterned ground, such as hummocks and the stone circles seen in figure 6. Underlying this is the force of separation between ice and other materials: in this context, we will consider the other materials to be silicates. We will consider how ice pushes on another material forming, for example, the ice needles seen in figure 7.

There are still some puzzles remaining. Figure 7 shows a laboratory experiment by Taber where a column of water-saturated soil was frozen by cooling at its top. It might be expected that a freezing front which moves downwards is observed, but instead a sequence of layers of alternating pure ice and partially frozen soil forms.

5 Student Problem

If two identical ice cubes are placed in glasses of water and whisky, where the liquids are at the same temperature, it is observed that the ice cube in the whisky melts more quickly than that in the water. Why? (Hint: It is not because the melting point of ice is lower in whisky than in water.)

Answer

Initially when the ice cube is placed into a glass of whisky at room temperature the ice melts, forming a layer of cold freshwater adjacent to the phase boundary. Since water is denser than alcohol and the the melted water is colder than the whisky, a plume forms that convects the cool fresh water downwards and brings warmer fluid with a higher alcohol concentration upwards. This convective mixing of the liquid below the ice cube supplies a heat flux at the phase boundary; this flux is stronger than the diffusive heat flux in the absence of convection.

6 Stefan Condition

The distinguishing feature of solidification or melting is the evolution of a phase boundary which separates solid and liquid. The speed of this interface can be determined by energy conservation, as illustrated in figure 8, which relates the rate of energy absorption or release to the difference in heat fluxes across this boundary. This is formulated mathematically as follows by considering a control volume around the phase boundary

$$\mathbf{q}_s \cdot \mathbf{n} - \mathbf{q}_l \cdot \mathbf{n} - \rho V_n H_s + \rho V_n H_\ell = 0 \Rightarrow \rho L V_n = \mathbf{n} \cdot (\mathbf{q}_l - \mathbf{q}_s). \quad (1)$$

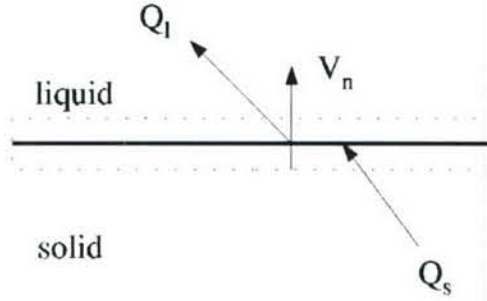


Figure 8: Illustration showing the control volume taken around the phase boundary and the energy fluxes into and out of it.

Here $\mathbf{q} = -k\nabla T$ is the heat flux from Fourier's law, k is thermal conductivity, \mathbf{n} is the unit normal vector pointing from solid to liquid, ρ is the density (assumed to be the same in each phase), V_n the interface velocity, H is the enthalpy, $L = H_\ell - H_s$ is the latent heat and subscripts s and ℓ denote solid and liquid respectively. We assume that the phase boundary is in equilibrium, implying that the temperature is constant on either side of the interface. This equation is known as the Stefan condition, attributed to Stefan in 1891.

7 Problem 1

We consider a problem posed by Stefan in 1891, where solid ice is growing into relatively warm ($T_m > T_B$) water from a cooled boundary at $z = 0$ (figure 9). We assume that the liquid portion is at the melting temperature T_m initially and therefore remains at this temperature. The governing equation is given by the thermal diffusion equation

$$\rho c_p \frac{\partial T}{\partial t} = \frac{\partial}{\partial z} \left(k \frac{\partial T}{\partial z} \right) \Rightarrow \frac{\partial T}{\partial t} = \kappa \frac{\partial^2 T}{\partial z^2}, \quad (2)$$

where the conductivity $k = \rho c_p \kappa$ is assumed to be constant and the thermal diffusivity is represented by κ . The boundary conditions for this equation are then

$$T(t, z = 0) = T_B, \quad T(t, z = a(t)) = T_m, \quad (3)$$

where $z = a(t)$ denotes the interface position and the unknown interface velocity is determined by the Stefan condition

$$\rho L \frac{da}{dt} = k \left. \frac{\partial T}{\partial z} \right|_{z=a(t)}. \quad (4)$$

7.1 Solution

This problem can be solved using a similarity solution, as there is no intrinsic length scale in the problem. We can determine the form of this similarity variable using a scaling analysis

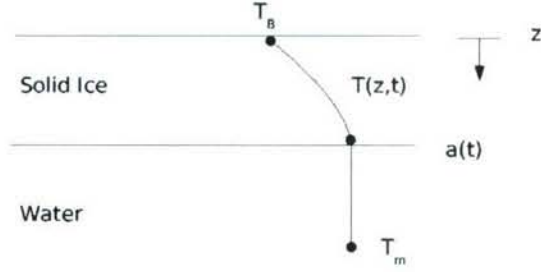


Figure 9: Growth of a planar solid into a liquid, maintained at the melting temperature T_m from a cooled boundary maintained at temperature T_B . The position of the interface as a function of time is given by $a(t)$.

and show that a fixed length scale cannot be formed. Let us define the appropriate scales, $\Delta T = T_m - T_B$, D and τ for the temperature, length of the domain and time respectively. From the diffusion equation (2) and the Stefan condition (8) we obtain the following

$$\frac{\Delta T}{\tau} \sim \kappa \frac{\Delta T}{D^2} \Rightarrow D \sim \sqrt{\kappa \tau}, \quad (5)$$

$$\rho L \frac{D}{\tau} \sim k \frac{\Delta T}{D} = \rho c_p \kappa \frac{\Delta T}{D} \Rightarrow D \sim \sqrt{\kappa \tau} S^{-1/2}, \quad (6)$$

where $S = L/(c_p \Delta T)$ is the Stefan number. Since the relationships between D and τ in (5) and (6) are the same, there is no intrinsic length scale, and a similarity solution is possible. In addition there therefore is no time scale so we choose $\tau = t$, the actual time, in which case $D \sim \sqrt{\kappa t}$.

We introduce the dimensionless variable f such that

$$T - T_B = \Delta T f\left(\frac{z}{D}, \frac{t}{\tau}\right) = \Delta T f\left(\frac{z}{\sqrt{\kappa t}}, 1\right) = \Delta T f(\eta). \quad (7)$$

We choose $\eta = z/2\sqrt{\kappa t}$ for mathematical convenience, as the similarity variable may be multiplied by an arbitrary constant. In addition we know from scale analysis, using the diffusion equation, that length and therefore interface position can be assumed to have the form

$$a = 2\mu\sqrt{\kappa t}, \quad (8)$$

where the parameter μ must be determined as part of the solution. Rewriting the model in terms of the similarity variable, we arrive at the final set of non-dimensional equations

$$f'' = -2\eta f', \quad (9)$$

$$f(\eta = 0) = 0, \quad (10)$$

$$f(\eta = \mu) = 1, \quad (11)$$

$$2S\mu = f'(\eta = \mu). \quad (12)$$

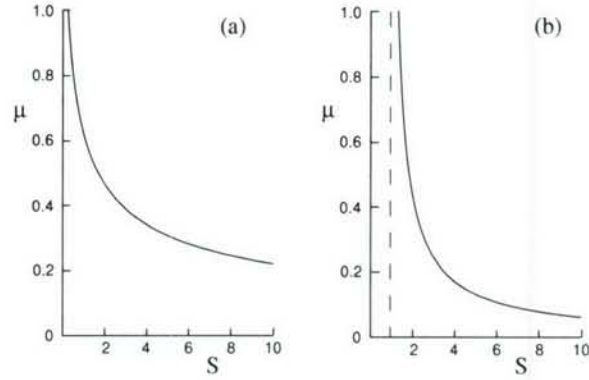


Figure 10: (a) Solution to equation (17) for the eigenvalue μ as a function of the Stefan number, S . (b) Solution to equation (7) of Lecture 2.

The solution to equation (9) is determined using an integrating factor and determining

$$f' = c_1 e^{-\eta^2} \Rightarrow f = c_1 \int_0^\eta e^{-y^2} dy + c_2 \Rightarrow f = \hat{c}_1 \text{erf}(\eta) + c_2. \quad (13)$$

The error function, $\text{erf}(\eta)$, is defined by

$$\text{erf}(x) = \frac{2}{\sqrt{\pi}} \int_0^x e^{-u^2} du, \quad (14)$$

with the following properties

$$\text{erf}(0) = 0, \quad (15)$$

$$\text{erf}(\infty) = 1. \quad (16)$$

Boundary condition (10) implies that $c_2 = 0$ and boundary condition (11) gives $\hat{c}_1 = 1/\text{erf}(\mu)$. Finally the Stefan condition (12) gives us an parameter equation to be solved for the parameter μ . From equation (12) we then have

$$\frac{1}{S} = \sqrt{\pi} \mu \text{erf}(\mu) e^{\mu^2} = F(\mu). \quad (17)$$

In figure 10 we plot the parameter μ as a function of Stefan number. We see that the growth speed increases as the Stefan number decreases, which corresponds to increasing the driving temperature difference or decreasing the amount of energy required to melt a unit mass of solid. We should note that the interface position is given by $a \propto \sqrt{t}$ and the interface velocity by $\dot{a} \propto 1/\sqrt{t}$ so that the growth rate of a solid decreases with time.

7.2 Quasi Stationary Approximation

For large Stefan numbers we have relatively small sensible heat compared to latent heat and the growth rate will be slow compared to the thermal diffusion rate. In this case, the temperature field will evolve more rapidly than the boundary position and we have a quasi-steady state regime for the the diffusion equation. This implies a linear profile of the solid

temperature that is slowly decreasing in slope as the boundary moves. Integrating Laplace's equation twice and applying boundary conditions given in (3) we obtain the linear solution

$$T = T_B + (T_m - T_B) \frac{z}{a}. \quad (18)$$

Substituting this solution into the Stefan condition (12) we arrive at the following expression for the interface position a

$$a \frac{da}{dt} = \frac{1}{S}, \quad a(0) = 0 \quad \Rightarrow \quad a = \sqrt{\frac{2}{S}} \sqrt{\kappa t}. \quad (19)$$

8 Student Problem

Question

Solve the Stefan problem given in problem 1 for the case $\rho_s \neq \rho_\ell$.

Answer

When the density between the solid and liquid differ by an appreciable amount there will be a normal velocity to the phase change surface due to the expansion or contraction of the liquid as it solidifies. To formulate this effect mathematically we draw a control volume around the moving surface and conserve mass and energy as follow

$$\frac{d}{dt} \int_V \rho dV = \int_S \rho_s (\dot{a} - V_s) dS_s - \int_S \rho_\ell (\dot{a} - V_\ell) dS_\ell, \quad (20)$$

$$\frac{d}{dt} \int_V \rho H dV = \int_S \rho_s H_s (\dot{a} - V_s) + \mathbf{n} \cdot \mathbf{q}_s dS_s - \int_S \rho_\ell H_\ell (\dot{a} - V_\ell) + \mathbf{n} \cdot \mathbf{q}_\ell dS_\ell. \quad (21)$$

In the limit as $dx \rightarrow 0$ the amount of mass and energy stored within the control volume becomes negligible and we are left with the following relationships

$$\rho_s (\dot{a} - V_s) = \rho_\ell (\dot{a} - V_\ell), \quad (22)$$

$$\rho_s H_s (\dot{a} - V_s) + \mathbf{n} \cdot \mathbf{q}_s = \rho_\ell H_\ell (\dot{a} - V_\ell) + \mathbf{n} \cdot \mathbf{q}_\ell. \quad (23)$$

Since there is no motion in the solid, $V_s = 0$ and the mass conservation relation gives us a relationship for the fluid velocity. Substituting this relationship into the energy conservation equation and noting that $L = H_s - H_\ell$ we obtain the modified Stefan condition. These conditions are

$$V_\ell = \frac{da}{dt} \left(\frac{\rho_\ell - \rho_s}{\rho_\ell} \right), \quad (24)$$

$$\rho_s L \frac{da}{dt} = (\mathbf{q}_\ell - \mathbf{q}_s) \cdot \mathbf{n}. \quad (25)$$

The addition of a fluid velocity on the liquid side adds an advective component to the governing temperature equation. The new model can be solved by a similarity solution

as a simple extension of the last section, but does not yield any new results. Since the temperature profile is homogeneous initially it must remain so for all time. On the other hand, if the liquid were under-cooled (as we shall see in the third lecture) or if we were melting the solid, the advective component would give a small correction to the interface speed as long as $\rho_s \approx \rho_\ell$.

References

- [1] Taber, S. 1929. Frost heaving. *J. Geol.*, 37, 428-461.

GFD 2006 Lecture 2: Diffusion-controlled solidification

Grae Worster; notes by Victor Tsai and Dan Goldberg

March 15, 2007

1 Finishing off Lecture 1

As shown in Lecture 1, an approximation for the diffusion time is

$$t = \frac{a^2}{\kappa}. \quad (1)$$

An experiment was conducted using a commercial hand warmer. This is a plastic bag containing a liquid (an aqueous solution of sodium acetate) in a metastable state i.e. at a temperature below its freezing point. Crystallisation is initiated by flexing a thin metal disk contained in the bag and was observed to proceed at a rate of about 1 cm s^{-1} . Taking $a = 10 \text{ cm}$, $\kappa = 10^{-2} \text{ cm}^2/\text{s}$ gives $t \approx 10^4 \text{ s} \approx 3 \text{ hrs}$ using equation (1). A different mechanism must operate in the heat pack than was analysed in Lecture 1. We will return to this later.

2 Diffusion-Controlled Solidification into a Supercooled Liquid

Instead of considering a solid cooled from a boundary, we now consider a solid, assumed to be at T_m , surrounded by a liquid with far-field temperature given by $T_\infty < T_m$ so that the liquid is supercooled. Again, we only consider a one-dimensional problem, with $x = 0$ at the center of the solid and $x = a(t)$ at the solid-liquid interface. We solve the diffusion equation (in the liquid) with the Stefan condition and with appropriate temperature boundary conditions ($T(a) = T_m$ and $T(\infty) = T_\infty$):

$$\frac{\partial T}{\partial t} = \kappa \frac{\partial^2 T}{\partial x^2}, \quad (2)$$

$$\rho L \dot{a} = -k \frac{\partial T}{\partial x} \Big|_{a^+}. \quad (3)$$

As before, we scale the equations and arrive at the similarity solution

$$\eta = \frac{x}{2\sqrt{\kappa t}}, \quad (4)$$

$$T = T_\infty + (T_m - T_\infty) \frac{\text{erfc}(\eta)}{\text{erfc}(\mu)}, \quad (5)$$

$$a = 2\mu\sqrt{\kappa t}, \quad (6)$$

$$\frac{1}{S} = F(\mu), \quad (7)$$

where

$$F(x) = \sqrt{\pi}xe^{x^2}\operatorname{erfc}(x). \quad (8)$$

Plotting $F(x)$, we find that $F(0) = 0$, and $F(x)$ has a maximum of 1 as $x \rightarrow \infty$ (see figure 10b of Lecture 1). Thus, no similarity solution exists for $1/S > 1$ or $S < 1$. In fact, all solutions become unbounded for $S < 1$. This inconsistency is remedied by relaxing the assumption of $T = T_m$ at the interface since this is strictly only true in equilibrium. For $S < 1$, however, growth is rapid, we are far from equilibrium, and molecular attachment kinetics are important. For ice, it is typically observed that attachment and detachment occur at a rate of approximately 1000 molecular layers per second. Below 0°C attachment is faster than detachment and above 0°C attachment is slower than detachment. The velocity of the boundary \dot{a} is proportional to the difference between attachment and detachment. Thus, our revised problem is given by: Diffusion equation (2) in $x \geq a$; Stefan condition (3) at $x = a$; $T(\infty) = T_\infty$; $T(a) = T_i$; and $\dot{a} = \mathcal{G}(T_m - T_i)$, where \mathcal{G} is a constant.

We again scale length with λ , time with τ and temperature difference with $\Delta T = T_m - T_\infty$. This results in

$$\lambda \sim \frac{\kappa}{\mathcal{G}\Delta T}, \quad (9)$$

$$\tau \sim \frac{\kappa}{\mathcal{G}^2\Delta T^2}. \quad (10)$$

Using the scaling $a = \lambda a'$, $x = \lambda x'$, $T = T_\infty + \Delta T \cdot \theta$, substituting and dropping primed notation results in

$$\frac{\partial \theta}{\partial t} = \frac{\partial^2 \theta}{\partial x'^2}, \quad (11)$$

$$S\dot{a} = -\left.\frac{\partial \theta}{\partial x}\right|_{a'}, \quad (12)$$

$$\dot{a} = 1 - \theta_i, \quad (13)$$

$$\theta(\infty) = 0 \quad \theta(a) = \theta_i. \quad (14)$$

We now consider two limits. If $S \gg 1$, then (12) gives $\dot{a} \ll 1$ so $\theta_i = 1 + O(S^{-1})$ or dimensionally, $T_i \approx T_m$, the analysis from lecture 1 holds and we recover the similarity solution presented there. If $S \ll 1$, then (12) does not constrain \dot{a} which is instead determined by the kinetic equation (13), which suggests looking for a solution of the form $\dot{a} = V$ where V is constant. Hence, we try $\theta = \theta(\eta)$, where $\eta = x - Vt$. Substitution leads to

$$\theta = \theta_i e^{-V\eta}, \quad (15)$$

$$a = Vt, \quad (16)$$

$$\theta_i = S, \quad (17)$$

and

$$V = 1 - \theta_i = 1 - S, \quad (18)$$

which is valid (exactly) if $S < 1$.

Finally, we note that the discrepancy between applying kinetics and using the previous ($S > 1$) similarity solution is typically small, especially at large time when the kinetic solution asymptotes to the similarity solution. Therefore, kinetics can often be neglected in many problems involving sea ice, for example.

3 Generalized Clapeyron Equation for Interfaces in Equilibrium

For a planar interface and at some reference pressure, the melting temperature is set by a balance of the temperature-dependent rates of the attachment and detachment of the solid phase – this is the reference melting/freezing point. But modification of the system pressure or a pressure difference between the solid and liquid phase can cause changes in the equilibrium interfacial temperature. The relation governing this phenomenon is

$$\frac{\rho_s L (T_m - T_e)}{T_m} = (p_s - p_l) + (p_l - p_m) \left(1 - \frac{\rho_s}{\rho_l}\right), \quad (19)$$

where T_m, p_m are the reference melting point and pressure. There are several examples of this effect that will appear later in these proceedings, briefly mentioned below.

3.1 Change in system pressure

Across a planar interface, pressures will be equal when the system is in mechanical equilibrium. But the overall system pressure may be elevated (or decreased), for example by hydrostatic effects. In this case the second term on the right-hand side of the Clapeyron equation comes into effect, with p_l equal to p . It is easy to see that the rate of change of the melting point with respect to pressure is given by

$$\frac{dT_e}{dp} = -\frac{T_m}{\rho_s L} \left(1 - \frac{\rho_s}{\rho_l}\right). \quad (20)$$

For example, in the ocean this allows us to find the melting point at depth. Hydrostatic balance gives us

$$\frac{dT_e}{dz} = -\rho_l g \frac{dT_e}{dp} \approx 7.5 \times 10^{-4} \text{K/m}. \quad (21)$$

3.2 Curved interface

At a curved interface, there is a force involved with the interfacial energy that factors into the force balance, and results in an imbalance between p_l and p_s . This is expressed by

$$p_s - p_l = \gamma(\nabla \cdot \mathbf{n}). \quad (22)$$

Here γ is the interfacial energy and \mathbf{n} is the unit normal to the interface, directed into the liquid. With $p = p_l$, this gives

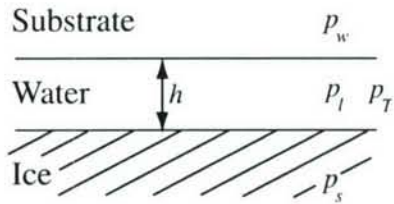


Figure 1: Interfacial premelting of a solid below the melting point. The hydrodynamic pressure (p_l) is lower than p_s because of the thermomolecular pressure p_T .

$$T_e = T_m - \Gamma(\nabla \cdot \mathbf{n}) \quad (23)$$

where

$$\Gamma \equiv \frac{\gamma T_m}{\rho_s L}. \quad (24)$$

Equation (23) is known as the Gibbs-Thomson equation.

3.3 Interfacial Premelting

When a solid near its bulk melting point is in contact with a gas or solid substrate, it is sometimes thermodynamically favorable for there to be a (very) thin liquid film between the solid and the substrate (figure 1). Among the determining factors are the interfacial energies per unit area between the solid and its liquid, the solid and the substrate, and the liquid and the substrate.

The liquid pressure in the film is actually lowered relative to the solid pressure, since intermolecular forces play a part in the mechanical equilibrium balance. This pressure difference is described as a Thermomolecular Pressure. A drop in interfacial temperature follows from the Clapeyron equation.

In thermodynamic terms, the chemical potential of the liquid – that is, the incremental change in free energy with respect to the addition of new material – is not equal to that of the solid, as it would be in a bulk equilibrium state, since intermolecular interaction potentials must be accounted for in minimizing the free energy of the system. The chemical potential is a state variable, and its change is accompanied by a change in hydrodynamic pressure.

4 Nucleation

The Gibbs-Thomson effect is nicely illustrated by a simple model of a solid particle nucleating into a supercooled liquid domain (figure 2). The dynamics of the initial formation of the particle are complex, but we will ignore such details and assume that the necessary events have already taken place for there to be a spherical solid particle with finite radius a at time t . The ambient temperature of the liquid is below its melting point, and furthermore, as before, we will assume that the Stefan number is large and make a quasi-stationary

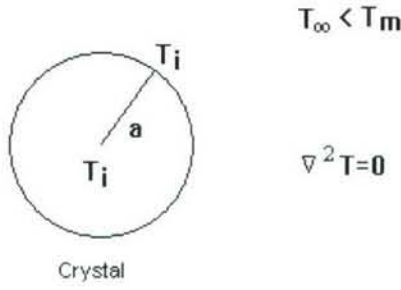


Figure 2: Nucleated spherical crystal in supercooled liquid with high Stefan number.

approximation, so that temperature is harmonic in the liquid and in the solid. Thus our system of equations is

$$\nabla^2 T = \begin{cases} 0 & r > a \\ 0 & r < a \end{cases}, \quad (25)$$

$$T = \begin{cases} T_\infty & r \rightarrow \infty \\ T_m - \Gamma(\nabla \cdot \mathbf{n}) & r = a \end{cases}. \quad (26)$$

This system is solvable for a given a , even though a is changing in time. Curvature is constant over the surface of the sphere (and is equal to $2/a$), so the equation and boundary conditions are spherically symmetric and we expect a symmetric solution. The temperature field in the solid is easy to diagnose: a harmonic function in a bounded domain with constant boundary condition is itself constant (and therefore the only flux at the interface is that on the liquid side). Our Stefan condition is then

$$\rho L \dot{a} = -k \frac{\partial T}{\partial r} \Big|_{r=a+}. \quad (27)$$

Given the spherical symmetry of the problem, the temperature field in the liquid must have the form $A + Br^{-1}$. Using the boundary conditions, we can deduce that, for $r > a$,

$$T = T_\infty + (T_m - \frac{2\Gamma}{a} - T_\infty) \frac{a}{r}. \quad (28)$$

With an isothermal solid, the Stefan condition then gives us

$$\rho L \dot{a} = ka^{-1} (T_m - \frac{2\Gamma}{a} - T_\infty). \quad (29)$$

Rather than solve for $a(t)$ exactly, it is instructive to examine the sign of the R.H.S. of (29) and also to consider the limiting cases of small and large radii. First, note that a is increasing (decreasing) when it is larger (smaller) than a critical radius, $a_c \equiv 2\Gamma / (T_m - T_\infty)$. So a_c is an unstable fixed point; larger particles will grow, and smaller particles will shrink.

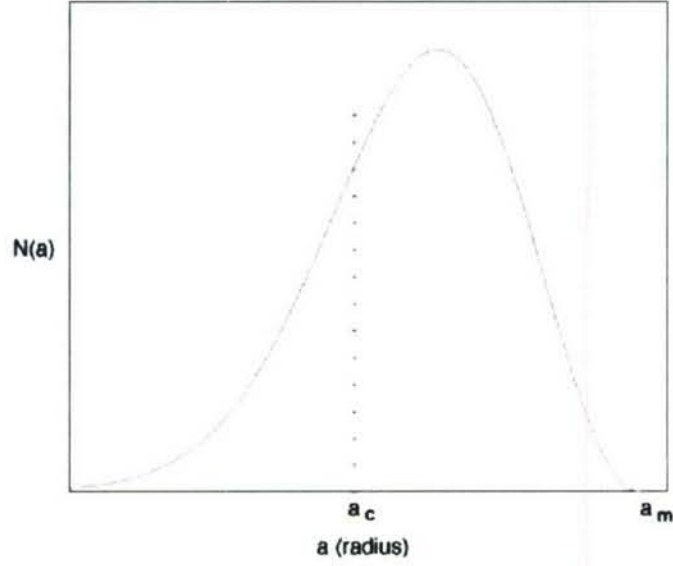


Figure 3: Scaled distribution of population of nucleating particles

(Note that this is just in our simple model – we are considering a single particle in a liquid whose far-field temperature does not change; see the discussion below.)

Furthermore, we can approximate the growth rate in the limit of large and small radii. For $a \gg a_c$, \dot{a} is nearly proportional to a^{-1} , and we get

$$a(t) \approx \sqrt{\frac{2\kappa t}{S}}. \quad (30)$$

On the other hand, for $a \ll a_c$, (29) becomes

$$\rho L \dot{a} \approx \frac{-2k\Gamma}{a^2} \quad (31)$$

$$\Rightarrow a(t) \approx \sqrt[3]{a(0)^3 - \frac{6k\Gamma}{\rho L}}, \quad (32)$$

so the solid disappears in finite time.

Though we do not give the details, it is worth noting the case where there is an entire population of nucleating crystals, and the temperature of the system away from a crystal is not constrained (indeed, there is heat being given off by the solidification, and so the system temperature on the whole will be increasing). An interesting result is that the resulting distribution of particle size is self-similar, meaning that the probability distribution function, scaled by $t^{\frac{1}{3}}$ (**not** by $t^{\frac{1}{2}}$), remains constant in time. Such a distribution is shown in figure 3. Note that there is a finite cutoff (denoted by a_m) since particles will not grow to arbitrarily large size after finite time.

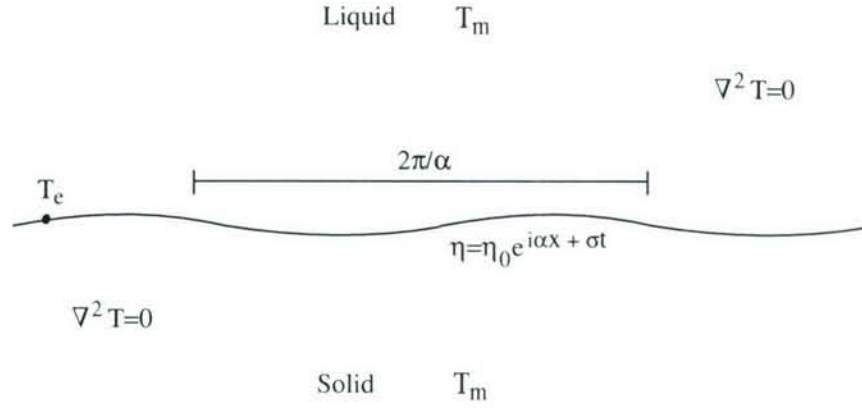


Figure 4: Student Problem

5 Student Problem

Consider perturbations to a 1-D planar interface in a 2-D system with large Stefan number and far-field temperature equal to the bulk melting point. The interface has an energy associated with it, and the disturbance has a small amplitude compared with its wavelength. For small times, and neglecting kinetics, how would the interface evolve?

Solution. Since the perturbation is small, this problem can be linearized, neglecting higher order terms in the small parameter $\eta_0\alpha$, where η_0 is the perturbation amplitude and α is its wavenumber. With large Stefan number we can make a quasi-stationary approximation and assume temperature is harmonic in both the liquid and solid domains (but not across the interface). Our equations are as follows:

$$\nabla^2 T = \begin{cases} 0 & z > \eta \\ 0 & z < \eta \end{cases}, \quad (33)$$

$$T = \begin{cases} T_m & z \rightarrow \pm\infty \\ T_m - \Gamma(\nabla \cdot \mathbf{n}) & z = \eta \end{cases}, \quad (34)$$

along with the Stefan condition

$$\dot{a} = -\frac{k}{\rho L} \frac{\partial T}{\partial n} \Big|_{z=\eta^+} + \frac{k}{\rho L} \frac{\partial T}{\partial n} \Big|_{z=\eta^-}, \quad (35)$$

where \dot{a} is the normal velocity of the interface, which is equal to

$$(\sqrt{1 + \eta_x^2})^{-1} \frac{\partial \eta}{\partial t}. \quad (36)$$

From the equation for the interface position $z - \eta(x, t) = 0$ we can determine

$$\mathbf{n} = \frac{(-\eta_x, 1)}{(1 + \eta_x^2)^{1/2}} \quad (37)$$

and

$$\nabla \cdot \mathbf{n} = -\frac{\eta_{xx}}{(1 + \eta_x^2)^{3/2}}. \quad (38)$$

Now we linearize, neglecting higher-order terms, and the problem simplifies. First of all, the smallness of the slope of the interface means that the normal derivative in (35) is a higher-order correction to the vertical derivative, and the smallness of η means that evaluation of the perturbed temperature field at η is a higher-order correction to its evaluation at zero. Likewise, the quadratic term in (36) is dropped, as is the one in (38). Our linearized system of equations is now

$$\nabla^2 T = \begin{cases} 0 & z > 0 \\ 0 & z < 0 \end{cases}, \quad (39)$$

$$T = T_m, \quad z \rightarrow \pm\infty, \quad (40)$$

$$T = T_m + \Gamma\eta_{xx}, \quad z = 0, \quad (41)$$

$$\eta_t = \frac{k}{\rho L} (-T_z|_{0+} + T_z|_{0-}). \quad (42)$$

Since this is a linear problem we can anticipate the form of the solution

$$\eta(x, t) = \eta_0 e^{i\alpha x + \sigma t}, \quad (43)$$

$$T(x, z, t) = T_m + \hat{T}(z) e^{i\alpha x + \sigma t}. \quad (44)$$

$$(45)$$

Laplace's equation and the decay condition along with (41) give

$$\hat{T}(z) = -\alpha^2 \Gamma \eta_0 e^{\mp \alpha z}, \quad (46)$$

depending on whether z is positive or negative. The Stefan condition then shows that

$$\sigma = -\frac{2\alpha^3 \Gamma k}{\rho L}. \quad (47)$$

Thus the interface is stable for all wave numbers and the decay constant is proportional to α^3 . The stabilizing effect is intuitive: “positive” bumps (areas where the solid protrudes into the liquid) have a lowered melting point due to Gibbs-Thomson, while “negative” bumps have elevated melting point. There is then a net heat flux from negative to positive bumps, which causes a melt/freeze pattern that counters the perturbation.

GFD 2006 Lecture 3: Interfacial instability in super-cooled fluid

Grae Worster; notes by Robert Style and Dominic Vella

21 June, 2006

For all the systems that we have considered so far, we have chosen only to model a planar solidification front. In many situations this is not realistic and the interface is in fact subject to instabilities. In this lecture, we consider small perturbations to the planar interface in order to investigate the properties of these instabilities: when do they exist, what is the growth rate of the instability and what is the characteristic length scale? We shall assume non-kinetic growth to simplify the analysis.

1 Mechanism for instability

For a planar solid growing from a cooled boundary, all isotherms in the system are parallel to the solid–liquid interface (see Fig. 1). When we introduce a perturbation onto the interface, the isotherms are deformed in response to the new boundary conditions (as shown in Fig. 1b). As a result of this, the isotherms are bunched where the solid protrudes into the liquid (crests) and are spread out where the solid lags behind (troughs). In the regions where the isotherms are bunched, the temperature gradient is large and so there will be enhanced heat transport from liquid to solid relative to the heat transport in the planar system. The protrusion is therefore eroded. Similarly, less heat will be transported to the troughs and so the rate of solidification is locally increased. These effects act to stabilize the interface by levelling out any deviation from the steady planar state.

For the case of a supercooled melt, the heat flows from the solid towards the liquid. As before, upon introduction of the perturbation, there is bunching of the isotherms above crests on the solid–liquid interface and enhanced spacing of isotherms above the troughs. However, the directions of the heat fluxes are reversed from the previous case, so that heat is transported more rapidly away from the crests and more slowly away from the troughs. This causes the interface to advance more rapidly at the crests, and relatively slower at the troughs, so that any corrugations will grow in amplitude (Fig. 1c). Thus the interface is unstable.

In the student exercise from the previous lecture, we saw that perturbations are stabilized due to the Gibbs-Thomson effect. We found that the curvature of the interface modifies the equilibrium melting temperature to

$$T_e = T_m - \Gamma \nabla \cdot \mathbf{n}, \quad (1)$$

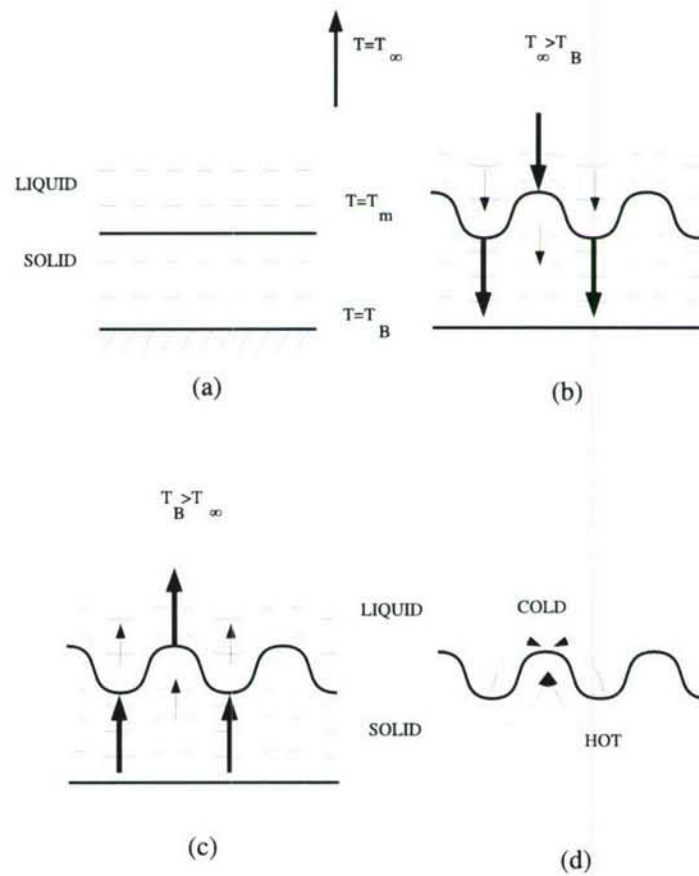


Figure 1: Schematic diagrams showing the direction of heat flow (arrows) during the evolution of the solid–liquid interface. (a) Planar solidification from a cooled front. (b) Stability of a front growing from a cooled boundary. (c) Instability of a front growing into a supercooled melt. (d) Stabilization as a result of the Gibbs-Thomson effect.

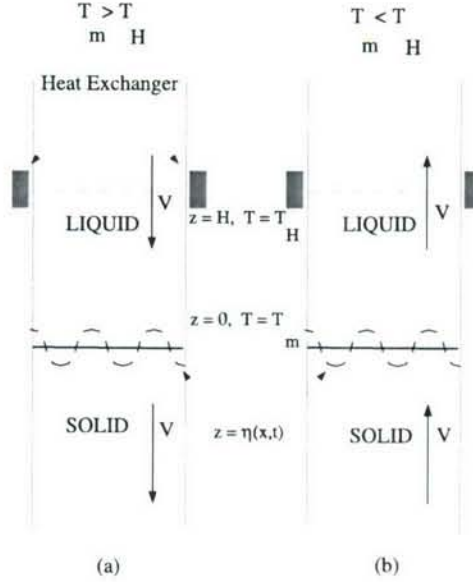


Figure 2: Schematic diagram for (a) solidification of liquid by pulling liquid downwards through a cooled heat exchanger and (b) melting of solid by pulling upwards through a heated heat exchanger.

where $\nabla \cdot \mathbf{n}$ is the interface curvature. Therefore, the interface temperature is reduced relative to T_m at crests in the interface and increased at troughs. Thus heat will flow from troughs to crests, causing the crests to melt back, while the troughs solidify faster, stabilizing the front (see Fig. 1d). In the following, we will consider the stability of a planar front growing into a supercooled melt including the Gibbs-Thomson effect. As will be seen, the Gibbs-Thomson effect stabilizes the front for small wavelengths, while the front becomes unstable at longer wavelengths.

2 Modelling interfacial instability

In order to explore stability of a planar surface growing into a supercooled melt, we consider the case of liquid being pulled down through a heat exchanger at a constant velocity V as shown in Fig. 2. The heat exchanger maintains the temperature at $T_H < T_m$ at a height $z = H$, and the interface is assumed to be initially planar at $z = 0$. In experiments it is V , rather than the position of the interface, H , which is controlled and so H is an unknown: in this problem, it will be determined from the Stefan boundary condition.

If we apply a small perturbation $z = \eta(x, t)$ to the solid-liquid interface, we can investigate the stability of the interface as follows. The pulling velocity introduces an advective term into the heat equation, which becomes:

$$\frac{\partial T}{\partial t} - V \frac{\partial T}{\partial z} = \kappa \nabla^2 T, \quad (2)$$

while the boundary conditions are

$$T = T_H \quad \text{at} \quad (z = H), \quad (3)$$

$$T = T_m - \Gamma \nabla \cdot \mathbf{n} \quad \text{at} \quad (z = \eta), \quad (4)$$

and

$$\rho L(V + \eta_t) = -k \left. \frac{\partial T}{\partial z} \right|_{z=\eta}. \quad (5)$$

Note that we have already linearized the Stefan boundary condition for small perturbations by assuming that the normal to the interface is parallel to the z -axis.

In order to non-dimensionalize the equations, we choose to scale lengths with H , time with SH^2/κ and write $T = T_H + (T_m - T_H)\theta$. In terms of these nondimensional variables, the advection–diffusion equation then becomes

$$\frac{1}{S} \frac{\partial \theta}{\partial t} - p \frac{\partial \theta}{\partial z} = \nabla^2 \theta, \quad (6)$$

while the Stefan boundary condition takes the form

$$Sp + \eta_t = -\theta_z, \quad (7)$$

where the Peclet number is defined as $p = VH/\kappa$ and measures the strength of advection relative to diffusion. The remaining boundary conditions can then be written as

$$\theta = 1 - \gamma \nabla \cdot \mathbf{n} \quad (z = \eta), \quad (8)$$

$$\theta = 0 \quad (z = 1), \quad (9)$$

where $\gamma = \Gamma/H\Delta T$ is the non-dimensional surface energy.

We initially seek a steady state such that $\theta = \theta(z)$ has no t or x dependence and $\eta = 0$. Equation (6) then simplifies to

$$\theta'' + p\theta' = 0 \quad (10)$$

and the temperature field in the liquid is given by

$$\theta = 1 - \frac{1 - e^{-pz}}{1 - e^{-p}}. \quad (11)$$

We can then apply the Stefan boundary condition to obtain the Peclet number (and thus the interface velocity) in terms of the Stefan number as

$$p = -\log(1 - S^{-1}). \quad (12)$$

When the Stefan number is large, we can expand Eqn. (12) in terms of S^{-1} to show that $p \approx S^{-1} \ll 1$. Therefore, when we consider Eqn. (6) in the large S limit, we can discard the time derivative and advection terms (the quasi-stationary approximation) to approximate the temperature field as

$$\theta \approx 1 - z. \quad (13)$$

With this quasi-stationary approximation, we can now perform a linear stability analysis by applying a small disturbance

$$\eta = \hat{\eta}e^{i\alpha x + \sigma t} \quad (14)$$

to the interface and letting the temperature field take the form

$$\theta = 1 - z + \hat{\theta}e^{i\alpha x + \sigma t}. \quad (15)$$

Substituting this expression for θ into the quasi-stationary form of Eqn. (6), we obtain

$$\hat{\theta}'' - \alpha^2 \hat{\theta} = 0, \quad (16)$$

so that

$$\hat{\theta} = A \sinh \alpha(1 - z), \quad (17)$$

in which we have applied the boundary condition at $z = 1$.

In order to determine the curvature of the interface, we note that for an interface determined by the equation $g(x, z, t) = 0$, the normal to the surface is given by

$$\mathbf{n} = \frac{\nabla g}{|\nabla g|}.$$

Here, $g = z - \eta(x, t)$ and so

$$\mathbf{n} = \frac{(-\eta_x, 1)}{(1 + \eta_x^2)^{1/2}} \approx (-\eta_x, 1), \quad (18)$$

while the curvature, $\mathcal{K} = \nabla \cdot \mathbf{n}$ takes the form

$$\nabla \cdot \mathbf{n} \approx -\eta_{xx}. \quad (19)$$

Using this expression for the curvature, we can apply the two remaining boundary conditions at the solid-liquid interface in order to obtain a dispersion relation controlling the rate of growth of the individual wavelengths. The Stefan condition gives

$$\sigma \hat{\eta} = -\hat{\theta}' = \alpha A \cosh \alpha, \quad (20)$$

and the Gibbs-Thomson condition gives that

$$\hat{\theta} - \hat{\eta} = -\gamma(-\eta_{xx}) = -\alpha^2 \gamma \hat{\eta},$$

which becomes

$$A \sinh \alpha - \hat{\eta} = -\alpha^2 \gamma \hat{\eta}. \quad (21)$$

Combining Eqns. (20) and $\sigma \times (21)$, we obtain

$$A \sigma \sinh \alpha - \alpha A \cosh \alpha = -\alpha^3 \gamma A \cosh \alpha, \quad (22)$$

from which we immediately have the dispersion relation

$$\sigma = \alpha \coth \alpha (1 - \gamma \alpha^2). \quad (23)$$

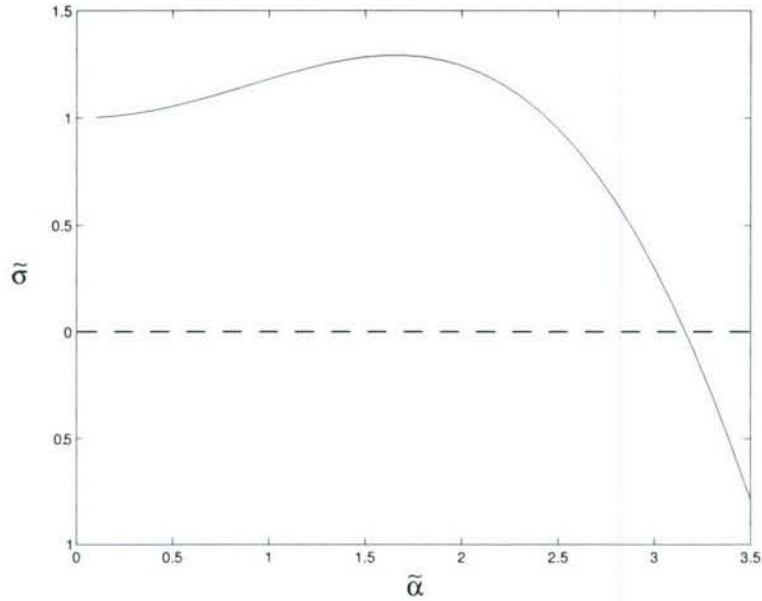


Figure 3: Plot of the dispersion relation (23) in the case $\gamma = 0.1$.

This can be simplified in the limits of small and large wavelength perturbations to

$$\sigma = \begin{cases} -\gamma\alpha^3, & \alpha \gg 1 \\ 1 + \alpha^2(\frac{1}{3} - \gamma), & \alpha \ll 1. \end{cases} \quad (24)$$

Equation (23) can be used to plot the dependence of σ on α , as demonstrated in Fig. 3. In particular, we note two interesting properties of equation (23). Firstly, there is a critical wavenumber, α_c , above which $\sigma < 0$ and perturbations decay in time; the interface is stable for $\alpha > \alpha_c$. There is therefore a minimum wavelength below which the instability is eliminated. Clearly,

$$\alpha_c = \gamma^{-1/2}. \quad (25)$$

We can then write the minimum wavelength, λ_c , in dimensional terms as

$$\lambda_c = \frac{2\pi H}{\alpha_c} = 2\pi (H\ell_c)^{1/2}, \quad (26)$$

where

$$\ell_c \equiv \frac{\gamma_{sl} T_m}{\rho L \Delta T} = \gamma H \quad (27)$$

is the capillary length. The minimum wavelength is therefore proportional to the geometric mean of the capillary length and H , which is a lengthscale for thermal diffusion. Typically for ice we have

$$\ell_c = \frac{(3 \times 10^{-2} \text{ N m}^{-1}) \times (300 \text{ K})}{(10^3 \text{ kg m}^{-3}) \times (3 \times 10^5 \text{ J kg}^{-1}) \times (1 \text{ K})} \sim 30 \text{ nm}. \quad (28)$$

In typical laboratory experiments, $H \sim 10^{-1}$ m and so we find that the minimum wavelength $\lambda_c \sim 300 \mu\text{m}$.

Secondly, we observe from Fig. 3 that there is a maximally unstable wavenumber, α_m , provided that $\gamma < 1/3$. Expanding (23) for $\alpha_m \gg 1$ and requiring that $\sigma'(\alpha_m) = 0$, we find that

$$\alpha_m = (3\gamma)^{-1/2} = \frac{\alpha_c}{\sqrt{3}}. \quad (29)$$

This wavenumber corresponds to a maximally unstable wavelength $\lambda_m = \sqrt{3}\lambda_c$. Since it is this mode that grows fastest, this is the wavelength that we might expect to observe in experiments. Recall also that typically $\ell_c \sim 30$ nm and $H \sim 0.1$ m so that

$$\gamma = \frac{\ell_c}{H} \sim 10^{-7} \ll 1, \quad (30)$$

and our approximation that $\alpha_m \gg 1$ is valid. Finally, we find that $\lambda_m \approx 0.5$ mm for typical laboratory experiments.

Student Problem *Show that a melting interface is stable by considering the above problem with $T_H > T_m$ and V with the opposite sign. (cf. Fig. 2b.)*

Solution We note that the system is effectively identical to the previous case, except that now $\tilde{V} = -V$ and $\tilde{\Delta}T = (T_H - T_m) = -\Delta T$, where tilde/no tilde distinguishes between the melting/freezing problem, respectively. We also see that $\tilde{p} = -p$, $\tilde{S} = -S$ and we can define $T = T_H - \tilde{\Delta}T\tilde{\theta}$. Thus when we non-dimensionalize the equations (and dropping tildes), we find that

$$\frac{1}{S} \frac{\partial \theta}{\partial t} + p \frac{\partial \theta}{\partial z} = \nabla^2 \theta, \quad (31)$$

$$Sp - \eta_t = -\theta_z \quad (z = \eta), \quad (32)$$

$$\theta = 1 + \gamma \nabla \cdot \mathbf{n} \quad (z = \eta), \quad (33)$$

and

$$\theta = 0 \quad (z = 1). \quad (34)$$

There is a steady state solution as before, such that

$$\theta = 1 - \left(\frac{1 - e^{pz}}{1 - e^p} \right), \quad (35)$$

and upon applying the Stefan boundary condition, we find that

$$p = \log(1 + S^{-1}) \quad (36)$$

so that $p \approx S^{-1}$ for $S \gg 1$.

As before, for large S , we can make a quasi-stationary approximation by discarding time derivative and advection terms in the diffusion–advection equation so that:

$$\theta \approx 1 - z. \quad (37)$$

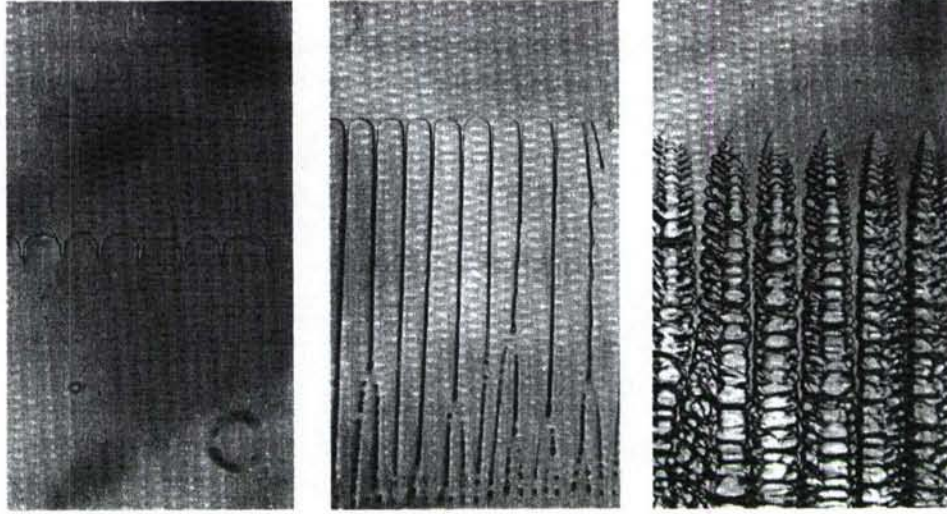


Figure 4: Photographs showing the development of the morphological instability discussed here. In the middle picture, pinching is observed leaving inclusions of liquid within the solid.

Finally, using this linear approximation as a basic state, we apply a small perturbation to the interface of the form

$$\eta = \hat{\eta}e^{i\alpha x + \sigma t} \quad (38)$$

along with

$$\theta = 1 - z + \hat{\theta}e^{i\alpha x + \sigma t} \quad (39)$$

which yields a similar dispersion relation to the freezing case:

$$\sigma = -\alpha \coth \alpha (1 + \gamma \alpha^2). \quad (40)$$

Note that the expression for σ is always negative, and so the interface is stable to small amplitude perturbations of all wavelengths.

3 Beyond linear theory: pinching

The morphological instability discussed in the last section is manifested as a fingering instability with typical finger morphologies shown in Fig. 4. As these fingers grow, their growth cannot any longer be understood by the linear stability analysis presented in the last section. Instead, nonlinearities become important and the fingers themselves become unstable to dendritic growth shown in Fig. 4. While the detailed morphology of these fingers is difficult to understand without detailed numerical simulations, the pinching instability of the fingers (illustrated in the middle frame of Fig. 4) can be understood by means of a simple model. This pinching is of particular interest since it results in pockets of fluid being trapped within the solid. Here we present a simple model of pinching, which is mathematically analogous to the model of the pinching of a liquid thread developed by Rayleigh and Plateau.

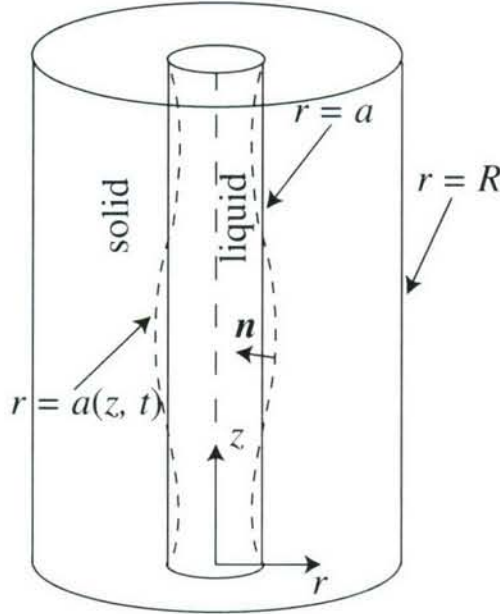


Figure 5: Setup showing the one dimensional model of pinching in solidification.

We consider a liquid cylinder of radius a within a concentric annulus of inner and outer radii a and $R > a$ respectively, as shown in Fig. 5. This is the simplest geometry that will lead to an instability since in two dimensions the surface energy acts to suppress pinching. With a third dimension, however, there are two competing curvatures: an axisymmetric perturbation in the cylinder radius increases the ‘ring’ curvature where the radius is smallest driving fluid away from that point and driving the instability further. We assume that the material properties of the two phases are identical.

The interface between liquid and solid is given by

$$g(r, z, t) = a(z, t) - r = 0, \quad (41)$$

where we are assuming that the system remains axisymmetric for all times. The normal (pointing from solid to liquid) is then given by

$$\mathbf{n} = \frac{(-1, a_z)}{\sqrt{1 + a_z^2}}, \quad (42)$$

so that

$$\begin{aligned} \nabla \cdot \mathbf{n} &= \frac{1}{r} \frac{d}{dr} \left(r \frac{-1}{\sqrt{1 + a_z^2}} \right) + \frac{d}{dz} \left(\frac{a_z}{\sqrt{1 + a_z^2}} \right) \\ &\approx -\frac{1}{r} + a_{zz} \approx -\frac{1}{a} + a_{zz}. \end{aligned}$$

The (equilibrium) temperature along the interface is therefore given by

$$T_e \approx T_m + \Gamma \left(\frac{1}{a} - a_{zz} \right). \quad (43)$$

This expression has to be combined with the conservation of heat to obtain a complete set of equations. For long wavelength deformations, the system has time to equilibrate across cross-sections at fixed z and so we assume that $T = T(z)$. The conservation of heat is considerably simplified by this approximation. In particular, if $H_{l,s}$ represents the specific enthalpy in the liquid/solid phases, then the conservation of heat for an element of height δz requires that

$$\rho \frac{\partial}{\partial t} [\pi a^2 \delta z H_l + \pi(R^2 - a^2) \delta z H_s] = [q(z) - q(z + \delta z)] \pi R^2, \quad (44)$$

where $q = -k\partial T/\partial z$ is the conductive heat flux in the system. Taking the limit $\delta z \rightarrow 0$, we find that

$$\rho(H_l - H_s) \frac{\partial}{\partial t} (\pi a^2) + \pi a^2 \rho \frac{\partial H_l}{\partial t} + \pi(R^2 - a^2) \rho \frac{\partial H_s}{\partial t} = -\pi R^2 \frac{\partial q}{\partial z}. \quad (45)$$

However, by definition we have $H_l - H_s = L$ and $(\partial H/\partial T)_p = c_p$ so that (45) first simplifies to

$$\rho L \frac{\partial}{\partial t} (\pi a^2) + \pi R^2 \rho c_p \frac{\partial T}{\partial t} = \pi R^2 \frac{\partial}{\partial z} \left(k \frac{\partial T}{\partial z} \right),$$

and then

$$\rho c_p \frac{\partial T}{\partial t} = \frac{\partial}{\partial z} \left(k \frac{\partial T}{\partial z} \right) - \rho L \frac{\partial}{\partial t} \left(\frac{\pi a^2}{\pi R^2} \right). \quad (46)$$

This can in turn be written in terms of the solid volume fraction $\phi = 1 - a^2/R^2$ to give

$$\rho c_p \frac{\partial T}{\partial t} = \frac{\partial}{\partial z} \left(k \frac{\partial T}{\partial z} \right) + \rho L \frac{\partial \phi}{\partial t}. \quad (47)$$

Note that (47) has the diffusive character of the heat equation that we have solved previously. However, we now have a source of heat arising from the latent heat produced in the conversion of liquid into solid. In this respect, (47) is very similar to the conservation of heat in a mushy layer, which we shall meet in a few lectures' time.

Under the assumption that there are no kinetic effects, T and a are related through the Gibbs-Thomson equation (43). We can therefore eliminate T from (46) in favour of a and rewrite (46) as a single equation for $a(z, t)$:

$$\rho c_p \Gamma \frac{\partial}{\partial t} \left(\frac{1}{a} - a_{zz} \right) = k \Gamma \frac{\partial^2}{\partial z^2} \left(\frac{1}{a} - a_{zz} \right) - \frac{\rho L}{R^2} \frac{\partial}{\partial t} (a^2). \quad (48)$$

If we perturb the initially cylindrical fluid inclusion then we can write $a(z, t) = a_0 + a_1(z, t)$ (where a_0 is a constant). Substituting this expression into (48) and linearizing, we find that

$$\rho c_p \Gamma \frac{\partial}{\partial t} \left(\frac{a_1}{a_0^2} - a_{1,zz} \right) = k \Gamma \frac{\partial^2}{\partial z^2} \left(\frac{a_1}{a_0^2} - a_{1,zz} \right) + \frac{2\rho L}{R^2} a_0 a_{1,t}. \quad (49)$$

We can then look for normal mode solutions with $a_1 \propto \exp(i\alpha x + \sigma t)$. The resulting dispersion relation is simplified by non-dimensionalizing lengths with R and times with

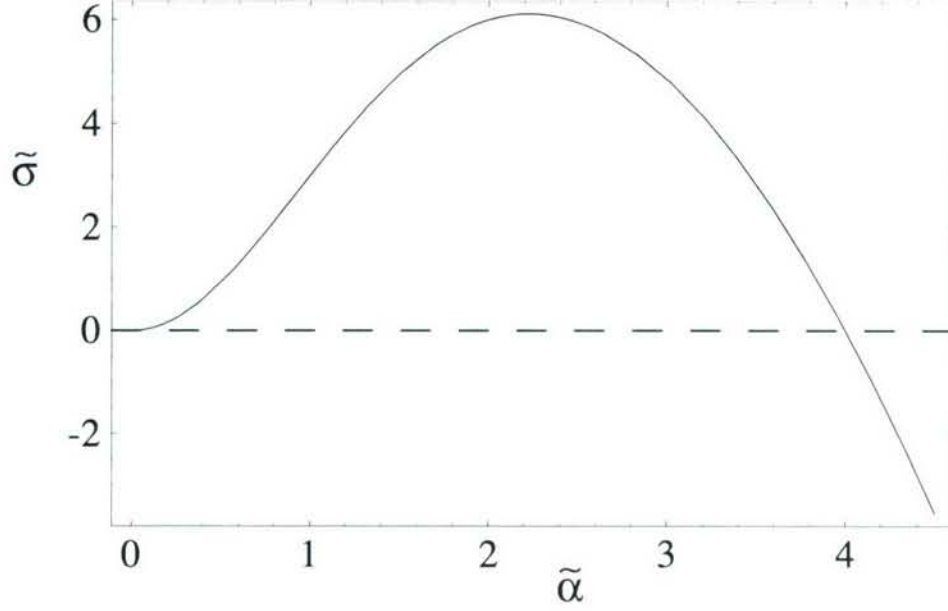


Figure 6: The dispersion relation (50) showing the existence of a maximally unstable wavenumber. Here $\hat{a}_0 = 0.25$ and $\mathcal{S} = 10$, so that (52) is satisfied.

R^2/κ — the thermal diffusion timescale. Denoting dimensionless quantities with $\tilde{\cdot}$ we find that

$$\tilde{\sigma} = \tilde{\alpha}^2 \frac{1 - \hat{a}_0^2 \tilde{\alpha}^2}{(2\mathcal{S} + \tilde{\alpha}^2)\hat{a}_0^2 - 1}, \quad (50)$$

where

$$\mathcal{S} \equiv \frac{LR}{c_p \Gamma} \quad (51)$$

is the relevant Stefan number in this problem. This dispersion relation is plotted in figure 6. Again, considering the behaviour of $\tilde{\sigma}(\tilde{\alpha})$ in the limits $\tilde{\alpha} \ll 1$ and $\tilde{\alpha} \gg 1$ reveals that there is a maximally unstable wavenumber in this problem, provided that

$$\mathcal{S} > \frac{1}{2} \hat{a}_0^{-2}. \quad (52)$$

We expect that this maximally unstable wavenumber would give rise to a well-defined wavelength in experiments.

GFD 2006 Lecture 4: Interfacial instability in two-component melts

Grae Worster; notes by Shane Keating and Takahide Okabe

March 15, 2007

So far, we have looked at some of the fundamentals associated with solidification of pure melts. When we try to solidify a solution of two or more components, salt and water, for example, the character of the solidification changes considerably. In particular, the presence of salt can depress the temperature at which ice and salt water can coexist in thermal equilibrium. This has an important consequence for the growth of sea ice: unless there is some other mechanism for the transport of the salt field, such as convection, the growth of the ice is limited by the rate at which excess salt can diffuse away from the interface. Finally, we will discuss the morphological instability in two-component melts. We shall see that the solute field is destabilizing and can give rise to morphological instability even when the liquid phase is not initially supercooled.

1 Two-component melts

1.1 A simple demonstration

We shall begin with a simple demonstration. Crushed ice at 0°C is placed in a cup with a thermometer. We add a handful of salt at room temperature and stir briskly. The ice begins to melt, but what happens to the temperature?

We notice that there is some melt water in the cup, which helps bring the ice and salt into contact, and see a fairly rapid decrease in the temperature measured by the thermometer: after a few minutes, it reads almost -10°C . What's happening here is *not* melting. Rather, we are observing dissolution of the pure ice into the mixture of salt and water. In this lecture, we will attempt to make more explicit the distinction between melting and dissolution.

1.2 Equilibrium phase diagrams

In Figure 1, we show the *equilibrium phase diagram* for a simple 2-component mixture, or *binary melt* – in this case, salt and water. The equilibrium state of a given mixture of salt and water at temperature T and composition C (i.e., concentration of salt) and at constant pressure can be represented on this diagram by the point (T, C) . The phase diagram is divided into regions of different phase; this diagram is “simple” in the sense that there are only two possible solid phases: pure ice, or solid salt. In Figure 1 these lie along the vertical axes at 0% and 100% concentration respectively. Apart from these two solid phases, we can

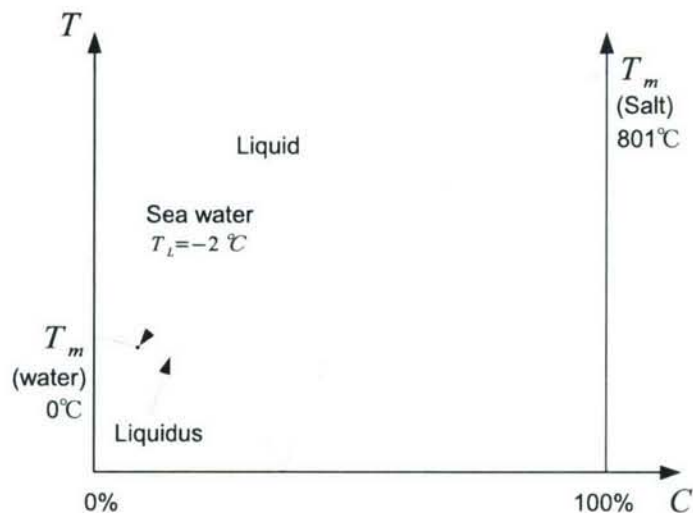


Figure 1: Equilibrium phase diagram for a solution of salt and water.

also form a liquid solution of the two *end members* (i.e., salt or water), or some liquid/solid mixture of the two substances. Other materials have more complicated solid phases and necessarily more complicated phase diagrams, which we will examine briefly later.

The curved line in Figure 1 is the *liquidus*, representing the temperature at which a binary melt of a given composition C can exist in equilibrium in both the liquid and solid phase. For 0% salt concentration, the *liquidus temperature* is simply the melting point of ice – 0°C – while for 100% salt it is 801°C .

When we contaminate pure water at 0°C with a small amount of salt, the equilibrium freezing temperature is *lowered*. Thus, when we added a small amount of salt to the ice in our experiment, we saw that we still had liquid even at temperatures as low as -10°C .

Equivalently, one could start with pure molten salt at 801°C and contaminate it with a small amount of water to lower the melting point. The two liquidus curves meet at a point (T_E, C_E) , called the *eutectic*: this is the minimum temperature at which solid and liquid saltwater can coexist in thermodynamic equilibrium¹.

If we slowly change the temperature or composition, the mixture will trace a trajectory on the phase diagram, as shown in Figure 1 for the case of seawater. We start by cooling seawater to -2°C where it reaches the liquidus curve $T_L(C)$ and starts to freeze. Below this temperature, we start to form pure solid ice in equilibrium with seawater of higher concentration. As more and more solid ice is formed, less water is available and so the salt concentration increases steadily. We can invert the liquidus curve $T = T_L(C)$ to find the

¹According to one popular story, German physicist Gabriel Fahrenheit (1686-1736) chose the *triple* eutectic temperature of water, salt and ammonium chloride, being the lowest temperature he could achieve in his laboratory, as the zero of his eponymous scale. Both Fahrenheit and Celsius are centigrade scales: Anders Celsius (1701-1744) chose 100°C to correspond with the boiling point of water at sea level; Fahrenheit likewise chose a reliable, easily reproducible, steady temperature for 100°F – the anal temperature of his horse. It should be noted, however, that wikipedia.org lists no less than six competing versions of the same story, so at the risk of punning, one should be advised to take such apocryphal tales with a pinch of salt.

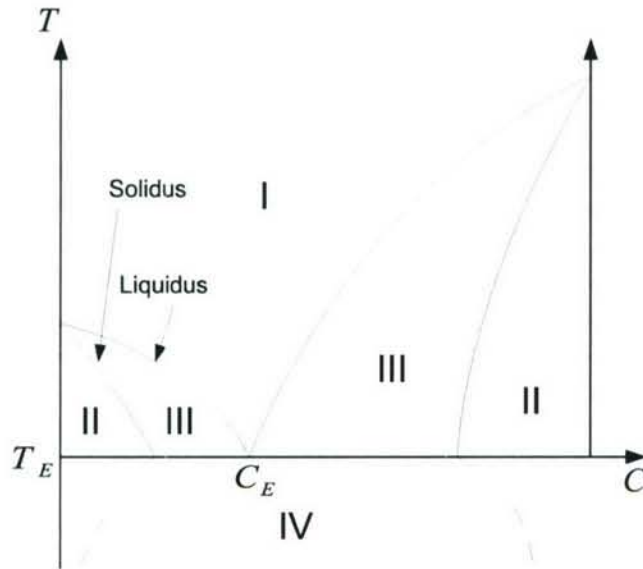


Figure 2: A more generic phase diagram. See text for details.

composition of the remaining liquid: $C = C_L(T)$.

It is worthwhile to extend the simple phase diagram for salt and water to one more typical of other binary melts, as shown in Figure 2. In addition to the liquidus, there is a *solidus* further subdividing the phase diagram. There are now four distinct phases, which we describe below.

Region I is a liquid solution of the two end members.

In region II, the mixture is in a *solid solution*, where the end members are mixed on the lattice scale. An example of this is the silicate compound olivine, $(\text{Fe,Mg})_2\text{SiO}_4$, although the phase diagram is quite different from the one shown in Figure 2. Iron and magnesium sit fairly equally in the lattice sites and will occur in different proportions depending upon the temperature. In contrast, salt and water do not form a solid solution, and will exist in the solid phase only as pure substances, at least as far as we are concerned in this course.

In region III, the solid solution and the liquid phase coexist in equilibrium.

Finally, in region IV, we have a mixture of crystals of the two end members: i.e., pure ice coexisting with pure salt crystals. In addition, there are regions of the equilibrium phase diagram mirroring region III, where pure crystals of one end members coexist with a solid solution of both end members. The exact location in the equilibrium phase diagram of the transition to this region, indicated in Figure 2 by a dashed line, is difficult to measure experimentally, because the compositional relaxation times below the eutectic are on the order of geological timescales. We ignore such detailed structure in our analysis.

Thus, the equilibrium phase diagram can tell us a great deal about what proportion of a mixture is in what phase, and what can coexist in equilibrium. However, it cannot tell us anything about the *geometry* of the solid phase formed; whether the ice forms in layers, or a slurry of ice crystals and salt water, or in the form of a *mushy layer* of dendritic ice crystals separated by interstitial seawater, as we shall examine in the next lecture. The microscopic details of the distribution of the phases depends strongly on how you lower the

temperature; however, the *ratio* of the phases will not depend on the history of the mixture.

1.3 A few approximations

Before we conclude this section, let us introduce some terminology and a few approximations. Firstly, we shall assume (when necessary) that the liquidus can be approximated by a straight line

$$T_L \approx T_m - mC \quad (1)$$

and that the solidus concentration is

$$C_S(T) \approx k_D C_L(T) \quad (2)$$

The parameter k_D is called the *distribution coefficient*, and is approximately zero for a salt and water solution. Thus we will assume that the solution will form only pure crystals of salt or ice.

2 Solidification of sea ice

2.1 The Stefan problem for a salt water solution

Let us now revisit the Stefan problem²; this time, however, we consider the case of *salt water* in contact with a boundary at a temperature below the liquidus temperature of the solution, as depicted in Figure 3

We denote by T_i and C_i respectively the interfacial temperature and composition of the salt water, to be determined. We further demand that the ice and the salt water at the interface are in thermodynamic equilibrium so that T_i is the liquidus temperature and

$$T_i = T_L(C_i). \quad (3)$$

This is in contrast to the Stefan problem where the interfacial temperature was simply the melting temperature of pure ice T_m . Here, however, the temperature at which the salt water freezes is set by the interfacial concentration of salt, and we shall see that the rate at which the interface advances is limited by the rate at which we can remove excess salt from the region near the interface.

The composition of salt inside the ice will be zero, as discussed above; however, we shall denote it by C_S to be a little more general. The far field temperature and composition of the sea water are T_∞ and C_0 respectively. The boundary temperature T_B will be *below the liquidus temperature of the undisturbed solute field*: $T_B < T_L(C_0)$.

The equations to be solved are the diffusion equation in the ice and the sea water

$$\frac{\partial T}{\partial t} = \kappa \frac{\partial^2 T}{\partial x^2} \quad \text{in } x < a \text{ and } x > a \quad (4)$$

²Note that in this treatment, we will neglect the effects of both kinetics and surface energy. The latter case would not arise anyway, as we are dealing only with a planar interface.

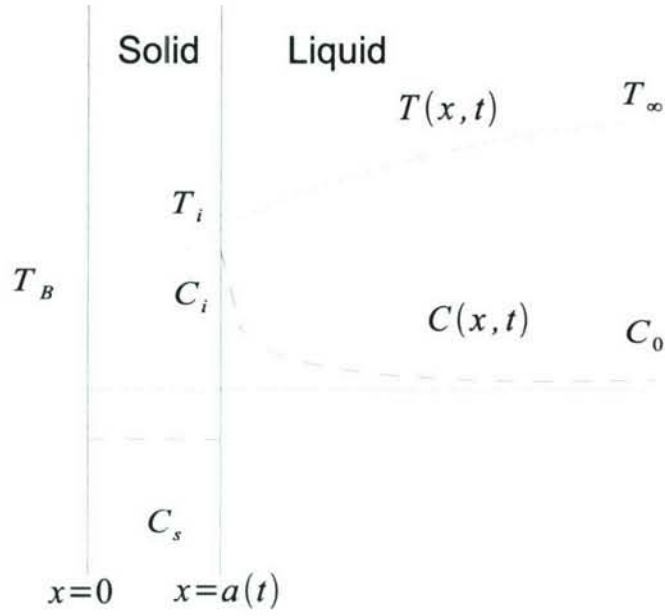


Figure 3: Freezing of salt water.

where, for simplicity, the thermal diffusivity κ is assumed to be the same in both solid and liquid. In addition, we must solve for the salt field in the liquid region

$$\frac{\partial C}{\partial t} = D \frac{\partial^2 C}{\partial x^2} \quad \text{in } x > a. \quad (5)$$

As the composition in the solid region is constant there will be no diffusion of salt there. The ratio of the solute diffusivity to the thermal diffusivity for seawater is of the order 10^{-2} and will play the role of a small parameter in our analysis.

In addition to the boundary and interfacial conditions, we have, as before, the Stefan condition for the interfacial heat flux:

$$\rho L \dot{a} = k \left(\frac{\partial T}{\partial x} \right)_{a-} - k \left(\frac{\partial T}{\partial x} \right)_{a+} \quad (6)$$

The final equation in this problem comes from the conservation of solute. The total quantity of salt must be conserved, so that the area under the composition curve must be constant:

$$C_s a + \int_{a(t)}^{\infty} C(x, t) dx = \text{const.} \quad (7)$$

The time derivative of this equation is

$$C_s \dot{a} - C_i \dot{a} + \int_a^{\infty} \frac{\partial C}{\partial t} dx = 0 \quad (8)$$

which, from the solute diffusion equation (5) becomes

$$(C_s - C_i) \dot{a} + \int_a^\infty \mathcal{D} \frac{\partial^2 C}{\partial x^2} dx = 0 \quad (9)$$

and finally,

$$(C_i - C_s) \dot{a} = -\mathcal{D} \left(\frac{\partial C}{\partial x} \right)_{x=a_+}. \quad (10)$$

Equation (10) has formally the same structure as the Stefan condition: instead of interfacial heat flux balancing the difference in heat content (enthalpy), however, equation (10) represents the balance of the difference in salt concentration with the flux of salt across the interface.

The solutions to the thermal diffusion equation (4) in the solid and liquid regions are, respectively,

$$T = T_B + (T_i - T_B) \frac{\text{erf}(\eta)}{\text{erf}\left(\frac{a}{2\sqrt{\kappa t}}\right)} \quad \text{in } x < a \quad (11)$$

$$T = T_\infty + (T_i - T_\infty) \frac{\text{erfc}(\eta)}{\text{erfc}\left(\frac{a}{2\sqrt{\kappa t}}\right)} \quad \text{in } x > a \quad (12)$$

Equations (11) and (12) are similarity solutions in the dimensionless variable

$$\eta = \frac{x}{2\sqrt{\kappa t}} \quad (13)$$

A dimensionless interfacial position is μ , which is defined by

$$a = 2\mu\sqrt{\mathcal{D}t} \quad (14)$$

where, in contrast to our previous analysis, $a(t)$ scales with the solute diffusivity \mathcal{D} rather than the thermal diffusivity κ . The dimensionless parameter μ remains to be determined. We shall show, *a posteriori*, that μ is $O(1)$. Had we chosen $a(t)$ to scale with κ instead, we would find μ to be $O(\epsilon^{-1})$, where,

$$\epsilon = \sqrt{\frac{\mathcal{D}}{\kappa}} \quad (15)$$

justifying our choice of the \mathcal{D} in equation (14) rather than κ .

The solute diffusion equation (5) and boundary conditions yield the solution

$$C = C_0 + (C_i - C_0) \frac{\text{erfc}(\epsilon\eta)}{\text{erfc}(\epsilon\alpha)} \quad \text{in } x > a \quad (16)$$

where ϵ appears in the arguments because, in the case of the solute, it is \mathcal{D} rather than κ that should appear in the definitions of the dimensionless variable μ in (14).

In addition to the parameter μ , the interfacial temperature T_i and interfacial concentration C_i will be determined using the Stefan condition (6), the solute conservation equation

(10) and the liquidus relation (3). Substituting (11), (12) and (14) into the Stefan condition yields

$$\frac{L}{c_p} = \frac{T_i - T_B}{G(\epsilon\mu)} - \frac{T_\infty - T_i}{F(\epsilon\mu)} \quad (17)$$

where,

$$G(z) = \sqrt{\pi}ze^{z^2}\operatorname{erf}z \quad (18)$$

and

$$F(z) = \sqrt{\pi}ze^{z^2}\operatorname{erfc}z \quad (19)$$

Similarly, the solute conservation equation (10) becomes

$$C_i - C_s = \frac{C_i - C_0}{F(\mu)} \quad (20)$$

For salt water, ϵ is reasonably small, so let us examine the case of $\epsilon \rightarrow 0$. The functions $G(z)$ and $F(z)$ have the asymptotic behaviour

$$G(z) \approx 2z^2 \quad \text{as } z \rightarrow 0 \quad (21)$$

$$F(z) \approx \sqrt{\pi}z \quad \text{as } z \rightarrow 0. \quad (22)$$

Thus, for small ϵ , the three terms in the Stefan condition (17) are of order 1 : ϵ^{-2} : ϵ^{-1} and so, to lowest order, $T_i = T_B + O(\epsilon)$. Inverting the liquidus relation (3) now gives us the interfacial concentration to lowest order: $C_i = C_B + O(\epsilon)$, where $C_B = C_L(T_B)$ is the liquidus concentration associated with the temperature of the boundary. The solute conservation equation (20) then gives

$$F(\mu) \approx \frac{C_B - C_0}{C_B - C_S} \equiv \mathcal{C}^{-1} \quad (23)$$

As shown in Figure 4 , the parameter \mathcal{C} is always strictly greater than or equal to one, with equality only for a pure melt. Thus, unlike the problem of a crystal growing into a supercooled melt, where we saw that for Stefan numbers of less than one there was no similarity solution, equation (23) always has a solution.

Furthermore, equation (23) implies that $\mu = O(1)$, justifying our choice of the solute diffusivity \mathcal{D} in (14) rather than the thermal diffusivity κ . Thus, the rate of advance of the planar interface is limited by the rate at which we can remove excess solute. Adjacent to the interface is a boundary layer of thickness $O(\sqrt{\mathcal{D}t})$, as shown in Figure 5. In fact, seawater does not behave like this because convection will also act to remove excess solute, which we have neglected here.

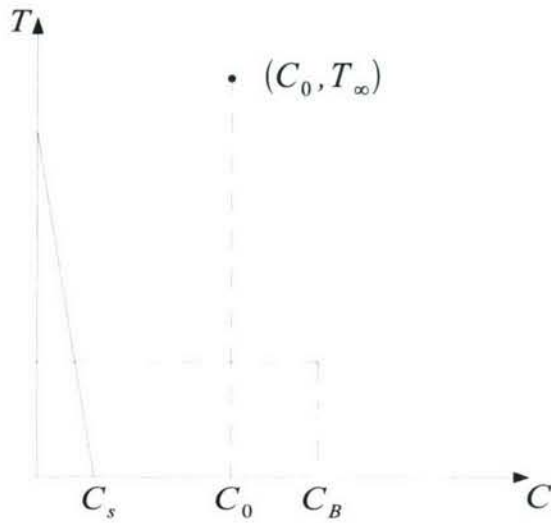


Figure 4: Proof that \mathcal{C} is greater than or equal to unity. \mathcal{C} is defined as the ratio of $C_B - C_S$ to $C_B - C_0$. C_0 is the far-field composition and lies above the solid composition C_S . C_B is the composition at the boundary and, by assumption, lies on the liquidus curve. As ice solidifies it leaves behind a residual of higher composition, so that C_B must be greater than that of the solution far from the boundary, C_0 . Thus, the ordering of C_S , C_0 and C_B is as shown in the figure, and \mathcal{C} is necessarily greater than or equal to unity.

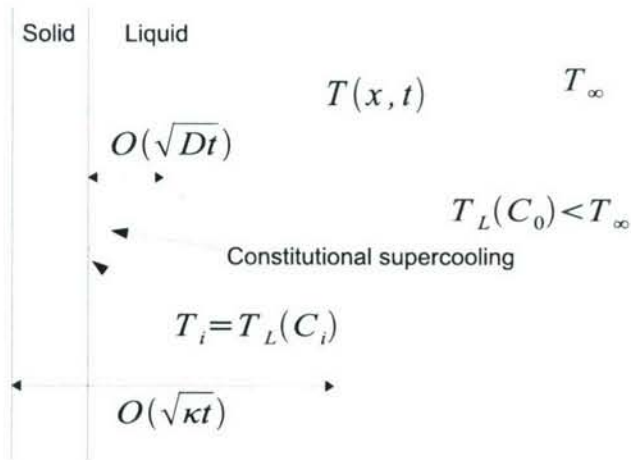


Figure 5: Comparison of the actual temperature field and the liquidus temperature associated with the compositional field. In the region where the $T_L(C) > T$, the liquid is constitutionally supercooled.

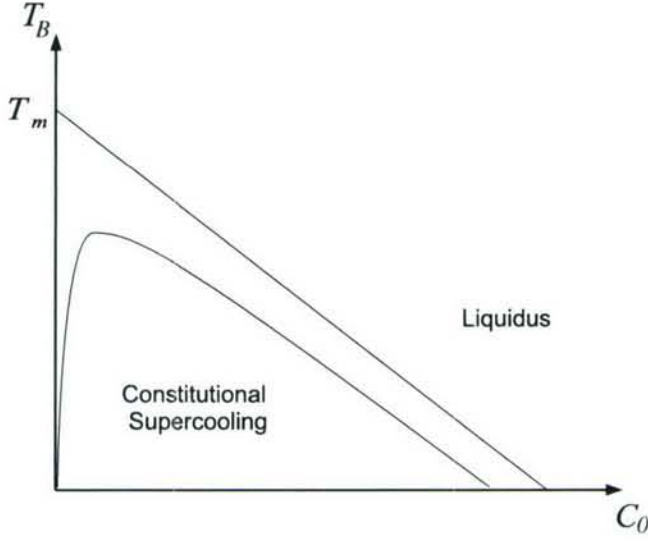


Figure 6: Cartoon indicating the values of boundary temperature below which supercooling occurs for a given initial composition C_0 .

2.2 Constitutional supercooling

Because the salt field and the temperature field have different scales of relaxation, there exists the possibility that, beside the interface, the actual temperature is *below* the local liquidus temperature. Thus the liquid is supercooled relative to its freezing temperature. The critical condition for such *constitutional supercooling* is that the liquidus temperature increase more rapidly than the actual temperature as we move away from the interface:

$$\left(\frac{\partial T}{\partial x}\right)_{a+} < \left(\frac{\partial T_L}{\partial x}\right)_{a+}. \quad (24)$$

Approximating the liquidus by a straight line $T_L(C) \approx T_m - mC$ and using our solutions for the temperature field and salt field in the liquid (12,16) we find that

$$\frac{\left(\frac{\partial T}{\partial x}\right)_{a+}}{\left(\frac{\partial T_L}{\partial x}\right)_{a+}} = \frac{T_\infty - T_i}{(C_i - C_0)m} \epsilon^2 \frac{F(\mu)}{F(\epsilon\mu)}. \quad (25)$$

From the asymptotic behaviour of $F(z)$ for small z (19), we can see that the right-hand side of (25) is typically $O(\epsilon)$. Thus, generically, the critical condition (24) is satisfied, and the liquid in the boundary layer is constitutionally supercooled.

Equation (25) can be solved to find the critical curve for constitutional supercooling on the equilibrium phase diagram, as depicted in Figure 6. Notice that the region of constitutional supercooling sits very close to the liquidus (for small ϵ), so that we do not have to lower the temperature much below the liquidus temperature for constitutional supercooling to be prevalent. Note also that it is possible to avoid constitutional supercooling in a region close to 0% composition. This is of relevance to the semiconductor industry, where

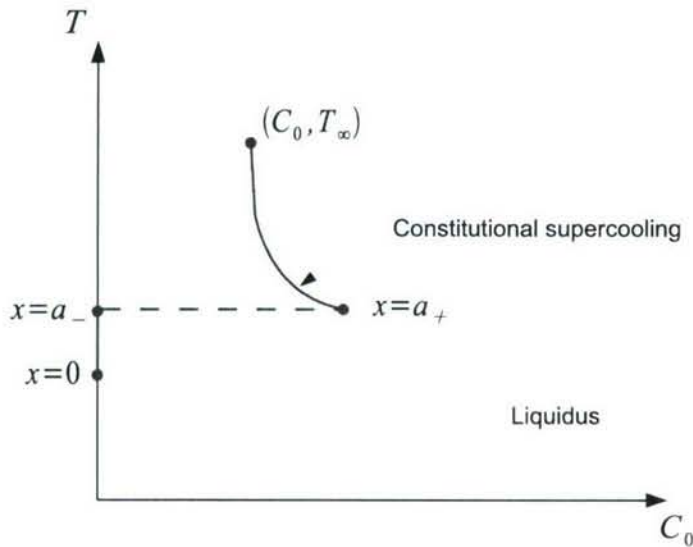


Figure 7: Temperature and compositional field on the equilibrium phase diagram.

constitutional supercooling is undesirable as it can give rise to morphological instability of a semiconductor crystal.

Finally, we show in Figure 7 how the temperature and composition change as we move from the boundary at $x = 0$, through the interface at $x = a(t)$, to the far-field position at $x \rightarrow \infty$. Within the ice ($0 < x < a_-$), the temperature changes smoothly while the composition is identically zero. As we move across the boundary, the composition and temperature change discontinuously to the liquidus curve at (C_i, T_i) . From the interface, the two fields change differently until they reach their far-field values. Because the thermal and compositional diffusivities are different, the solute field changes more rapidly than the thermal field, and so the (C, T) -curve dips *below* the liquidus, indicating constitutional supercooling.

2.3 Morphological instability of sea-ice growth

As we have already seen in this lecture series, ice growing into a supercooled melt is unconditionally unstable to small perturbations of the interface. When the liquid is constitutionally supercooled, the morphological instability takes on some new characteristics, which we discuss here in broad terms.

1. As in the case of the Stefan problem, the thermal field has a stabilizing influence on the interface (Figure 8a). Isotherms are compressed near peaks in the interface, enhancing the heat flux at those points, and rarefacted near troughs, suppressing the heat flux. The heat flux inhibits the growth of ice at the peaks, while reinforcing it at the troughs, stabilizing the interface.
2. The compositional field, which was not present in our original Stefan problem, is destabilizing (Figure 8b). Like isotherms, surfaces of constant concentration are compressed near peaks, enhancing the flux of solute away from the interface. Thus, the

ice can grow more quickly at peaks because the solute, which inhibits growth, can diffuse away more quickly, leading to instability.

3. As we saw in the problem of crystal growth into a supercooled liquid, surface energy is stabilizing (Figure 8c) A divergent normal on a curved interface lowers the equilibrium temperature near peaks and raises it at troughs, giving rise to a heat flux from the troughs to the peaks. As in the case of the thermal field, this stabilizes the interface.

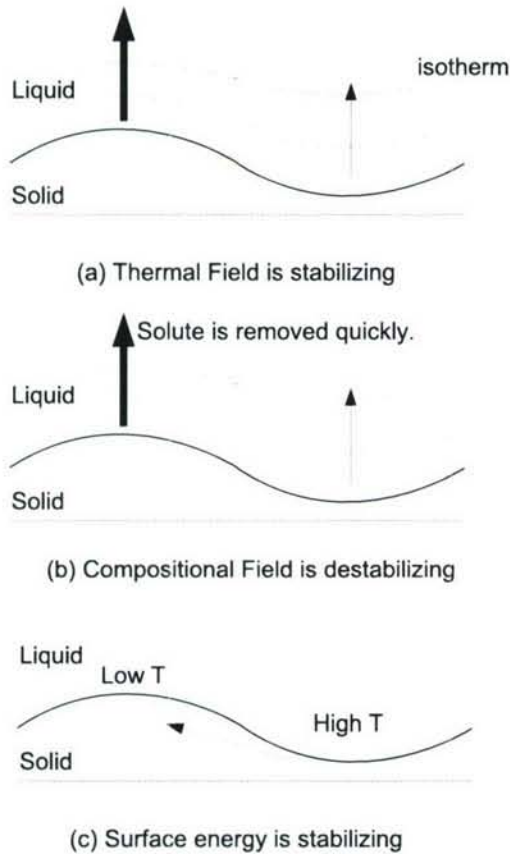


Figure 8: Mechanisms contributing to the morphological instability in sea ice.

These three mechanisms operate on three different lengthscales: in decreasing order they are the thermal diffusion lengthscale, the compositional diffusion lengthscale, and the capillary lengthscale. Thus, the interface is *conditionally unstable*: the interface may be unstable, marginally stable, or completely unstable, depending upon the precise lengthscales involved.

The condition for instability can be translated into a critical solidification rate, as shown in the neutral stability curve in Figure 9. Likewise, we can plot the critical solidification rate V_C as a function of the initial composition of the melt C_0 (Figure 10). For a given value of C_0 , the interface is stable for sufficiently low solidification rates (typically around $1\mu\text{ms}^{-1}$), but as we increase the solidification rate, the interface can go unstable. If we

increase the solidification rate more, to say 1ms^{-1} , the interface can be stable again. Such rapid solidification is generally not of interest in ice studies, but is relevant to spot welding.

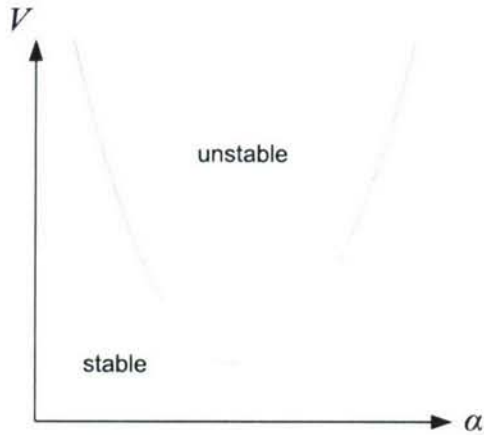


Figure 9: Neutral stability curve for the morphological instability. Here, V is the solidification rate and α is the wavenumber.

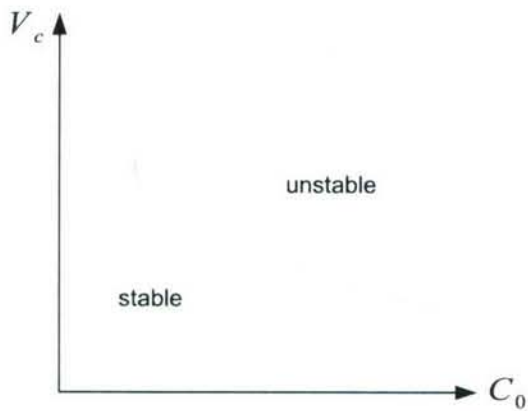


Figure 10: Critical solidification rate versus initial concentration of the melt.

Student Problem

Consider a lump of sea ice floating in the ocean. Both the ice and the sea water are at uniform temperature $T_0 = -2^\circ\text{C}$, say, such that, T_0 is greater than the liquidus temperature of the far field concentration C_0 . There is no gravity, so convection does not play a role. What happens, and how quickly?

Solution:

By solving the diffusion equation for the concentration field, we get

$$C = C_0 + (C_i - C_0) \frac{\text{erfc}(x/2\sqrt{Dt})}{\text{erfc}(a/2\sqrt{Dt})} \quad (x > a), \quad (26)$$

where D is the diffusion coefficient of the concentration field. On the other hand, we have the concentration conservation:

$$-C_i \dot{a} = D \frac{\partial C}{\partial x} \Big|_{a+0} \quad (27)$$

Therefore,

$$\dot{a} = \frac{C_i - C_0}{C_i} \sqrt{\frac{D}{\pi t}} \frac{1}{\operatorname{erfc}(a/2\sqrt{Dt})} e^{-a^2/4Dt} \quad (28)$$

Because $C_0 > C_i$, $\dot{a} < 0$: the ice is dissolving. Because of the absorption of the latent heat, the system cannot be isothermal: the temperature is depressed at the phase boundary.

GFD 2006 Lecture 5: Formation of mushy layers

Grae Worster; notes by Shane Keating and Ian Eisenman

March 15, 2007

1 Dissolution versus melting

In this lecture we will try to elucidate the difference between melting and dissolution of a solid in the presence of a two-component liquid mixture. We will consider pure solid ice at temperature $T_{-\infty} < T_m$ which is brought into contact with salt water that has a temperature higher than the liquidus temperature associated with its salt concentration C_0 : $T_{\infty} > T_L(C_0)$.

The solution to this problem is very similar to a result from Lecture 4: the temperature and composition fields in the liquid and solid admit the similarity solution

$$T = \begin{cases} T_{-\infty} + (T_i - T_{-\infty}) \frac{\operatorname{erf}(\epsilon\eta)}{\operatorname{erf}(\epsilon\mu)} & \eta < \mu \text{ (ice)} \\ T_{-\infty} + (T_i - T_{-\infty}) \frac{\operatorname{erfc}(-\epsilon\eta)}{\operatorname{erfc}(-\epsilon\mu)} & \eta > \mu \text{ (liquid)} \end{cases}, \quad (1)$$

$$C = \begin{cases} 0 & \eta < \mu \text{ (ice)} \\ C_0 + (C_i - C_0) \frac{\operatorname{erfc}(\eta)}{\operatorname{erfc}(\mu)} & \eta > \mu \text{ (liquid)} \end{cases}, \quad (2)$$

$$\eta \equiv \frac{x}{2\sqrt{Dt}}, \quad (3)$$

$$\mu \equiv \frac{a}{2\sqrt{Dt}}. \quad (4)$$

The parameter $\epsilon \equiv \sqrt{D/\kappa}$ is assumed much less than unity. Rearranging (4), the interface location can be written as

$$a = 2\mu\sqrt{Dt}. \quad (5)$$

We seek the time evolution of the solid–liquid interface. From conservation of solute we have

$$C_i \dot{a} = -D \left(\frac{\partial C}{\partial x} \right)_{a+}. \quad (6)$$

Substitution of (2) and (5) into (6) yields

$$C_i = \frac{C_0}{1 - F(\mu)}, \quad (7)$$

where $F(z) \equiv \sqrt{\pi}ze^{z^2} \operatorname{erfc}(z)$.

The initial concentration in the salt water is C_0 , and as it is diluted by ablation of the ice, we expect $C_i < C_0$; hence $F(\mu)$ is negative. It is clear from Fig. 1 that this can only occur for negative values of μ . Thus $a(t)$ is receding in the negative x -direction and the picture of ice ablation causing reduced salt concentration near the interface is self-consistent.

The Stefan condition here is

$$\rho L \dot{a} = k \left[\frac{\partial T}{\partial x} \right]_{a^-}^{a^+}. \quad (8)$$

Plugging in (1) and (5) leads to

$$\sqrt{\frac{D}{\kappa}} \frac{L}{c_p} \mu = \frac{(T_i - T_{-\infty}) e^{-\epsilon^2 \mu^2}}{\sqrt{\pi} \operatorname{erfc}(-\epsilon \mu)} - \frac{(T_i - T_{\infty}) e^{-\epsilon^2 \mu^2}}{\sqrt{\pi} \operatorname{erfc}(\epsilon \mu)}. \quad (9)$$

We can simplify this result using the function $F(z)$:

$$\frac{L}{c_p} = \frac{T_i - T_{-\infty}}{F(\epsilon \mu)} - \frac{T_i - T_{\infty}}{F(-\epsilon \mu)}. \quad (10)$$

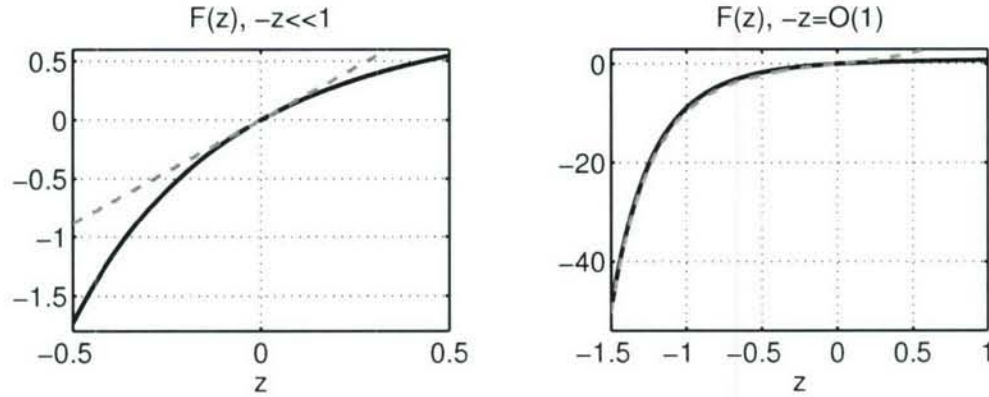


Figure 1: The function $F(z) \equiv \sqrt{\pi}ze^{z^2} \operatorname{erfc}(z)$ appearing in (7) and (10). The function is plotted in two different ranges of z , and approximations for $-z \ll 1$ and $-z \gg 1$ are indicated by gray dashed lines.

The similarity variable μ is unspecified at this point apart from its sign (μ is negative since we are considering ablation). In the following subsections, we will find two different mechanisms for the ablation of ice – dissolution and melting – which occur for different ranges of μ . A summary of the results of the remainder of this section is presented in Table (1).

1.1 Dissolution ($\mu = O(1)$)

Let us consider first the case where $\mu = O(1)$. For small z , the function $F(z) = \sqrt{\pi}z + O(z^2)$ (see Fig. 1), so that the Stefan condition (10) becomes

$$\frac{L}{c_p} = \left(\frac{T_i - T_{-\infty}}{\sqrt{\pi}(\epsilon \mu)} - \frac{T_i - T_{-\infty}}{\sqrt{\pi}(-\epsilon \mu)} \right) (1 + O(\epsilon)). \quad (11)$$

	Dissolution	Melting
Parameter scaling	$-\mu = O(1)$	$-\mu = O(\epsilon^{-1})$
Interface position	$a = O(\sqrt{Dt})$	$a = O(\sqrt{\kappa t})$
Interfacial temperature	$T_i < T_m$	$T_i \approx T_m$
Ablation limited by	Solute diffusion	Heat diffusion

Table 1: A comparison of the two different ablation mechanisms: dissolution and melting

Multiplying both sides by ϵ leads to

$$0 = \frac{T_i - T_\infty}{\sqrt{\pi\mu}} - \frac{T_i - T_{-\infty}}{\sqrt{\pi}(-\mu)} + O(\epsilon). \quad (12)$$

The interfacial temperature is thus approximately the mean of the far-field temperatures¹:

$$T_i = \frac{1}{2}(T_\infty + T_{-\infty}) + O(\epsilon). \quad (13)$$

Since the interface temperature is assumed in equilibrium, it must lie on the liquidus, $T_i = T_L(C_i)$. The liquidus is a decreasing function of salt concentration (for concentration less than C_E), and concentration in the liquid at the interface is $C_i > 0$, so the solid-liquid interface is colder than the salt-free melting temperature, $T_i < T_m$. It is therefore clear that the interface temperature is too low to melt the ice simply by means of heat transfer: the ice requires the presence of the solute field to depress the local liquidus temperature sufficiently in order to change phase. This situation is depicted in Fig. 2.

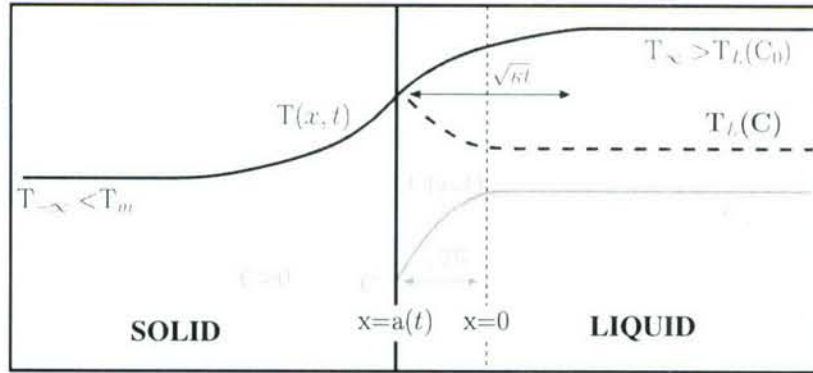


Figure 2: Dissolution of sea ice. Ablation rate is controlled by the transport of *salt* in the liquid.

As we can see from Fig. 2, the thickness of the melt layer $a(t)$ is of the same order as the thickness of the compositional boundary layer (Dt); this is indicated by the fact that

¹Note that in Student Problem 4 the solid ice and liquid sea water were both at the same temperature ($T_{-\infty} = T_\infty$). In this situation, the interfacial temperature T_i is depressed below the far-field temperatures by an $O(\epsilon)$ correction, as implied by (12). It is this $O(\epsilon)$ term which we calculated.

$\mu = O(1)$. The rate of dissolution of the solid layer is limited by the rate at which we can supply salt to the interface: without enough solute, the liquidus temperature of the water adjacent to the interface will not be sufficiently below the actual temperature of the water and the solid ice cannot change phase. Thus, this is truly dissolution in the sense that the phase change from solid to liquid requires the presence of the salt field.

The phase diagram for this process of dissolution is shown in Fig. 3.

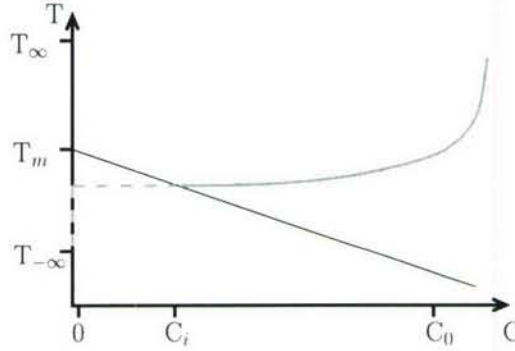


Figure 3: Phase diagram for dissolution. Solid curve represents the trajectory in temperature vs concentration space from the solid–liquid interface to the liquid far–field; continuation of trajectory on solid side of interface is indicated by dashed line. Diagonal line indicates liquidus.

In reality, gravity can play an important role in transporting solute to the interface via convection on a faster timescale than that given by diffusion alone. In the next lecture we will examine a situation incorporating convection.

1.2 Melting ($\mu = O(\epsilon^{-1})$)

For the case of $\mu \sim \epsilon^{-1}$ the interface will advance at a rate proportional to $\sqrt{\kappa t}$. In this situation, ablation of the ice is controlled by heat transfer. In contrast to the previous section, this is ablation caused by heating the material above the freezing temperature and hence is true melting. In the case of dissolution we used a small $-z$ approximation for $F(z)$ in (9); here, we will use a large $-z$ approximation for $F(z)$ in (7). For $-\mu \gg 1$, $\operatorname{erfc}(\mu) \approx 2$, and we have (see Fig. 1)

$$F(\mu) \approx -2\pi\mu e^{\mu^2} \quad -\mu \gg 1. \quad (14)$$

Inserting this result, (7) becomes

$$C_i \approx \frac{C_0}{2\sqrt{\pi}\mu e^{\mu^2}}, \quad (15)$$

which approaches zero exponentially quickly as $|\mu| \rightarrow \infty$. Thus, the interface temperature is very close to the melting temperature of fresh water: $T_i = T_L(C_i) \approx T_L(0) = T_m$. As can be seen from Fig. 4, the interface recedes at a rate proportional to $\sqrt{\kappa t}$, leaving behind a salt-poor melt layer and a compositional boundary layer at $x = 0$. Note that the slope in the temperature field changes discontinuously as it moves through $x = a(t)$ due to the

release of latent heat. In the dissolution case this was an $O(\epsilon)$ effect, but here it can be quite significant.

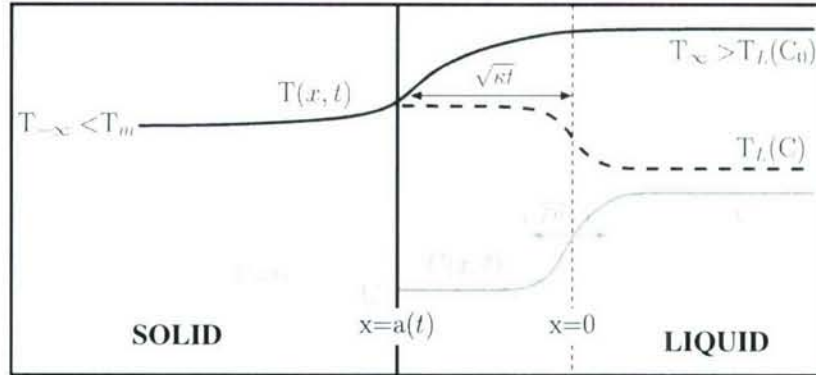


Figure 4: Melting of sea ice. Ablation rate is controlled by the transport of *heat* in the liquid.

The phase diagram for this scenario is depicted in Fig. 5. Note that no constitutional supercooling is possible during dissolution or melting of sea ice.

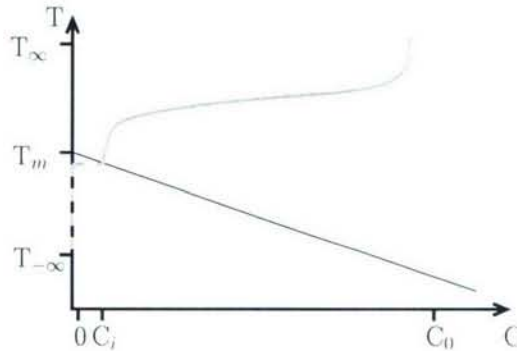


Figure 5: Phase diagram: as in Fig. 3, but for melting.

2 Mushy Layers

In Lecture 1, we saw that as a planar boundary solidifies into a supercooled melt, the interface is morphologically unstable to perturbations with a small but finite spatial wavelength. For the case of a binary melt, we saw in Lecture 4 that it was not necessary to supercool the liquid: differences in the rates of diffusion of heat and solute can give rise to a region where the actual temperature of the liquid is *less than the local liquidus temperature associated with the compositional field*. This phenomenon is known as *constitutional supercooling* and triggers morphological instability of the interface.

The evolution of the instability is depicted in cartoon form in Fig. 6. Initially small sinusoidal perturbations can be treated using weakly nonlinear analysis (which we do not consider here); it is observed that troughs narrow into crevasses while peaks become broader

and flatter. Experimental and numerical studies show that the instability proceeds via tip-splitting and side-branching until a matrix of fine dendritic crystals is formed. At this point, we must abandon all hope of following the exact solid–liquid interface and treat these crystals as a region of mixed phase: a so-called *mushy layer*. In the case of sea-ice, the crystals have a scale of about a millimeter; we are generally interested in scales of a meter or more, so it is appropriate to seek an averaged description of the mushy layer. We consider some arbitrary control volume containing representative elements of both solid and liquid, and we average over scales intermediate between the fine scale of the solid–liquid interface and the macroscopic scale of the sea-ice.

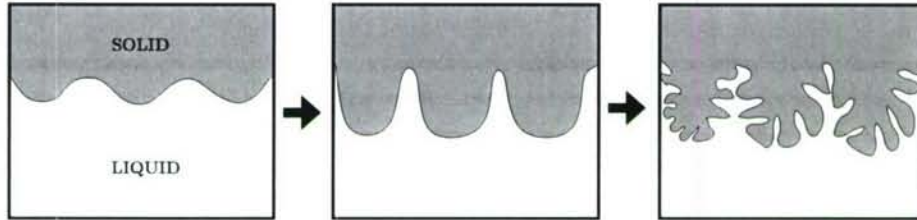


Figure 6: Evolution of the morphological instability

As we saw in the previous lecture, there are three natural lengthscales that characterize the morphological instability driven by constitutional supercooling: the thermal diffusion lengthscale is assumed much larger than either the solutal diffusion length or the capillary length. Thus, we may assume that the temperature field has enough time to relax to equilibrium between the solid and liquid phases within the mushy layer. The smallest scale, the capillary length, is much smaller than the mesoscale homogenization and details on this scale will be averaged out. Opinions differ, however, on whether the homogenization scale should be larger or smaller than the solutal diffusion lengthscale, and this, as we shall see, can impact the exact form of the field equations.

We seek an averaged description of the following fields:

- Mean temperature of the solid/liquid mixture $T(x, t)$,
- Concentration of the liquid phase $C(x, t)$,
- Volume fraction of the solid phase $\phi(x, t)$.

Averages will be taken over the control volume D bounded by surface δD and with unit normal \mathbf{n} (Fig. 7).

We begin with conservation laws for this control volume. Here we will present only the calculation for conservation of mass. From continuity,

$$\frac{d}{dt} \int_D \bar{\rho} dV = - \int_{\delta D} \rho_l \mathbf{n} \cdot \mathbf{u} dS, \quad (16)$$

where $\bar{\rho}$ is the average density in the mushy layer,

$$\bar{\rho} = \rho_s \phi + (1 - \phi) \rho_l. \quad (17)$$

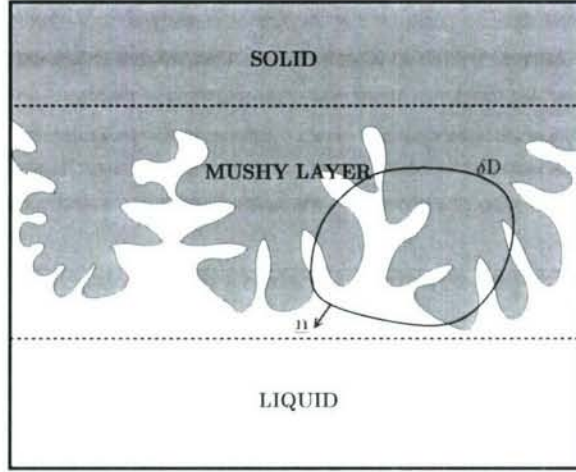


Figure 7: Control volume containing solid and liquid in a mushy layer.

Here the densities of the solid and liquid phases are ρ_s and ρ_l , respectively. We assume that the solid matrix is rigid and stationary² (although the ice can continue to grow), and that the only thing moving is the liquid. Thus, the mushy layer is a porous medium, and the velocity \mathbf{u} in (16) is the *Darcy velocity*, or the mean volume flux of the liquid per unit area of the medium. The Darcy velocity is equal to the liquid volume fraction times the interstitial velocity, $u = (1 - \phi)u_i$.

Averaging over the control volume D and applying the divergence theorem, (17) becomes

$$\int_D \left(\frac{\partial \bar{p}}{\partial t} + \nabla \cdot (\rho_l \mathbf{u}) \right) dV = 0. \quad (18)$$

Since (18) is true for an arbitrary control volume D , the integrand itself must be zero,

$$(\rho_s - \rho_l) \frac{\partial \phi}{\partial t} + \rho_l \nabla \cdot \mathbf{u} = 0, \quad (19)$$

where we have employed a Boussinesq approximation, assuming that the densities of liquid and solid phases are constant. Introducing the density ratio parameter $r \equiv \rho_s/\rho_l$, (19) can be rewritten as the divergence of a non-solenoidal velocity field,

$$\nabla \cdot \mathbf{u} = (1 - r) \frac{\partial \phi}{\partial t}. \quad (20)$$

Thus, if the solid fraction ϕ is increasing (e.g., salt water is solidifying inside sea ice), then the fact that ice has a lower density than water means that the salt water will be squeezed out of the porous medium (we will neglect changes in density caused by salinity gradients). This phenomenon is known as *brine expulsion* in sea ice.

²When studying processes in large ice sheets, one might need to worry about compaction and deformation of the ice matrix. For example, fresh melt water beneath an ice shelf can depressurize and form ice crystals that “snow” upwards onto the bottom of the shelf. This layer can be compacted significantly, and in this case the matrix deformation cannot be neglected.

In a similar way, conservation of heat leads to

$$\overline{\rho c_p} \frac{\partial T}{\partial t} + \rho_l c_{pl} \mathbf{u} \cdot \nabla T = \nabla \cdot (\bar{k} \nabla T) + \rho_s L \frac{\partial \phi}{\partial t}. \quad (21)$$

Overbars represent mesoscale averaging. The gradient lengthscale of the temperature field is assumed much longer than the homogenization scale, and so is not averaged over. The average specific heat capacity is given by the exact expression

$$\overline{\rho c_p} = \phi \rho_s c_p + (1 - \phi) \rho_l c_{pl}, \quad (22)$$

where c_{ps} and c_{pl} are the heat capacities of the solid and liquid phases.

The latent heat capacity is the difference in the enthalpies of the solid and liquid,

$$L(T, C) = H_l - H_s. \quad (23)$$

While L is in general a function of both T and C , we will assume that the mushy layer is in thermodynamic equilibrium, and hence the temperature field and the compositional field are linked by the liquidus relation. This allows us to write L as a function of only T or C .

The volume-averaged conductivity will, in general, be a function of the solid fraction, although what this functional dependence is depends upon the geometry of the mushy layer. For laminate layers, one can derive exact expressions for the conductivities: For the case where the heat flux is parallel to the laminar surfaces, the conductivity is

$$\bar{k} = k_{\parallel} = \phi k_s + (1 - \phi) k_l \quad \text{parallel heat flux,} \quad (24)$$

while for a perpendicular heat flux,

$$\bar{k} = k_{\perp} = \frac{1}{\phi/k_s + (1 - \phi)/k_l} \quad \text{perpendicular heat flux.} \quad (25)$$

It can be shown that for any porous medium the conductivity is bounded by the two laminar cases described above, so that

$$k_{\perp} \leq \bar{k} \leq k_{\parallel}, \quad (26)$$

as depicted in Fig. 8.

In the case of mushy layers in sea ice, the primary dendrites are plate-like and tend to align themselves with the prevailing temperature gradient: in this case, we shall take $\bar{k} = k_{\parallel}(\phi)$ to be a good approximation.

When considering the conservation of heat (21), the large separation of scales between the microscale and the thermal gradient length led to a robust averaging procedure. As mentioned earlier in this section, the separation of scales in the case of the solute field is less obvious. Thus, one representation of the solute conservation equation is (for liquidus/solidus distribution coefficient $k_D = 0$, as is approximately the case for sea-ice):

$$(1 - \phi) \frac{\partial C}{\partial t} + \mathbf{u} \cdot \nabla C = \nabla \cdot (\bar{D} \nabla C) + rC \frac{\partial \phi}{\partial t}. \quad (27)$$

Ambiguity arises in the first term on the right-hand side of (27): by including it, we are implicitly assuming that the solutal diffusion lengthscale is larger than the homogenization

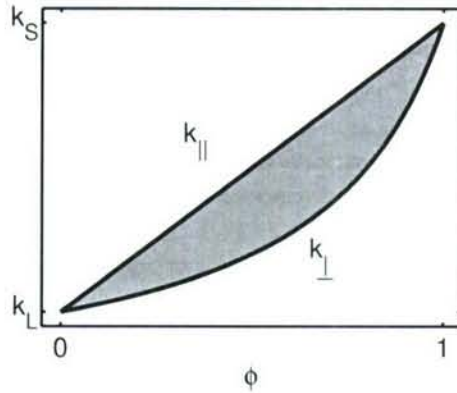


Figure 8: The conductivity of a porous medium is bounded by the laminar cases of parallel and perpendicular heat flux. The range of possible porous medium conductivities is indicated by the shaded region.

scale. If, on the other hand, the diffusion scale is comparable to or smaller than the scale on which we are taking volume averages, then this term vanishes. Indeed, the argument is related to where one draws the interface between the mushy layer and the liquid phase, which in turn raises questions about how one describes the mushy layer itself. In what follows, we shall scale out the offending term; however, it is worthwhile noting that this is a subject of ongoing investigation.

As in the case of the volume-averaged conductivity, the salt diffusivity takes the form

$$\bar{D} = D_l (1 - \phi) = D_{\parallel}. \quad (28)$$

The final term in (27) describes the increase of the concentration in the interstitial region as the ice grows.

We further make the assumption that the mushy layer is in thermal equilibrium so that

$$T = T_L(C) \quad (29)$$

everywhere in the mushy layer. Hence the salt field and the thermal field are tied to one another inside the mushy layer by the liquidus curve, which precludes the possibility of any double-diffusive convection.

Finally, we require a transport equation for the liquid velocity \mathbf{u} . Since we are describing the mushy layer as a porous medium, it is appropriate to use Darcy's equation for flow through a porous medium:

$$\mu \mathbf{u} = \Pi (-\nabla P + \rho \mathbf{g}). \quad (30)$$

Here, μ is the kinematic viscosity, P is the pressure field, \mathbf{g} is the gravitational acceleration, and Π is the permeability of the mushy layer. The latter will in general be a function of ϕ and geometry: we take it to be constant for simplicity. The introduction of the gravitational field introduces for the first time the possibility of convection, altering the heat flux from the liquid region (see later lectures, and Student Problem 5).

Equations (20), (21), (27), (29) and (30), along with the relevant boundary conditions and the equations for the liquid region, can be solved to obtain the temperature field,

concentration field, solid fraction and fluid velocity in the mushy layer in a frame of reference that is fixed with respect to the rigid stationary solid matrix. We consider solutions of these equations in the next lecture.

Student Problem 5: Effect of convection on melt rate for ice in pure water

Problem: Consider pure (i.e., salt-free) water with far-field temperature $T_\infty > T_m$ which is forced in an inviscid convective flow against ice at temperature $T = T_m = 0^\circ\text{C}$ (Fig. 9). Work in an axis system that moves with the ice edge, such that the ice-liquid interface is always at $z = 0$. In this frame, the water velocity field is

$$\mathbf{u} = (Ex, -Ez). \quad (31)$$

What is the melt rate V of the ice interface?

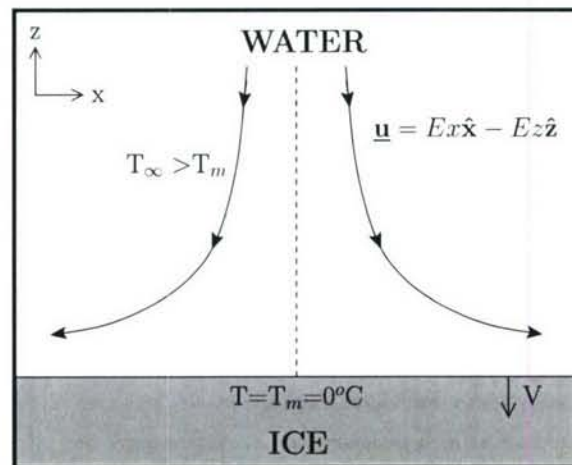


Figure 9: Student Problem 5. What is the melt velocity of the ice interface in the presence of convecting water?

Solution: We begin by seeking the temperature field in the water. In the moving axis system, T should be stationary in time; we also assume it is homogeneous in x . Introducing a dimensionless variable $\theta(z)$ to describe the z -dependence of the temperature field, we can write

$$T_\infty - T(z) = (T_\infty - T_m)\theta(z). \quad (32)$$

Equivalently,

$$T(z) = T_\infty - \Delta T\theta(z), \quad (33)$$

where we have defined $\Delta T \equiv T_\infty - T_m$. The water temperature boundary conditions are now

$$\theta(0) = 1, \quad (34)$$

$$\theta(z \rightarrow \infty) = 0. \quad (35)$$

The temperature field in the water satisfies the diffusion equation,

$$\frac{\partial T}{\partial t} + \mathbf{u} \cdot \nabla T = \kappa \nabla^2 T. \quad (36)$$

Inserting (33) and (31) into (36) yields

$$\theta''(z) = -\frac{Ez}{\kappa} \theta'(z). \quad (37)$$

The solution to (37) subject to (34) and (35) is, by analogy to similar differential equations solved in previous lectures,

$$\theta(z) = \operatorname{erfc}\left(\frac{z}{\lambda}\right), \quad (38)$$

with $\lambda \equiv \sqrt{\frac{2\kappa}{E}}$.

Given this temperature field we can find the interface velocity using the Stefan condition:

$$\rho LV = -k \frac{\partial T}{\partial z} \Big|_{0^+}. \quad (39)$$

The derivative of the temperature field from (33) and (38) is

$$\frac{\partial T}{\partial z} \Big|_{0^+} = -\Delta T \theta'(0) = \Delta T \frac{2}{\sqrt{\pi} \lambda}, \quad (40)$$

where we have used the definition of the erfc function to evaluate the derivative. Inserting (40), $k = \rho c_p \kappa$ (the definition of κ), the Stefan number $S \equiv L / (c_p \Delta T)$, and the definition of λ , we can solve (39) to get the interface velocity

$$V = -\frac{1}{S} \sqrt{\frac{2E\kappa}{\pi}}. \quad (41)$$

As in all examples, the ice melts faster if the Stefan number is small. We see here that the velocity of the melting interface depends on the square root of the convection velocity times the diffusion rate (as we might have guessed from dimensional analysis). The flow toward the phase boundary compresses the thermal boundary layer, which, by dimensional arguments, has thickness $\delta \sim \sqrt{\kappa/E}$. The compressed boundary layer leads to a steeper temperature gradient, thereby enhancing the heat flux from the liquid that causes melting.

GFD 2006 Lecture 6: Idealized mushy layers

Grae Worster; notes by Devin Conroy and Rachel Zammett

March 15, 2007

1 Introduction

In previous lectures we considered solidification at a planar boundary, and we found that in this case there was the possibility of constitutional supercooling in the liquid region ahead of the solidification front. Such constitutional supercooling causes morphological instability of the phase boundary, and the interface evolves until a ‘mushy layer’ (region of mixed phase) is formed. A mushy layer is modeled as a two-component, reactive porous medium. We have also seen that the growth of a mushy layer is governed by the rate of thermal diffusion.

The morphological instability of the interface, caused by constitutional supercooling, increases its specific surface area, and thereby enhances the latent heat release, leading to a temperature that is greater than that obtained for a planar boundary. Increased specific surface area also enhances the release of solute from the solid, which increases the concentration of the interstitial fluid; this increase in concentration acts to lower the liquidus temperature in the mushy layer.

Therefore, if a region of constitutional supercooling is present in a mushy layer, the liquidus temperature in the interstitial region decreases, due to enhanced release of solute, and the actual temperature increases, due to the enhanced release of latent heat. These temperature changes continue until the region of supercooling in the mushy layer has been eliminated (as shown in Figure 1); the temperature and the liquidus temperature in the mushy layer evolve until they are equal. We therefore assume that throughout the mushy layer the temperature is equal to the local liquidus temperature.

Our goal here is to establish the position of the interface between the liquid and the mushy region (and also the solid and the mushy region), and to do this we treat the mushy region separately as an inhomogeneous porous medium. We therefore have two unknown boundaries to determine as part of our solution.

2 Governing equations

From lecture 5, we have that the governing equations describing the evolution of the mean temperature $T(\mathbf{x}, t)$, mean concentration of the liquid phase $C(\mathbf{x}, t)$ and solid fraction $\phi(\mathbf{x}, t)$

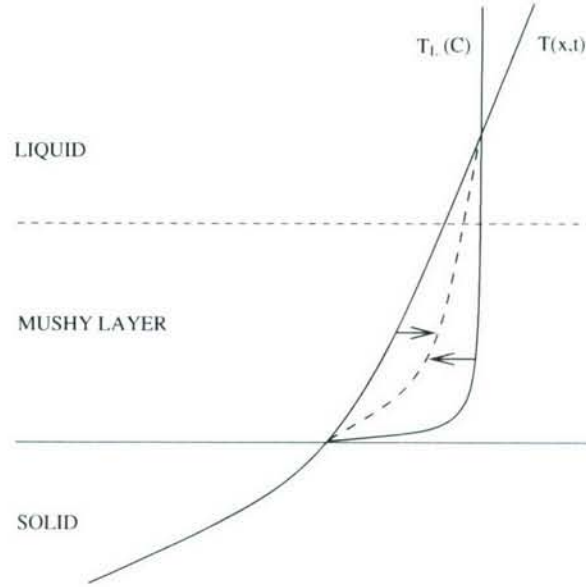


Figure 1: Schematic representation of the effect of increased specific surface area on a region of constitutional supercooling in a mushy layer. As the specific surface area increases, enhanced latent heat release increases the temperature, while enhanced release of solute lowers the liquidus temperature. Thus the temperature reaches an equilibrium where $T = T_L(C)$; this equilibrium is shown by the dashed line which lies between the original temperature and liquidus temperature curves.

in a mushy layer are

$$\nabla \cdot \mathbf{u} = (1 - r) \frac{\partial \phi}{\partial t}, \quad (1)$$

$$\frac{\rho c_p}{\partial t} \frac{\partial T}{\partial t} + \rho_l \mathbf{u} \cdot \nabla T = \nabla \cdot (\bar{k} \nabla T) + \rho_s L \frac{\partial \phi}{\partial t}, \quad (2)$$

$$(1 - \phi) \frac{\partial C}{\partial t} + \mathbf{u} \cdot \nabla C = \nabla \cdot (\bar{D} \nabla C) + rC \frac{\partial \phi}{\partial t}, \quad (3)$$

$$T = T_L(C), \quad (4)$$

$$\mu \mathbf{u} = \Pi(-\nabla p + \rho \mathbf{g}), \quad (5)$$

where $r = \rho_s/\rho_l$ and the remaining symbols have their usual meaning (as described in previous lectures), and we have assumed that the solid phase is pure. Equations (1) – (3) arise from conserving mass, heat and solute. Equation (4) describes the assumption that the temperature and concentration of the interstitial liquid lie on the liquidus, and the final equation (5) is the transport equation for the Darcy velocity \mathbf{u} .

If we consider the case in which the solid in the mushy layer (ice) is growing, then noting that $\rho_s < \rho_l$, equation (1) shows that the velocity field will have a positive divergence. We have an advection-diffusion equation (2) to solve for the temperature, which is forced by latent heat release in the mushy layer. We also have an advection-diffusion equation for the

solute (3), which is modified by a source term to reflect the increase in concentration of the interstitial fluid as a result of the formation of pure ice crystals.

We are interested in dynamically generated fluid flows, particularly under the action of gravity, and therefore use Darcy's law (5), which states that the fluid velocity is proportional to the negative pressure gradient.

Equations (1)–(5) are solved in the mushy layer; the Navier-Stokes equations coupled with advection-diffusion equations for heat and solute are solved in the liquid region, while we consider pure diffusion in the solid phase.

2.1 Internal Disequilibrium

In earlier lectures, we saw that for the kinetically driven solidification of a planar interface, the normal velocity of the phase boundary could be described by

$$v_n = G(T_m - T), \quad (6)$$

where G is the kinetic coefficient, which is assumed constant. In the case of a mushy layer, equation (6) can be modified to

$$\dot{\phi} = GA[T_L(C) - T], \quad (7)$$

where A denotes the specific surface area of the internal phase boundaries in the mushy layer. Thus if $T \neq T_L(C)$ in the interior of the mushy layer, the surface area A increases and as the product GA becomes large $T \simeq T_L(C)$.

3 Interfacial conditions

To generate boundary conditions for the governing equations, we apply the conservation laws at both interfaces. The first interfacial condition, derived from equation (1) is

$$[\mathbf{u} \cdot \mathbf{n}] = -(1 - r)v_n[\phi]. \quad (8)$$

In most circumstances, ϕ is continuous between the mushy layer and the liquid, and therefore $[\phi] = 0$. At the interface between the solid and the mushy layer, however, there may be a discontinuity in ϕ , and we would expect only to be able to impose continuity of ϕ at one boundary as there is only one partial derivative of ϕ in the governing equations.

The second boundary condition is analogous to the Stefan condition, and is given by

$$\rho_s L[\phi]v_n = [\bar{k} \mathbf{n} \cdot \nabla T]. \quad (9)$$

Note that there is no advective term in condition (9) as the equations of mass and heat conservation imply that $[T] = 0$ at the interface; it is not obvious, however, that the same will be true for the mean concentration, C .

The third condition, applied at the interface of the mushy layer and the liquid, is

$$[(v_n - \mathbf{u} \cdot \mathbf{n})C]_m^l + C_m \phi v_n = [-D \mathbf{n} \cdot \nabla C]_m^l. \quad (10)$$

The subscript l denotes evaluation in the liquid; m denotes evaluation in the mushy layer.

As we have homogenized the mushy layer on some scale, we cannot interrogate it on a length scale that is smaller than this. In deriving these interfacial conditions we can therefore no longer consider the interface between the mushy layer and the solid or liquid phase to be a line; instead, we must consider it to be a region with a thickness that is comparable to the homogenization scale, δ .

Boundary conditions (8) and (9) are robust in this sense; condition (10) is more controversial, and depends on the relative sizes of the homogenization length scale and the length scale of diffusion, l_D . The choice $\delta < l_D$ allows the retention of solute diffusion in equation (3), which means that the mean concentration of the liquid phase, C , is continuous. Boundary condition (10) may therefore be simplified to

$$C_m \phi v_n = [-D \mathbf{n} \cdot \nabla C]_m^l. \quad (11)$$

It is also possible to suppose $\delta \sim l_D$ and consider the limit where $D/\kappa \rightarrow 0$, but more slowly than $\delta \rightarrow 0$. In this case, the term representing diffusion of solute is removed from equation (3), meaning that we can no longer impose continuity of C . An analogous situation occurs in fluid mechanics if the viscosity of a fluid tends to zero. In this case it is no longer possible to enforce continuity of the velocity field, and it is therefore possible to obtain shear layers.

The three boundary conditions (8) – (10) come from the conservation of mass, heat and solute, equations (1) – (3). However, these must be supplemented due to the presence of the additional dependent variable ϕ . Early work imposed $\phi = 0$ at the interface and required ϕ to be continuous, but for certain parameter regimes the problem is then mathematically ill-posed. There is also no good physical justification for this condition; again, it is not possible to interrogate the system on length scales which are smaller than δ , which implies that a jump in ϕ is allowed.

Instead, we return to our earlier descriptions of a solid–liquid interface. In this case, we saw that there was the possibility of forming a region of constitutional supercooling, and this drove the morphological instability at the interface and thus the formation of the mushy layer. The criterion for formation of such a region of constitutional supercooling was

$$\left. \frac{\partial T}{\partial n} \right|_l < \left. \frac{\partial T_L}{\partial n} \right|_l, \quad (12)$$

and as the mushy layer thickens, this inequality tends to an equality. We therefore make the assumption that the mushy layer grows just quickly enough that any residual supercooling in the liquid ahead of it is eliminated, which allows us to write the final boundary condition (assuming the interface is solidifying),

$$\left. \frac{\partial T}{\partial n} \right|_l = \left. \frac{\partial T_L}{\partial n} \right|_l. \quad (13)$$

The final boundary condition consists of a specified temperature at the solid–mushy layer interface. We now have a complete set of equations (1) – (5) with boundary conditions (8), (9), (10) and (13). This system has solutions for all parameter values.

4 ‘Ideal’ mushy layers

The aim of this section is to simplify the governing equations for the evolution of a mushy layer while retaining all the necessary interactions. To do this, we make the following

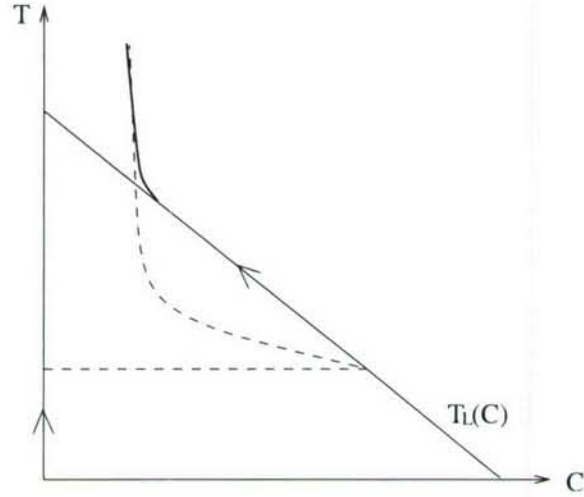


Figure 2: The trajectory of T and C in the phase diagram for a mushy layer (solid curve) compared with that when there is a planar solid liquid interface (dashed curve). The liquidus temperature $T_L(C)$ is given by $T = T_m - mC$ for some positive constant m . The temperature in the mushy layer follows the liquidus curve and thus there is no possibility of constitutional supercooling. Note that in this case the temperature field in the liquid region emerges at a tangent to the liquidus. In contrast, the temperature field in the solid-liquid system has a portion lying below the liquidus and thus constitutional supercooling is possible.

assumptions. Firstly, we assume that the densities of the solid and liquid phases are equal, i. e. $\rho_s = \rho_l$. Thus we have that $r = 1$, and conservation of mass, equation (1), gives that the velocity is solenoidal.

We next assume that $D \ll \kappa$, which allows us to eliminate the second derivative term in the conservation of solute equation. Although this may appear to be a singular perturbation, it is justified because we have a relationship between T and C in the mushy layer (equation (4)), and we retain the second derivative in the conservation of heat equation (2). Finally, we make the assumptions that properties are independent of phase and that the system is above the eutectic temperature.

Using these assumptions, the governing equations (1) – (5) become

$$\frac{\partial T}{\partial t} + \mathbf{u} \cdot \nabla T = \kappa \nabla^2 T + \frac{L}{c_p} \frac{\partial \phi}{\partial t}, \quad (14)$$

$$(1 - \phi) \frac{\partial C}{\partial t} + \mathbf{u} \cdot \nabla C = C \frac{\partial \phi}{\partial t}, \quad (15)$$

$$T = T_L(C), \quad (16)$$

$$\mu \mathbf{u} = \Pi_0 (-\nabla p + \rho \mathbf{g}), \quad (17)$$

$$\nabla \cdot \mathbf{u} = 0. \quad (18)$$

Here we assume that κ is constant in the ideal mushy layer and also that ρ is constant; later we will consider $\rho = \rho(T, C)$.

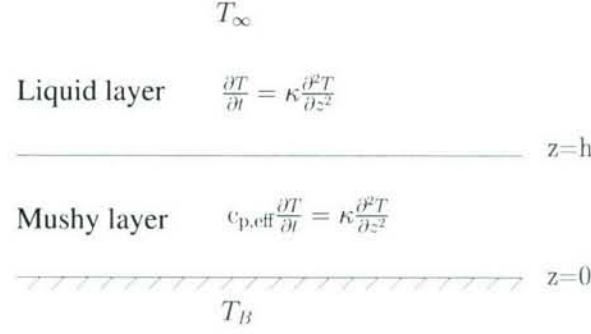


Figure 3: Growth of a mushy layer from a cooled boundary at $z = 0$. The mush–liquid interface is at $z = h(t)$ and the position of the cooled boundary is at $z = 0$.

The above assumptions can also be used to simplify the boundary conditions: during solidification, equations (8), (9) and (10) become

$$[\mathbf{u} \cdot \mathbf{n}] = 0, \quad (19)$$

$$[\phi]_m^l = 0, \quad (20)$$

$$[\mathbf{n} \cdot \nabla T]_m^l = 0. \quad (21)$$

In this case there is no solid layer: only the mushy layer and the liquid region above it.

5 The case of no flow

When there is no pressure gradient in the mushy layer and convection is not possible because there is a stable density field, the Darcy velocity is zero. In this case there is no flow in the system and the advective part of the transport equations (14)–(18) can be eliminated to obtain

$$\frac{\partial T}{\partial t} = \kappa \nabla^2 T + \frac{L}{c_p} \frac{\partial \phi}{\partial t}, \quad (22)$$

$$(1 - \phi) \frac{\partial C}{\partial t} = C \frac{\partial \phi}{\partial t}, \quad (23)$$

$$T = T_L(C). \quad (24)$$

The second of these equations can be rearranged and integrated as follows

$$\frac{\partial}{\partial t} [C(1 - \phi)] \Rightarrow (1 - \phi) C = \bar{C}(\mathbf{x}), \quad (25)$$

implying that the total amount of species C is constant in time but variable in space according to the function $\bar{C}(\mathbf{x})$. If initially this function is constant in the liquid ($\bar{C}(\mathbf{x}) = C_0$) then equation (25) reduces to

$$\phi = 1 - \frac{C_0}{C}, \quad (26)$$

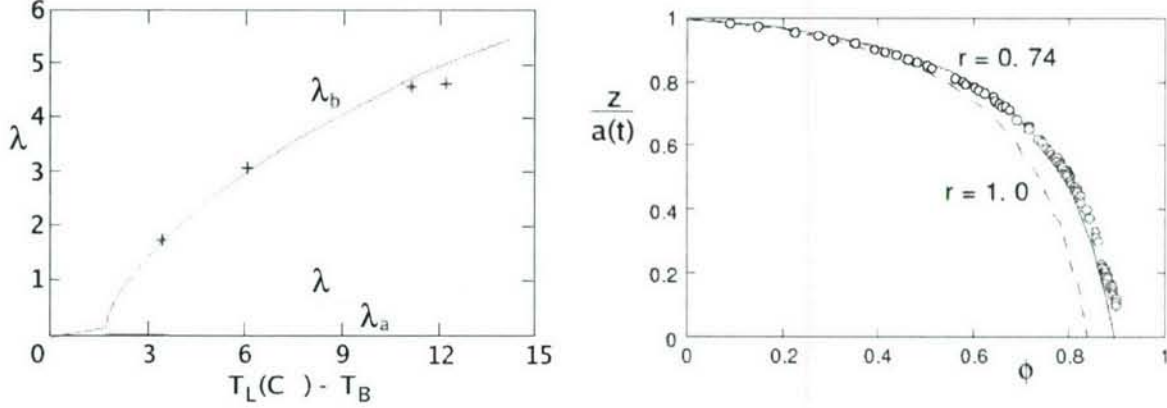


Figure 4: The plot on the left shows the normalized interface position for the solid-liquid interface, λ_a and the mush-liquid interface, λ_b as a function of $T_L(C_0) - T_B$ for experiments (crosses) and numerics (solid line). The plot on the right shows the solid fraction as a function of height for numerics (dashed line) and experiments (circles) corresponding to $r = .74$.

which effectively constrains the amount of solid by the deviation in concentration from its initial value. This equation can be differentiated with respect to time to obtain

$$\frac{\partial \phi}{\partial t} = \frac{C_0}{C_L(T)^2} \frac{\partial C_L(T)}{\partial t} = \frac{C_0}{C_L^2} \frac{dC_L}{dT} \frac{\partial T}{\partial t}, \quad (27)$$

in which we assume that the concentration follows the liquidus line as a function of temperature. This new relationship for the void fraction provides closure to the temperature equation (22), which now becomes

$$\left[1 - \frac{C_0 L}{c_p C_L^2} \frac{dC_L}{dT} \right] \frac{\partial T}{\partial t} = \kappa \nabla^2 T \Rightarrow c_{p,\text{eff}} \frac{\partial T}{\partial t} = \kappa \nabla^2 T, \quad (28)$$

where $c_{p,\text{eff}}$ is the non-dimensional effective specific heat. This is a nonlinear diffusion equation for T in which the effective heat capacity is enhanced by the internal release of latent heat.

In summary we have the setup shown in figure 3 with the following governing equations

$$\frac{\partial T}{\partial t} = \kappa \frac{\partial^2 T}{\partial z^2}, \quad (29)$$

$$c_{p,\text{eff}} \frac{\partial T}{\partial t} = \kappa \frac{\partial^2 T}{\partial z^2}, \quad (30)$$

for the temperature evolution in the liquid and mushy layers respectively. In the far field liquid we use the constant boundary condition $T(t, \infty) = T_\infty$ and at the base of the mushy layer we use $T(t, 0) = T_B$. As described previously we have the following interface conditions

$$T = T_L(C_0), \quad \left[\frac{\partial T}{\partial z} \right]_M^L = 0, \quad [T]_M^L = 0, \quad (31)$$

	Cooled from below stable Temperature	Cooled from above unstable Temperature
$C_\infty < C_E$ Heavy fluid released	2. No convection Mushy Layer	6. Mushy layer Thermal and compositional convection
$C = A, C_E, B$ No compositional effects	1. Planar no convection	3. Planar thermal convection
$C_\infty > C_E$ light fluid released	5. Compositional convection in liquid and mushy layer	4. Mushy layer thermal convection in the liquid

Table 1: Organization of the different convective regimes as explained thoroughly in the text. In all cases we assume that the density of the fluid increases with the concentration, C and increases with a decrease in the temperature, T . Here C_E is the eutectic concentration and C_∞ is the concentration far from the phase boundary.

at $z = h$.

In general these equations have a similarity solution with the similarity variable $\eta = z/2\sqrt{\kappa t}$ and interface position $h = 2\lambda\sqrt{\kappa t}$. Figure 4 shows the numerical solutions and experimental results for the normalized interface position λ as a function of $T_L(C_0) - T_B$ and the solid fraction as a function of height scaled with the moving interface.

6 Solidification and convection

During the solidification of a binary melt there are some interesting physical features, such as the formation of mushy layers and the onset of convection, that depend on the properties of the released fluid and the solidification boundary. In table 6 we organize these features according to the location of the solidification boundary and the concentration, which increases with density, of the rejected fluid in comparison to the far field concentration, C_∞ . We now discuss each of these cases in turn.

1. In this case there is no excess solute produced by the solidifying front and the compositional density field remains uniform. Since the temperature is lowest at the bottom, and thus the density decreases with height the temperature field is stable as well. As a result convection will not occur and the growth rate will proceed as in the Stefan problem.
2. Here the concentration of the melt is less than that of the solid and in general a mushy layer will form. Since the rejected solute makes the fluid adjacent to the moving boundary denser the compositional density field is stable. In addition the thermal density field is stable, owing to the cold lower boundary, and convection will not occur.
3. Similar to case 1 except that now the temperature is higher at the top and therefore the density increases with height. The thermal density field is unstable and may lead

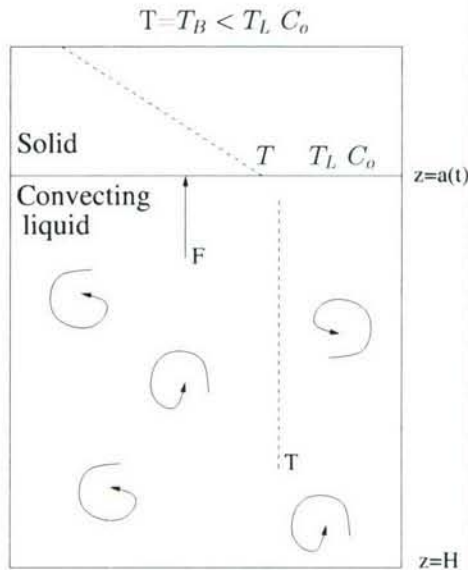


Figure 5: Schematic illustration of a solid growing into a binary melt, cooled from above. Since the density is larger at the top due to a lower temperature, there is thermal convection. Here F is the flux of heat by thermal convection in the liquid.

to convection if the Rayleigh number is large enough.

4. In this case the residual melt adjacent to the phase boundary is lighter than the melt in the far field, resulting in a stable compositional density field. On the other hand, the thermal density field is unstable and thermal convection can occur. This convection will occur in the liquid only; the mush will remain stagnant.
5. In this case the thermal density field is stable, whereas the compositional density field is unstably stratified. Double-diffusive convection can occur in the liquid in the form of fingers but will not occur in the mushy layer as the temperature and concentration are constrained by the liquidus relationship and are therefore not independent. There may be convection in the mushy layer leading to the formation of dissolution channels.
6. Here the melt is cooled from above and heavy fluid is released from the phase boundary. The thermal and compositional density fields are both unstable and will act together to produce convection. In addition, convection will occur in the mushy layer, which may alter the micro-structure of this porous medium. This is the regime for the formation of sea ice.

Cases 3 and 4

For cases 3 and 4 of table 6 the convection generated in the liquid acts to transport heat from the bottom to the solidifying interface as illustrated in figure 5. The Rayleigh number for this situation was assumed to be large ($Ra \gg 1$) and therefore the interior of the liquid

is well mixed up to the thermal boundary layer. The Stefan condition will have the form

$$\rho_s L \dot{a} = -k \left. \frac{\partial T}{\partial z} \right|_s - F, \quad (32)$$

where F is the heat flux from the liquid to the solid. Naturally this heat flux will be a function of the temperature difference between the interface and far field liquid temperature and the strength of the fluid advection, given by

$$F = B \left(\frac{\alpha g}{\kappa \nu} \right)^{\frac{1}{3}} [T - T_L(C_o)]^{\frac{4}{3}}. \quad (33)$$

Here B is an experimentally determined number, ν is the kinematic viscosity, α is the coefficient of thermal expansion and g is the acceleration due to gravity. Since we must conserve energy, the liquid will cool down according to

$$\rho c_p (H - a) \frac{\partial T}{\partial t} = -F, \quad (34)$$

due to the transfer of heat from the liquid to solid.

The position of the phase boundary as a function of time is shown in figure 6 with some distinct, quantitatively different regimes due to the onset and development of convection. We can make the quasi-stationary approximation

$$k \frac{T_L - T_B}{a} = \rho L \dot{a} + F. \quad (35)$$

At early time, labeled 1 in figure 6, the solid thickness is small ($a \ll 1$), the growth rate is large ($\dot{a} \gg 1$) and the convective flux is negligible. The dominant balance is between the first and second terms in equation (35) and the solution proceeds as in the planar case with $a \propto \sqrt{t}$. Eventually buoyancy forces due to the unstable thermal gradient dominate viscous dissipation and convection ensues (region 2 in figure 6). At early times the advective transport of thermal energy from the bottom to the top is enough to balance the transfer of heat away into the solid and the growth rate slows. Later on, the liquid cools down, reducing the convective heat transfer in the liquid, according to equation (34) and the growth rate proceeds according to equation (35). At long time, indicated by region 3 in figure 6, the temperature of the liquid has cooled down sufficiently so that the convective heat transfer is much smaller than conduction in the solid. The dominant balance is again between the first and second terms in equation (35) and the solution proceeds as in the planar case with $a \propto \sqrt{t}$.

7 Student problem 6

Determine the position of the interface between the mushy layer and liquid for the constant solidification rate shown in figure 7. The governing equations and appropriate boundary conditions in the liquid region and the mushy layer respectively, are as follows

$$\frac{\partial T}{\partial t} = \kappa \frac{\partial^2 T}{\partial z^2}, \quad T(t, \infty) = T_\infty, \quad T(t, h) = T_L(C_0) \quad z > h, \quad (36)$$

$$\frac{\partial T}{\partial t} = C(T) \kappa \frac{\partial^2 T}{\partial z^2}, \quad T(t, 0) = T_E, \quad T(t, h) = T_L(C_0) \quad 0 < z < h, \quad (37)$$

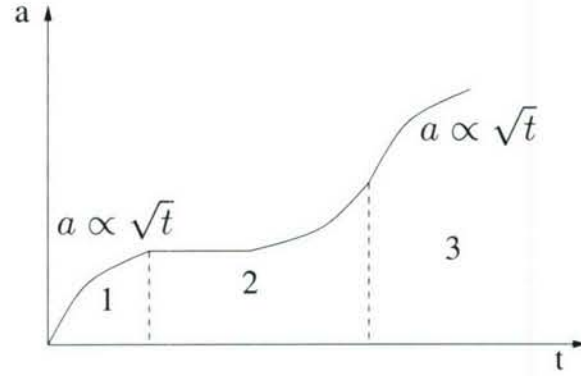


Figure 6: Interface position of a solidifying binary melt as a function of time. There are three distinct regimes, labeled 1,2 and 3, which are distinguished by the relative strength of convection occurring in the liquid region.

where $C(T) = 1 - LC'_L C_0 / c_p C_L^2$. Along the liquidus line we have the linear expression $C_L = C_0 + mT$, where $m = (C_0 - C_E) / (T_L(C_0) - T_e)$ is the slope. In addition we have the following interfacial condition

$$\left. \frac{\partial T}{\partial z} \right|_{\text{liquid}} = \left. \frac{\partial T}{\partial z} \right|_{\text{mushy layer}}, \quad (38)$$

at $z = h$.

Answer

The non-dimensional version of the specific heat can be expressed as

$$C(T) = 1 - \frac{\frac{S}{\xi}}{\left(1 + \frac{1}{\xi} \frac{T}{T_L(C_0) - T_E}\right)^2}, \quad (39)$$

where S is the Stefan number and $\xi = C_0 / (C_0 - C_E)$ is a concentration ratio. In the limit $\xi \gg 1$ and $S \gg 1$, while $S/\xi = O(1)$ we obtain $C(T) = 1 - S/\xi = \Omega$. Note that $\Omega > 0$.

For a constant growth rate V we can move the coordinate system by making a Galilean transformation so that we are in a steady reference frame. Mathematically this is written as, $\bar{x} = z - Vt$, so that $\frac{\partial}{\partial t} = -V \frac{\partial}{\partial z}$. In addition it is convenient to non-dimensionalize the equations using the following scales

$$\theta = \frac{T - T_L}{T_E - T_L}, \quad \hat{z} = z \frac{\kappa}{V}, \quad (40)$$

so that equations (36)–(37) become

$$\theta'' + \theta' = 0, \quad \theta(\infty) = \theta_\infty, \quad \theta(\hat{h}) = 0 \quad z > h, \quad (41)$$

$$\theta'' + \Omega \theta' = 0, \quad \theta(0) = -1, \quad \theta(\hat{h}) = 0 \quad 0 < z < h. \quad (42)$$

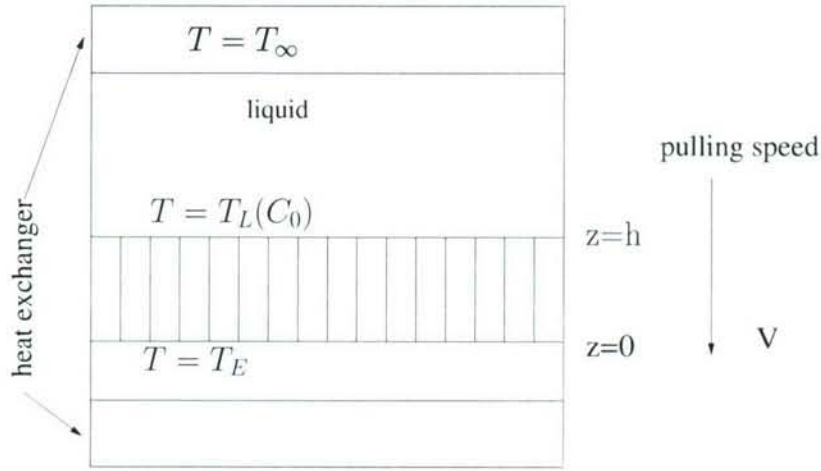


Figure 7: Setup for the student problem, showing the growth of a mushy layer into a liquid from a cooled boundary at $z = 0$. The apparatus is being pulled at a constant velocity through heat exchangers such that we are in a steady frame of reference.

The solutions of these equations are

$$\theta = \theta_\infty - \theta_\infty e^{\hat{h}-z} \quad z > h, \quad (43)$$

$$\theta = \frac{1}{1 - e^{\Omega \hat{h}}} \left[e^{\Omega(h-z)} - 1 \right] \quad 0 < z < h. \quad (44)$$

The position of the interface is calculated by using the flux condition (38) $\theta'|_{\text{liquid}} = \theta'|_{\text{mushy layer}}$ to obtain

$$\hat{h} = \frac{1}{\Omega} \ln \left[1 + \frac{\Omega}{\theta_\infty} \right]. \quad (45)$$

GFD 2006 Lecture 7: Convection in mushy layers

Grae Worster; notes by Ian Eisenman and Victor Tsai

March 15, 2007

1 Convection Setup

Here we perform the analysis governing the regions 5 and 6 of the table shown in Lecture 6. Under these conditions we expect convection to occur within the mushy layer. We note that under strong convection, channels form within the mushy layer and are called chimneys by the metallurgical community or brine channels in sea ice. When these channels are discussed (later), it will be assumed that the scale of the mushy layer and the scale of the channels are greater than the scale of the dendrites.

We begin our analysis with the ideal mushy layer equations, as derived in Lecture 6. The results will therefore describe the physics of the convecting mushy layer but will not agree quantitatively with experiments. Taking

$$\rho = \rho_0[1 - \alpha(T - T_0) + \beta(C - C_0)], \quad (1)$$

$$T \equiv T_L(C) = T_0 - m(C - C_0), \quad (2)$$

$$\theta = \frac{T - T_0}{T_0 - T_B} = \frac{C - C_0}{C_0 - C_B}, \quad (3)$$

$$\Delta T \equiv T_0 - T_B, \quad (4)$$

the ideal mushy layer equations simplify to:

$$\frac{\partial \theta}{\partial t} + \mathbf{u} \cdot \nabla \theta = \kappa \nabla^2 \theta + S \frac{\partial \varphi}{\partial t}, \quad (5)$$

$$(1 - \varphi) \frac{\partial \theta}{\partial t} + \mathbf{u} \cdot \nabla \theta = -(\xi - \theta) \frac{\partial \varphi}{\partial t}, \quad (6)$$

$$\mathbf{u} = -\frac{\Pi}{\mu} [\nabla p + \rho_0 \beta^* \Delta C \theta \mathbf{g}], \quad (7)$$

where $S = L / (C_P \Delta T)$, $\xi = C_0 / (C_E - C_0) = C_0 / \Delta C$ and $\beta^* = \beta + m \alpha$.

Typically $m \alpha < \beta$ which is the reason for denoting β^* as above. For boundary conditions, we have bottom temperature equal to the eutectic temperature, i.e. $T(z = 0) = T_B = T_E$. We also have $T(z = h) = T_0$ and $T(\infty) = T_\infty$. These boundary conditions are for a one-dimensional problem, but are easily generalized to multiple dimensions.

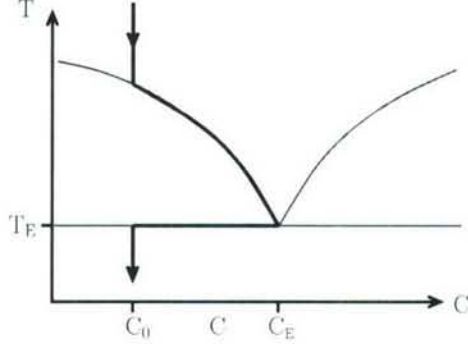


Figure 1: Phase diagram for near-eutectic approximation. In this approximation, ΔC is taken to be much less than C_0 .

2 Near-Eutectic Approximation

The near-eutectic approximation (see Fig. 1) is that

$$\xi \gg 1 \quad (8)$$

and

$$S \gg 1 \quad (9)$$

with

$$\frac{S}{\xi} = O(1). \quad (10)$$

Taking this approximation yields $\varphi \sim 1/\xi \ll 1$. Thus (6) yields

$$-\xi \frac{\partial \varphi}{\partial t} \approx \frac{D\theta}{Dt}. \quad (11)$$

Substituting this result into (5) and defining $\Omega = 1 + S/\xi$ leads to

$$\Omega \frac{D\theta}{Dt} = \kappa \nabla^2 \theta. \quad (12)$$

Equations (7) and (12) are equivalent to those for convection in a passive porous medium.

To solve the equations, we first scale length with h , time with $h^2\Omega/\kappa$, velocity with $\kappa/(h\Omega)$, and pressure with $\beta^*\Delta C\rho_0gh$. Thus, (12) and (7) become

$$\frac{\partial \theta}{\partial t} + \mathbf{u} \cdot \nabla \theta = \nabla^2 \theta \quad (13)$$

and

$$\mathbf{u} = R_m[\nabla p - \theta \hat{\mathbf{k}}], \quad (14)$$

where

$$R_m = \frac{\beta^* \Delta C \rho_0 g \Pi h \Omega}{\kappa \nu} \quad (15)$$

and $\nu = \mu/\rho_0$. Now all variables are dimensionless.

Solving for the basic state (no time dependence or x dependence), we set $\partial/\partial t = \partial/\partial x = 0$ which yields $\theta = -1 + z$ and $\mathbf{u} = 0$. Next we solve the two-dimensional problem with convection solely within the mushy layer and with a planar interface. Introducing a stream function for the 2-dimensional velocity such that, $\mathbf{u} = (\psi_z, -\psi_x)$, and adding a perturbation θ' to the base state temperature field, $\theta = -1 + z + \theta'$, (13) and (14) lead to

$$\nabla^2 \theta' = -\psi_x + \frac{\partial \theta'}{\partial t}, \quad (16)$$

$$\nabla^2 \psi = -R_m \theta'_x. \quad (17)$$

Assuming no flow at either (planar) interface of the mushy layer, the boundary conditions are

$$\theta'(z = 0) = 0, \quad (18)$$

$$\theta'(z = 1) = 0, \quad (19)$$

$$\psi(z = 0) = 0, \quad (20)$$

$$\psi(z = 1) = 0. \quad (21)$$

One should note that this problem is not realistic since convection in the mushy layer will induce convection in the liquid above so that boundary condition (21) is not satisfied in practical situations. However, the problem is still a useful conceptual problem to solve.

To start the stability analysis, we look for perturbations of the form

$$\theta' = \hat{\theta}(z)e^{i\alpha x + \sigma t}, \quad (22)$$

$$\psi = \hat{\psi}(z)e^{i\alpha x + \sigma t}. \quad (23)$$

Marginal equilibrium then occurs when $\sigma = 0$, or by setting $\frac{\partial}{\partial t} = 0$. Substitution with this condition yields

$$\left(\frac{d^2}{dz^2} - \alpha^2\right) \hat{\theta} = i\alpha \hat{\psi} \quad (24)$$

$$\left(\frac{d^2}{dz^2} - \alpha^2\right) \hat{\psi} = -i\alpha R_m \hat{\theta} \quad (25)$$

The solution to these coupled ODEs is

$$\hat{\theta} = A_n \sin(n\pi z), \quad (26)$$

$$\hat{\psi} = B_n \sin(n\pi z), \quad (27)$$

$$-R_m = \frac{(n^2 \pi^2 + \alpha^2)^2}{\alpha^2}. \quad (28)$$

Plotting $-R_m$ at marginal equilibrium as a function of α we note that the first instability (lowest value of $-R_m$) occurs for $n = 1$, thus the curve

$$-R_m = R_b(\alpha) \equiv \frac{(\pi^2 + \alpha^2)^2}{\alpha^2} \quad (29)$$

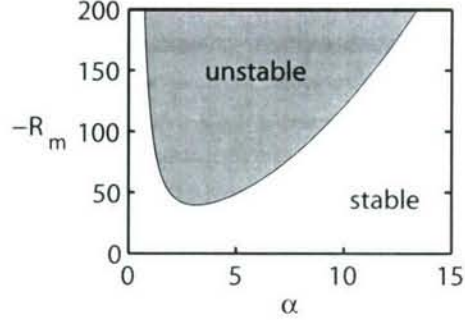


Figure 2: Stability of perturbations with Rayleigh number R_m and wavenumber α .

is the boundary between stability ($-R_m < R_b$) and instability ($-R_m > R_b$) (as a function of α) as shown in Fig. 2. The minimum value of $R_b(\alpha)$ occurs at $R_b(\alpha) = R_c \equiv 4\pi^2$. If $R_m > R_c$ then instability occurs.

Summary of key points

- R_m is a porous-medium Rayleigh number and is proportional to Πh , where Π is permeability of the mushy layer and h is the thickness.
- R_m depends on *compositional* buoyancy but on *thermal* diffusivity. In general, the Rayleigh number is the ratio of buoyancy to dissipation.
- The critical condition is modified by $\Omega = 1 + S/\xi$, so convection is more likely when S is large.

3 Parcel Argument

Consider a parcel in the mushy layer, and hence on the liquidus, that is moved to a different region in the mushy layer where the fluid is warmer and saltier (but still on the liquidus). As is illustrated in Fig. 3, the parcel initially gets warmed to the temperature of its new surroundings; it then dissolves some crystals to increase its salinity and arrive on the liquidus. The dissipation of buoyancy, then, is through a combination of thermal diffusion and dissolution.

Large Stefan number S or small ξ means that there is less phase change per unit temperature change, and hence less dissipation of buoyancy, leading to greater instability. This is also the basic mechanism of channel formation.

From equation (11), we see that there is dissolution where the temperature of a fluid parcel increases. This requires the flow to be larger than the isotherm propagation speed.

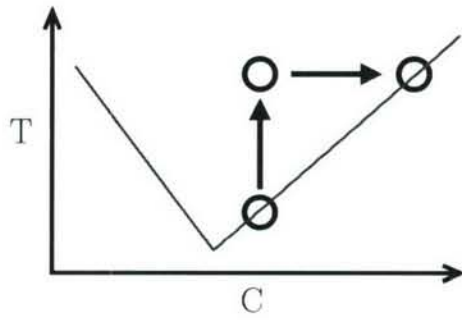


Figure 3: Phase diagram for parcel being moved to warmer region within mushy layer.

GFD 2006 Lecture 8: Interfacial pre-melting

Grae Worster; notes by Robert Style and Dominic Vella

29 June, 2006

1 Interfacial Premelting

In the previous lectures, we have concentrated on solidification of ice on large scales. In the last two lectures, we will switch to microscopic scale and study a phenomenon of *pre-melting*: the existence of a thin liquid film on the surface of a solid below the bulk freezing temperature. Although the thickness of the films generated by premelting are typically of the order of 100 molecular diameters, we will see that they are highly relevant: for example premelting plays an important role in the generation of frost heave.

The existence of premelted films was first postulated by Faraday and Tyndall in the 19th century in order to explain the observation that snow sticks together when compacted, unlike most granular solids. The idea being that upon contact of two ice grains, the thin film will freeze at the contact line to join the two crystals (see Fig. 1). At the time however, it was accepted that an increase in pressure also caused melting and so in the absence of proof of the existence of premelted films, the pressure melting view prevailed. Recently however, experiments have delivered proof of the existence of the films, and this, coupled with the theoretical evidence showing that pressure melting can not possibly explain all observed effects has finally confirmed the validity of Faraday and Tyndall's ideas.

The presence of the film stems from a repulsive force between the solid and the air, due to van der Waals forces. As we will see, this force means that it is energetically favourable for some of the solid to melt, increasing the gap between the solid and the air. However, as the system is below the bulk freezing temperature of the liquid, the film is limited to microscopic thicknesses. It is this competition between repulsive force and freezing drive that determines the equilibrium thickness of the film.

2 van der Waals Forces

van der Waals forces are attractive forces arising from fluctuations in the dipole field of molecules giving rise to fluctuations in nearby molecules. These fluctuations cause electrostatic forces to act between the molecules, giving rise to a potential between two molecules that takes the form

$$\phi = -\frac{k_{12}}{r^6}, \quad (1)$$

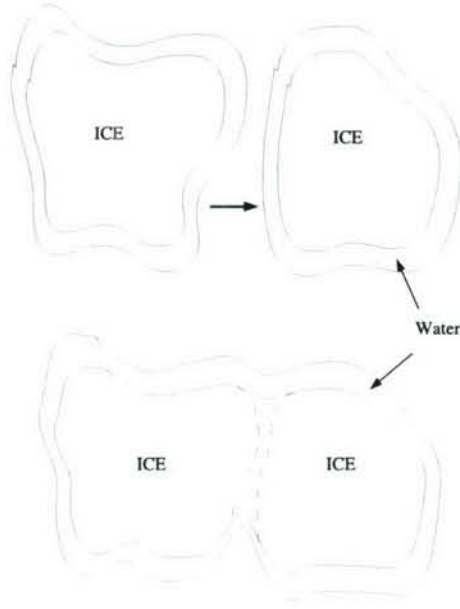


Figure 1: The sintering of two ice blocks upon contact by freezing of the premelted film.

where k_{12} is a constant depending on the properties of molecules 1 and 2, and r is the distance between the molecules.

2.1 Force between a molecule and an extended solid

From this expression, we can work out the attractive force between a molecule of phase 2, separated from a semi-infinite plane of phase 1 by a distance h (see Fig. 2(i)). Letting ρ_1 be the number density of molecules in phase 1 and \mathcal{D} be the semi-infinite domain of phase 1, we can then integrate in cylindrical polar co-ordinates to yield the total potential

$$\phi = \int_{\mathcal{D}} \frac{-\rho_1 k_{12} dV}{[r^2 + (h+z)^2]^3} = -\frac{\pi k_{12} \rho_1}{6 h^3}. \quad (2)$$

2.2 Interaction between a slab and a semi-infinite material

We can now use this potential to calculate the potential per unit area between an infinite slab of thickness h and a semi-infinite solid (Fig. 2(ii)), by integrating over the molecules that make up the infinite slab. Integrating equation (2) between $z = 0, h$, we find that the potential per unit area is

$$\phi = \int_0^h -\frac{\pi k_{12} \rho_1 \rho_2}{6 (z+d)^3} dz = \frac{A_{12}}{12\pi} \left[\frac{1}{(h+d)^2} - \frac{1}{d^2} \right], \quad (3)$$

where $A_{12} = \rho_1 \rho_2 k_{12}$ is the Hamaker constant for materials 1 and 2.

From this expression, we can obtain the surface energy when two infinite solids of phases 1 and 2 are in contact. By assuming that there is a molecular cutoff distance $d = \sigma_{12}$ that separates phases in contact, corresponding to the repulsive forces between molecules at

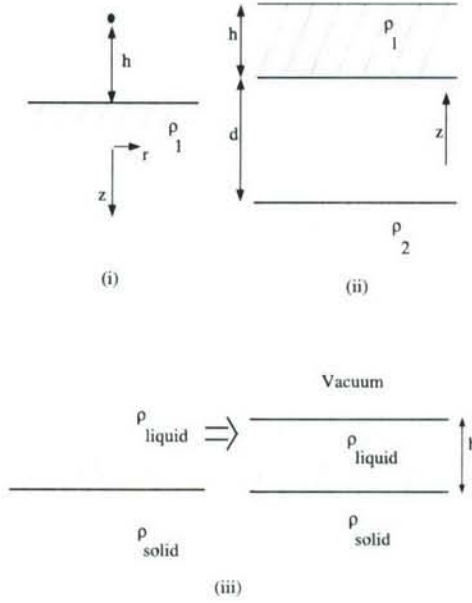


Figure 2: (i) The potential between a molecule and a semi-infinite solid. (ii) The potential between a semi-infinite solid and a slab. (iii) The derivation of the potential for a liquid film. The reference state (LHS) is modified to achieve the desired potential (RHS).

short distances, when $h \rightarrow \infty$ in the above expression, we find that the potential per unit area between two semi-infinite phases separated by a gap of thickness d is

$$\phi = -\frac{A}{12\pi d^2}, \quad (4)$$

and letting $d \rightarrow \sigma_{12}$, we obtain the surface energy, given by

$$\gamma_{12} = -\phi = \frac{A_{12}}{12\pi\sigma_{12}^2}. \quad (5)$$

2.3 Thin liquid films

We are now in a position to calculate the potential of thin liquid film of thickness h on top of a semi-infinite solid. We will find the potential by starting with a reference state of known energy and then modify it, while tracking the energy changes associated with the modifications (Fig. 2(iii)). In this case, we start with a half-plane of solid underlying a half-plane of liquid. As we have seen, this has a surface-energy of γ_{sl} . We then remove the upper portion of liquid to leave the desired configuration. In doing so, we have removed the energy associated with the attractive forces between the removed chunk of liquid and the film, and the removed chunk of liquid and the underlying solid. Therefore the energy per unit area of the new state is

$$\phi = -\gamma_{sl} - \left[\frac{A_{sl}}{12\pi h^2} + \frac{A_{ll}}{12\pi} \left(\frac{1}{(h + \sigma_{ll})^2} - \frac{1}{\sigma_{ll}^2} \right) \right], \quad (6)$$

which (as $h \gg \sigma_{ll}$) gives

$$\phi = \text{const.} - \frac{A}{12\pi h^2}, \quad (7)$$

where $A = A_{sl} - A_{ll}$. We note that A can have either sign depending on the magnitude of A_{sl} and A_{ll} , so the force acting on the liquid can be either attractive or repulsive, leading to film rupture or wetting respectively. This force is known as the *disjoining pressure* and is given by

$$p_T = \frac{A}{6\pi h^3} = -\frac{\partial\phi}{\partial h}, \quad (8)$$

so that the force is attractive when $A < 0$, and repulsive when $A > 0$.

2.4 Two materials with an intervening liquid layer

As we will see, in real situations the liquid layer tends to be in between two phases, such as vapour and solid, or substrate and solid. Therefore, by using a similar argument to that of the previous section, it is possible to build the potential for a liquid layer of thickness h between two semi-infinite materials of phases 1,2 to find that

$$\phi = \text{const} - \frac{A}{12\pi h^2}, \quad (9)$$

where $A = A_{1l} + A_{2l} - A_{12} - A_{ll}$ can take both signs, so that the film can also either be wetting, or be unstable leading to rupture.

3 Premelting

Imagine a liquid film of water sandwiched between a semi-infinite block of ice and another substrate (e.g. water vapour or a solid wall). In equilibrium, the Clausius-Clapeyron equation gives

$$\frac{\rho_s L(T_m - T)}{T_m} = p_s - p_l + (p_l - p_m)(1 - \rho_s/\rho_l). \quad (10)$$

Here we shall assume, for simplicity, that $\rho_s = \rho_l$ so that the last term on the right-hand side of (10) disappears. This term is associated with pressure melting (since it includes the difference between the liquid pressure and the reference pressure, p_m) and so we are neglecting pressure melting in the calculation that follows. Now, $p_s - p_l = p_T$, the disjoining pressure, which is given in terms of the film thickness h by (8). Equation (10) therefore simplifies further to:

$$\frac{\rho_s L(T_m - T)}{T_m} = p_T = \frac{A}{6\pi h^3}, \quad (11)$$

where h is the thickness of the melt layer above the ice.

If $A > 0$, so that the layer is wetting, then we find immediately that

$$h \propto (T_m - T)^{-1/3}, \quad (12)$$

provided that $T < T_m$. Notice from (12) that as $T \nearrow T_m$, $h \rightarrow \infty$ so that the film thickness diverges as the temperature approaches the equilibrium melting temperature. Physically,

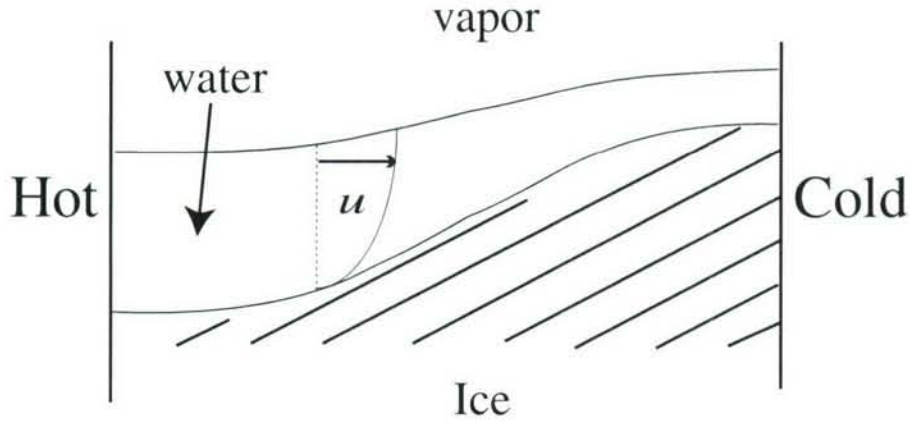


Figure 3: Diagram showing an ice block and its premelted film in a horizontal temperature gradient.

this is as expected because at the equilibrium melting temperature, we can have bulk liquid in coexistence with ice.

Equation (12) shows that below its equilibrium melting temperature, ice can coexist with a thin layer of water. This thin layer of water has important consequences that we shall investigate further in the last lecture. We begin by considering a simple mechanism by which flow can be driven in a premelted layer and compare this to a more conventional thin layer flow.

3.1 Premelting driven flow

Consider a semi-infinite block of ice between two vertical walls with a liquid film sitting between the ice and its vapour as shown in Fig. 3. If the walls are maintained at different temperatures (both with $T < T_m$) then a temperature gradient is set up across the width of the system. For the liquid film to remain in thermodynamic equilibrium, the film must be thicker at the hotter end of the experiment and so the ice melts a little here. However, this means that the thermomolecular pressure p_T is lower here and so, since $p_l = p_s - p_T$, the liquid pressure is higher. Therefore there is flow in the premelted film from hot to cold (i.e. from left to right in the setup shown in Fig. 3).

Here we neglect gradients in the surface tension coefficient resulting from the temperature change and so there is no traction on the interface. The pressure in the liquid film is therefore given by

$$p_l = -\gamma_{lv}H_{xx} - \frac{A}{6\pi h^3}, \quad (13)$$

where $H(x)$ is the interface position and *not* the film thickness $h(x)$. Here the Hamaker constant $A = A_{sl} + A_{lv} - A_{ll} - A_{sv}$ depends on the Hamaker constants of the different pairs of materials in the system.

The flow in the liquid layer is driven by the gradient in p_l and acts to eliminate this gradient. Eventually a static situation is reached with $p_l = \text{const.}$ everywhere but with the

	Premelting	Marangoni
Driving force	Disjoining Pressure (normal to interface)	Surface tension gradient (tangent to interface)
Direction of mass transport	Hot to cold	Hot to cold
Morphology of underlying solid	Yes	No
Equilibrium	Stationary	Dynamic
Film Thickness Determined:	Thermodynamically	Dynamically

Table 1: Comparison of main characteristics of the Premelting- and Marangoni-driven film flow problems.

interface deformed. Here the curvature force (surface tension) balances the thermomolecular forces. This means that in regions of high disjoining pressure (thin films), we expect to see large interfacial curvatures in steady state.

3.2 Marangoni driven flow

We now contrast this with the case of a thin wetting film on a rigid, solid substrate, such as glass. Again a temperature gradient is imposed across the system but now we account for the gradients in surface tension caused by the temperature gradient. In particular, we note that for water, the surface tension is higher at the cold end than at the warm end and so there is a surface tension gradient from warm to cold. This exerts a surface traction, $\tau = \mu \partial u / \partial n$, which balances the surface tension gradient. We therefore have

$$\mu \frac{\partial u}{\partial n} = \frac{\partial \gamma_{lv}}{\partial s}, \quad (14)$$

where s denotes the arc length measured along the interface. Unlike the previous case, at equilibrium the liquid is not quiescent (see figure (4)). The gradient in surface tension will drive a flow along the surface of the liquid from hot to cold, while the pressure reduction under the cold region of high curvature will drive a return flow underneath the surface flow. The equilibrium shape of the surface in this situation is controlled by a dynamic flow balance.

Although the flow of the two liquid films are similar in many respects, there are also several differences. These differences are summarized in table 1. In addition to these differences, we also note that when the vapour phase is replaced with a deformable solid, the Marangoni effect disappears but the premelting flow remains. We will consider such deformations in the final lecture.

Student Problem Consider a thin disk of weight W , radius R and against which ice premelts, just ahead of an interface that is solidifying at a speed V (see Fig. 5). Find the maximum speed for which there is a steady state in which the disk translates ahead of the ice.

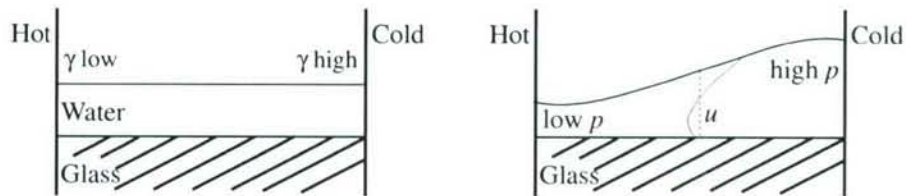


Figure 4: Diagram showing a thin film of water wetting a rigid substrate in a horizontal temperature gradient. Left: The initial configuration in which a layer of liquid lies above the solid. Right: The steady state in which flow in the layer continues because of the surface tension gradient.

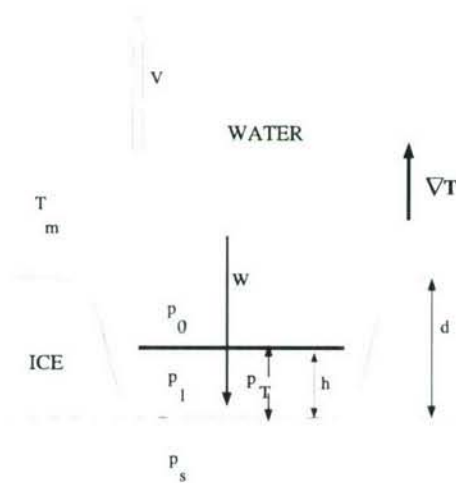


Figure 5: Diagram for the student problem: a disc of radius R is pushed ahead of a steadily translating ice-liquid interface.

Solution Because of the presence of the disk, there will be a pre-melted liquid layer, of constant thickness h , separating the disk from the solid interface. Assuming that $h \ll R$ so that the gap is ‘thin’, we can neglect effects associated with the edges of the disk. The liquid film exerts a disjoining pressure

$$p_T = \frac{A}{6\pi h^3}$$

on the disk, where A is the Hamaker constant. The disjoining force $p_T \times \pi R^2$ repels the disk from the ice phase.

Two forces are acting to move the disk in the direction of the ice. The first of these is the disk’s weight W , while the second force is a suction force resulting from the inward flow of liquid beneath the disk. This force can be calculated using lubrication theory, as follows.

In the thin gap, the horizontal fluid velocity is

$$u = \frac{1}{2\mu} z(z-h) \frac{\partial p}{\partial r}, \quad (15)$$

where $p(r)$ is the unknown fluid pressure. The depth integrated radial fluid flux is then

$$Q = \int_0^h u \, dz = -\frac{h^3}{12\mu} \frac{\partial p}{\partial r}. \quad (16)$$

Using the continuity equation $h_t + \nabla \cdot \mathbf{Q} = 0$, we then have

$$V = \frac{h^3}{12\mu} \frac{1}{r} \frac{\partial}{\partial r} \left(r \frac{\partial p}{\partial r} \right), \quad (17)$$

which can immediately be integrated twice to give

$$p = \frac{3\mu V}{h^3} (r^2 - R^2) \quad (18)$$

where we have defined zero pressure to be at $r = R$. This pressure force can be integrated to give the value of the lubrication induced adhesion between the disk and the ice:

$$F_{adh} = \int_0^R 2\pi r p(r) \, dr = -\frac{3\pi\mu V R^4}{2h^3}. \quad (19)$$

Balancing the three forces acting on the disk we have

$$0 = \pi p_T R^2 - W + F_{adh}, \quad (20)$$

which can be rearranged to give the velocity of interface advance V in terms of the gap thickness, h :

$$V = \frac{A}{9\pi\mu R^2} - \frac{2h^3 W}{3\pi\mu R^4}. \quad (21)$$

Of course in an experiment V is likely to be the control parameter, rather than h . In this case (21) can be rearranged to give $h(V)$. However, the form in (21) is more convenient

for our purposes since it demonstrates immediately that the steady state we have supposed can exist only if

$$V - \frac{A}{9\pi\mu R^2} < 0, \quad (22)$$

so that

$$V < V_{\max} \equiv \frac{A}{9\pi\mu R^2}. \quad (23)$$

If $V > V_{\max}$ this equilibrium configuration no longer exists and we conclude that the disk is engulfed by the ice.

It is interesting to calculate the temperature of the ice–water interface beneath the disc, T_i . From (11) we have that

$$\frac{A}{6\pi h^3} = \frac{\rho_s L (T_m - T_i)}{T_m}. \quad (24)$$

Using this expression to eliminate h from (21) and rearranging we find that

$$T_m - T_i = \frac{A}{6\pi} \frac{T_m}{\rho_s L} \frac{2}{3\pi\mu R^4} \left(\frac{A}{9\pi\mu R^2} - V \right)^{-1} \quad (25)$$

so that as $V \rightarrow V_{\max}$, $T_i \rightarrow -\infty$. In other words the disk is well below the undisturbed phase boundary.

GFD 2006 Lecture 9: Thermomolecular flow, thermal regelation and frost heave

Grae Worster; notes by Takahide Okabe and Dan Goldberg

30 June, 2006

1 Review

In the last lecture, interactions that cause macroscopic disjoining pressure between two materials separated by a third material were discussed. Microscopically, that disjoining pressure may be due to non retarded Van der Waals forces, or may be due to retarded Van der Waals forces, or to electrostatic forces. But the main results discussed below are independent of the microscopic theory. As we will see, everything boils down to the Generalized Clapeyron equation, which is derived from the Gibbs-Duhem relation and gives the difference in pressure between solid and liquid phases of the same material.

Marangoni flow vs. thermomolecular flow

Let us review the discussion of the last lecture in pictures. We compared Marangoni flows (Figure 1) with thermomolecular flows (Figure 2). Marangoni flows are driven by gradients of the surface tension at the fluid interface, between liquid and vapor, for example. The temperature gradient gives the gradient of the surface tension: surface tension is low at the warm end, and high at the cold end. That provides the surface traction on the film that pulls the surface water to the right, building up the liquid pressure on the right due to curvature, which can drive the bottom water to the left. Thus, it is possible to achieve steady state in this way. By contrast, in thermomolecular flows, the driving force is differential normal stresses. The temperature gradient gives the gradient of the thermomolecular pressure: thermomolecular pressure is low at the warm end and high at the cold end. Therefore hydrodynamic pressure is high at the warm end and low at the cold end in order to balance the solid pressure. That causes flow from the warm end to the cold. This distinction between Marangoni flows and thermomolecular flows is the distinction between being driven by tangential stress or normal stress, and in the thermomolecular case, film thickness is determined only by the temperature field, whereas, in Marangoni flow, it is determined dynamically as water moves from one end to another. But tangential stress as a driver goes away if vapor is replaced by solid, and we have only to consider thermomolecular flows. We concentrate on this situation in today's lecture.

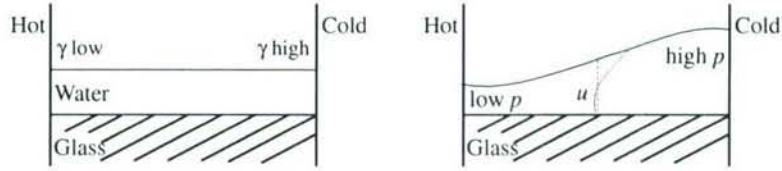


Figure 1: Marangoni flow. Initially, water is level on the glass, but if the temperature gradient is given externally, it causes the difference in surface tension. This results in the flow of surface water, and water is built up on the right. Then the pressure at the bottom is higher at the cold end, which causes the flow of the bottom water to the left.

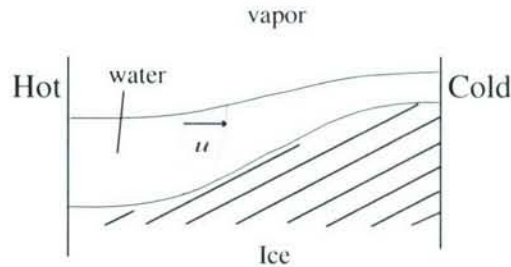


Figure 2: Since water is on ice, thermomolecular pressure plays an important role. Thermomolecular pressure is determined by temperature: low at the hot end and high at the cold end. Since thermomolecular pressure plus liquid pressure is equal to solid pressure, liquid pressure is high at the hot end and low at the cold end, which causes the flow to the cold end.

2 Premelted Film in a Capillary Tube

Let us consider the following thought experiment. Imagine we have a capillary tube, which is filled with water, with one end colder than T_m . Since the left end is below the freezing temperature, then there is ice on the left and water on the right. This is a classical Stefan problem with fixed temperature field varying from cold to warm. As we saw in the previous lecture, the interface between ice and water simply stops when it reaches the position at which $T = T_m$. Now imagine this is a real capillary tube: we need to take into account interactions between the material of the wall of the tube and the ice, which in principle can cause the ice to be premelted, producing a thin layer of water next to the wall. Because the left side is colder, we have relatively large disjoining pressure and low liquid pressure on the left. This pressure gradient has a tendency to move fluid from warm to cold. If this is a theoretician's ideal rigid capillary tube, nothing more happens: the differential stress is accommodated by the wall (Figure 3). However if this wall is elastic, then the water in the premelted film can flow. This situation is depicted in Figure 4. We will make a particular assumption about the elastic tube: that it just exerts a hoop stress (circumferential stress), not taking account of any bending moment of the wall.

The film is thick where it is warm and thinner where it is cold. We are going to take a

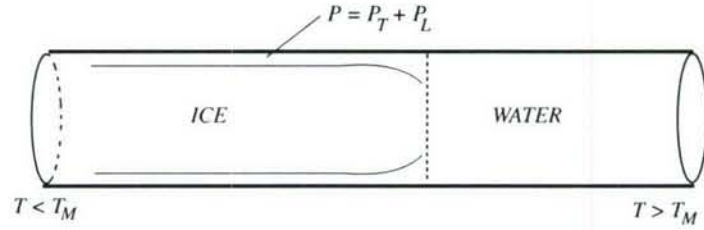


Figure 3: Rigid capillary tube

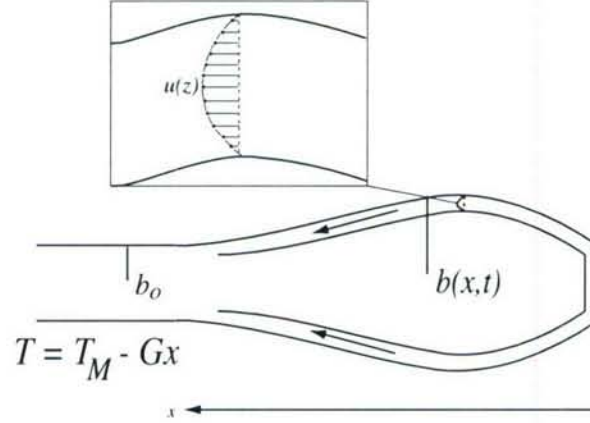


Figure 4: Elastic capillary tube

1-dimensional coordinate system x as depicted in Figure 4. Then the temperature field is $T = T_m - Gx$. Let the radius of the capillary be $b(x, t)$. Because we treat the elastic hoop stress only, the pressure of the wall is equal to the pressure of the solid:

$$p_w = p_s = k(b - b_0), \quad (1)$$

$$p_l = p_s - p_T = k(b - b_0) - \frac{\rho_s L}{T_m} (T_m - T). \quad (2)$$

Where the temperature is colder, $T_m - T$ is larger and the liquid pressure is lower. Liquid pressure is decreasing in the positive x -direction, and this pushes fluid in the direction toward the cold end. The premelted film has thickness d given by

$$\rho_s L \frac{T_m - T}{T_m} = \frac{A}{6\pi d^3}. \quad (3)$$

Because the temperature field is stationary, the film thickness d is also independent of time. Later, we will consider how to modify the formulation in the presence of a curved solid-liquid interface. For the moment, we ignore this curvature. Lubrication theory gives volume flow rate (in 2D)

$$q = \frac{d^3}{12\mu} \left(-\frac{\partial p_l}{\partial x} \right). \quad (4)$$

Conservation of mass gives

$$\frac{\partial b}{\partial t} + \frac{\partial q}{\partial x} = 0 \quad (5)$$

$$\Rightarrow \frac{\partial b}{\partial t} = \frac{\partial}{\partial x} \left[\frac{d^3}{12\mu} \frac{\partial p_l}{\partial x} \right] \quad (6)$$

$$= \frac{\partial}{\partial x} \left[\frac{AT_m}{6\pi\rho_s L} \frac{1}{Gx} \frac{1}{12\mu} \left(k \frac{\partial b}{\partial x} - \frac{\rho_s L}{T_m} G \right) \right]. \quad (7)$$

Therefore

$$\frac{\partial b}{\partial t} = \frac{AT_mk}{72\pi\mu\rho_s LG} \frac{\partial}{\partial x} \left[\frac{1}{x} \left(\frac{\partial b}{\partial x} - \frac{\rho_s LG}{kT_m} \right) \right]. \quad (8)$$

This can be regarded as a modified diffusion equation with spatially varying diffusivity. There is a similarity solution to (8). By using the following variables

$$b - b_0 = \frac{\rho_s LG}{T_mk} \left(\frac{k\Gamma^3 t}{12\mu G} \right)^{\frac{1}{3}} g(\eta) \quad (9)$$

where

$$d = \Gamma(T - T_m)^{-\frac{1}{3}}, \quad (10)$$

$$\Gamma = \left(\frac{AT_m}{6\pi\rho_s L} \right)^{\frac{1}{3}}, \quad (11)$$

$$\eta = \left(\frac{12\mu G}{k\Gamma^3} \right)^{\frac{1}{3}} \frac{x}{t^{\frac{1}{3}}}, \quad (12)$$

(8) becomes dimensionless:

$$g'' = \frac{-1 + g'}{\eta} + \frac{1}{3}\eta g - \frac{1}{3}\eta^2 g' \quad (13)$$

with boundary conditions

$$g = 0 \quad (\eta = 0), \quad (14)$$

$$g \rightarrow 0 \quad (\eta \rightarrow \infty). \quad (15)$$

where g is the dimensionless displacement. The displacement is 0 at the end, because there is no force there (we are only considering the hoop stress. If we were considering curvature stress as well, it would be nonzero.) The displacement is increasing in time. The tube expands at first, but eventually stops expanding, because the elastic hoop stress which pushes back on the ice balances with the thermomolecular pressure pushing out. If we leave it for infinitely long time, we get a linear deformation profile, matching the linear temperature profile.

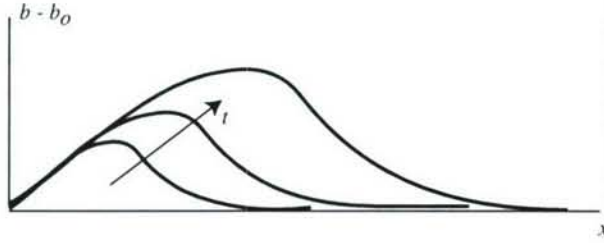


Figure 5: Similarity solution. Typical values for $b - b_0$ are $\sim 1\mu\text{m}$ when $x \sim 100\mu\text{m}$. Corresponding timescales are on the order of several days.

3 Thermal Regelation

Imagine there is a big block of ice containing an immersed solid particle. We impose a temperature gradient $\nabla T = \mathbf{G}$ such that the temperature is everywhere below the bulk freezing point. There is a premelted film against the object which is thinner where the temperature is lower (Figure 6). The thermomolecular force of the film is greater where it is thinner, so there is a net force on the particle, pushing the particle downwards. Movement of the particle can take place by the melting of ice on one side and freezing on the other, a process known as *regelation*. In order for regelation to take place, liquid must be transported within the film from the melting front to the freezing front. And in general the particle migrates from cold region to warm region. We want to understand how to calculate this phenomenon.

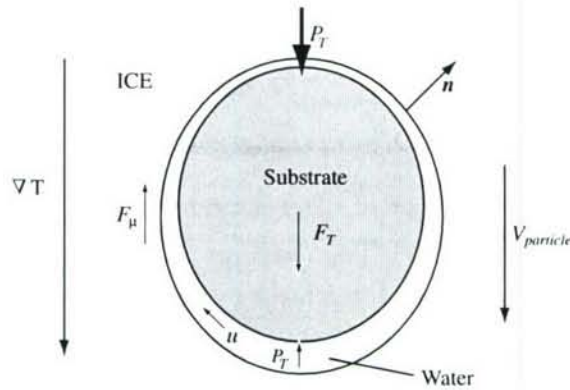


Figure 6: Solid particle in ice.

For small particles, premelting is affected by curvature of the solid-liquid interface:

$$p_s = p_l + p_T + \gamma_{sl} \nabla \cdot \mathbf{n} \quad (16)$$

where p_s is solid pressure, p_l is liquid pressure, p_T is the pressure due to disjoining force. The unit normal \mathbf{n} points into the ice. The last term is a pressure due to curvature of the

interface. We need to take the Generalized Clapeyron equation into account:

$$\rho_s L \frac{T_m - T}{T_m} = p_s - p_l \quad (17)$$

$$= \frac{A}{6\pi d^3} + \gamma_{sl} \nabla \cdot \mathbf{n}. \quad (18)$$

Because (total force on the particle) = -(total force on the ice),

$$\mathbf{F} = - \int_{\partial \mathcal{D}} p_s (-\mathbf{n}) dS \quad (19)$$

$$= \int_{\partial \mathcal{D}} p_l \mathbf{n} dS + \int_{\partial \mathcal{D}} \rho_s L \frac{T_m - T}{T_m} \mathbf{n} dS \quad (20)$$

$$= \mathbf{F}_\mu + \mathbf{F}_T \quad (21)$$

where \mathcal{D} is the whole region that is not occupied by ice. F_μ is due to lubrication pressure and F_T is the thermomolecular force.

$$\mathbf{F}_T = \int_{\partial \mathcal{D}} \rho_s L \frac{T_m - T}{T_m} \mathbf{n} dS = \frac{\rho_s L}{T_m} \int_{\mathcal{D}} \nabla T dV. \quad (22)$$

If the thermal properties of all phases are the same, then $\nabla T = \mathbf{G}$ throughout. Under this assumption,

$$\mathbf{F}_T = \frac{\rho_s L}{T_m} \mathbf{G} \cdot (\text{volume that is not ice}) \quad (23)$$

$$= \frac{L}{T_m} \mathbf{G} \cdot (\text{mass of displaced ice}). \quad (24)$$

This looks similar to the principle of Archimedes, which states that the upthrust on a body immersed in water is proportional to the mass of water displaced. This motivates the term “thermodynamic buoyancy” to describe the total thermomolecular force on an immersed particle. The result is independent of the particular intermolecular interactions that underly the thermomolecular pressure.

To find the regelation velocity, \mathbf{F}_μ must also be dealt with, generally using lubrication theory, or some closure such as Darcy’s Law. In the next section this is done in investigating the phenomenon of frost heave.

4 Frost Heave

Frost heave is a phenomenon that involves upheaval of soil from formation of ice within the soil, and is known in some cases to cause the formation of “lenses” - layers of ice containing little or no soil particles (figure 7).

Frost heave is essentially the process of thermal regelation on a large scale in frozen soil. There is an external temperature gradient that leads to a thermomolecular force on the soil particles, as in the previous example of regelation, and that balances the viscous forces from the transport of water necessary for the regelation.



Figure 7: A column of frozen soil in which lenses (dark) have formed in between layers of frozen soil (light). From Taber (1929).

In the model presented here, the temperature gradient is assumed to be constant and directed downwards, so at some depth ($z = 0$) the temperature is at the bulk freezing point. However, the soil is not frozen all the way down to $z = 0$; the ice formed in the soil pores has an associated curvature because of the geometry of the pores, and so the Gibbs-Thomson effect prohibits ice formation at temperatures below the freezing point. And so there is a *fringe* region of frozen soil with lower boundary $z_f > 0$ and upper boundary z_l (the lens boundary). z_f is set by the geometry of the soil, so if $z_l < z_f$, there is no fringe region. Figure 8 shows the situation where there is a fringe.

First assume that a fringe does exist. A force balance on the fringe section can be calculated, as long as certain properties of the ice-soil system (e.g. volume fraction, permeability) are known. The total upward thermomolecular force F_T is equal to the thermomolecular pressure integrated over the substrate surface:

$$F_T = \hat{\mathbf{z}} \cdot \int_{\Gamma} p_T \mathbf{n} \, d\Gamma = \hat{\mathbf{z}} \cdot \frac{\rho_s L G}{T_m} \int_{\Gamma} z \mathbf{n} \, d\Gamma, \quad (25)$$

where $G = |\nabla T|$ and Γ is the surface of the ice. The divergence theorem lets us write

$$F_T = \frac{\rho_s L G}{T_m} \int_0^{z_l} (1 - \phi) dz, \quad (26)$$

where ϕ is the volume fraction of ice in the soil, assumed to be only a function of z . Also acting on the mass of ice is the hydrodynamic pressure necessary to bring water to the freezing front (or take water away from the melting front). We can use Darcy's Law to infer the relation between pressure and pore transport, and we can use continuity to find the magnitude of this transport:

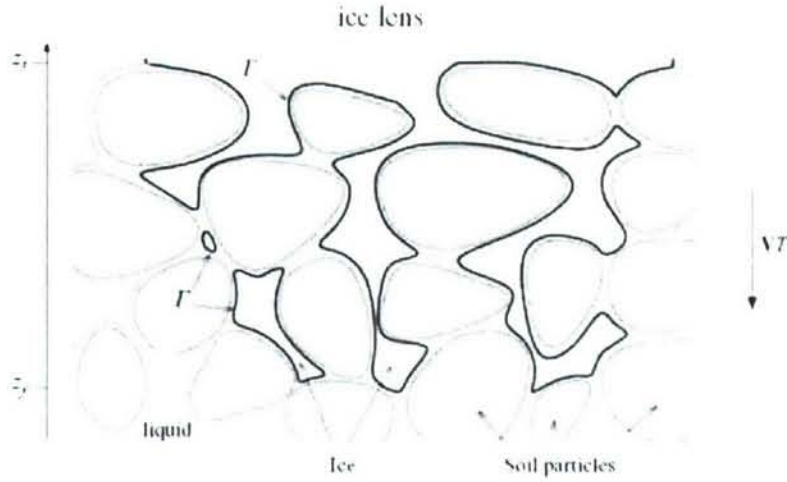


Figure 8: Cross section through the fringe region. z_f and z_l mark the lower and upper boundaries of the fringe. Γ is the ice boundary, with unit normal pointing into the ice, as in the previous regelation example. From Rempel *et al* (2004).

$$W = (1 - \phi)V_h \quad (27)$$

and

$$\mu W = -\Pi(\phi)\nabla p_L. \quad (28)$$

Here W is the area-averaged vertical water transport, V_h is the heave velocity, p_L is the hydrodynamic water pressure driving the flow, and Π is the permeability of the soil. Π is, in general, dependent on many factors, including soil particle geometry. However, it is written as a function of ice volume fraction only to emphasize the fact that permeability decreases as ice volume fraction increases. So if $\phi(z)$ and $\Pi(\phi)$ are known functions, we can calculate the hydrodynamic force acting on the fringe section:

$$\begin{aligned} F_\mu &= \hat{\mathbf{z}} \cdot \int_{\Gamma} p_L \mathbf{n} d\Gamma \\ &= - \int_{z_h}^{z_l} \frac{\partial p}{\partial z} (1 - \phi) dz \\ &= \mu V_h \int_{z_h}^{z_l} \frac{(1 - \phi)^2}{\Pi(\phi)} dz. \end{aligned} \quad (29)$$

z_h is a reference point below the fringe where p_L goes to zero. The choice of z_h is somewhat arbitrary, but the result above is not likely to be sensitive to z_h as most of the pressure drop occurs near z_l , where permeability is greatly reduced due to the high ice concentration.

Before proceeding, note that the above analysis also applies when $z_l < z_f$, i.e. there is no frozen fringe. The expression for F_T , for example, reduces to $\rho_s L (T_m - T(z_l)) T_m^{-1}$, the expression for the thermomolecular force at the temperature at the lens boundary.

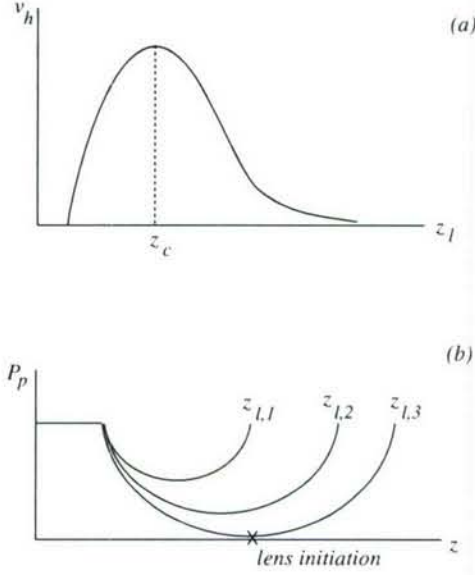


Figure 9: (a) Frost heave rate as a function on z_l (in the domain where freezing occurs). (b) Soil particle effective stress as a function of depth for different lens heights.

The only other force acting on the mass of ice is the weight above it, P_0 . Solving for V_h gives

$$V_h = \left[\frac{\rho_s LG}{T_m} \int_0^{z_l} (1 - \phi) dz - P_0 \right] \left[\mu \int_{z_h}^{z_l} \frac{(1 - \phi)^2}{\Pi(\phi)} dz \right]^{-1}. \quad (30)$$

In general, the vertical distribution of ϕ and the associated permeability dependence must be known or calculated. Rempel *et al* (2004) use an idealized model for ice saturation and permeability dependence, but certain properties of the dependence of V_h on z_l can be deduced for more general cases. For instance, the thermomolecular force $(\rho_s LG \int_0^{z_l} (1 - \phi) dz / T_m)$ is monotonic in z_l , and so the heave velocity is zero for a certain value z_l and positive for higher values. Further, we expect the permeability will tend to zero as the ice fraction goes to 1, so we expect that the denominator of ((30) becomes large with large z_l , and so V_h tends to zero. We can then expect that V_h goes through a maximum at some point. Rempel *et al* find a curve similar to that shown in figure 9(a) for the heave rate.

The frost heave phenomenon can be demonstrated in a lab setting. A column of frozen soil with a lens is placed longitudinally in a temperature gradient that is fixed (w.r.t. the lab frame) as in figure 10. The entire column can be moved at constant velocity through the gradient. Meanwhile, the lens position can move relative to the moving frame due to frost heave. A steady state can be found in which the lens does not move relative to the lab frame. One can view the setup as the lens being pulled through the soil, which remains in place as the liquid flows through it, providing the hydrodynamic force that balances the thermomolecular force.

From figure 9(a) it is obvious that for a range of V (the rate at which the column in

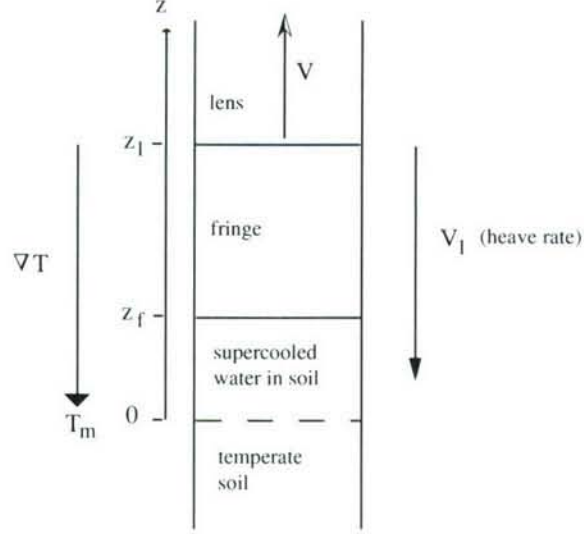


Figure 10: The experiment described in Rempel *et al.* The entire system is pulled upward, while positive heave rates push the soil in the opposite direction.

the experiment is moved through the temperature gradient) there are 2 steady heave rates. However, only one state (the one with $z_l < z_c$) is stable to small perturbations; if $V_h(z_l)$ is sloping downwards, then a small increase in z_l will slow the heave rate, and the lens front will move forward (increasing z). Physically, a decrease in permeability limits the amount of liquid that can be brought to the front. The situation is similar for small decreases in z_l .

Lens Initiation

One might ask how a lens will form initially. To determine where this might occur, the vertical force between soil particles (F_p) is examined. At each point, F_p balances the sum of the overburden, the thermomolecular force, and the hydrodynamic force. Thus p_p (inter-particle force per unit area) can be calculated from

$$F_p(z) = V_h \mu \int_{z_h}^z \frac{(1 - \phi)^2}{\Pi(\phi)} dz + P_0 - \frac{\rho_s L G}{T_m} \left[\int_0^z (1 - \phi) dz - z(1 - \phi(z)) \right]. \quad (31)$$

Note the similarity to (30) with z_l replaced by z . The last term, $\rho_s L G z(1 - \phi(z))/T_m$, can be seen as the additional force that would act on the volume of integration (that is, a volume similar to that bounded by Γ in figure(8)) were the ice fraction at z equal to unity. If p_p becomes zero at some point, there is virtually nothing holding the soil particles together, and a lens has the potential to form.

Again, this expression depends on the specific forms of ϕ and $\Pi(\phi)$. For the idealized configuration mentioned above, Rempel *et al* calculated $p_p(z)$ for different values of z_l , and found that the minimum p_p decreases with increasing z_l , and at some point $p_p(z)$ becomes zero at a height less than z_l (figure 9(b)). If a lens were to form at this height, then z_l would be effectively decreased. One can imagine a situation, such as in the lab experiment

described above, in which the lens front is continually moving upward, with new lenses periodically forming below the previous lens front. Such a phenomenon has in fact been observed in the laboratory, and is believed to be responsible for similar patterns that are formed in situ (figure 7).

References

- [1] Rempel, A.W., Wettlaufer, J.S. & Worster, M.G. 2004. Premelting Dynamics in a Continuum Model of Frost Heave. *J. Fluid Mech.*, **498**, 227-244.
- [2] Taber, S. 1929. Frost heaving. *J. Geol.*, *37*, 428-461.

Some useful Statistical Thermodynamics

John Wetlauffer; Notes by Rachel Zammett and Devin Conroy

March 15, 2007

1 Introduction

We are all familiar with gases, liquid and solids, which make up the 3 possible states of a pure substance. These states of solid, liquid and gas are functions of pressure, P and temperature, T as depicted qualitatively in the phase diagram figure 1. The negatively sloped dashed line represents ice in contact with water; the former floating on the latter. There are few other substances with this property and most other materials have a positively sloped solid-liquid coexistence line. Despite substantial advances in our understanding of microscopic phenomena, no phase diagram in its entirety can be computed solely from information about intermolecular interactions; phase diagrams are principally empirically determined.

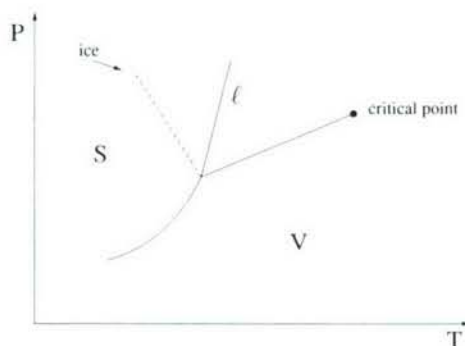


Figure 1: Phase diagram for a pure substance, showing the lines of pressure and temperature delineating the 3 possible phases of matter; gas, liquid and water. The dashed line represents the special case of ice, which has a negatively sloped solid-liquid phase boundary.

2 First Law of Thermodynamics

In 1850 Rudolph Clausius first stated what is now referred to as the first law of thermodynamics: the change in internal energy E of an isolated system is equal to the heat

absorbed by the system dQ minus the work done by the system on its surroundings dW . Mathematically this can be written as

$$dE = dQ - dW, \quad (1)$$

where the symbol d denotes the path dependence of a differential, namely, that it is an *inexact* differential.

3 Second Law of Thermodynamics

Consider an isolated system consisting of two subsystems A and A' , as shown in figure 2. The boundary between A and A' allows conduction and may move like a piston, but is impermeable to particles i. e. there is no mass transfer across it. We assume that all changes which occur to the system are quasi-static; interactions happen on a long timescale relative to the relaxation time of the system.

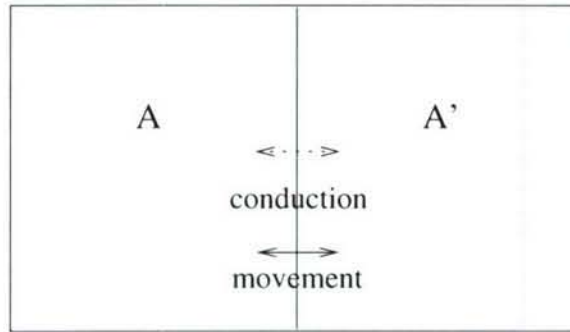


Figure 2: An isolated system consisting of A adjacent to A' . Heat conduction is permitted between the subsystems, and the boundary may move as a piston.

The second law states that the number of accessible micro-states of an isolated system, Ω , never decreases. If we consider subsystem A to contain an ideal atomic gas, then the number of accessible micro-states of A is simply the number of places in space that may be occupied by the gas atoms. Thus, A has Ω_A micro-states and we assume that the volume of A equals the volume of A' which contains no gas. We then remove the barrier between A and A' . Initially, the system has not relaxed, but at some later time, the whole system $A + A'$ is available to the gas atoms that were confined to A .

The probability p that a particular micro-state is occupied is given by

$$p \propto \frac{\Omega_A}{\Omega_A + \Omega_{A'}}. \quad (2)$$

Moreover, because $\Omega_A \propto V_A^N$, where V_A is the volume of subsystem A and N is the number of particles in the system (which is typically of the same order as Avogadro's number, 6.02×10^{23}). We therefore have that $p \propto (\frac{1}{2})^N$.

Finally, because the entropy, S , of a system is defined by

$$S = k_b \ln \Omega, \quad (3)$$

where k_b is Boltzmann's constant, $k_b = 1.381 \times 10^{-23} \text{ J K}^{-1}$. Whence, the second law is written as

$$\Omega_{A'+A} - \Omega_A \geq 0 \Rightarrow dS \geq 0, \quad (4)$$

so that the entropy of a system approaching equilibrium always increases with the equality in equation (4) occurring when the system has reached equilibrium. We can write

$$dQ = TdS, \quad (5)$$

thereby demonstrating that T is an integrating factor for the second law, and hence in the case in which there are no mechanical interactions (no volume change) we find

$$dS_{Total} = dS_A + dS_{A'} = \left(\frac{1}{T_A} - \frac{1}{T_{A'}} \right) \partial Q_A. \quad (6)$$

We therefore see that if $T_A > T_{A'}$, heat will flow from A to A' until equilibrium is reached.

4 Thermodynamic Potentials

Thermodynamic potentials are homogeneous functions that are the principal tools used to understand phase equilibria. They have the following properties

- Thermodynamic potentials have units of energy.
- They all involve the entropy and several, denoted say P , are such that $P \propto -S$.
- For all systems approaching equilibrium, $dS \geq 0$, therefore for the potentials P ,
- for all systems approaching equilibrium, $dP \leq 0$: the thermodynamic potential is a minimum.

By way of example, the internal energy of a system, $E(S, V)$, satisfies

$$dE = TdS - pdV, \quad (7)$$

and hence is a minimum for constant entropy and volume. The enthalpy of a system, $H(S, p)$, is often used when a system is at constant pressure, and is defined by

$$H = E + pV, \quad (8)$$

such that $dH = 0$ for constant entropy, isobaric processes. The Helmholtz free energy is given by

$$F(V, T) = E - TS, \quad (9)$$

and hence is conserved in an isothermal, constant volume process, while the Gibbs free energy is given by

$$G(T, p) = F + pV = E - TS + pV, \quad (10)$$

From equations (7) and (10), we find

$$dG = -SdT + Vdp, \quad (11)$$

and we note therefore that $dG = 0$ for systems at constant temperature and pressure.

If we consider a system consisting of a solid in contact with a liquid and we ignore the effect of surface energy, along the solid-liquid phase boundary the phases will have equal free energies, i. e.

$$dG_s = dG_l, \quad (12)$$

where the subscript s denotes evaluation in the solid and l evaluation in the liquid. Note that we are considering solid/liquid coexistence and thus pressure and temperature are constrained to a line, defined by $T_m(p) = p_m(T)$, due to the Gibbs phase rule. From equations (11) and (12) we can write this as

$$-S_s dT_m + V_s dp = -S_l dT_m + V_l dp, \quad (13)$$

for continuous temperature and pressure across the interface. Rearranging equation (13) gives

$$\frac{dT_m}{dp} = \frac{V_l - V_s}{S_l - S_s} = \frac{T_m}{L} (V_l - V_s). \quad (14)$$

where the latent heat of fusion is L , and is defined as $L = \frac{\Delta S}{T_m}$. In the case of ice, where $V_l < V_s$, we see that $\frac{dT_m}{dp}$ will have negative slope. Hence, from equation (14), we can write the *Clausius-Clapeyron* equation in the following form

$$\frac{dT_m}{dp} = -\frac{T_m}{\rho_s L} \left(1 - \frac{\rho_s}{\rho_l} \right), \quad (15)$$

where ρ_s and ρ_l are the densities of the solid and liquid phases, respectively.

It should be stressed that this treatment only deals with bulk free energies and interfacial and nucleation problems require consideration of the surface energies. This is because the free energy of the system can be shifted due to the surface energy of the phase boundary, intermolecular forces and other effects which extend the equilibrium domain of the liquid phase into the solid region of the bulk phase diagram. In general, for any system in which the surface energy plays a significant role, we can express the total Gibbs free energy as the sum of bulk and surface contributions,

$$G = G_B + G_{surface}, \quad (16)$$

where G_B represents the bulk free energy and is proportional to the volume of the system and $G_{surface}$ is proportional to the surface area. Thus, the specific form of the surface area of the solid/liquid interface in question dictates the detailed nature of the shift in equilibrium and thereby leads to the specific effects referred to often in the principal lectures such as the Gibbs-Thomson effect and interfacial premelting. These are reviewed in (1).

References

- [1] J.G. DASH, A.W. REMPEL AND J.S. WETTLAUFER, *The physics of premelted ice and its geophysical consequences*, Rev. Mod. Phys. **78**, 695 (2006).

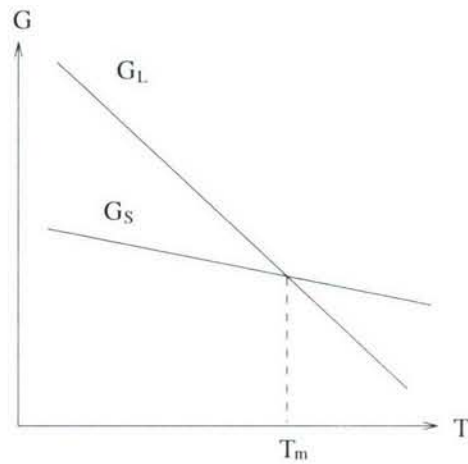


Figure 3: An equilibrium phase diagram of Gibbs free energy G as a function of temperature T , where pressure is assumed constant. G_L denotes the Gibbs free energy associated with the liquid phase; G_S that associated with the solid phase. We see that below the melting temperature T_m , the liquid has a greater free energy than the solid, which implies that there is a barrier to forming the solid phase.

GFD 2006 Project

Glancing Interactions of Internal Solitary Waves

Dan Goldberg
Advisor: Karl Helfrich

March 15, 2007

Abstract

The Extended Kadomtsev-Petviashvili (eKP) equation is studied as a model for weakly two-dimensional interactions of two-layer solitary waves. It is known that closed forms for two-soliton solutions to the Kadomtsev-Petviashvili (KP) equation can be found by means of Hirota's bilinear transform, but it is determined that no such solution can be found for eKP. A numerical model is developed that agrees with analytical results for reflection of KP solitary waves from a wall. Numerical reflection experiments are carried out to determine whether nonlinear eKP interactions lead to amplitude increases similar to those seen in KP interactions. It is found that when the cubic nonlinear term is negative, the interaction amplitude does not exceed the maximum allowed amplitude for an eKP solitary wave solution, except in the case where the incident wave amplitude is close to this maximum amplitude. When coefficient of the cubic nonlinear term is positive, stationary solutions that are qualitatively different than those of the KP equation are found.

1 Introduction

Long water waves whose amplitudes are small compared to the mean depth are quite common in many geophysical settings, such as free surface disturbances and as interfacial disturbances in a 2-layer system (internal waves). Solitary waves have an extensive history of observations in such settings. Attempts at describing such waves have led to many simplified models. Among the simplest is the Korteweg de Vries (**KdV**) equation for unidirectional propagation. The KdV equation captures the important aspects of long, finite-amplitude waves: nonlinear steepening due to advection and dispersion from nonhydrostatic pressure.

Additional effects can be included by small modifications to the KdV equation. If transverse variation is small but nonzero, the Kadomtsev-Petviashvili (**KP**) equation can be used. One can view the KP equation as a model for three dimensional interactions of long waves. (The term 'three dimensional' is misleading although it is standard – though the KP equation is derived by considering depth variation, it describes a function independent of the vertical coordinate.) On the other hand, if unidirectional internal waves are being considered and the mean layer depths are nearly equal, the Extended KdV (**eKdV**) equation, which

includes cubic nonlinearity, is a better asymptotic approximation to the governing equations. It is also a useful phenomenological model for large-amplitude waves. Combining the two effects results in the Extended KP (**eKP**) equation. The inclusion of both effects in a model is advantageous because internal solitary waves occur with some regularity where currents flow over bathymetry, as do three dimensional interactions of these waves. The modeling of such interactions using the eKP equation is the focus of this study.

In the following two sections, the above equations are given and known closed-form solutions are discussed, as are limitations of the machinery used to generate those solutions. Then in subsequent sections, a numerical model to study three dimensional interactions of internal waves is described, numerical results are presented, and the behavior of numerical solutions of the KP and eKP equations are compared and contrasted. Recommendations for the use of eKP as a viable model for 3D interactions of internal waves are made.

2 KdV, mKdV, KP, and mKP

The derivation of KdV and KP from the governing equations for inviscid single- or two-layer flow is not trivial. Here, the equations are simply stated for a two-layer model (without rotation), and the dependence of coefficients on physical parameters is stated as well. See [9] for a derivation.

Korteweg-de Vries and Kadomtsev-Petviashvili

It makes sense to first present the KdV and KP equations for 2-layer internal waves, although it will be seen briefly that these are often not the best equations to use. Let \hat{h}_i ($i = 1, 2$) be the equilibrium depths of the layers. There are three relevant parameters:

$$A \equiv \frac{a}{h_0}, \quad B \equiv \left(\frac{h_0}{L_x}\right)^2, \quad \Gamma \equiv \left(\frac{L_x}{L_y}\right)^2 \quad \left(h_0 = \frac{\hat{h}_1 \hat{h}_2}{\hat{h}_1 + \hat{h}_2}\right), \quad (1)$$

where a is the scale of the wave amplitude, and L_x and L_y are the length scales in the x - and y -directions. These parameters are all assumed small. If they are of the same order, then neglecting lower order terms within the governing equations leads to the KP equation, given here in dimensional form:

$$\left(\eta_t + (c_0 + \hat{\alpha}_1 \eta) \eta_x + \hat{\beta} \eta_{xxx}\right)_x + \hat{\gamma} \eta_{yy} = 0, \quad (2)$$

where η is the interfacial disturbance. A rigid lid and flat bottom have been assumed. The coefficients are known functions of the stratification and equilibrium layer depths:

$$\hat{\alpha}_1 = \frac{3}{2} c_0 \frac{\hat{h}_1 - \hat{h}_2}{\hat{h}_1 \hat{h}_2}, \quad \hat{\beta} = \frac{c_0 \hat{h}_1 \hat{h}_2}{6}, \quad \hat{\gamma} = \frac{1}{2} c_0, \quad c_0^2 = g' \hat{h}_0, \quad \hat{h}_0 = \frac{\hat{h}_1 \hat{h}_2}{\hat{h}_1 + \hat{h}_2}, \quad (3)$$

where c_0 is the linear wave speed and g' is the reduced gravity. If we scale η , x and y by $H = \hat{h}_1 + \hat{h}_2$, t by H/c_0 , and let $h_i = \hat{h}_i/H$ ($i = 1, 2$), and furthermore make the change of variables $(x, t \rightarrow x - t, t)$, so that we are in a slowly evolving frame moving at the linear wave speed, (2) becomes

$$(\eta_t + \alpha_1 \eta \eta_x + \beta \eta_{xxx})_x + \gamma \eta_{yy} = 0, \quad (4)$$

$$\alpha_1 = \frac{3}{2} \frac{h_1 - h_2}{h_1 h_2}, \quad \beta = \frac{h_1 h_2}{6}, \quad \gamma = \frac{1}{2}. \quad (5)$$

It should be underlined that formally, the KP equation describes propagation of two or more waves in *nearly* the same direction (in this case, positive x). Propagation cannot be in the negative x direction. The angle with the x -axis must be small. This is the difference between *glancing* interactions of plane waves (where there is a small, but nonzero, angle between propagation directions) and *oblique* interactions (where the angle is not small). This is important to keep in mind because closed-form solutions to (4) exist and are not limited by these constraints.

If there are no transverse effects (if $L_y = \infty$, $\gamma \rightarrow 0$), then (4) reduces to the KdV equation:

$$\eta_t + \alpha_1 \eta \eta_x + \beta \eta_{xxx} = 0. \quad (6)$$

Extended KdV and Extended KP

In many situations, α_1 can be small. If it is small enough (formally, if it is $O(A)$), then in order to balance dispersion with advection the regime of interest becomes $B \sim O(A^2)$, and a higher order term is included:

$$(\eta_t + \alpha_1 \eta \eta_x + \alpha_2 \eta^2 \eta_x + \beta \eta_{xxx})_x + \gamma \eta_{yy} = 0, \quad (7)$$

$$\alpha_2 = \frac{3}{(h_1 h_2)^2} \left[\frac{7}{8} (h_1 - h_2)^2 - \frac{h_1^3 + h_2^3}{h_1 + h_2} \right]. \quad (8)$$

The coefficient α_2 is negative definite. Again, neglecting transverse variation gives the eKdV equation,

$$\eta_t + \alpha_1 \eta \eta_x + \alpha_2 \eta^2 \eta_x + \beta \eta_{xxx} = 0. \quad (9)$$

3 Solitary Wave Interactions

Equation (7) has the following solitary wave solution [4]:

$$\eta = \frac{\eta_0}{b + (1 - b) \cosh^2 [k(x + my - ct)]}, \quad (10)$$

where the above parameters satisfy the relations

$$b = \frac{-\alpha_2 \eta_0}{2\alpha_1 + \alpha_2 \eta_0}, \quad k = \sqrt{\frac{\hat{c}}{4\beta}}, \quad \hat{c} = \frac{\eta_0}{6} (2\alpha_1 + \alpha_2 \eta_0), \quad c = \hat{c} + \gamma m^2. \quad (11)$$

Here η_0 is the wave amplitude, k is the wavenumber in the x -direction, c is the phase speed, and m is the aspect ratio, that is, the tangent of the angle between the direction of propagation and the x -axis. Note that (10) and (11) reduce to solitary waves for the

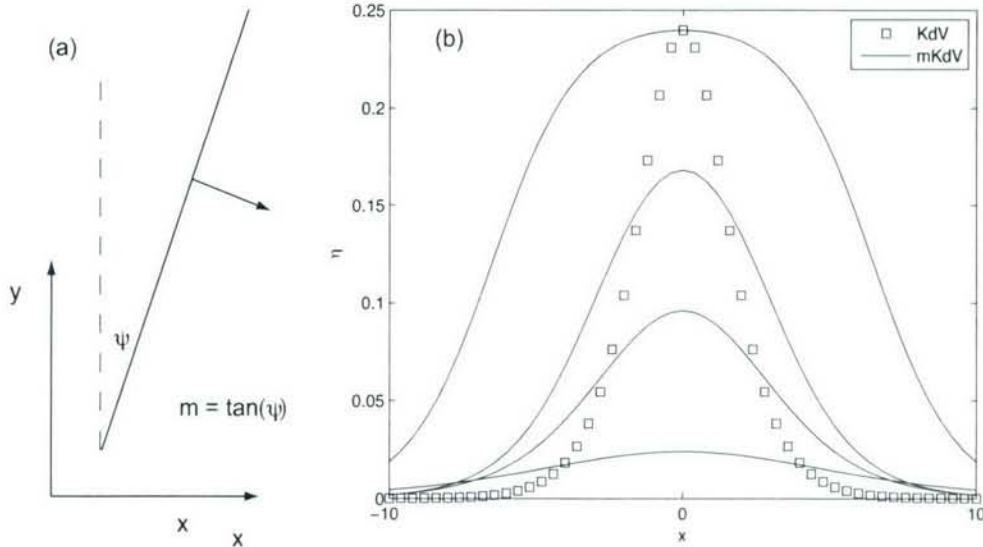


Figure 1: (a) A wave crest (solid line), or plane wave, propagating at an angle θ to the x -axis. (b) exact solitary wave solutions. A single KdV solitary wave (plus signs) is compared with eKdV solitary waves (solid lines) of different amplitudes, all less than $\eta_{0,max} = 0.2524$.

KP ($\alpha_2 = 0$), eKdV ($m = 0$), and KdV ($\alpha_2 = m = 0$) equations. Also note that, while the KP and eKP equations describe (weakly) 2-dimensional systems, the above solution is essentially 1-dimensional. For $\alpha_2 \leq 0, \eta_0 \alpha_1 > 0$. That is, η_0 carries the sign of α_1 , so for definiteness we assume α_1 is positive. Also, when α_2 is negative, as is generally the case for internal waves, η_0 has a maximum value of

$$\eta_{0,max} = -\alpha_1/\alpha_2. \quad (12)$$

Figure 1(a) shows the configuration of the wave. The crest moves in the positive x -direction with angle ψ to the y -axis. (m is equal to $\tan(\psi)$.) Figure 1(b) shows a KdV solitary wave (at a given y) against several eKdV solitary waves of varying amplitudes, all of which are less than the maximum amplitude given above. Putting terminology introduced earlier in context, we will talk about waves with smaller ψ (smaller m) as glancing and with larger ψ (larger m) as more oblique.

The interactions of multiple solitary waves traveling in the same direction (same m) have interesting behavior. A large-amplitude wave that is initially behind a small-amplitude wave will travel faster and eventually catch up with the smaller wave. When that happens, there is a transient nonlinear interaction, but each wave asymptotically retains its identity and structure as $t \rightarrow \infty$, except for a positive and negative phase shift of the larger and smaller wave, respectively (figure 2). KdV and eKdV solitary waves exhibit this behavior, as do KP and eKP solitary waves traveling in the same direction (but as mentioned above, the latter two cases essentially reduce to KdV and eKdV).

This solution is also interesting because it can be described by an exact analytical

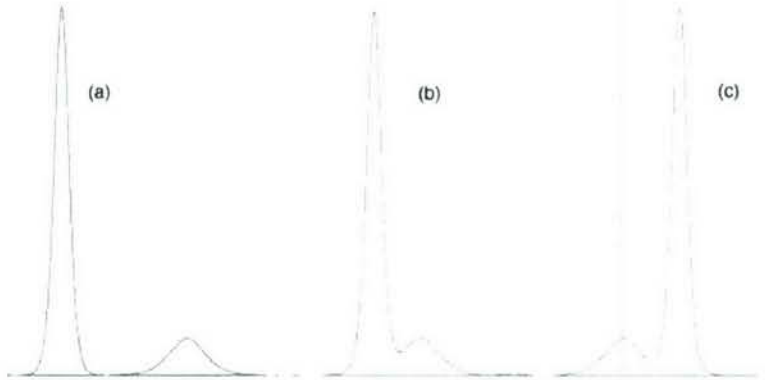


Figure 2: Interaction of two eKdV solitary waves. The larger wave, initially behind (a), eventually passes through the smaller one (b), but the two waves asymptotically retain their identity (c).

solution. In general, trains of N solitary KdV or eKdV waves (where N is finite) can be described by inverse scattering theory [11] or by Hirota's Bilinear Method ([11], or [5]). The former is more powerful, but the latter is algebraic in nature and very easy to apply. Hirota's method involves finding a dependent-variable transform of the equations such that the solitary wave solutions have the form of exponentials.

Exact solution for KP reflection

It turns out that Hirota's method also yields exact solutions of the KP equation (2) for two-dimensional solitary wave interactions. Miles ([6],[7]) derived the interaction pattern and investigated its properties, and found behavior qualitatively different than the 1-D case. We first summarize Miles's solution. Given two solitary wave solutions to the KP equations with wavenumbers k_i ($i = 1, 2$), and propagation directions such that their angles with respect to the x -axis have tangents m_i , the following solution is found [8]:

$$\eta = \left(\frac{48\beta}{\alpha_1} \right) \frac{k_1^2 e^{-2\theta_1} + k_2^2 e^{-2\theta_2} + (k_1 - k_2)^2 e^{-2\theta_1 - 2\theta_2} + A_{12} \{ (k_1 + k_2)^2 + k_2^2 e^{-2\theta_1} + k_1^2 e^{-2\theta_2} \} e^{-2\theta_1 - 2\theta_2}}{[1 + e^{-2\theta_1} + e^{-2\theta_2} + A_{12} e^{-2\theta_1 - 2\theta_2}]^2}, \quad (13)$$

where

$$\theta_i = k_i (x + m_i y - c_i t), \quad A_{12} = \frac{(m_1 - m_2)^2 - \frac{12\beta}{\gamma} (k_1 - k_2)^2}{(m_1 - m_2)^2 - \frac{12\beta}{\gamma} (k_1 + k_2)^2}, \quad (14)$$

and c_i , k_i , m_i satisfy (11) with $\alpha_2 = 0$. There are several things to notice about this solution. First, since the phase lines are not aligned, we can take the limit $\theta_2 \rightarrow 0$ or ∞ with θ_1 constant (and vice versa), and this limit has the form (10); that is, the waves retain their identities after interacting with each other. Second, the interaction parameter A_{12} can be negative when

$$(m_1 - m_2) \in \left(\sqrt{\frac{12\beta}{\gamma}}(k_1 - k_2), \sqrt{\frac{12\beta}{\gamma}}(k_1 + k_2) \right) \equiv (2m_-, 2m_+), \quad (15)$$

and it turns out that solutions in this parameter range, while mathematically admissible, are nonphysical (this point will be returned to briefly). Third, the interaction can be much larger in amplitude than a superposition of the two waves. In fact, for waves of the same amplitude, the amplitude increase can be up to four-fold, as compared with a two-fold increase from linear superposition.

Slightly changing focus, we can consider the kinematic resonance condition for three solitary waves:

$$k_1 \pm k_2 = k_3, \quad m_1 k_1 \pm m_2 k_2 = m_3 k_3, \quad \omega_1 \pm \omega_2 = \omega_3 \quad (\omega_i = c_i k_i), \quad (16)$$

where ω is frequency. In fact, given two KP solitary waves, a third satisfying (16) exists only if one of the bounds of (15) is achieved.

It must be stressed that (16) is an algebraic constraint, and alone is not a sufficient condition for resonant interaction of solitary waves. However, Miles showed that the limiting form of (13), as the upper bound of (15) is approached, is equal to

$$\eta = \left(\frac{48\beta}{\alpha_1} \right) \frac{k_1^2 e^{2\theta_1} + k_2^2 e^{-2\theta_2} + (k_1 + k_2)^2 e^{2\theta_1 - 2\theta_2}}{[1 + e^{2\theta_1} + e^{-2\theta_2}]^2}. \quad (17)$$

Furthermore, it can be shown that this solution is asymptotic to three interacting waves – the two waves considered in (13) and a third wave that is resonant with the first two. This can be shown by holding constant one of each of the three phase variables involved, and letting the other two go to zero or ∞ . Figure 3 shows (13) both for an oblique interaction and for a near-resonant interaction. Both are symmetric, i.e. $k_1 = k_2$ and $m_1 = -m_2$. The large interaction in 3(b) resembles a third resonant wave, although it is not actually a resonant wave until the angle predicted by (15) is reached.

The above discussion can be applied to glancing reflections of solitary waves against a wall. The results are the same since the condition of no normal flow ($\eta_y = 0$) at the wall allows one to extend the solutions by symmetry. The theory allows for regular reflection, as described by (13) with $k_1 = k_2$ and $m_1 = -m_2$, for $m_1 > m_{res}$, where

$$m_{res} \equiv \sqrt{\frac{12\beta}{\gamma}} k_1 = \sqrt{\frac{\alpha_1 \eta_0}{\gamma}}, \quad (18)$$

where η_0 is the amplitude of the incident wave. If, however, $m_1 \leq m_{res}$, regular reflection is no longer allowed. Instead, the interaction is described by (17), where the subscripts 1 and 2 correspond to the incident and reflected waves, respectively, and a third wave is resonant. This third wave, which has no transverse wavenumber and travels parallel to the wall, is known as the **mach stem** by analogy with a phenomenon seen in gas dynamics. Since the transverse wavenumber of the mach stem is zero, and the waves are in resonance, the amplitude of the mach stem and of the reflected wave can be inferred from the kinematic resonance constraint (16):

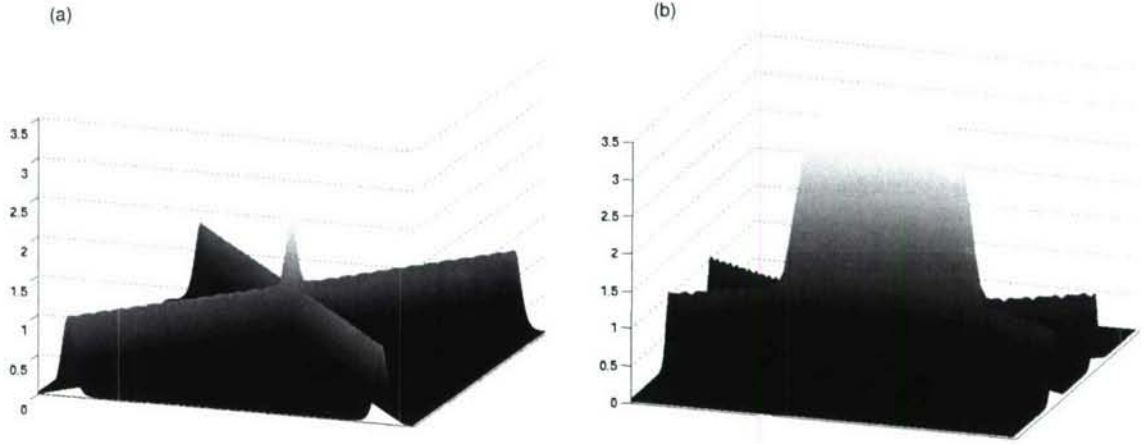


Figure 3: (a) Oblique interaction. (b) Near-resonant interaction.

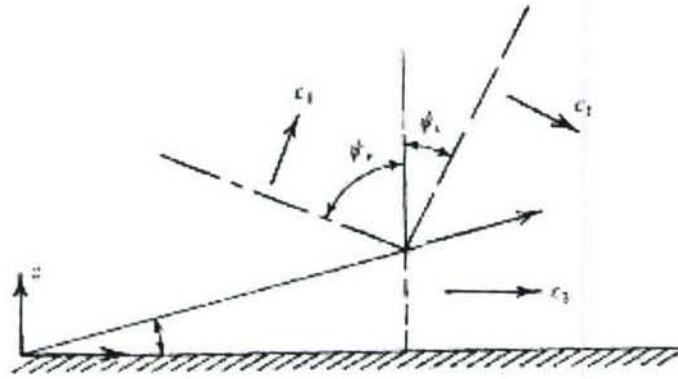


Figure 4: Mach reflection. The incident wave (---) moves into the wall with phase velocity c_1 , and the reflected wave (· · ·) moves away at c_2 . The intersection of the incident and reflected waves with the mach stem (—) moves away from the wall. Taken from [7].

$$m_2 = m_{res}, k_2 = k_1 \frac{m_1}{m_{res}}, \eta_{0,2} = \frac{12\beta}{\alpha_1} k_2^2, k_{mach} = \left(1 + \frac{m_1}{m_{res}}\right) k_1, \eta_{0,mach} = \frac{12\beta}{\alpha_1} k_{mach}^2. \quad (19)$$

In this case, if $k_2 < k_1$, the interaction pattern will move away from the wall with time, and thus the mach stem will grow in length. This configuration is shown in figure 4. The maximum amplitude, or *runup*, at the wall can then be calculated as a function of m :

$$\frac{\eta_{max}}{\eta_0} = \begin{cases} 4 \left(1 + \sqrt{1 - (m_{res}/m)^2}\right)^{-1} & m > m_{res} \\ (1 + m/m_{res})^2 & m < m_{res} \end{cases}, \quad (20)$$

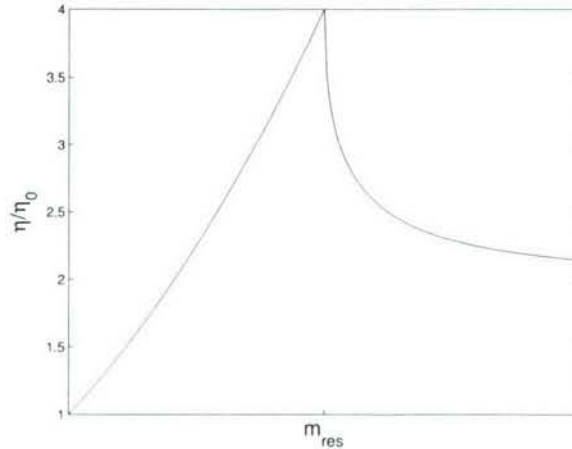


Figure 5: Theoretical KP runup at wall versus m (tangent of incident angle)

(see figure 5), which is useful since it is easy to verify by lab or numerical experiment.

Modified KP Interactions

It may be apparent to the reader that the word *soliton* has not been used liberally up to this point, although the term applies to the interacting solitary waves described above. One can use the term to describe solitary waves that can pass through each other and still retain their identity, in which case the term applies, in a very limited way, to eKP solitary waves (see below). But one could also think of solitons in a loose sense as solitary wave solutions that are amenable to the various transform methods (e.g. Hirota's Bilinear method) used to make analytical headway in describing their interactions. It is shown in [2] that the same bilinear transform methods that work quite well on KdV, eKdV, and KP (as well as many other nonlinear wave equations that support solitons) break down when applied to the eKP equation, except for the degenerate case in which all solitary waves are traveling in the same direction. Further, it can be shown that the eKP equation does not pass the Painlevé test, a criterion in determining whether an equation is completely integrable. This does not prove that eKP is non-integrable, but it demonstrates that exact solutions will, at the very least, not be easy to find. For that reason, the focus of this study is numerical in nature; since (20) predicts a large amplitude increase, while (10) gives a maximum amplitude constraint when a cubic term is present, it is unclear what the results of such an experiment will be.

4 Numerical Model

There is a difficulty inherent in solving (7) numerically. If we integrate the equation in x , assuming that disturbances are locally confined, then

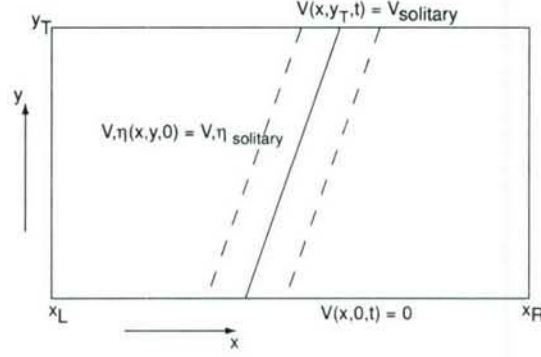


Figure 6: Model schematic.

$$\int_{-\infty}^{\infty} \eta_{yy}(x, y, t) dx = \frac{\partial^2}{\partial y^2} \int_{-\infty}^{\infty} \eta dx = 0, \quad (21)$$

a condition known as the "mass condition." In particular, a given initial condition must satisfy this constraint; otherwise it can be shown there are waves present with infinite group speed which propagate to $x = -\infty$ [1]. Alternatively, one can examine the evolution equation that results from an integration in x :

$$\eta_t + \alpha_1 \eta \eta_x + \alpha_2 \eta^2 \eta_x + \beta \eta_{xxx} - \gamma \int_x^{\infty} \eta_{yy} dx = 0. \quad (22)$$

If a discretized form of (21) is not satisfied, then disturbances will appear instantaneously far behind the initial condition. To avoid this problem, eKP is written in the form given in section 2, but with the time derivative left in the y -momentum equation [9]:

$$\eta_t + \alpha_1 \eta \eta_x + \alpha_2 \eta^2 \eta_x + \beta \eta_{xxx} + \gamma V_y = 0, \quad (23)$$

$$V_t - V_x + \eta_y = 0. \quad (24)$$

The time derivative is neglected in the derivation of eKP for asymptotic consistency, but here is left in in order to regularize the equation, and the numerical model now solves for both η and V .

Most of the numerical experiments involved a single solitary wave with a transverse component ($m \neq 0$) directed into a wall ($y = 0$) as an initial condition. In this case V was held at zero at $y = 0$ for all t , and was set to the analytical solution for such a wave at y_T , which was effectively considered to be $y = +\infty$ (figure 6). η and V were solved on grids that were coincident in x but staggered in y . In the y -direction, the topmost and bottom-most points were V -points, so boundary conditions were imposed on V but not on η (unless the domain was doubly-periodic). Spatial derivatives were approximated by centered differences. First derivatives in x were 4th order, while all others were 2nd order. The nonlinear terms were approximated by straightforward multiplication (no averaging was done). The timestepping scheme was an Adams-Bashforth predictor-corrector method involving two previous timesteps, where the two initial steps were done by Heun's method.

Very often a simulation was restarted using the final state as a new initial condition; in this case the two previous timesteps were not saved. A few doubly-periodic simulations were done where the initial condition was a superposition of different solitary waves, but the bulk of the numerical experiments done were with the wall model described above.

Since no wave was expected to propagate faster than the incident wave, η and V were set to zero at x_R . However, conditions at x_L were not as straightforward, and were handled as follows: the solution on the first two gridpoints in the x -direction was extrapolated linearly backward. This was in order to allow any disturbances, which presumably would be traveling to $x = -\infty$ in the frame in which (23) and (24) are defined, to pass through x_L rather than reflect back into the domain. In addition, a linear damping of the form

$$\begin{aligned}\eta_t &= \dots - \mu(x)\eta \\ V_t &= \dots - \mu(x)V\end{aligned}$$

was added, where μ (≥ 0) is nonzero only in a small neighborhood of x_L . This is justified physically by the assumption that the incident wave, its reflection, and their interaction are the fastest-moving disturbances in the system, and so long as they are sufficiently resolved away from x_L , then what happens near x_L should not affect their behavior. Resolution was often higher in x than in y . The timestep was made short enough to avoid a CLF-type instability. The upper bound was determined more empirically than by theoretical means due to the nonlinearity of the equations.

A simple rescaling (not given here) of η , x , y and t (where x and y are scaled identically so that angles are preserved) allows us to replace α_1 , β , and γ as given in section 2 with any values we choose. For programmatic ease, these parameters were set to 1.5, 0.125, and 0.5, respectively. Values of α_2 were found by (8) and then applying the same scaling.

5 Numerical Results

In the wall experiment, if η is scaled to the amplitude of the incident wave, η_0 , then (23) becomes

$$\hat{\eta}_t + \alpha_1 \eta_0 \left(\hat{\eta} - \frac{\eta_0}{\eta_{0,max}} \hat{\eta}^2 \right) \hat{\eta}_x + \beta \hat{\eta}_{xxx} \dots \quad (25)$$

where $\eta_{0,max}$ was defined in section 3. If the nondimensional parameter $\eta_0/\eta_{0,max}$ is zero, we recover KP (or, according to our model, a regularized version of KP), so the larger this parameter, the more departure we expect from KP reflection behavior. So numerical experimentation began by benchmarking the numerical model's ability to reproduce known results. Except where explicitly stated, the values of α_1 , β and γ in all of the experiments described below were 1.5, 0.125, and 0.5, respectively, and α_2 was computed using $h1 = 0.67$.

Unidirectional eKP

As mentioned above, one should be able to generate a 2-soliton solution to the eKP equation, as long as both solitary waves are traveling in the same direction. Though it does not involve reflection, this is still an important result. A doubly periodic domain was used, with a large

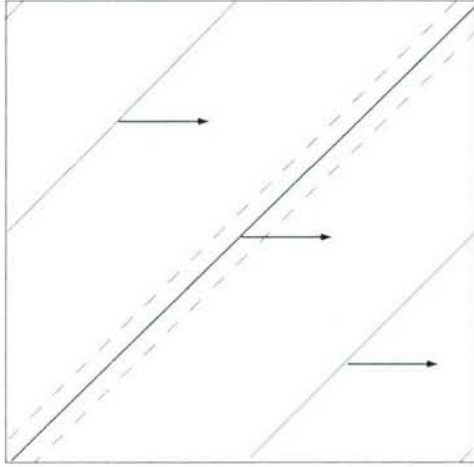


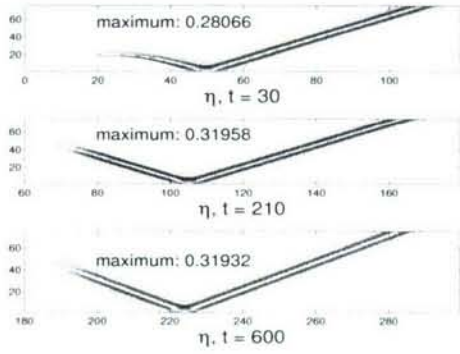
Figure 7: Doubly periodic domain used to simulate eKP soliton interactions. The initial condition is shown here; the narrower wave crest is larger in amplitude.

wave behind a small wave as an initial condition (figure 7). This simulation was shown to produce the typical 1-D soliton interaction pattern. Figure 2 actually shows cross-sections of snapshots of this simulation for $m = 0.4$.

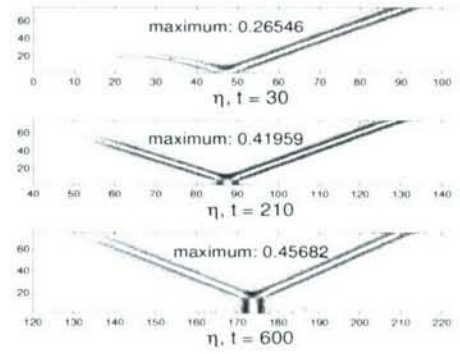
KP and eKP Reflection

Figures 8(a)-8(c) show the development of a KP interaction pattern for different incident angles. In all KP experiments, the incident amplitude $\eta_0 = 0.12$, $m_{res} = 0.6$. Figures are shown for $m_{incident}$ greater than, equal to, and less than the resonant value. For $m_{incident} = 0.8$, the reflection pattern is symmetric, with the maximum wall amplitude $\approx 2.6\eta_0$. For $m_{incident} = 0.6$, the resonant angle, we see a mach stem slowly forming with amplitude close to $4\eta_0$. Theory predicts a mach stem will not grow at the resonant angle, and that the maximum amplitude achieved is $4\eta_0$; however, since this is a numeric approximation it is perhaps not surprising that resonance is not achieved exactly. The fact that stem growth is very slow and amplitude increase is close to 4 is encouraging. At $m_{incident} = 0.15$, the reflected wave is difficult to see because it is so small and obscured by its own reflection from the far wall. It is, as predicted, clearly at a far more oblique angle than the incident wave. Also, the mach stem has an amplitude $\eta_{wall} = 1.6\eta_0$ that is very close to that of the incident wave.

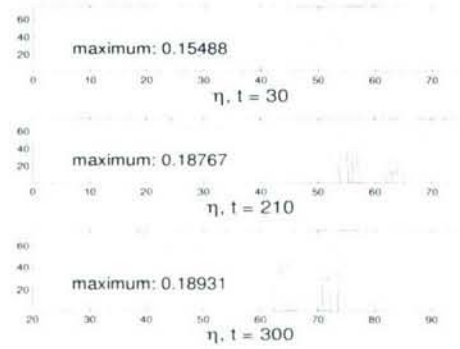
It should be stressed that the theory concerns stationary solutions, not transient development from arbitrary initial conditions. Comparing transient solutions for $m_{incident} = 0.6$ with those for $m_{incident} = 0.8$ and $m_{incident} = 0.15$ shows that a near-resonant interaction takes a long time to develop. This can be seen by plotting the maximum wall amplitude of η at the wall as a function of time. This is shown for the same simulations in figure 8(d). All of the plots show convergence to a stationary amplitude. The small oscillations around this mean can be explained by failure to completely resolve the peak of the wave crest; however, this is likely not detrimental to the overall solution.



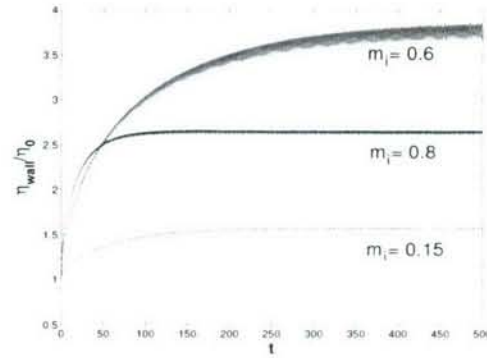
(a) $m_{incident} = 0.8$. Reflection is regular.



(b) $m_{incident} = 0.6$. Reflection is near-resonant. Note maximum amplitude and beginning of mach stem formation.



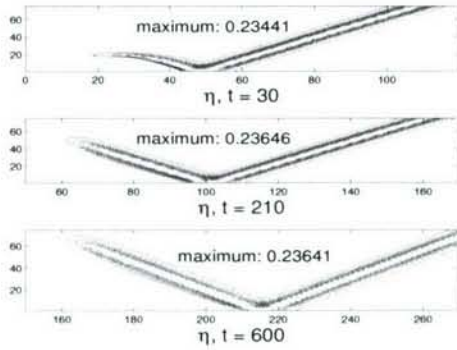
(c) $m_{incident} = 0.15$. Mach Reflection. Note fully-developed mach stem which grows in time.



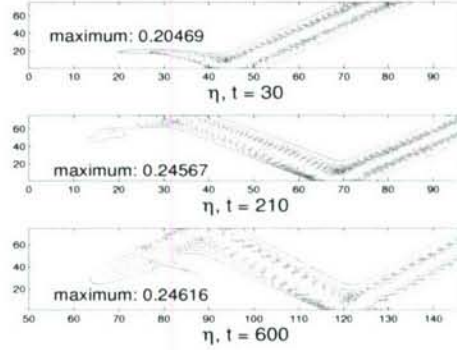
(d) Maximum amplitude versus time for all three simulations. Oscillations likely from failure to fully resolve highest peak.

Figure 8: KP reflection, $\eta_0 = 0.12$.

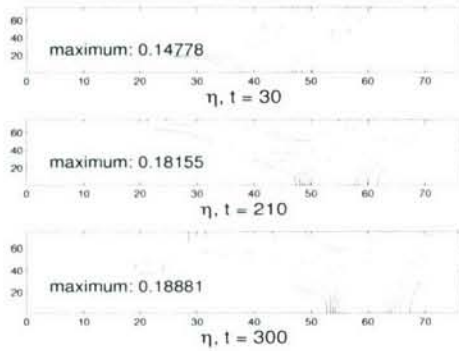
Figures 9(a)-9(c) show analogous results for eKP interactions with $\eta_0 = 0.12$. A value of 0.67 was chosen for h_1 as given in section 2, giving $\eta_{0,max} = 0.2524$, and $\eta_0/\eta_{0,max} \approx 0.48$. Comparing figures 8(a) and 9(a), we again see regular reflection, but the interaction amplitude is smaller for the eKP case, and in fact is smaller than $\eta_{0,max}$. Figure 9(b), resulting from an incident angle with tangent 0.45, appears to show a reflected wave with angle equal to the incident, trailed by smaller crests with more oblique angles, in contrast with the mach reflection pattern that would be seen with KP, and a maximum amplitude just greater than $\eta_{0,max}$. For $m_{incident} = 0.15$, shown in figure 9(c), we do see a pattern that looks qualitatively like mach reflection, although it is not clear whether this term actually applies to the interaction. Still, with relatively little apparent transverse variation near the wall, one can anticipate that the profile at the wall looks very similar to an eKdV solitary



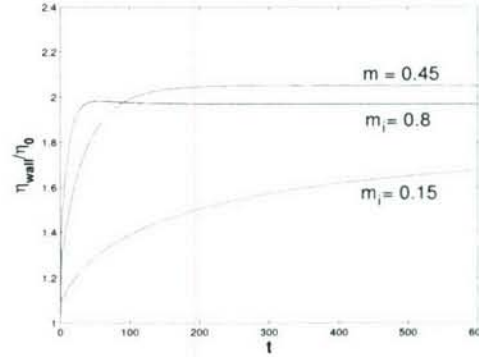
(a) $m_{incident} = 0.8$. Reflection is regular.



(b) $m_{incident} = 0.45$. Maximum amplitude is near $\eta_{0,max}$ (see figure 10(c)). Note smaller, more oblique wave crests trailing the reflected wave.



(c) $m_{incident} = 0.15$. Interaction pattern resembles mach reflection.



(d) Maximum amplitude versus time for all three simulations.

Figure 9: KP reflection, $\eta_0 = 0.12$, $h_1 = 0.67$ (see section 2).

wave, and this was found to be the case.

Comparing the maximum runup of KP simulations to theory, figure 10(a), we see very good agreement for angles less than the resonant angle. However, for angles larger than the resonant angle the agreement is not so good. This is certainly an issue, and may be a consequence of the use of regularized equations (see Discussion section). Still, all of the qualitative aspects of the theory were captured, and for small angles the quantitative agreement was good as well.

Figure 10(b) shows the same results as figure 10(a) along with the results from eKP simulations for different values of η_0 , where $m_{incident}$ has been scaled to m_{res} , as given by (18). Values of η_0 used were 0.024, 0.05, 0.12, and 0.24, while $\eta_{0,max} = 0.2524$ for all cases. Recalling (25), notice that, for $\eta_0 = 0.024$ and $\eta_0 = 0.05$ (dots and triangles, respectively),

the runup plot has a qualitatively similar shape to that of KP, but the maximum occurs at a smaller (scaled) incident angle and is not as large. The same could be said of $\eta_0 = 0.12$, though the maximum is barely visible, and we have seen qualitatively different results for this amplitude. In fact, it does seem as though the eKP runup plots may coincide with that of KP where the incident angles are small enough that $\eta_{wall} < \eta_{0,max}$. These points correspond to interaction patterns that look similar to mach reflection (cf. figure 9(c)), though there is not space to show all of the results. Again, it is stressed that the development of these interaction patterns is transient. In a few cases, the growing "mach stem" reached the far wall before the wall amplitude became stationary, and in these cases, the result given in figures 10(b), 10(c) is that taken just before this intersection occurred.

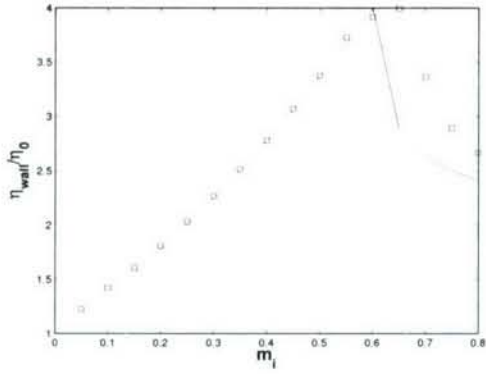
Obviously, the above statements do not apply to the case $\eta_0 = 0.24$, since $\eta_0/\eta_{0,max} \simeq 1$. Indeed, the runup plot for $\eta_0 = 0.24$ is very different than the others. Figure 10(c) shows the same results as those in figure 10(b) without scaling amplitude by η_0 . Here it is seen that when $\eta_0 = 0.024, 0.05, 0.12$, the runup is never greater than $\eta_{0,max}$ (solid line), but is for $\eta_0 = 0.24$. This contrast suggests that the range $0.12 < \eta_0 < \eta_{0,max}$ should be investigated for transition between the two behaviors, but this was not done in the current study. Figure 10(d) shows the result of one of the simulations where $\eta_0 = 0.24$.

One might ask if a resonant interaction actually does occur in the eKP simulations. Though (16) is not sufficient for resonance, it is necessary and can be checked. It is easiest to check the first two conditions of (16) since they relate only to the wavenumbers and not the phase speeds, and wavenumbers are calculated from amplitudes using (11). Further, the requirement that one of the bounds of (15) be satisfied for the kinematic resonance condition to apply holds for eKP as well as KP. This can be observed as follows. Consider two (1 and 2) solitary wave solutions to eKP. Imagine that both wavenumbers (k_1 and k_2) are known, and the direction of the first (m_1) is known (but not of the second), and the waves are constrained to satisfy (16) for some solitary wave with wavenumber and direction k_3 and m_3 . From (11), we can give wavenumbers in terms of frequencies and propagation directions:

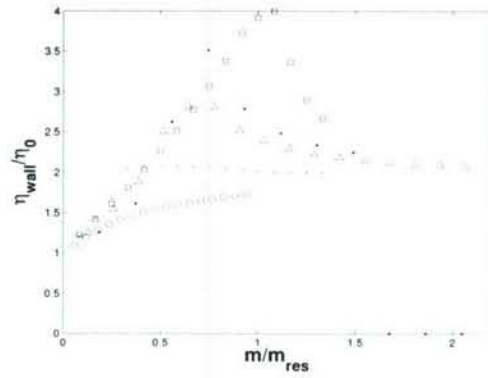
$$4\beta k_i^2 = \frac{\omega_i}{k_i} - \gamma m_i^2, i = 1, 2. \quad (26)$$

Together with (16), these two equations form a set of 5 algebraic equations for the unknowns $m_2, m_3, k_3, \omega_2, \omega_3$, which can then be solved for two possible values of m_2 . The important thing to notice is that the above equations do not depend on α_2 , and so, even when eKP solitary waves are considered, the results still correspond to the bounds of (15), even though the corresponding phase velocities and amplitudes are different than the KP case.

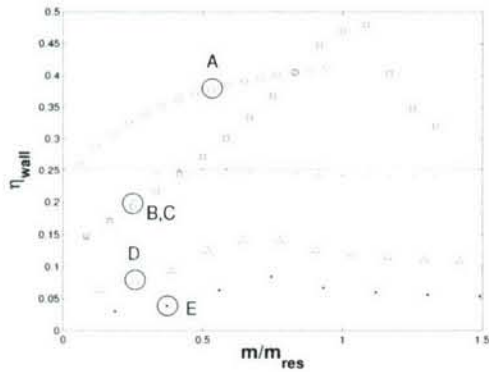
Table 1 shows calculated wavenumbers for the incident and reflected waves, as well as the mach stem, assuming solitary wave solution (10). (The term "mach" is used here for lack of a better one; as mentioned before, the eKP simulations show behavior qualitatively like mach reflection.) As in Miles' analysis, for KP we assume that the mach stem is at right angles to the wall and the the reflected angle is the resonant angle, i.e. $m_{mach} = 0$ and $m_{refl} = m_{res}$. By inspection, we also set $m_{mach} = 0$ for eKP, but with out an exact solution there is no reason to assume $m_{refl} = m_{res}$, and so m_{refl} had to be measured. This measurement is done by examination of the numerical solution of η . However, the reflected wave crest is often either not fully developed, obscured by the far wall or the stem crest,



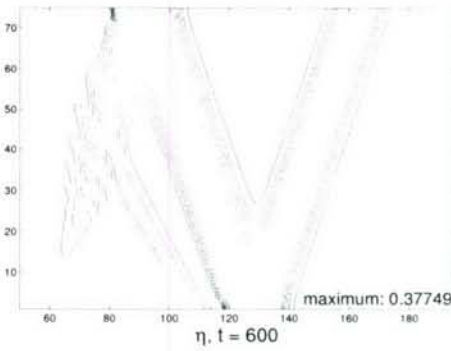
(a) KP reflection runup. Comparison of results with theory.



(b) eKP reflection runup for different values of η_0 : 0.24 (circles), 0.12 (x's), 0.05 (triangles), 0.024 (dots), compared with KP runup, $\eta_0 = 0.12$ (squares). Values are normalized by η_0 .



(c) Same as (b), but not normalized by η_0 . Solid line is $\eta_{0,max}$. B,C,D,E correspond to the results in Table 1.



(d) eKP, $\eta_0 = 0.24$, $m_{incident} = 0.45$ (corresponds to A in (c)). For this simulation, the wall amplitude is stationary.

Figure 10: Reflection runup

very short in length, or very small in magnitude, or all of the above. Measurement of k_{refl} is problematic for these reasons, and measurement of m_{refl} even more so. Still, there is no other method of verifying whether (16) is satisfied. It can be seen from Table 1 that agreement is not bad for KP. It is worse for eKP, but improves with decreasing amplitude.

Positive α_2

In certain cases, vertical shear and stratification can conspire to make α_2 positive [3]. Equation (10) still applies, only now the amplitude can take on either sign (we are still

Expt		k_{inc}	k_{refl}	k_{mach}	m_{refl}	$\frac{k_{inc}m_{inc}}{m_{refl}}$	$k_{inc} + k_{refl}$
KP	$\eta_0 = 0.12, m_{inc} = 0.15$.3464	.099	.4322	0.6	.0866	.4454
eKP	$\eta_0 = 0.12, m_{inc} = 0.15$.3011	.1385	.3412	0.52	.0869	.4396
eKP	$\eta_0 = 0.05, m_{inc} = 0.1$.2199	.0653	.242	0.45	.0489	.2852
eKP	$\eta_0 = 0.024, m_{inc} = 0.1$.1511	.0465	.1709	1.0	.0151	.1976

Table 1: Incident, reflected, and mach stem wavenumbers (k_{inc} , k_{refl} , and k_{mach} , resp). (the term ‘mach’ is used even if it is not clear that there is resonance.) Equality of the last column with k_{mach} and of the second-last column with k_{refl} is required by the kinematic resonance condition. The former criterion involves angle measurements, which are more problematic than wavenumber measurements, while the latter does not.

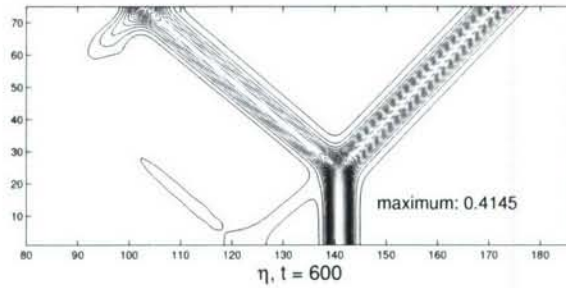
using the convention that α_1 is positive). If η_0 is positive, there is no maximum amplitude; if η_0 is negative, it must be larger (in absolute value) than $2\alpha_1/\alpha_2$. Several simulations were carried out with positive α_2 , however the sweep of the parameter space was not nearly as complete as for negative α_2 . Some results are shown in figures 11(a)-11(c). Figure 11(a) is the result of a simulation in which $\eta_0 = 0.12$ and $m_{incident} = 0.6$, as for figure 8(b). α_2 is positive and set to +1, and the coefficients α_1 , β , and γ remain as above. We see a pattern very similar to the KP result, but with a small radiative pattern shed from both the incident and reflected waves in the bottom left corner. More interesting are the results where η_0 is negative, as in figure 11(b). Here $\eta_0 = -0.3$, and $m_{incident} = 0.4$. There is a similar radiation pattern, but it is more developed. In fact, when the profile at the wall is examined, the radiation pattern is shown to have the same profile as the incident wave, and to have traveled the same distance. Figure 11(c) shows the development of the profile at the wall. The larger peak is the stem seen in 11(b); the smaller peak is the intersection of the radiated wave crests. When compared with figure 2, the wall profile of η looks very similar to the interaction of two unidirectional solitons. Given that transverse variation appears small near the wall in 11(b), it is perhaps not surprising that the profile at the wall is similar to an eKdV solution; however, it is surprising that interaction of the incident wave with its reflection develops into something similar to a two-soliton solution.

A result similar to figure 11(b) is shown in [10], though in that study the Modified KP equation (which is similar to eKP with positive α_2 and no quadratic term) was being investigated. Also, the profile of the intersection of the radiated wave crests was not examined in that study.

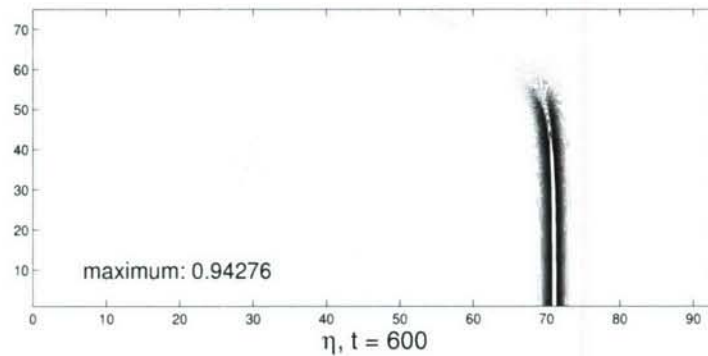
The investigation of positive α_2 was not taken further – it was meant only as a brief exploration of different behavior and possible starting point for further study.

6 Discussion

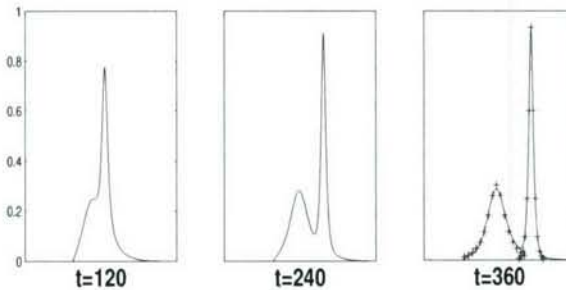
We have seen that a numerical model which gives reasonable agreement with theory concerning the glancing interaction of two KdV solitary waves (figs. 5, 10(a)) produces somewhat different behavior when two eKdV solitary waves interact, with the degree of difference depending on the magnitude of the incident amplitude relative to $\eta_{0,max}$. When the interaction amplitude is close to the maximum possible amplitude of an eKdV solitary wave, we see



(a) eKP: $\alpha_2 = +1$, $\eta_0 = 0.12$, $m_{incident} = 0.6$. Note radiation trailing the interaction.



(b) eKP: $\alpha_2 = +1$, $\eta_0 = -0.3$, $m_{incident} = 0.4$. Trailing radiation more developed than in (a).



(c) Snapshots of profile at wall from simulation leading to (b). At $t = 360$, analytical solutions (+) are superimposed on profile, centered on the peaks: on the smaller peak, the boundary condition at the far wall, and on the large peak, and eKdV solitary wave with the same amplitude.

Figure 11: Positive α_2

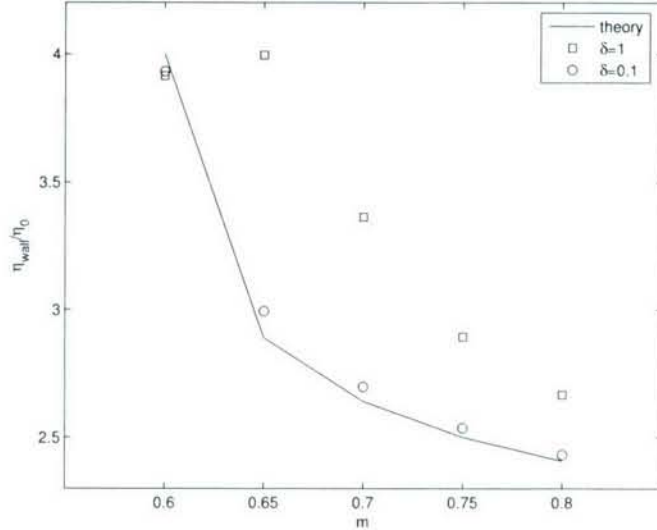


Figure 12: Runup results comparing different regularization schemes, where δ is as in (27). $\delta = 1$ corresponds to the results shown in figure 10(a), and $\delta = 0.1$ gives results closer to theory.

what appears to be dispersion occurring near the intersection of the interacting waves. This is not surprising because the nonlinear term in the eKP equation is small when amplitude is close to $\eta_{0,max}$, but there is no reason to expect the dispersive term to be small.

In some cases, the eKP simulation results in a pattern that resembles a mach stem and a nonsymmetric reflected wave, as in the KP simulations. However, it is not clear whether this is a stationary solution, or whether it is a resonance of three solitary waves. Long-time simulations (e.g. figure 9(c)) seem to suggest that such a pattern is stationary and would last until effects of the far wall became important. Table 1 suggests that the kinematic resonance condition is not satisfied. However, there are difficulties in measuring the properties leading to this conclusion. We have also seen that when the incident amplitude is near the maximum amplitude (figs. 10(d), 10(c)) the interaction does not resemble KP interaction at all.

It was suggested above that the disagreement with theory with respect to wall amplitude in KP reflection when $m_{incident} > m_{res}$ (figure 10(a)) may be a result of regularization in the numerical model. This claim was investigated by generalizing (24) to

$$\delta V_t - V_x + \eta_y = 0, \quad (27)$$

where δ is a parameter between 0 and 1. Preliminary results (figure 12) show better agreement with theory for $m_{incident} > m_{res}$ when δ is small.

7 Conclusions and further work

One of the early goals of this study was to find a closed form solution for the eKP equation (aside from the degenerate one where all waves move in the same direction). The literature

seemed to suggest that such a solution would be extremely difficult to find. Indeed, the fact that some results were highly dispersive seems to indicate that the eKP equation, unlike the KP equation, does not have soliton solutions for three dimensional solitary wave interactions.

That issue aside, the results of this study constitute a tool to gauge the KP and eKP equations as representative models of internal waves with small transverse variation. Oceanographic data was not used in this study; however, the two models exhibit qualitatively different behavior, and this behavior can be compared with that of actual internal solitary waves. For instance, tidal flow over bathymetry may cause glancing internal solitary wave interaction with some regularity, and might be useful to be able to predict the nonlinear amplitude increase based on known parameters such as stratification and background currents.

The results shown in figure 12 suggest that the disagreement with theory shown in figure 10(a) is due to regularization, and that a different regularization such as (27) with δ small might yield better agreement. However, this must be investigated further, and this investigation is the subject of ongoing work.

The investigation of the eKP equation with positive α_2 was not very extensive, but it still yielded interesting results. There were small radiative waves in all eKP simulations (including those with negative α_2 , although they are not visible in the plots shown), but we saw from figures 11(b), 11(c) that these radiative waves may have interesting structure. Further analysis of the parameter space is certainly warranted.

References

- [1] Akylas, TR, 1994. Three-dimensional long water-wave phenomena. *Annu. Rev. Fluid Mech.* **26**, 191-210.
- [2] Chen Y, P Liu, 1998. A generalized modified Kadomtsev-Petviashvili equation for interfacial wave propagation near the critical depth level. *Wave Motion* **27** (4), 321-339.
- [3] Grimshaw R, E Pelinovsky, T Talipova, A Kurkin, 2004. Simulation of the transformation of internal solitary waves on oceanic shelves. *J. Phys. Oceanogr.* **34**, 277491.
- [4] Helfrich, K and K Melville, 2006. Long nonlinear internal wave. *Annu. Rev. Fluid Mech.* **38**, 395-425.
- [5] Hirota, R. The Direct Method in Soliton Theory. Cambridge University Press, 2004.
- [6] Miles, J, 1977. Obliquely interacting solitary waves. *J. Fluid Mech.* **79**, 157-169.
- [7] Miles, J, 1977. Resonantly interacting solitary waves. *J. Fluid Mech.* **79**, 171-179.
- [8] Soomere, T and J Engelbrecht, 2006. Weakly two-dimensional interaction of solitons in shallow water. *European Journal of Mechanics B*, in press.
- [9] Tomasson, GG, 1991. Nonlinear waves in a channel: Three-dimensional and rotational effects. Doctoral Thesis, M.I.T.

- [10] Tsuji, H and M Oikawa, 2004. Two-dimensional Interaction of Solitary Waves in a Modified KadomtsevPetviashvili Equation. *J. Phys. Soc. Japan.* **73** (11), 3034-3043.
- [11] Whitham, GB. Linear and Nonlinear Waves. John Wiley and Sons, 1974.

Mush–liquid interfaces with cross flow

Devin Conroy

March 15, 2007

1 Introduction

The solidification of a binary melt growing into a supercooled region may lead to the formation of a mushy layer as a result of morphological instability of the plane boundary. Mushy layers are reactive porous media that suppress constitutional supercooling caused by the rejection of residual solute. When the rejected solute causes a statically unstable density stratification, compositional convection can occur, provided the Rayleigh number is large enough. Past experiments and theoretical results have shown that channels can form between convection cells, where fluid of high solute concentration has a maximum vertical velocity, which acts to dissolve the interior of the mushy layer. The channels grow in time, providing the path of least resistance for the continually convecting fluid, which is fed by the continual growth of solid and rejection of solute.

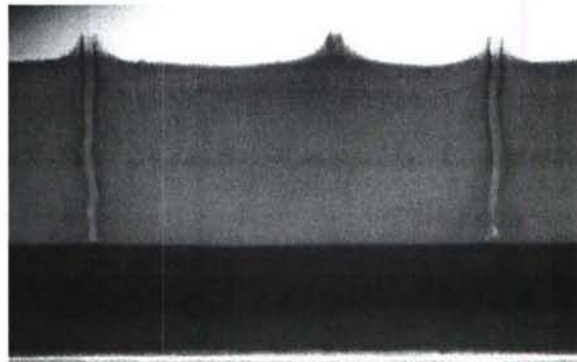


Figure 1: Mushy layer of ammonium chloride crystal grown from an aqueous solution, showing the structure of two complete chimneys. Taken from Worster (2000)

Fluid contained within the interior of a mushy layer, as shown in figure (1), is convected out through the chimneys and replaced by fluid from above. Along the walls of the chimney, fluid is then flowing from mush to liquid across a solidifying interface, and along the top of the mushy layer fluid is flowing from liquid to mush across a solidifying interface. Recently Schulze and Worster (1999, 2005) have examined the appropriate boundary conditions to be

applied at these interfaces in order to determine the position of the mush–liquid interface. In general there are four separate cases corresponding to a solidifying or dissolving boundary and whether the flow of material is from mush to liquid or from liquid to mush. Three of those conditions have been explored using one-dimensional models but the fourth, which is the topic of this study, requires the flow to be at least two dimensional. The dissolving boundary occurs initially when the chimney first forms from a liquid inclusion but later on the walls of the chimney are actually in a solidifying regime. In this case the fluid is leaving the mush across a solidifying boundary and we want the time-rate of change of temperature following a material particle at the interface to be zero. This condition, which is equivalent to the isotherms being tangent to the streamlines, is a relatively new idea that still requires exploration in order to fully understand the nature and consequences of it.

2 Governing Equations

In this analysis we are looking at the configuration illustrated in figure 2 (see Le Bars et al. 2006), which is a simplified model designed to explore the nature and consequences of a solidifying mush–liquid interface having material flowing from mush to liquid. It is a convenient way of exploring a 2–dimensional flow with a 1–dimensional analysis. In addition we require a 2-D temperature field in which the upper and lower boundary temperatures vary linearly with x in order to maintain the same mathematical structure as the stream function ψ . In addition we require the solid fraction and interface position to be independent of the horizontal distance x .

Fluid flows from the bottom boundary into the mushy layer at a velocity W_B and out of the top boundary at a velocity W_T , where $W_T \leq W_B$. Since we are strictly interested in the case in which the mushy layer is growing, we take the lower boundary to be colder than the upper boundary ($m_1 < m < m_2$), where m is the slope of the liquidus curve in the phase diagram. The mushy layer is solidifying at a rate da/dt , where $a(t)$ is the position of the interface. In addition we are pulling the whole apparatus downwards at a constant speed V which will be equivalent to the growth rate of the mush–liquid interface in the non-moving reference frame at steady state.

2.1 Mushy Layer

Within the mushy layer ($0 < z < a$) we have a reactive porous medium that requires appropriately volume averaged equations for temperature, T and concentration, C . Here we assume that the ideal mushy layer equations apply (see Worster 1997), namely

$$\frac{\partial T}{\partial t} + \mathbf{q} \cdot \nabla T = \kappa \nabla^2 T + \frac{L}{c_p} \frac{\partial \phi}{\partial t} - \frac{VL}{c_p} \frac{\partial \phi}{\partial z}, \quad (1)$$

$$(1 - \phi) \frac{\partial C}{\partial t} + \mathbf{q} \cdot \nabla C = (C - C_s) \left(\frac{\partial \phi}{\partial t} - V \frac{\partial \phi}{\partial z} \right), \quad (2)$$

$$T = T_L(C) = -mC, \quad (3)$$

where the diffusion of salt is assumed to be negligible and the temperature field in the mush is constrained to the concentration field by the liquidus relationship. Here $q = \mathbf{u} - V\hat{\mathbf{k}}$, κ is

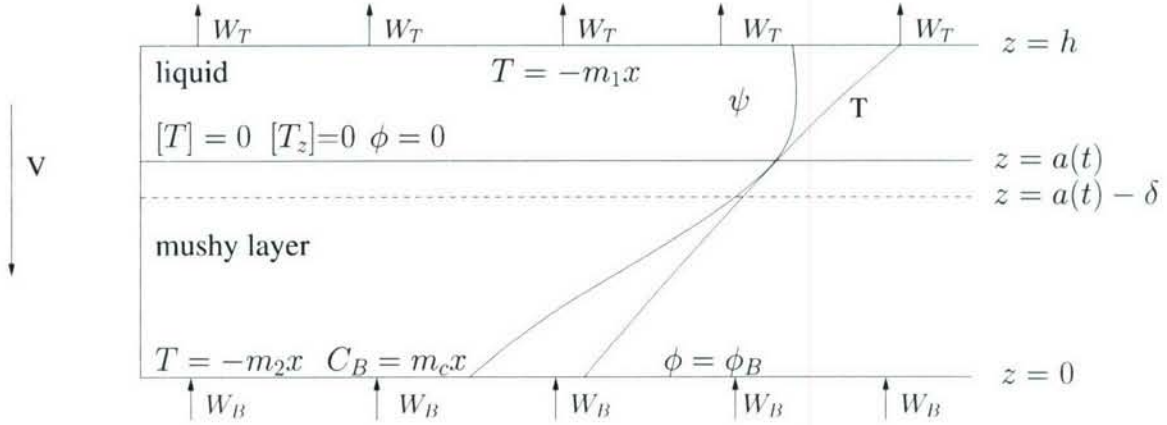


Figure 2: Diagram showing a channel of infinite length with a mushy layer contained in the region $z < a$ and a liquid layer above. There is a flow of relatively cool fluid from the bottom boundary at a rate W_B and a flow out of the channel at a smaller velocity, W_T . The left hand boundary is fresh, i.e. no solute, and non-permeable.

the thermal diffusivity, L is the latent heat, c_p is the specific heat, ϕ is the solid fraction and C_s is the concentration in the solid. In this analysis we will assume that the solid is pure, i.e. $C_s = 0$, and that the liquidus temperature T_L decreases linearly with solute concentration. At the bottom of the channel we assume that the temperature and bulk concentration vary linearly with distance x as

$$T(x, 0, t) = -m_2 x, \quad C_{\text{bulk}}(x, 0, t) = (1 - \phi_B) C(T) = (1 - \phi_B) m_b x, \quad (4)$$

where $m_b = m_2/m$ is the slope of the solute concentration and ϕ_B is the lower boundary solid fraction that must be determined as part of the solution. It should be noted that the bulk concentration presented here comes from some outer solution and only applies when the q flow is from mush to liquid. If the flow is in the opposite direction then as we will see in the next section, the bulk concentration must be imposed at the upper surface.

2.2 Liquid Layer

In the liquid layer above the mush ($a < z < h$) we again assume that the diffusion of salt is negligible compared to advection and we use the following equations

$$\frac{\partial T}{\partial t} + \mathbf{q} \cdot \nabla T = \kappa \nabla^2 T, \quad (5)$$

$$\frac{\partial C}{\partial t} + \mathbf{q} \cdot \nabla C = 0. \quad (6)$$

At the upper surface we also assume that the temperature decreases linearly from the boundary $x = 0$ with the relationship

$$T(x, h) = -m_1 x, \quad (7)$$

where the condition $m_1 < m < m_2$ must be imposed for a solidifying interface.

Since the concentration field is controlled by the advection equation and we have imposed a solid fraction at the lower boundary the concentration equation (6) is decoupled from the system provided that the q -flow is out of the top boundary. The concentration field, without the effect of diffusion, just follows the streamlines with the unknown mush–liquid concentration. On the other hand if the q flow is from liquid to mush then the advection of bulk concentration from the upper boundary must be used to determine the temperature at the mush–liquid interface. In this case we impose a bulk concentration at the upper boundary of the form

$$C_{\text{bulk}}(x, h) = C(T) = m_l x, \quad (8)$$

where the solid fraction is zero.

2.3 Interface Conditions

At the interface between the mush and liquid layers ($z = a$) we follow Worster (2000) and use the conditions

$$[T] = 0, \quad [T_z] = 0, \quad \phi = 0, \quad z = a, \quad (9)$$

where the last one comes from the assumption that the diffusion of solute is negligible.

A subtle boundary condition presented in Schultz (2005) based on the complete removal of constitutional supercooling, requires that streamlines be tangent to isotherms in the case that fluid flows from the mush to the liquid across a solidifying boundary. This condition essentially means that the change in temperature moving with a material particle is zero at the interface, expressed mathematically as

$$\frac{D^q T}{Dt} = 0 \rightarrow \frac{\partial T}{\partial t} + (\mathbf{u} - V\hat{k}) \cdot \nabla T = 0, \quad (10)$$

where q represents the mean velocity of the material particles, \hat{k} is the unit vector in the vertical direction and we have shifted our coordinate system to move at the pulling speed V .

This condition can be justified by considering the change in temperature following a material particle, which according to the idea of equilibrium (see Worster 2000) will have the following property

$$\frac{D^q T}{Dt} \geq \frac{D^q T_L(C)}{Dt} \quad (11)$$

in the liquid at the mush–liquid interface $z = a$. In order to ensure that the liquid is not locally supercooled we require the change in solute concentration to be zero, $D^q T/Dt = 0$ and from the liquidus condition this translates to $D^q T_L(C)/Dt = 0$. Therefore a fluid particle moving at the mean velocity q must be warming up as it crosses the interface. On the mush side of the interface equation (2) can be expressed as

$$\frac{D^q C}{Dt} = \phi \frac{\partial C}{\partial t} + C \frac{D^v \phi}{Dt} \quad (12)$$

where the superscript v represent the mean velocity of the solid particles i.e. $D^v/Dt = \partial/\partial t - V\hat{k} \cdot \nabla$. Since the solid fraction is zero at the mush-liquid interface the first term on the right-hand side is zero. For a solidifying mush the change in solid fraction with time moving with the solid must be increasing $D^v \phi/Dt \geq 0$ and therefore equation (12) give the opposite condition

$$\frac{D^q T}{Dt} \leq 0 \quad (13)$$

on the mush side of the interface. As long as the temperature gradients and velocities are continuous across this interface then equation (10) must be true.

2.4 Velocity Profiles

In the setup shown in figure (2) we assume that the velocity profiles have the same structure as the well known solution for a corner flow (e.g. Batchelor 1967) in the case of a pure fluid, which are given in terms of a stream function by

$$\mathbf{u} = (u, w) = \left(\frac{\partial \psi}{\partial z}, -\frac{\partial \psi}{\partial x} \right), \quad \psi = -Vxf(z). \quad (14)$$

This formulation applies in both the mushy and liquid layers and allows us to satisfy continuity exactly in the case of a two-dimensional incompressible flow. We impose the following conditions on the boundaries of the domain

$$w(x, 0) = W_B, \quad u(x, h) = 0, \quad w(x, h) = W_T, \quad \left. \frac{\partial u}{\partial z} \right|_{x, z=0} = 0 \quad (15)$$

where the last condition expresses no horizontal shear and is only used for the Darcy-Brinkman formulation (see below).

2.4.1 Stokes-Darcy Formulation

Darcy's equation is commonly used in the study of porous media and has had success when compared to experimental observation (See Bear 1972). Strictly the equation applies for a low Reynolds number flow when the permeability is sufficiently small, which is the case in most types of porous media. Outside the mushy layer we have a thin channel that obeys Stokes equation for a thin gap. These equations are

$$-\nabla P = \frac{\mu}{\Pi} \mathbf{u} \quad 0 \leq z \leq a - \delta, \quad (16)$$

$$\nabla P = \mu \nabla^2 \mathbf{u} \quad a - \delta \leq z \leq h, \quad (17)$$

where the permeability Π is given by the following non-divergent function

$$\Pi = \Pi_0(1 - \phi)^3, \quad (18)$$

in terms of the solid fraction ϕ and δ is the thickness of a transition zone to be explained next.

At the mush–liquid interface it is well known and expected that the pressure and vertical mass flux are continuous, although this is not necessarily the case for the horizontal velocity. Since we cannot interrogate the porous media very close to the interface there is a region of depth δ where Darcy’s equation is not valid. In this region the pressure is balanced by both fluid–solid and fluid–fluid interactions, where the thickness of the transition zone δ then is defined to be the depth at which viscous dissipation at the solid walls dominate. Following Le Bars et.al. (2006) the depth of this transition zone is given by

$$\delta = c \sqrt{\frac{Da k_i}{1 - \phi_i}}, \quad (19)$$

where c is a scaling coefficient $k = \Pi/\Pi_0$, $Da = \Pi/h^2$ is the Darcy number and subscript, i indicates the level $a - \delta$. Since this thickness is normally small, $\phi_i \ll 1$ and we can to leading order write this equation as

$$\delta \sim c\sqrt{Da}. \quad (20)$$

Within the transition zone the appropriate equation is not straightforward but the simplest approach is to extend either Darcy’s or Stokes equation into this region. Beavers and Joseph (1969) verified experimentally that Darcy’s equation works well. The problem with this approach is that the horizontal velocity is not continuous which is inconsistent with condition (10). As an alternative Le Bars et. al. (2006) extended Stokes equation into the transition zone which also matches well to the results of Beavers and Joseph (1969). The advantage to this method is that the velocities are continuous at the mush–liquid interface and so we use this approach here. With this method the matching conditions at the level $z = a - \delta$ between the two regions are

$$[u] = 0, \quad [w] = 0, \quad [P] = 0 \quad z = a - \delta, \quad (21)$$

where the brackets denote a jump in the enclosed quantity.

Equations (16) and (17) can be simplified by substituting in the stream function relationship and eliminating the pressure to get the following equations

$$\frac{\partial}{\partial z} \left(\frac{f'}{\Pi} \right) = 0, \quad (22)$$

$$f'''' = 0. \quad (23)$$

in the mush and liquid respectively. Finally the boundary conditions in terms of f are

$$f'(h) = 0, \quad f(h) = \frac{W_T}{V}, \quad f(0) = \frac{W_B}{V}, \quad (24)$$

with the following matching conditions in terms of f at $z = a - \delta$

$$[f] = 0, \quad [f'] = 0, \quad f''''_+ = -\frac{f''_-}{\Pi}, \quad (25)$$

where $+$ denotes the liquid and $-$ the mushy layer.

2.4.2 Darcy-Brinkman formulation

An alternative to the above approach is to use a continuous formulation in terms of the Darcy-Brinkman equation

$$\nabla P = \frac{1}{1-\phi} \nabla^2 \mathbf{u} - \frac{\mathbf{u}}{\Pi} H(\phi), \quad (26)$$

which turns into Stokes equation in the liquid where the step function $\phi = 0$ and $H(\phi) = 0$. This equation has the advantage of being solvable on a single domain, which makes it favorable for problems in more than one-dimension, particularly when there are intricate changes in topography. Since fluid-fluid stresses are taken into account in this formulation the velocity is continuous at the mush-liquid interface and a transition zone does not need to be defined. Eliminating the pressure and substituting in the relationship for the stream function we get

$$f'''' = f''' \left[(\phi - 1) \frac{d}{dz} \left(\frac{1}{1-\phi} \right) \right] + f'' \left[\frac{1-\phi}{\Pi(\phi)} \right] H(\phi) + f' \left[(1-\phi) \frac{d}{dz} \left(\frac{H(\phi)}{\Pi(\phi)} \right) \right] \quad (27)$$

where the boundary conditions in terms of the unknown function, f , are

$$f'(h) = 0, \quad f(h) = \frac{W_T}{V}, \quad f(0) = \frac{W_B}{V}, \quad f''(0) = 0. \quad (28)$$

2.5 Non-dimensionalization

We seek a steady solution in the moving reference frame ($\partial/\partial t = -V \partial/\partial z$) and non-dimensionalize temperature and concentration with the imposed boundary conditions as follows

$$T = x [-m_2 + (m_2 - m_1)\theta(z)], \quad C = x \left[\frac{m_2}{m} + \frac{m_1 - m_2}{m} \theta(z) \right] \quad (29)$$

We then scale the length with the width of the channel, h , and the velocity with the interface speed, V . Equations (1), (2) and (5) become

$$\theta'(f-1) - f'(\theta - \mathcal{C}) = Pe \theta'' - \frac{S}{x} \phi' \quad 0 \leq z \leq a, \quad (30)$$

$$\frac{d}{dz} [(\phi-1)\theta - \mathcal{C}\phi] = f'(\theta - \mathcal{C}) - f\theta' \quad 0 \leq z \leq a, \quad (31)$$

$$\theta'(f-1) - f'(\theta - \mathcal{C}) = Pe \theta'' \quad a \leq z \leq 1, \quad (32)$$

where $Pe = k/(Vh)$ is an inverse Peclet number and $S = L/(C_p h(m_2 - m_1))$ is a Stefan number. Here $\mathcal{C} = m_2/(m_2 - m_1)$ is the deviation in the horizontal temperature gradient of the lower boundary m_2 from the upper boundary m_1 and essentially gives us a measure of the temperature difference. This non-dimensional parameter could be recast in terms of solute concentrations as $\mathcal{C} = m_b/(m_b - m_1/m)$, where $m_b = m_2/m$ is the concentration of solute at the lower boundary and m_1/m is the gradient in the solute concentration at the liquidus temperature. Since we assume the channel to be infinitely long we will look for

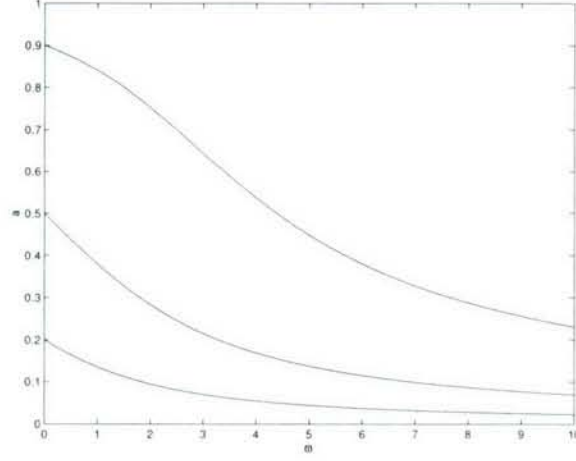


Figure 3: Mush-liquid interface position $a(\varpi, \theta)$ as a function of ϖ for $\theta_a = .2, .5$ and $.9$ corresponding to the lower, middle and upper lines respectively.

large x solutions such that, $S/x \sim 0$, which reduces our system of equations to functions of z only. The boundary conditions in the new variable θ become

$$\theta(0) = 0, \quad \theta(1) = 1, \quad (33)$$

$$\phi = 0, \quad [\theta] = 0, \quad [\theta_z] = 0 \quad z = a \quad (34)$$

with the unknowns θ, ϕ, a and the velocity f determined from either the Darcy-Stokes formulation as

$$\frac{\partial}{\partial z} \left(\frac{f'}{k} \right) = 0, \quad f'''' = 0. \quad (35)$$

$$f'(1) = 0, \quad f(1) = W_T, \quad f(0) = W_B. \quad (36)$$

$$[f] = 0, \quad [f'] = 0, \quad f_s''' = -\frac{f_D'}{D_a k}, \quad z = a - \delta. \quad (37)$$

or the Darcy-Brinkman formulation as

$$f'''' = f'''' \left[(\phi - 1) \frac{d}{dz} \left(\frac{1}{1 - \phi} \right) \right] + f'' \left[\frac{1 - \phi}{k(\phi) D_a} \right] H(\phi) + f' \left[\frac{1 - \phi}{D_a} \frac{d}{dz} \left(\frac{H(\phi)}{k(\phi)} \right) \right], \quad (38)$$

$$f'(1) = 0, \quad f(1) = W_T, \quad f(0) = W_B, \quad f''(0) = 0. \quad (39)$$

In the above equation $D_a = \Pi_0/h^2$ is the Darcy number and in the liquid layer the governing equation reduces to $f'''' = 0$

3 Solutions for $W_B = W_T < V$

It is of interest to obtain a solution in which the direction of flow in the moving reference frame is from liquid to mush along a solidification boundary. In this case the condition

required to determine the location of the mush–liquid interface is different from condition (10) as has been discussed previously. When the velocity of the upper and lower boundaries are equal, an exact solution is possible and its solution has interesting qualitative features that we would like to understand. In this case the governing equations, obtained by taking $f = W_B$ and $f' = 0$ in equations (30)–(32) are

$$\theta'(W_B - 1) = Pe\theta'' \quad (40)$$

$$\frac{d}{dz}[(\phi - 1)\theta - \mathcal{C}\phi] = -W_B\theta', \quad (41)$$

$$\theta'(W_B - 1) = Pe\theta''. \quad (42)$$

The solution to the temperature equations (40) and (42) in general are $\theta = A\exp(-z\varpi) + B$ where $\varpi = (1 - W_B)/Pe$. Applying the boundary conditions $\theta(0) = 0$, $\theta(a) = \theta_a$ and $\theta(1) = 1$ we get

$$\theta = \theta_a \frac{e^{-z\varpi} - 1}{e^{-a\varpi} - 1} \quad 0 \leq z \leq a \quad (43)$$

$$\theta = 1 + (\theta_a - 1) \frac{e^{-z\varpi} - e^{-\varpi}}{e^{-a\varpi} - e^{-\varpi}} \quad a \leq z \leq h \quad (44)$$

The position of the mush–liquid interface is determined such that the first derivatives of the temperature field are continuous, which is determined, with a little algebra, from

$$a = -\frac{1}{\varpi} \ln [\theta_a e^{-\varpi} + 1 - \theta_a]. \quad (45)$$

By integrating equation (41) and applying the boundary condition $\phi(a) = 0$ at the mush–liquid interface, we obtain

$$\phi = \frac{(1 - W_B)(\theta - \theta_a)}{\theta - \mathcal{C}}, \quad (46)$$

which gives the solid fraction as a function of the temperature profile equation (43).

In this frame of reference there is effectively a flow from the liquid to the mush in which case information about the solute concentration is transported from the upper boundary. Since there is only 1-dimensional flow with no solute diffusion the concentration in the liquid is constant and given by equation (8). This concentration translates to the mush side of the interface because of local equilibrium (see Schulze and Worster 1995) and gives a relationship for the interface temperature in non-dimensional form as

$$\theta_a = \mathcal{C} \left(1 - \frac{m m_t}{m_2} \right). \quad (47)$$

From this equation we can obtain a relationship for the solid fraction at the lower boundary in the form

$$\phi_B = \left(\frac{m m_t}{m_2} - 1 \right) (1 - W_B) \quad (48)$$

which is obtained by evaluating equation (46) at $z = 0$.

The solution to equation (45) has been plotted in figure (3) as a function of the parameter ϖ for different values of the interface temperature θ_a . From these profiles it is immediately evident that the position of the mush-liquid interface decreases with ϖ which can be interpreted as an increase in the velocity W_B . In this case there is a larger transport of relatively cool fluid from below that decreases the average temperature of the system and the thickness of the mushy layer must increase.

Similarly the position of the mush-liquid interface is shown to increase with the interface temperature, which can be better understood by recasting this temperature in the form

$$\theta_a = \mathcal{C} \left(1 - \frac{m_t}{m_b} \right) = \mathcal{C} r, \quad (49)$$

where $m_b = m_2/m$ is the horizontal derivative of the concentration at the lower boundary. The first term on the right hand side gives us a measure of the temperature difference in the system in that a large value of \mathcal{C} can be thought of as decreasing the temperature of the upper boundary. The second term is a ratio of the horizontal concentration gradient between the top and bottom boundaries, in which a large value of r implies a larger concentration of solute. In either case a large \mathcal{C} or r indicates that the average temperature in the system is cooler and the position of the mush-liquid interface must grow into the channel in order to reduce the amount of constitutional supercooling.

4 Numerical solution

We have solved the full set of equations (30)–(32) and either the Stokes–Darcy formulation (35) or the Darcy–Brinkman formulation (38) numerically using a shooting method combined with a fourth-order Runge-Kutta ode solver. The position of the mush-liquid interface is determined such that $\phi = 0$ and $q \cdot \nabla T = 0$ as a function of the 6 parameters, W_T , W_B , \mathcal{C} , Da , Pe and c in our system of equations.

In figure (4) we show the general characteristics of the numerical solution for a fixed set of parameter values. Here we have used the Darcy–Brinkman formulation for consistency and reserve a discussion concerning the comparison between the two formulations for the next section. The four plots show typical profiles for the solid fraction, ϕ , temperature, θ , first derivative of the temperature, θ' , vertical velocity, f and the horizontal velocity, f' . In addition we have plotted the non-dimensional form of condition (10), which is written as

$$G = \theta'(f - 1) - \frac{df}{dz} (\theta - \mathcal{C}), \quad G(a) = 0. \quad (50)$$

This condition can be interpreted as the point at which the isotherms are tangent to the streamlines or equivalently the point at which horizontal advection is balanced by vertical advection of thermal energy.

4.1 Comparison between Darcy-Brinkman and Stokes-Darcy formulations

Le Bars et. al. (2006) showed that the Stokes–Darcy and Darcy–Brinkman formulations are nearly equivalent for a suitably chosen transition zone depth and in the limit of small Darcy

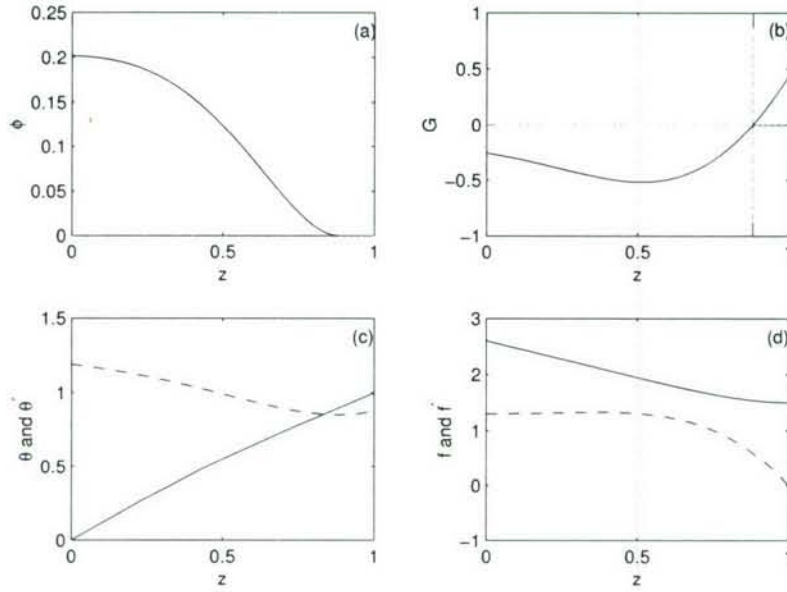


Figure 4: Numerical solution to the full set of coupled equations showing the solid fraction, ϕ , temperature, θ (solid line), temperature gradient, θ' (dashed line), advective component of the thermal energy equation, G , the vertical velocity, f (solid line) and the horizontal velocity, $-f'$ (dashed line). In plot (b) the dotted lines show the zero level and interface position. Here we use the following parameter values $\phi_B = .2019$, $\mathcal{C} = 1.667$, $W_T = 1.5$, $W_B = 2.6$ and $Pe = 1$.

number. The former method is somewhat less convenient in that it requires the solution to be broken up into two domains and the results are sensitive to the choice of scaling coefficient, c . We have plotted a typical solution in figure (5), comparing the numerical solutions for both approaches in which the best choice for the scaling coefficient is $c = 1$. As we expect the difference in the temperature, volume fraction, vertical velocity and horizontal velocity profiles are very small for the Darcy number $Da = 1 \times 10^{-4}$ chosen for comparison. In this case the transition zone thickness is $\delta = .01$, which is a small fraction of the domain height. By numerical experimentation we found that the discrepancy between the two formulations did indeed decrease with Darcy number but had a lower bound since the liquid layer $(1 - a) \rightarrow 0$ as $Da \rightarrow 0$.

4.2 Diagnostics

In this section we will compare the effect of the four parameters, Da , \mathcal{C} , W_T and W_B on the the mush-liquid interface position, a and the lower boundary solid fraction, ϕ_B . We fix the Peclet number to unity and use the Darcy-Brinkman formulation for consistency.

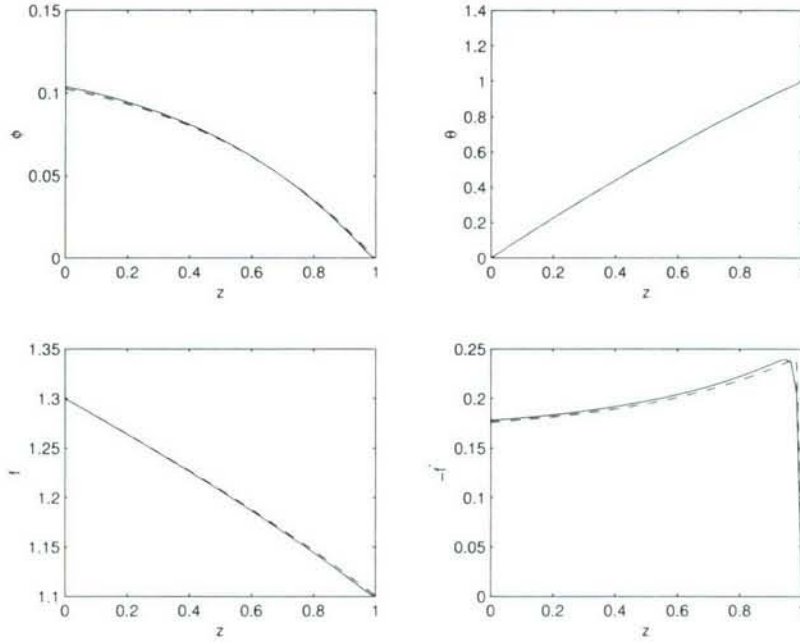


Figure 5: Comparison between the profiles for solid fraction ϕ , temperature θ , vertical velocity f and horizontal velocity f' for the Darcy-Brinkman (solid line) and Stokes-Darcy formulations (Dashed line). Here we have used the following parameter values $\mathcal{C} = 3.333$, $W_T = 1.1$, $W_B = 1.3$, $Pe = 1$ $Da = 1 \times 10^{-4}$ and $c = 1$.

4.2.1 Effect of Da

The Darcy number is a scale for the permeability in that a large Da implies less resistance to the flow and a small Da implies more resistance. Therefore we would expect that as Da decreases the flow rate would also decrease. In our case we have forced a constant velocity at the lower boundary and must conserve mass at any point in our system. The result than of a decrease in Da is to decrease the horizontal pressure gradient in the mush forcing the horizontal velocity to decrease. From figure (6) we see that as Da is made smaller the position of the mush-liquid interface must increase in order to satisfy the tangency condition (10). Since in this case the horizontal velocity is decreasing the streamlines will tend to straighten out and therefore diverge from the tangency condition. Since the vertical velocity must decrease at the end of the channel and a horizontal velocity must exist at some point in the system in order to conserve mass, there will only be sufficient curvature towards the upper boundary.

In the second graph of figure (6) we have plotted the solid fraction profiles $\phi(z)$ for three values of the Darcy number. As a consequence of the horizontal velocity decreasing with Da , the advection of thermal energy becomes smaller near the lower boundary of the mushy layer. From equation (31) we can see that the solid fraction gradient must also decrease in this region and for small Da , ϕ' approaches zero. Away from the lower boundary the horizontal velocity must increase, which leads to larger thermal advection and a steeper solid fraction gradient.

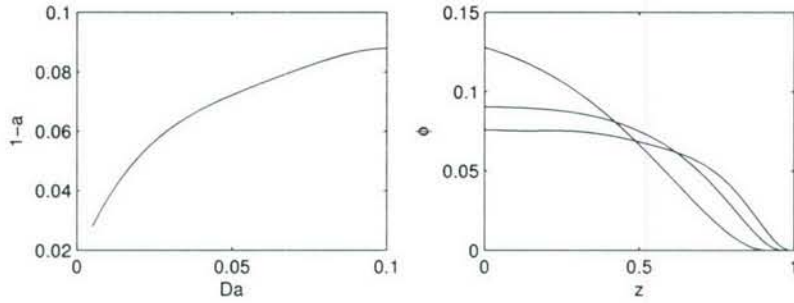


Figure 6: Numerical solution to the full set of coupled equations showing the thickness of the liquid layer (left), $1 - a$ as a function of the Darcy number Da and the solid fraction profiles (right) for $Da = .002, .01$ and $.1$ corresponding to $\phi_B = .077, .09$ and $.128$ respectively. Here the other three parameter values are set to $W_T = 1.1$, $W_B = 1.6$ and $\mathcal{C} = 1.43$.

4.2.2 Effect of \mathcal{C}

The parameter \mathcal{C} is defined as the deviation in the horizontal temperature gradient of the lower boundary m_2 from the upper boundary m_1 and really gives us a measure of the temperature difference in the system. As in the analytic solution of section (3), an increase in \mathcal{C} has the effect of decreasing the thickness of the liquid layer, as seen in figure (7). Since a large value of \mathcal{C} can be thought of as decreasing the temperature of the upper boundary, the average temperature in the system is lower and at steady state the mushy layer must grow further into the channel. In addition we require condition (10) to be satisfied, in which the position of the mush-liquid interface must occur at a point where the isotherms and streamlines are locally tangent. For fixed velocity boundary conditions the streamlines are to leading order independent of \mathcal{C} and we can concentrate on the form of the isotherms as a function of the temperature boundary conditions. As was indirectly indicated to above, the vertical temperature gradient decreases with an increase in \mathcal{C} since the difference in temperature across the channel is decreasing. Because of the form of the streamlines in the channel the position of the tangency point occurs more towards the upper boundary as the isotherms straighten out.

In addition figure (7) shows a plot of the lower boundary solid fraction as a function of \mathcal{C} . As this parameter is increased the thermal gradient decreases, as discussed above, but since the non-dimensional temperature gradient scales with \mathcal{C} , θ' actually increases. As a result of this the thermal advection term in non-dimensional form becomes larger. With reference to equation (31), we can see that in this case the solid fraction gradient increases and with it ϕ_B .

4.2.3 Effect of velocity

The velocity boundary conditions have a strong effect on the structure of the velocity field within the mush and liquid layers and is an important parameter controlling the advective flux of solute and temperature throughout the system. In figure (8) we have plotted the thickness of the liquid layer as a function of the lower boundary velocity W_B for different

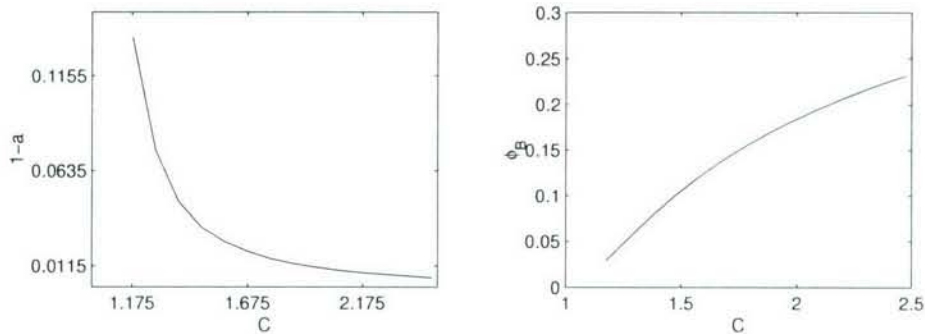


Figure 7: Numerical solution to the full set of coupled equations showing the thickness of the liquid layer (left), $1 - a$ and the lower boundary solid fraction (right), ϕ_B as a function of \mathcal{C} . Here the other three parameter values are set to $W_T = 1.1$, $W_B = 1.6$ and $Da = .01$.

values of the upper boundary velocity W_T . This figure shows that the position of the mush–liquid interface increases with W_B , which is not surprising since we would expect there to be a larger flux of cool fluid from the bottom. In addition a larger lower boundary flux has the effect of increasing the horizontal velocity and stretching the stream lines further down the channel. As a result the mush–liquid interface is driven further upwards in order to both suppress constitutional supercooling and find a point of local tangency between the isotherms and the streamlines. By the same reasoning an increase in W_T will straighten out the streamlines and thus increase the thickness of the liquid layer as shown in figure (8).

Similarly to the discussions in section (4.2.1) and (4.2.2) an increase in lower boundary velocity acts to increase the advective transport of thermal energy. This causes the solid fraction to increase and with it the solid fraction at the lower boundary ϕ_B as shown in figure (8).

5 Conclusion

In this paper we have explored the behavior of a boundary condition originally presented by Schulze and Worster (1999). This condition requires local tangency between the isotherms and streamlines at a mush–liquid interface when the flow is from mush to liquid across a solidifying boundary. The condition naturally occurs along the chimney walls of a mushy layer and requires a two dimensional flow and temperature field to be satisfied. For this reason we constructed a simplified model that has these properties built in but that can be reduced to a one-dimensional problem. The appropriate equations to use for the velocity field within the reactive porous media can be separated into two groups, Darcy and Darcy–Brinkman, which are only equivalent in the limit of a small Darcy number. The first is a two-domain approach that requires a transition zone of order $Da^{\frac{1}{2}}$ to be defined and the second is a continuous domain approach. We solved the governing equations (31)–(32) with either the Stokes–Darcy formulation (35) or the Darcy–Brinkman formulation (38) numerically and compared solutions for both of these formulations. From comparisons of velocity, temperature and solid fraction profiles we discovered, as we expected, that the difference between the two formulations decreased as the Darcy number was made

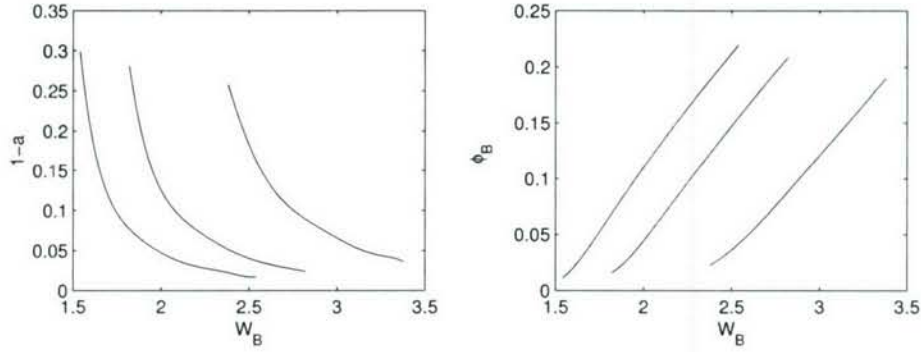


Figure 8: Numerical solution to the full set of coupled equations showing the thickness of the liquid layer (left), $1 - a$ and the lower boundary solid fraction (right), ϕ_B as a function of W_B for $W_T = 1.2, 1.3$ and 1.5 . Here the other two parameter values are set to $\mathcal{C} = 1.43$ and $Da = .01$.

smaller. In addition we used the numerical solution with the Darcy-Brinkman formulation to determine the behavior of the liquid layer thickness, $1 - a$ and the lower boundary solid fraction ϕ_B as a function of the four parameters Da , \mathcal{C} , W_B and W_T . Since a small Darcy number tends to decrease the horizontal velocity within the mushy layer the position of the mush-liquid interface must occur near the upper boundary were mass conservation forces the streamlines to have sufficient curvature in order to satisfy the tangency condition. The lower velocity also decreases the advective transport of the thermal energy near the lower boundary which tends to suppress the solid fraction gradient. In the case of large \mathcal{C} , the thermal gradient decreases and therefore straightens out the isotherms, which results in the point of tangency occurring closer to the upper boundary. Because the non-dimensional form of the temperature is scaled with \mathcal{C} , the non-dimensional temperature gradient increases, resulting in a larger thermal advection term and therefore an increase in ϕ_B . Similarly an increase in the lower boundary velocity W_B results in a larger advection of thermal energy which lengthens out the streamlines. This forces the tangency point to occur further up the channel and increases the solid fraction at the lower boundary.

6 Future Work

The problem presented in this paper has been solved numerically for the steady state case and could lead to a larger study. The next step in the analysis would be to reformulate the equations in terms of enthalpies. Since in this case the temperature and solid fraction are consolidated into a single equation the numerical procedure would be simplified. With this new formulation we could more easily solve the transient problem numerically to gain a better understanding of how the mushy layer evolves with our current setup.

Experiments have found that tributaries form along the chimney walls, most likely due to some instability within the reactive porous medium. We have used our simplified model to examine the initiation of this feature, using linear stability analysis. In this case the basic state is the numerical solutions presented here and we look to see under what conditions the perturbations grow in time. This analysis is still in the beginning stages and still needs

more refining to obtain a reasonable solution.

7 Acknowledgments

I would like to thank Grae Worster for supervising me on this project and Alan Rempel for enlightening conversations on the porch. I would also like to thank all of the staff and fellows for making this a great summer.

References

- [1] M. L. BARS AND M. G. WORSTER, *Interfacial conditions between a pure fluid and a porous medium: implications for binary alloy solidification*, J. Fluid Mech., 550 (2006), pp. 149–173.
- [2] G. K. BATCHELOR, *An introduction to fluid dynamics*, Cambridge University Press., 1967.
- [3] J. BEAR, *Dynamics of Fluids in Porous Media*, Dover, 1972.
- [4] G. S. BEAVERS AND D. D. JOSEPH, *Boundary conditions at a naturally permeable wall*, J. Fluid Mech., 30 (1967), pp. 197–207.
- [5] T. P. SCHULZE AND M. G. WORSTER, *Weak convection, liquid inclusions and the formation of chimneys in mushy layers*, J. Fluid Mech., 388 (1999), pp. 197–215.
- [6] ———, *A time-dependent formulation of the mushy-zone free boundary problem*, J. Fluid Mech., 541 (2005), pp. 193–202.
- [7] M. G. WORSTER, *Convection in mushy layers*, Annu. Rev. Fluid Mech., 29 (1997), pp. 91–122.
- [8] ———, *Solidification of Fluids. In Perspectives in Fluid Dynamics (ed. G.K. Batchelor, H.K. Moffat & M.G. Worster)*, pp. 393–446, Cambridge University Press., 2000.

Arctic catastrophes in an idealized sea ice model

Ian Eisenman

March 15, 2007

Abstract

With recent observations of diminishing summer Arctic sea ice extent, the hypothesis of a “tipping point” in summer ice cover has been the focus of a number of studies. This view suggests that as summer Arctic sea ice cover retreats it will reach a critical point after which the ice–albedo effect will cause the summer ice cover to disappear altogether. We have examined the heuristic argument behind this hypothesis using an idealized, but observationally constrained, model of Arctic sea ice with representations of ice and ocean mixed layer thermodynamics, varying open water fraction, an energy balance atmosphere, and scalable CO_2 . We find that summer ice cover retreats toward an ice-free summer ocean at an accelerating rate in a scenario with exponentially increasing CO_2 . However, we find no critical CO_2 concentration or “tipping point” using observationally based parameter values. We identify in the extended parameter space a bifurcation associated with multiple summer ice cover states and a cusp catastrophe, and we find that it occurs far from the physically realistic parameter regime. Our results suggest that the argument for a “tipping point” in summer Arctic ice cover brought on by ice albedo may not hold up when quantified. The reason is related to the fact that ice cover has only just begun to retreat at the time of maximum sunlight (June), and the minimum ice area occurs in September when there is very little Arctic sunlight.

1 Introduction

The retreat of summer sea ice cover in the Arctic is one of the most dramatic signals of recent climate change. While winter ice cover has remained fairly constant, summer ice extent has diminished significantly during the past few decades (Fig. 1), with annual minimum extent shrinking by 20% between 1979 and 2005 [34]. The high sensitivity of Arctic sea ice cover is believed to be related to the difference in albedo (i.e., reflectiveness) between sea ice and the open water that is exposed when it melts. Bare or snow-covered sea ice reflects most sunlight back to space, while the dark ocean surface absorbs most incident light. Global climate models have long predicted reduced Arctic sea ice cover as an amplified response to global warming (e.g., Manabe and Stouffer [15]), prompting speculation more than a decade ago about the use of Arctic ice observations to provide an early indicator of climate change [35].

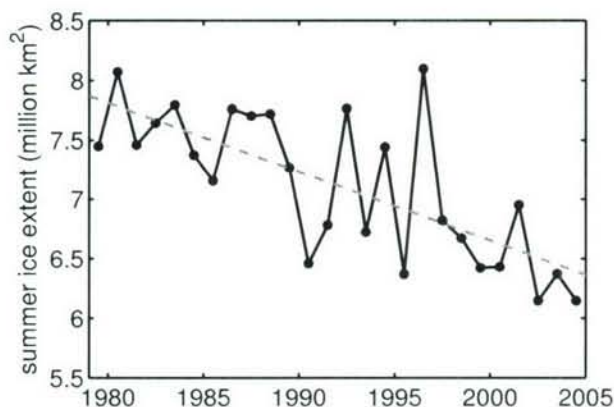


Figure 1: Diminishing Northern Hemisphere summer sea ice extent based on satellite observations [3]. Ice extent is defined as the area of grid boxes with ice concentration of at least 15%, and September monthly mean values are plotted (note that September is the month of minimum ice cover). The gray dashed line indicates a linear fit.

The ice–albedo effect could potentially lead to multiple states, and scientists have long conjectured that the Arctic might support a second stable state under current climate forcing which is at least seasonally ice-free (e.g., Ewing and Donn [5]). Heuristically, one might indeed expect that ice-free and ice-covered stable states could exist, separated by an unstable state in which the Arctic is partially covered by ice and absorbs just enough sunlight to maintain the ice edge at the freezing temperature: adding a slight amount of additional ice to this intermediate state would lead to less solar absorption, cooling, and hence further expanded ice cover. As the background climate is warmed, the unstable state would require more and more ice so that it reflects enough sunlight for the ice edge to remain at the freezing temperature. This warming could be caused by rising greenhouse gas levels, for example, or by some mechanism leading to increased heat transport into the Arctic. At a particular level of warming, the background climate would become so hot that the Arctic ocean would remain above the freezing point even if it were fully covered with ice. At this point the stable ice-covered state and unstable intermediate state would merge and disappear in a saddle-node bifurcation, leaving only the ice-free state. This scenario suggests that if the Arctic were in the ice-covered state and climate were warmed beyond the bifurcation point, it would make a rapid and irreversible transition to the ice-free state, exhibiting behavior which is described mathematically as a catastrophe.

In light of the continued recent retreat of summer Arctic sea ice cover [29], the idea that we may be approaching a threshold has been receiving a tremendous amount of attention in the popular press. Often employing the term made popular by the title of Malcolm Gladwell’s bestselling sociological treatise *The Tipping Point* (2000), widespread speculations have suggested that the ice–albedo effect may cause an otherwise gradual global warming to pass a point of no return, beyond which the Arctic would rapidly approach a state which is ice-free each summer. The cover of the 3 April 2006 issue of *Time Magazine* suggests in large bold letters: “Be Worried. Be Very Worried.... Earth at the tipping point.” Diminishing Arctic sea ice is a major focus of the cover story. A news feature in *Nature* on 15

June 2006 titled “The tipping point of the iceberg” discusses the increasing interest in the idea of tipping points in the climate system. The article states that among several plausible tipping points under discussion, Arctic sea ice has received the most recent attention. It reports that 234 newspaper articles mentioned a tipping point in connection with climate change during the first five months of 2006, a stark increase from 45 such articles in 2004.

In the scientific literature, discussions about a bifurcation point in summer sea ice are slightly less abundant, but several recent papers speculate about it. Lindsay and Zhang [14] write, “The late 1980s and early 1990s could be considered a tipping point during which the ice-ocean system began to enter a new era of thinning ice and increasing summer open water because of positive feedbacks. It remains to be seen if this era will persist.... However, at this point we can only state the tipping point as a hypothesis.” This is based on forcing an ice-ocean model with atmospheric observations and finding significantly increased heat absorption since the 1980s associated with ice albedo; they do not actually look for hysteresis. Overpeck et al [25] conclude that the arctic appears to be heading on “a trajectory to a new, seasonally ice-free state” because of the ice–albedo feedback. They add, “The processes and interactions among primary components of the Arctic system, as presently understood, cannot reverse the observed trends toward significant reductions in ice”, implying that the system has passed a bifurcation point and ice will continue to decrease until it arrives at a new state. Serreze and Francis [28] speculate about similar bifurcation behavior: “We are likely near the threshold when absorption of solar radiation during summer limits ice growth the following autumn and winter, initiating a feedback leading to a substantial increase in Arctic Ocean surface air temperatures.” These papers do not actually claim that there is a “tipping point”. Rather, they express it as a hypothesis and discuss its plausibility.

It is not at all obvious, however, that the ice–albedo effect would lead to multiple Arctic sea ice states and hence allow for the possibility of a catastrophe. There are many stabilizing feedbacks in the Arctic climate system. Perhaps the most important of these in the context of sea ice is the fact that thin ice grows considerably more rapidly than thick ice. For example, Untersteiner [33] gives an annual increase in thickness of 0.8m for ice that is 0.6m thick at the start of the growing season, but an increase of only 0.2m for ice that is initially 2.2m thick. Furthermore, if there were a second stable state that is at least seasonally ice-free, it would seem likely that both states would have been explored by the climate system in the past during the significant variability associated with glacial cycles. But most paleoclimate reconstructions suggest that there was year-round Arctic sea ice for at least the past million years (e.g., Moran et al [21]).

In this project, we have attempted to quantitatively investigate the plausibility of a catastrophe in summer Arctic sea ice cover. One possible approach for such an inquiry would be to employ the sophisticated global climate models which are used to predict future climate change. As described in Section 2, however, these models disagree markedly in their simulations of Arctic sea ice changes in a warming climate. Instead, we have approached the problem by constructing an idealized model of the coupled Arctic ice-ocean-atmosphere system. The model is physically stripped down to essentials, but it is observationally constrained and includes all the ingredients in the heuristic argument for multiple summer ice cover states brought on by the ice–albedo effect. To that extent, a positive result would imply only the plausibility of a “tipping point”, but a negative result provides a somewhat

stronger refutation. The model is described in Section 3. It is an extension of the Arctic sea ice and atmosphere model of Thorndike [31] with additions to allow for partial ice cover, an ocean mixed layer which is always active, a simple parameterization of ice dynamics, scalable CO_2 , and a change in the treatment of atmospheric heat transport which is expected to be more realistic in climate states that may be very different from today. The model is represented by four coupled ordinary differential equations that evolve ice volume, ice area, ice surface temperature, and ocean mixed layer temperature. These equations have thresholds at the freezing temperature for the ice surface and ocean mixed layer, as well as a threshold in the evolution of ice area associated with whether the ice volume is decaying.

The model results are described in Section 4. We begin by examining the model solution in the parameter regime representing the climate today. We find only one sea ice state, in contrast to the “tipping point” hypothesis. An exponential increase in CO_2 leads to retreating summer ice cover at an accelerating rate. When CO_2 is increased somewhat beyond the point where the ocean becomes ice-free each summer, the Arctic continues to be completely ice-covered every winter. When CO_2 is further increased, however, this seasonally ice-covered state gives way to a state which is ice-free year-round. Only at this point do multiple states exist: for a range of CO_2 values, both seasonal ice cover and ice-free year-round states are possible, leading to a fold catastrophe in winter ice cover as CO_2 is varied.

This suggests that the stabilizing effect of the growth-thickness relation may quantitatively outweigh the ice–albedo effect. To quantify the extent to which the former dominates in this model, we explore the parameter space in search of a region with multiple summer ice cover states. We find such a region, bounded by a saddle-node bifurcation of cycles, when we significantly reduce the latent heat of sea ice fusion. An investigation of the cusp catastrophe in CO_2 –latent heat parameter space reveals that the actual Arctic appears to be far from the region where CO_2 changes can cause a “tipping point” in summer sea ice cover.

Concluding remarks and caveats regarding limitations of the idealized model are discussed in Section 5.

2 Arctic sea ice changes predicted by global climate models

Sophisticated global climate models (GCMs) have been used extensively to predict future climate change associated with increasing levels of atmospheric CO_2 . About two dozen of these models are being evaluated for the incipient Fourth Assessment Report (AR4) of the Intergovernmental Panel on Climate Change (IPCC). The models typically have horizontal resolutions of 1° to 4° in the ocean component and similar equivalent spectral resolutions in the atmospheric component; the atmosphere and ocean components each typically have 10 to 50 vertical layers. All of the GCMs include representations of sea ice, with varying levels of complexity in the sea ice models.

A possible approach to address the plausibility of a catastrophe in summer Arctic sea ice cover would be to increase CO_2 in one of these GCMs, continue the simulation until the model is sufficiently spun up, and then decrease CO_2 and look for hysteresis in the ice cover. This hysteresis would imply a bifurcation or “tipping point”. The simulation would be rather computationally intensive, as it would likely take more than 1000 simulation years

to sufficiently reach a steady state for the elevated CO₂ value.

The first 100 years of a similar experiment has already been evaluated with many of these GCMs for the Special Report on Emission Scenarios (SRES) A1B scenario, which is one of the CO₂ future emission scenarios investigated in the IPCC AR4. The IPCC AR4 Model Output Database at the Lawrence Livermore National Laboratory Program for Climate Model Diagnosis and Intercomparison currently has ice cover data for the “Climate of the 20th Century” and “SRES A1B” experiments from 16 of the models. We acquired the monthly gridded data from Run 1 for each of these experiments and computed the time series of total Northern Hemisphere sea ice extent by summing the area of grid boxes with ice concentration greater than 15%. The 16 models are as follows: BCCR BCM2 (Norway), CGCM3.1 T47 (Canada), CGCM3.1 T63 (Canada), CNRM CM3 (France), CSIRO Mk3 (Australia), ECHAM5 (Germany), GISS AOM (United States), GISS ER (United States), HadCM3 (United Kingdom), HadGEM1 (United Kingdom), INM CM3 (Russia), IPSL CM4 (France), MIROC3.2 low resolution (Japan), MIROC3.2 high resolution (Japan), MRI CGCM 2.3.2a (Japan), and NCAR CCSM3.0 (United States).

The average seasonal cycle in Northern Hemisphere ice extent during 1980-1999 for each of the 16 models is plotted in the top panel of Fig. 2. Ice extent during the same period computed from ice concentration measurements derived by Cavalieri et al [3] from satellite observations is included for comparison. The agreement between models and observations is decent (cf. Parkinson et al [26]): observed ice extent varies between 6 and 16 million km² during the seasonal cycle, and the intermodel spread is roughly ± 3 million km² (although it is slightly greater than this during summer).

Predicted Northern Hemisphere summer minimum sea ice extent during 2000-2100 for the “SRES A1B” experiment varies widely between the models. While the MIROC3.2 high resolution model simulates an ice-free summer Arctic starting in 2030, GISS ER simulates that in 2100 summer ice cover will be reduced by only 15%. The other models fill the space of predictions in between. It should be noted that these GCMs show better agreement in their predictions of future global mean temperatures, which is the result typically receiving the most attention. This formidable intermodel spread in simulated ice cover discourages the use of GCMs to assess the possibility of a future catastrophe in Arctic sea ice cover. It motivates an approach using an idealized model with more transparent physics, which is the method pursued in this report.

In a related project carried out this summer (Eisenman, Untersteiner, and Wettlaufer, *in prep*), we used an idealized model to examine the possibility that the spread in IPCC AR4 sea ice predictions is related to the sea ice models in the GCMs having been tuned to simulate observationally reasonable ice cover today, despite a large spread in simulated Arctic cloudiness which would otherwise lead to widely differing simulated present ice cover. The detailed results of the project have been left out of this report for brevity.

3 Model description

Here the idealized model of the coupled Arctic sea ice, ocean, and atmosphere used in this project is described. It is an extension of the model of Thorndike ([31], hereafter T92), which is a single-column model with representations of vertical sea ice thermodynamics and a thermal radiative balance atmosphere. When the ice melts to zero thickness in

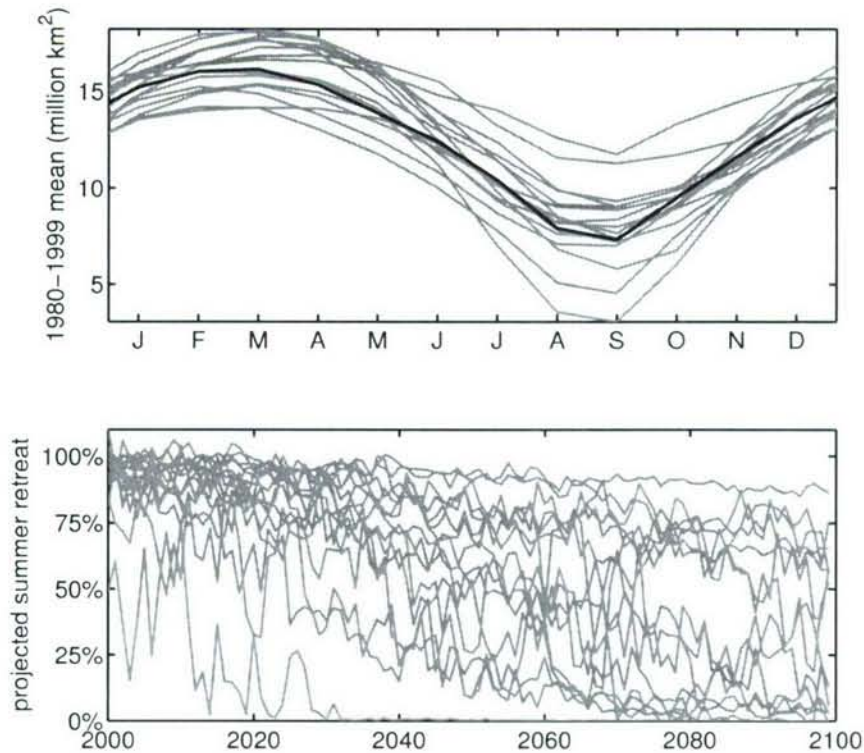


Figure 2: Simulated Northern Hemisphere sea ice extent in 16 IPCC AR4 GCMs. (Top panel) Average seasonal cycle during 1980-1999 from “Climate of the 20th Century” experiment. Ice extent derived from satellite observations during the same period is indicated by a black line. Note the decent agreement between models and observations. (Bottom panel) Predicted decrease in annual minimum monthly mean ice extent during 2000-2100 from “SRES A1B” experiment. Minimum extent is plotted for each model as a percent of the minimum in the 1980-1999 mean seasonal cycle. The intermodel spread is formidable, discouraging the use of GCMs to assess the possibility of a future ice catastrophe and motivating the use of an idealized model.

Thorndike’s model, a thermodynamic ocean mixed layer is evolved until it reaches the freezing temperature, at which point sea ice begins to form again. Thorndike’s model displays two stable states. One is state ice-covered year-round and the other is ice-free year-round. A third state also exists with seasonal ice cover, but it is unstable.

The model used here is extended to allow partial ice cover, which requires an ocean mixed layer which is always in communication with the atmosphere unless the ocean is completely ice-covered. The ice area is evolved using a methodology based on Hibler [10]. A simple parameterization of ice dynamics is included. The atmosphere used here is nearly identical to Thorndike’s, except that CO_2 can be varied and meridional heat transport into the model domain depends on the implied meridional temperature gradient rather than being specified at a constant value.

The state variables (Table 1) are ice volume, ice area, ice surface temperature, and ocean mixed layer temperature. Their evolution is represented by four ordinary differential

Table 1: Model state variables.

V	Ice volume divided by area of box (units of m).
A	Ice area (fraction of box covered by ice).
T_i	Ice surface temperature ($^{\circ}\text{C}$).
T_{ml}	Ocean mixed layer temperature ($^{\circ}\text{C}$).

equations with thresholds associated with the freezing temperature of the ice surface and ocean mixed layer, as well as a threshold in the evolution of ice area associated with whether the ice volume is growing or decaying. The physical derivation of these equations is described below.

3.1 Sea ice

3.1.1 Ice thermodynamics

Here we discuss the derivation of the idealized thermodynamic equations in T92, which have been used in this model, starting from the fundamental conservation law for heat transport in a two-phase, two-component system. We discuss the equations of Maykut and Untersteiner [19] as an intermediate step.

As sea ice grows, differences in the rates of diffusion of heat and salt in seawater give rise to a region adjacent to the ice-water boundary where the water is constitutionally supercooled. This triggers morphological instability of the interface: perturbations to a planar interface grow because they protrude into the constitutionally supercooled region. Due to this effect, sea ice develops a lamellar solid-liquid interface characterized by millimeter-scale blades of ice with brine filling the narrow spaces between them. This is in contrast to the more familiar situation of lake ice, which experiences none of these salinity-related phenomena and grows with a planar solid-liquid interface.

At thermodynamic equilibrium, the interstitial brine in sea ice is at the freezing temperature, maintaining the same temperature as the ice crystals immersed in it. As explained by Maykut and Untersteiner [19], a rise in temperature causes ice crystals to melt until the brine is diluted sufficiently to raise its freezing point to the new temperature. Hence the heat capacity of a slab of sea ice is different from that of a simple solid: the brine pockets serve as a thermal reservoir, enhancing the effective heat capacity.

This suggests a treatment of sea ice in which quantities are averaged over regions containing both ice and interstitial brine. A region of mixed phase for a two-component fluid (here salt and water) is called a mushy layer. Sea ice thermodynamics can thus be described as a problem of vertical heat conduction in a mushy layer with the upper boundary condition determined by the balance of surface fluxes.

The mushy layer equation for conservation of heat can be written (Worster [36], equation 6.20)

$$c_m \frac{\partial T}{\partial t} + c_b \mathbf{u} \cdot \nabla T = \nabla \cdot (k_m \nabla T) + \mathcal{L} \frac{\partial \phi}{\partial t} + A_R \quad (1)$$

where T is the mushy layer temperature, ϕ is the solid fraction (i.e., fraction of the volume which is ice), \mathcal{L} is the latent heat of fusion per unit volume (proportional to the difference in

enthalpy between brine and ice), and A_R represents the absorption of solar radiation that has passed through the surface of the ice. Here the mean volumetric specific heat capacity, $c_m = c_i\phi + c_b(1 - \phi)$, is related to the volumetric specific heat of ice (c_i) and brine (c_b). The mean thermal conductivity of the mushy layer is approximated to be $k_m = k_i\phi + k_b(1 - \phi)$, where k_i and k_b are the thermal conductivities of pure ice and brine; this relationship is exact if the ice lamellae are oriented parallel to the heat flux, which is a good approximation for sea ice. Note that in (1) we have corrected the typographical error (verified via personal communication with Grae Worster) in the factor multiplying the advective term in Worster [36] equation 6.20.

Feltham et al [6] showed that under certain physical assumptions the mushy layer conservation equation (1) reduces to the temperature diffusion equation in the model of Maykut and Untersteiner [19], which most current models of sea ice thermodynamics are based on. Here we present a brief summary of the derivation in Feltham et al. Assuming local thermodynamic equilibrium (i.e., brine is at freezing temperature) and a linear liquidus relationship (i.e., linear dependence of brine freezing temperature, T_L , on brine salinity, S), we can relate the temperature to the brine salinity as

$$T = T_L(S) = T_L(0) - \Gamma S. \quad (2)$$

We introduce the bulk salinity, $S_{bulk} = (1 - \phi)S$, using the assumption that the concentration of salt incorporated into the ice crystals is negligible compared to the brine salinity. This allows us to write the solid fraction ϕ in terms of brine salinity and hence, by (2), in terms of temperature:

$$\phi = -\frac{\Gamma S_{bulk}}{\theta}. \quad (3)$$

Here we have defined $\theta \equiv T - T_L(0) = T - 273^\circ\text{C}$.

Maykut and Untersteiner [19] use a prescribed time-independent vertical salinity profile for S_{bulk} , neglect brine flow ($\mathbf{u} = 0$), and consider temperature variations in the vertical only. Under these assumptions, (1) becomes

$$c_{\text{eff}} \frac{\partial T}{\partial t} = \frac{\partial}{\partial z} \left(k_{\text{eff}} \frac{\partial T}{\partial z} \right) + A_R. \quad (4)$$

with $c_{\text{eff}} \equiv c_m - \mathcal{L} \frac{d\phi}{d\theta}$ and $k_{\text{eff}} \equiv k_m$. Inserting (3) and the definitions of c_m and k_m , the effective mushy layer heat capacity and conductivity can be written

$$c_{\text{eff}} = c_i - \frac{\Gamma S_{bulk}}{\theta} (c_b - c_i) + \mathcal{L} \frac{\Gamma S_{bulk}}{\theta^2} \quad (5)$$

and

$$k_{\text{eff}} = k_i - \frac{\Gamma S_{bulk}}{\theta} (k_b - k_i). \quad (6)$$

Equations (5) and (6) are equivalent to Feltham et al [6] equations 14 and 15 (with their equation 14 corrected for a typographical error, verified by personal communication with Danny Feltham, in the sign of the second term).

Approximate formulas for effective heat capacity and conductivity were derived by Untersteiner [32]. Because they were found to be in good agreement with the theoretical

expressions of Schwerdtfeger [27] and Ono [24], they were used by Maykut and Untersteiner [19]. Feltham et al [6] demonstrate that sea ice heat capacity and conductivity obtained by Schwerdtfeger [27] are identical to the mushy layer result (5)-(6) when \mathbf{L}/ρ_i is assumed constant, the conductivity of bubbly ice is assumed equal to k_i , the volumetric heat capacity of pure water is assumed equal to c_b , and the densities of pure water, pure ice, and sea ice are all assumed equal.

The equation in Maykut and Untersteiner [19] describing the evolution of the temperature profile (their equation 6) has capacity and conductivity terms with parameters multiplying powers of temperature and salinity in identical form to (5)-(6), with the exception that they do not have the S_{bulk}/θ term in (5). By illustrating this equivalence, Feltham et al [6] demonstrate that these terms in the thermodynamic model of Maykut and Untersteiner [19] are firmly grounded in the physics of mushy layers, thereby showing exactly how the terms account for both the fractional inclusion of brine pockets and the energy associated with phase change when this fraction evolves.

Maykut and Untersteiner [19] use a scaling argument to neglect the vertical derivative of k_{eff} , simplifying (4) to

$$c_{\text{eff}} \frac{\partial T}{\partial t} = k_{\text{eff}} \frac{\partial^2 T}{\partial z^2} + A_R. \quad (7)$$

They specify seasonally varying snowfall and include a layer of snow above the ice in which temperature evolves according to

$$c_{\text{snow}} \frac{\partial T}{\partial t} = k_{\text{snow}} \frac{\partial^2 T}{\partial z^2} + A_R. \quad (8)$$

In this layer, unlike in the mushy sea ice, the volumetric heat capacity (c_{snow}) and conductivity (k_{snow}) are constant parameters. The boundary condition at the upper surface, $z = h_T$, is a flux balance when the ice is below the freezing temperature and a Stefan condition for surface melt otherwise:

$$k_{\text{snow}} \left[\frac{\partial T}{\partial z} \right]_{h_T} - F_{\text{top}} = \begin{cases} 0 & T(h_T) < 0^\circ\text{C} \\ L \frac{dh_T}{dt} & T(h_T) = 0^\circ\text{C} \end{cases} \quad (9)$$

where L is the latent heat of fusion of the surface material and F_{top} represents the sum of sensible, latent, downward and upward longwave, and shortwave heat fluxes at the surface. All but the upward longwave flux are specified in their model based on observations. The fluxes balance at the snow-ice interface ($z = h_{si}$):

$$k_{\text{snow}} \left[\frac{\partial T}{\partial z} \right]_{h_{si}^+} = \left[k_{\text{eff}} \frac{\partial T}{\partial z} \right]_{h_{si}^-}. \quad (10)$$

At the base of the ice layer, $z = h_B$, a Stefan condition for ice growth or melt is applied:

$$- \left[k_{\text{eff}} \frac{\partial T}{\partial z} \right]_{h_B} - F_{\text{bot}} = -L \frac{dh_B}{dt}. \quad (11)$$

Here F_{bot} is the flux from the ocean mixed layer into the base of the ice, which is a specified constant. Note from (9) and (11) that Maykut and Untersteiner evolve the upper and lower

surfaces of the ice, h_T and h_B , separately. The actual predicted ice and snow thicknesses are $h_{ice} = h_{si} - h_B$ and $h_{snow} = h_T - h_{si}$.

The thermodynamic sea ice model of Maykut and Untersteiner [19] is summarized by (7)-(11). They solved it numerically on a 10cm vertical grid with 12 hour time steps using a \$3 million 1960s IBM mainframe computer.

The simplified thermodynamic equations in T92 can be derived from (7)-(11) by neglecting snow and sensible and latent surface heat fluxes, assuming the sea ice effective heat capacity and conductivity to be independent of temperature and salinity ($c_{eff}(T, S) = c$, $k_{eff}(T, S) = k$), approximating all shortwave radiation to be absorbed at the upper surface ($A_R = 0$), and applying the quasi-stationary approximation to the diffusion equation (7). This leads to equations for the evolution of surface temperature T_i and ice thickness $h \equiv h_T - h_B$. The quasi-stationary approximation, which is based on assuming a large Stefan number $S \equiv L/(c_p \Delta T)$, allows the left hand side of (7) to be integrated with the assumption of a linear temperature profile:

$$\int_{h_B}^{h_T} dz \left(c \frac{\partial T}{\partial t} \right) = c \int_{h_B}^{h_T} dz \left(\frac{\partial}{\partial t} \left(\frac{z - h_B}{h_T - h_B} T_i \right) \right) = \frac{ch}{2} \frac{dT_i}{dt}. \quad (12)$$

This leads to an integrated version of the diffusion equation (7),

$$\frac{ch}{2} \frac{dT_i}{dt} = k \left[\frac{\partial T}{\partial z} \right]_{h_T} - k \left[\frac{\partial T}{\partial z} \right]_{h_B}. \quad (13)$$

Inserting into (13) the boundary conditions (9) and (11) leads to two sets of equations depending on whether or not the surface is melting. In either case, the linear internal temperature gradient is used for the lower boundary term ($k [\partial T / \partial z]_{h_B} = kT_i/h$) because of the Stefan condition at the edge, and the lower boundary condition (11) becomes

$$-L \frac{dh_B}{dt} = -k \frac{T_i}{h} - F_{bot}. \quad (14)$$

When $T_i < 0^\circ\text{C}$, the first upper boundary condition in (9) gives $k [\partial T / \partial z]_{h_T} = F_{top}$. Inserting this into (13) and using $dh/dt = d/dt (h_T - h_B) = -dh_B/dt$ in (14) leads to

$$\frac{ch}{2} \frac{dT_i}{dt} = F_{top} - kT_i/h, \quad (15)$$

$$L \frac{dh}{dt} = -k \frac{T_i}{h} - F_{bot}. \quad (16)$$

When $T_i = 0^\circ\text{C}$, the Stefan condition at the upper edge leads to the use of the internal temperature gradient for the upper boundary term, $k [\partial T / \partial z]_{h_T} = kT_i/h$. Using the second upper boundary condition in (9), $Ldh_T/dt = kT_i/h - F_{top}$, (13) and (14) become

$$\frac{dT_i}{dt} = 0, \quad (17)$$

$$L \frac{dh}{dt} = -F_{top} - F_{bot}. \quad (18)$$

Thorndike [31] separates the sea ice seasonal cycle into discrete steps representing cooling, growing, warming, and melting. He uses (15)-(16) during growing and (17)-(18) during melting, and during the warming and cooling steps he uses equations to evolve T_i and h which are equivalent to letting $dh_B/dt = 0$ in the lower boundary condition (11).

In the model presented here, we use a continuously evolving seasonal cycle, using (15)-(16) or (17)-(18) depending on whether $T_i < 0^\circ\text{C}$. Because we allow partial ice cover, unlike in the models of Maykut and Untersteiner [19] and Thorndike [31], we evolve ice volume rather than ice thickness. In the ice-covered fraction of the model domain A , this vertical thermodynamic growth of the ice is represented by re-writing (16) and (18) as

$$L \frac{dV}{dt} = A \left(-k \frac{T_i}{h} - F_{bot} \right), \quad (19)$$

and

$$L \frac{dV}{dt} = A (-F_{top} - F_{bot}). \quad (20)$$

3.1.2 Evolution of ice area

T92 describes the entire Arctic by a single ice thickness, using a thermodynamic ocean mixed layer model which becomes active only when all the ice melts. In the model used here, an open water fraction is included. When the open water fraction is small, it describes the area of the Arctic covered by leads; when it is large, it describes extended regions of open water.

While the thermodynamic sea ice equations in this model are derived from fundamental physics, the area evolution is based on the observationally motivated methodology of Hibler [10]. Hibler introduced this methodology to evolve ice concentration (fraction of grid covered by ice) in each model grid box, allowing models to account for the presence of subgrid-scale leads. Many of the GCMs today with the most sophisticated sea ice representations include similar parameterizations of subgrid-scale leads and thickness distributions based on this methodology. The box model used here effectively includes a single grid box, so Hibler's methodology can be similarly applied to the ice area in this box.

It should be noted that the open water fraction in this model, as in Hibler [10] and similar models, is not meant to represent a truly ice-free region. Rather, the model domain is split into a fraction containing thick ice, with the rest covered by a mixture of exposed ocean and thin ice as in observed leads. The volume of this thin ice is assumed to be negligible compared to the thick ice volume.

Hibler [10] presents a dynamic model in which the thermodynamic sea ice growth rate is specified as a function of ice thickness and season, and concentration grows based on the growth rate for zero-thickness ice. Here the thermodynamics are computed, and concentration increases when T_{ml} reaches zero and tries to keep cooling: the mixed layer flux imbalance F_{ni} goes to making new ice volume as

$$\frac{dA}{dt} = \frac{F_{ni}}{Lh_0}. \quad (21)$$

As in Hibler, an equivalent thickness h_0 must be assigned to the new volume to give it a horizontal area. This parameter controls the rate at which ice cover grows; it is not to be viewed literally as the typical thickness of new ice.

Area grows only when the mixed layer freezes; when the Stefan condition at the ice base leads to volume growth, the ice grows vertically downward and area remains fixed.

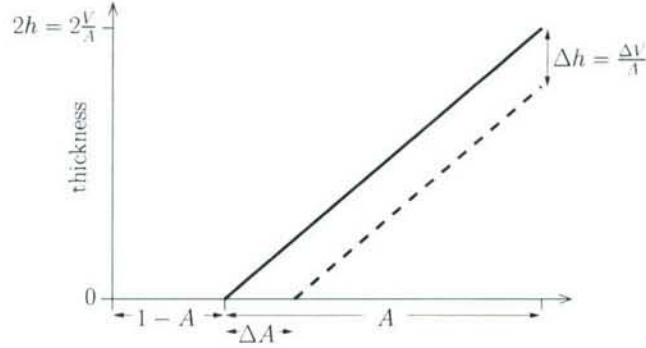


Figure 3: Schematic illustrating the proportionality between the rate of change of ice area and the thermodynamic decrease of volume. This methodology follows Hibler [10].

Area decays, however, when volume is thermodynamically lost. Following the treatment in Hibler, when $\frac{dV}{dt} < 0$ area decreases as

$$\frac{dA}{dt} = \frac{A}{2V} \frac{dV}{dt}. \quad (22)$$

The proportionality between volume and area rates of change is based on an argument in Hibler about the ice thickness distribution in the model domain. Assume that the ice is distributed evenly in thickness between 0 and $2V/A$. This gives a mean thickness of V/A . (Note, however, that in both Hibler’s model and the model presented here the thermodynamic growth of ice is a nonlinear function of thickness and is computed under the assumption that all ice is of the mean thickness V/A , rather than using an even distribution between 0 and $2V/A$.) It is assumed that all ice in the 0 to $2V/A$ distribution melts at the same rate. Hence the rate of area decay is given by the rate of thickness decay times the inverse slope of the thickness distribution

$$\Delta A = \Delta h \frac{dA}{dh} = \frac{\Delta V}{A} \frac{A}{2V/A} = \frac{A}{2V} \Delta V. \quad (23)$$

This is illustrated schematically in Fig. 3.

Note that new ice area forms at $T_i = 0$, hence increasing the subzero ice surface temperature when area is expanding during the growing season. This would add the term $-(T/A)dA/dt$ to dT/dt . Since T typically changes between 0° and 30°C while A evolves between 0.75 and 1, $(1/T)dT/dt$ tends to be far larger than $(1/A)dA/dt$, and the term is expected to be insignificant and has been neglected.

Dynamics are represented in the model by requiring that $A \leq 0.95$ (because of the constant convergence and divergence of the wind field) and by imposing a net annual export of 10% of the ice area based on observations of Kwok et al [13]. The latter adds the terms $-v_0 A$ and $-v_0 V$ to the area and volume evolution equations.

3.2 Atmosphere

3.2.1 Radiative equilibrium

The model has a gray-body thermal equilibrium atmosphere, as in T92 (cf. Goody and Yung [9], Section 9.2), which is used to compute the downward longwave radiation at the surface as a function of the surface temperature. To find this relationship it is necessary to derive the full atmospheric vertical profiles of temperature and downward and upward propagating longwave radiation. The atmosphere is assumed to be transparent to shortwave (solar) radiation. A poleward atmospheric heat transport into the Arctic, D , is accounted for in the model.

With longwave extinction coefficient $\kappa(z)$ and atmospheric density $\rho(z)$, the amount of upward propagating longwave F_{UP} at a given height can be found using $dF_{UP}/dz = \rho(z)\kappa(z)F_{UP}(z)$. This can be solved for intensity as a function of height,

$$F_{UP}(z) = F_{UP}(0) \exp\left(\int_0^z \rho\kappa dz'\right) = F_{UP}(0) \exp(\eta(z)), \quad (24)$$

where $F_{UP}(0)$ is longwave radiated from the surface. Here we have defined the optical height, $\eta(z) \equiv \int_0^z \rho\kappa dz'$. An advantage of measuring height using η instead of z is that $\kappa(z)$ and $\rho(z)$ drop out of the equations and the atmosphere can be described by a single parameter, the total optical thickness $N \equiv \eta(\infty)$. Physically, an optical thickness of N means that a longwave photon typically passes through $1/N$ of the atmosphere before being absorbed.

The longwave radiation from the surface can be linearized in surface temperature, T_s , about the freezing temperature, $T_s = 0^\circ\text{C}$:

$$F_{UP}(0) = \sigma(T_s + 273\text{K})^4 \approx a + bT_s. \quad (25)$$

Here T_s is assumed to be measured in $^\circ\text{C}$.

The atmosphere is absorbing and reradiating longwave radiation at all heights. The intensity of downward radiation from the atmosphere above is given by $F_{DN}(\eta)$, which must be zero at the top of the atmosphere:

$$F_{DN}(N) = 0. \quad (26)$$

The amount of radiation absorbed by a layer of thickness $d\eta$ is $(F_{UP}(\eta) + F_{DN}(\eta)) d\eta$. We assume the poleward heat transport is distributed evenly in optical height, so each layer gains $D/Nd\eta$ of heat from this advection. The longwave radiation from a given layer is given by $2R(\eta)d\eta$, where $R(\eta) = a + bT(\eta)$ and the factor of 2 accounts for radiation from the top and bottom of the layer. In thermodynamic equilibrium, this leads to

$$F_{UP}(\eta) + F_{DN}(\eta) + \frac{D}{N} = 2R(\eta). \quad (27)$$

The fluxes vary in height because of absorption and reradiation:

$$\frac{dF_{UP}(\eta)}{d\eta} = -F_{UP}(\eta) + R(\eta), \quad (28)$$

$$\frac{dF_{DN}(\eta)}{d\eta} = F_{DN}(\eta) - R(\eta). \quad (29)$$

Equations (27)-(29) are a system of one algebraic and two differential equations. They can be solved using the boundary conditions (25)-(26) to give R , F_{UP} , and F_{DN} at all heights η . The only part of the solution which is needed for the model is the dependence of the downward longwave radiation at the surface on surface temperature, which is found to be

$$F_{DN}(0) = (a + bT_s) \frac{N}{2 + N} + \frac{D}{2}. \quad (30)$$

3.2.2 Seasonal cycle

The seasonal cycle in this model is forced by varying specified shortwave radiation F_{sw} , atmospheric optical thickness N , and 0–70°N temperature which is used to compute the poleward heat transport D (described in Section 3.2.3). T92 uses a step-function seasonal cycle, with summer values of N and F_{sw} for half the year and winter values for the other half. This allows him to arrive at a closed form analytical solution to the model equations. We solve the equations numerically, and hence we can use a continually varying seasonal cycle.

Maykut and Untersteiner [19] force their model with specified shortwave forcing based on observations of solar radiation incident at the surface. The values differ significantly from the astronomically constrained top-of-the-atmosphere radiation, because the transmissivity of the Arctic atmosphere is typically only 40–70% [17]. We forced the model with a non-negative sine-wave approximation to the monthly mean data used by Maykut and Untersteiner (Fig. 4).

The optical thickness is higher during summer than winter because of increased cloudiness. T92 tuned the values of N to simulate a seasonal cycle in ice thickness similar to the more complicated model of Maykut and Untersteiner [19]; although the choice of N values was motivated by matching $F_{DN}(0)$ with observed surface downward longwave flux, using summer and winter values of N which better match the cited $F_{DN}(0)$ observations (and simulated surface temperature) cause all the ice to melt in the model of T92 for any initial condition (not shown). The requirement that N be tuned to some extent is not surprising in light of the many simplifications in the model, including neglecting sensible and latent heat fluxes.

Björk and Söderkvist [2] constructed a single-column model with a sophisticated representation of the Arctic ocean, 40 evolving ice thickness categories, and an atmospheric thermal equilibrium model based on T92. They prescribed N to follow the observed annual cycle of cloudiness but tuned its magnitude to give an observationally reasonable cycle of ice thickness. We followed a similar procedure, using a non-negative sine-wave approximation to the Arctic cloudiness observations made by Maykut and Church [17] (Fig. 4). This leaves the seasonal maximum and minimum values of N as tunable constants, and we chose values to give a physically reasonable seasonal cycle in ice thickness.

3.2.3 Poleward heat transport

T92 specifies a constant poleward heat flux in the atmosphere equivalent to a vertical flux of 100W/m², which is based on observations [23]. He finds a state similar to the observed present-day Arctic, as well as a second stable state in which the Arctic is ice free with ocean

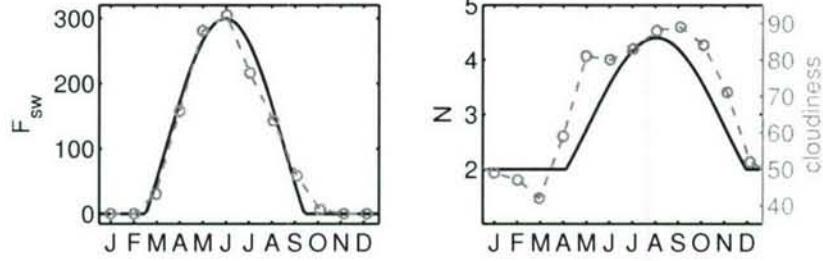


Figure 4: Seasonal cycle in specified model forcing (black lines), and observations the forcing is based on (gray circles and dashed line). (left) Shortwave radiation (W/m^2) chosen to fit observed incident solar flux at the surface [19]. (right) Optical thickness of the model atmosphere, which is scaled to match Arctic cloudiness (percent) [17].

mixed layer temperatures varying seasonally between 6° and 14°C . As mentioned in T92, it is unlikely that the real atmosphere would maintain the present-day poleward heat transport with the meridional temperature gradient significantly reduced. Thorndike later expanded on this idea, letting D be a function of the meridional temperature gradient between two boxes in a highly idealized climate model with no seasonal cycle or ice thermodynamics [30]. This method of approximating D is frequently employed in idealized atmospheric models (e.g., Chen et al [4]), and we have adopted it here.

We let

$$D(T_s) = k_D (T_{0-70N} - T_s) \quad (31)$$

with T_{0-70N} specified to vary seasonally based on NCEP-NCAR [12] observed climatological 1000mb temperature which was averaged both zonally and 0° - 70°N . We used $k_D = 3.3$, equivalent to the value in Thorndike [30], which matches observed poleward heat transport [23] fairly well using T_s from the standard model run (Fig. 5). Note that when this parameterization for D is inserted into the model of T92 the ice-free states disappears, leaving only the state resembling the present-day Arctic.

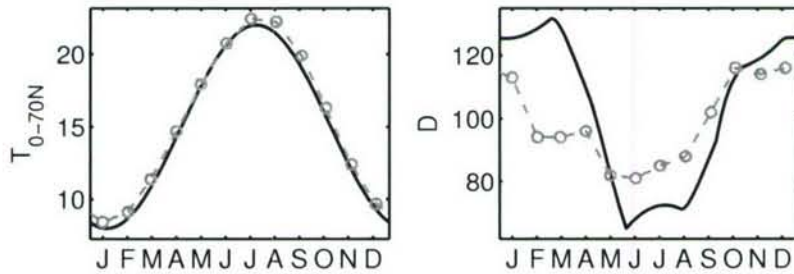


Figure 5: (left) Observed 0 - 70°N mean seasonal cycle in 1000mb atmospheric temperature T_{0-70N} (gray circles and dash) and a sinusoidal fit used in the model (black). (right) Observed poleward heat transport D (gray circles and dash), and computed values of D , which use T_{0-70N} and simulated Arctic surface temperature T_s , in the standard model run.

3.2.4 Surface flux exchange

The surface is split into a region containing ice and an open water region, with average surface temperature

$$T_s = AT_i + (1 - A)T_{ml}. \quad (32)$$

Surface downward longwave radiation, $F_{DN}(0)$, was computed in Section 3.2.1 using the average surface upward radiation $F_{UP}(0) = a + bT_s$. We assume that the downward longwave radiation is everywhere uniform in the model domain and depends only on T_s , but we compute the upward radiation separately for ice and open water as $F_{UP}(0) = a + bT_i$ and $F_{UP}(0) = a + bT_{ml}$ respectively. The longwave emissivities of ice and open water, both roughly 0.95 or greater, have here been approximated to 1. (Note, however, that open water and ice differ significantly in microwave emissivity, which is what satellite observing systems like SSM/I are based on.) This leads to a surface longwave radiation imbalance above ice or open water of

$$\epsilon(T, T_s) \equiv F_{UP}(0) - F_{DN}(0) = \frac{2a}{2 + N} - \frac{D(T_s)}{2} + b \left(T - T_s + \frac{2T_s}{2 + N} \right), \quad (33)$$

with $T = T_i$ or $T = T_{ml}$ inserted.

Shortwave radiation is also absorbed at the surface, adding an energy flux $(1 - \alpha)F_{sw}$ with $\alpha = \alpha_{ml}$ over open water and $\alpha = \alpha_i$ over ice. When ice is melting at the surface ($T_i = 0$), a lower albedo is used to account for the ice and the presence of melt ponds (α_{mp}). The value of α_{mp} is chosen based on observations of fractional pond cover in summer and melt pond albedos [7].

3.2.5 Addition of CO₂

We can crudely vary CO₂ in the model by enhancing the Arctic optical thickness and adjusting T_{0-70N} in the equation determining poleward heat transport. Changes in radiative forcing are typically approximated to have a logarithmic dependence on CO₂ concentration, and values associated with CO₂ doubling are commonly discussed. The IPCC TAR [11] cites a range of 1.5 to 4.5°C for the equilibrium response of an atmospheric GCM to each doubling of CO₂, so we add 3°C to T_{0-70N} for CO₂ doubling.

The IPCC TAR gives a range of 3.5-4.1 W/m² for the direct longwave radiative forcing due to a doubling of CO₂, suggesting 3.7 W/m² as the best estimate (their Section 6.3.1). Solving (30) for N , we can write the relationship between optical thickness and longwave forcing as

$$N = 2 \frac{F_{DN}(0) - D/2}{a + bT_s - F_{DN}(0) + D/2}. \quad (34)$$

Replacing N with $N + \Delta N$ and replacing $F_{DN}(0)$ with $F_{DN}(0) + \Delta F$, this shows that the change in optical thickness associated with an increase in longwave forcing is

$$\Delta N = \frac{N(1 + N/2)}{F_{DN}(0) - D/2} \Delta F + O \left(\frac{\Delta F}{F_{DN}(0)} \right)^2. \quad (35)$$

We insert into (35) mean values for N , $F_{DN}(0)$, and D from the standard model run, which leads to an increase in N of $\Delta N = 0.2$ associated with the enhancement in radiative forcing of $\Delta F = 3.7$ W/m².

Based on this, we vary CO₂ in the model by replacing N with $N + \Delta N \log_2(\text{co2})$ and replacing T_{0-70N} with $T_{0-70N} + \Delta T \log_2(\text{co2})$, where co2 represents the factor multiplying present-day atmospheric CO₂ concentrations, $\Delta N = 0.2$, and $\Delta T = 3^\circ$.

3.3 Ocean mixed layer

The mixed layer is modeled as a thermodynamic reservoir. Its characteristic depth is $H_{ml} = 50\text{m}$ as in T92 (cf. observations of Morison and Smith [22]).

The flux of heat entrained through the bottom of the mixed layer is specified to be $F_{ent} = 0.5\text{W/m}^2$ based on observations [22]. The turbulent heat flux between the ocean and the base of the ice is given by $F_w = \rho c_p c_h u_{*0} \Delta T$, where ρ and c_p are the density and specific heat of seawater, $c_h = 006$ is the heat transfer coefficient, u_{*0} is the friction velocity (square root of kinematic stress at ice-ocean interface), and ΔT is the difference in temperature between ocean and ice [20]. Using a typical value of $u_{*0} = 0.5\text{cm/s}$ based on observations [18] and inserting $\Delta T = T_{ml}$ (since $T = 0$ at the base of the mixed layer) leads to

$$F_w = \gamma T_{ml} \quad (36)$$

with $\gamma \equiv \rho c_p c_h u_{*0} = 120\text{W/m}^2$.

The total heat flux into the mixed layer is thus

$$F_{ml} = (1 - A)(-\epsilon(T_{ml}, T_s) + (1 - \alpha_{ml})F_{sw}) - A\gamma T_{ml} + F_{entr}. \quad (37)$$

If $T_{ml} > 0$, this leads to heating or cooling according to

$$c_{ml} H_{ml} \frac{dT_{ml}}{dt} = F_{ml}, \quad (38)$$

and no new ice area is formed, $F_{ni} = 0$. When the mixed layer reaches the freezing temperature ($T_{ml} = 0$) and tries to keep cooling, the temperature remains at the freezing point ($dT_{ml}/dt = 0$) and any additional heat loss goes into the formation of new ice ($F_{ni} = -F_{ml}$).

3.4 Summary

The model is described schematically in Fig. 6. It consists of four coupled ODEs which are first-order and non-autonomous (F_{sw} , N , and D have time dependence). The model equations described in Sections 3.1-3.3 are summarized below.

The surface longwave radiation imbalance is

$$\epsilon(T, T_s) = \frac{2a}{2 + N} - \frac{D(T_s)}{2} + b \left(T - T_s + \frac{2T_s}{2 + N} \right) \quad (39)$$

with surface temperature $T_s = AT_i + (1 - A)T_{ml}$ and atmospheric poleward heat transport given by

$$D(T_s) = k_D (T_{0-70N} - T_s). \quad (40)$$

The mixed layer flux imbalance,

$$F_{ml} = (1 - A)(-\epsilon(T_{ml}, T_s) + (1 - \alpha_{ml})F_{sw}) - A\gamma T_{ml} + F_{entr}, \quad (41)$$

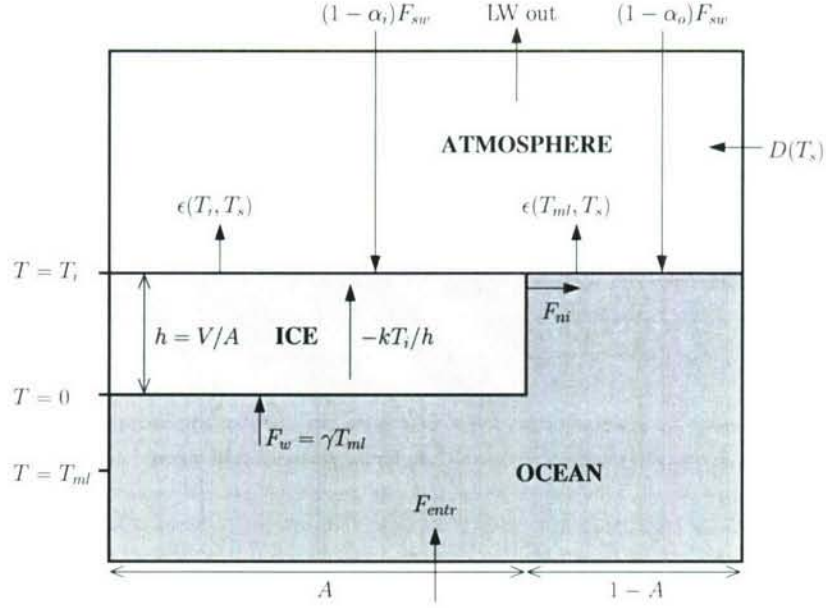


Figure 6: Schematic summarizing the model sea ice, atmosphere, and ocean thermodynamics.

normally causes warming and cooling in the mixed layer and no production of new ice area,

$$c_{ml}H_{ml}\frac{dT_{ml}}{dt} = F_{ml} \quad \text{and} \quad F_{ni} = 0. \quad (42)$$

When $T_{ml} = 0$ and $F_{ml} < 0$, however, the mixed layer flux imbalance goes into forming new ice,

$$\frac{dT_{ml}}{dt} = 0 \quad \text{and} \quad F_{ni} = -F_{ml}. \quad (43)$$

The equations for ice surface temperature and volume evolution are

$$\frac{ch}{2}\frac{dT_i}{dt} = -\epsilon(T_i, T_s) + (1 - \alpha_i)F_{sw} - \frac{kT_i}{h}, \quad (44)$$

$$L\frac{dV}{dt} = A\left(-\frac{kT_i}{h} - \gamma T_{ml}\right) + F_{ni} - v_0LV, \quad (45)$$

except during surface melt, $T_i = 0$ and $-\epsilon(0, T_s) + (1 - \alpha_i)F_{sw} > 0$, when ice melts at the top and bottom according to

$$\frac{dT_i}{dt} = 0, \quad (46)$$

$$L\frac{dV}{dt} = A(\epsilon(0, T_s) - (1 - \alpha_{mp})F_{sw} - \gamma T_{ml}) - v_0LV. \quad (47)$$

Here we have used the ice thickness, $h = V/A$.

The area evolves as

$$\frac{dA}{dt} = \frac{F_{ni}}{Lh_0} - \frac{A}{2V}\mathcal{R}\left(-\frac{dV}{dt}\right) - v_0A \quad (48)$$

where the ramp function $\mathcal{R}(x)$ is 0 if $x < 0$ and $\mathcal{R}(x) = x$ if $x > 0$.

The model parameters are listed in Table 2.

Table 2: Model parameters.

<i>Fundamental physical parameters</i>		
c	ice heat capacity	$2 \times 10^6 \text{ J/m}^3/\text{K}$
L	ice latent heat of fusion	$3 \times 10^8 \text{ J/m}^3$
c_{ml}	mixed layer heat capacity	$4 \times 10^6 \text{ J/m}^3/\text{K}$
k	ice thermal conductivity	$2 \text{ W/m}^2/\text{K}$
a	for LW radiation: $\sigma (T_f)^4$	320 W/m^2
b	for LW radiation: $4\sigma (T_f)^3$	$4.6 \text{ W/m}^2/\text{K}$
<i>Parameters based closely on observations</i>		
F_{sw}	shortwave radiation at ice or ocean surface	seasonal, 0 to 300 W/m^2
T_{0-70N}	0° – 70° mean temperature	seasonal, 8 to 22°C
α_i	ice albedo	0.65
α_o	ocean albedo	0.20
α_{mp}	ice albedo during surface melt	0.55
γ	ocean–ice heat exchange coefficient	$120 \text{ W/m}^2/\text{K}$
H_{ml}	mixed layer depth	50 m
F_{entr}	heat flux entrained into mixed layer	0.5 W/m^2
k_D	atmospheric heat transport constant	$3.3 \text{ W/m}^2/\text{K}$
v_0	dynamic export of ice from model domain	0.10 yr^{-1}
$1 - A_{max}$	minimum lead fraction	0.05
h_0	equivalent thickness for newly formed ice	0.5 m
<i>Tunable parameter, based loosely on observations</i>		
N	optical thickness	seasonal, 2 to 4.4

4 Results and discussion

The standard model run, using the parameter values in Table 2, is presented in Fig. 7. Ice thickness ($h = V/A$) varies seasonally from 2.5 to 3.7m, in rough agreement with observations. This agreement in simulated thickness extrema, while encouraging, is not surprising since we were able to tune the maximum and minimum seasonal values of N . Thickness reaches a minimum in late October and a maximum in late May, which agrees fairly well with Maykut and Untersteiner [19] who find minimum thickness in October/November and maximum thickness in June.

The ice surface temperature (T_i) varies between 0° and -32°C , and the associated trajectory in T_i versus V state space matches fairly well with the results of Maykut and Untersteiner [19] and similarly Thorndike [31].

The minimum area occurs in September, in agreement with observations. The model domain represents roughly the entire Arctic Ocean. Satellite observations [3] of the 1980–1999 mean seasonal cycle in ice extent north of 70°N (solid gray line) and 75°N (dashed gray line) are plotted next to simulated ice area for comparison. Note the fairly good agreement.

The mixed layer temperature varies between 0° and 0.23°C . When multiplied by γ , it gives the ocean–ice heat flux. The annual average flux is $F_w = 5.4 \text{ W/m}^2$, which compares well with the observational estimate by Maykut and McPhee [18] of 5.1 W/m^2 .

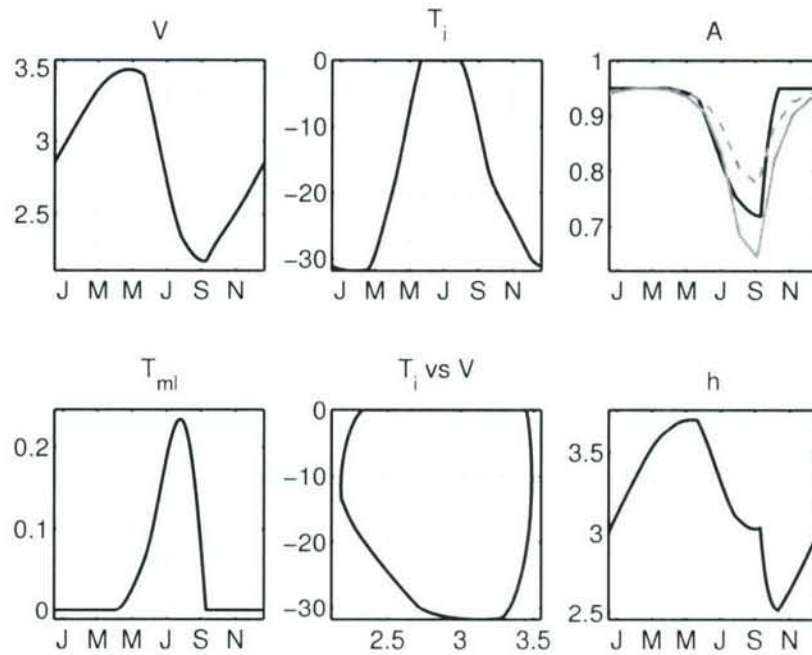


Figure 7: Standard run results. There is only one stable periodic orbit in this parameter regime, and any initial condition eventually converges on it. Plots represent evolution of the model state during the course of the annual cycle. The first four are the state variables: ice volume divided by box area V (m), ice surface temperature T_i ($^{\circ}\text{C}$), ice area A (fraction of box covered by ice), and ocean mixed layer temperature T_{ml} ($^{\circ}\text{C}$). The bottom center plot represents the model trajectory through the state space projected onto the T_i - V plane. The bottom right plot shows the evolution of ice thickness ($h = V/A$); note that the bump in September is related to ice area rapidly expanding while volume slowly grows, causing the average thickness to abruptly drop. Satellite observations [3] of the 1980-1999 mean seasonal cycle are included in the ice area plot for comparison; the solid gray line indicates ice extent north of 70°N and the dashed gray line indicates ice extent north of 75°N (both are plotted in units normalized to have a maximum value of 0.95).

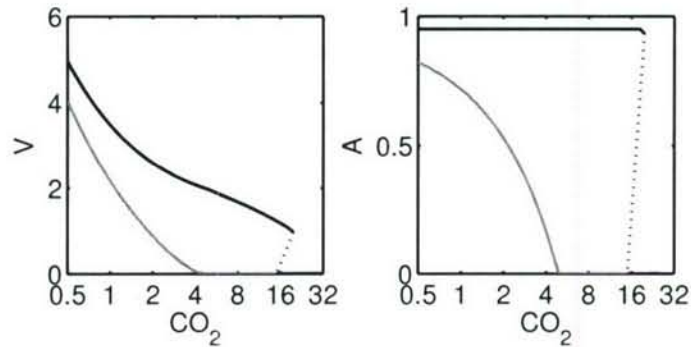


Figure 8: Response of the model solution to scaling the CO_2 parameter, which is crudely related to atmospheric CO_2 concentration. Values on the horizontal axis represent factors multiplying the CO_2 concentration today, with each tick mark representing one doubling. For each level of CO_2 , the model solution is a periodic orbit in the 4-dimensional state space. Solutions are represented here by four numbers: the summer (gray) and winter (black) extrema of ice volume (left) and ice area (right). There is no hysteresis (or “tipping point”) in summer ice cover. When CO_2 levels reach about $5\times$ the present-day value in this model, the Arctic becomes ice-free each summer. Further increase of CO_2 leads to multiple states and hysteresis in winter ice cover, with an associated fold catastrophe: one state has ice only in winter and the other is ice-free year-round. The multiple states exist in a narrow range on the plots around the CO_2 level of $16\times$ the present-day value. The straight dotted lines indicate the presence of an unstable state.

Varying the initial condition leads to no multiple states in the standard parameter regime: every initial condition eventually converges on the limit cycle plotted in Fig. 7. This disagrees with the “tipping point” hypothesis in which a second stable state which is ice-free each summer would exist today.

We varied CO_2 , gradually raising the value and lowering it again to look for hysteresis and hence multiple states. The summer and winter extrema in ice volume and ice area are plotted in Fig. 8. A scenario in which CO_2 exponentially increases in time is equivalent to moving to the right on the horizontal axis at a constant speed: note the accelerating approach to an ice-free summer (right; gray line). However, we find no “tipping point” in summer ice cover.

When CO_2 is further increased to the point where the ocean becomes ice-free year-round, multiple states appear in a fairly narrow region of the parameter space. The region is bounded on each side by a saddle-node bifurcation of cycles where a fold catastrophe or “tipping point” occurs. Here, in an increasing CO_2 scenario, when the CO_2 level crosses a threshold the climate rapidly switches from a state characterized by nearly ice-covered winters to a state which is ice-free year-round. Note that the slight kink in the black line on the right in Fig. 8 ($\text{CO}_2 \approx 16$, $A \approx 0.95$) corresponds to a solution in which ice cover grows continuously throughout the winter and nearly fills the model domain each year before it begins to melt.

As indicated in Fig. 8, a catastrophe brought on by the demise of multiple sea ice states can occur when one state is ice-free year-round, but not when one state is ice-covered year-

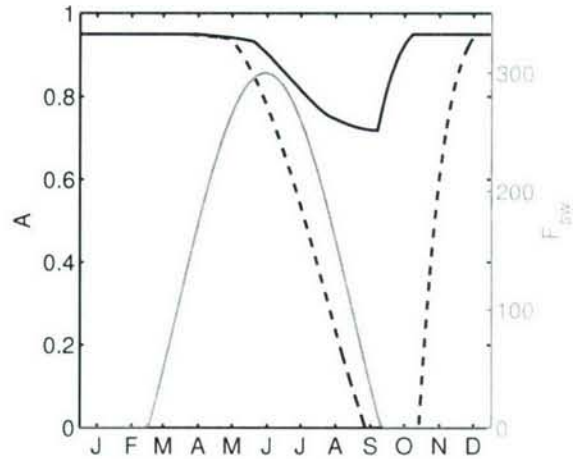


Figure 9: Simulated ice area in the standard run (black solid line) and a seasonal ice cover run with CO_2 increased by $5.3\times$ (black dashed line), compared with solar forcing in the model (gray line; W/m^2). In the seasonal ice cover state, as in present-day observations, the minimum in ice area occurs several months after the maximum in sunlight, leading to limited overlap between significant open water and intense Arctic sunlight. This mitigates the ice–albedo effect, causing it to be outweighed by stabilizing effects and hence avoiding a “tipping point” in the approach to an ice-free summer.

round as today. As an ice-free summer is approached in an increasing CO_2 scenario, the stabilizing thermodynamic thickness–growth effect (i.e., thin ice grows fastest) appears to outweigh the destabilizing ice–albedo effect. In an attempt to understand why the heuristic argument for a “tipping point” discussed in Section 1 failed in this model for the case the present-day Arctic Ocean approaching ice-free summers, we consider why the argument seemed to succeed for the approach to an ice-free year-round state.

Fig. 9 compares the model solar forcing, which is based on Arctic surface observations (cf. Fig. 4), with simulated ice cover, which agrees fairly well with observed ice cover (cf. Fig. 7). In both the standard run (solid line) and the enhanced CO_2 seasonal ice cover solution (dashed line), there is a significant phase lag between the times of maximum sunlight and the times of minimum ice cover. This is indeed to be expected: the ice area rate of change correlates fairly well with solar intensity. For the ice–albedo effect to lead to multiple states and a catastrophe, the seasonal ice cover state must absorb significantly more sunlight than a state which is ice-covered year-round with the same parameters. But the temporal overlap in the seasonal ice state between having small ice area and experiencing a high intensity of sunlight is somewhat limited: the sun shines on a fairly extended ice cover for much of the summer. Compared to the seasonal ice state, the ice–albedo effect leads to a far bigger change when making the transition to a year-round ice-free state in which the sun shines on open water all summer.

To assess the extent to which the ice–albedo effect failed to lead to a “tipping point” in summer ice cover, we investigated whether a region exists anywhere near the physically realistic parameter regime where there are multiple summer ice cover states. We began by pushing the disparity between ice and ocean albedo to the extreme. This was not

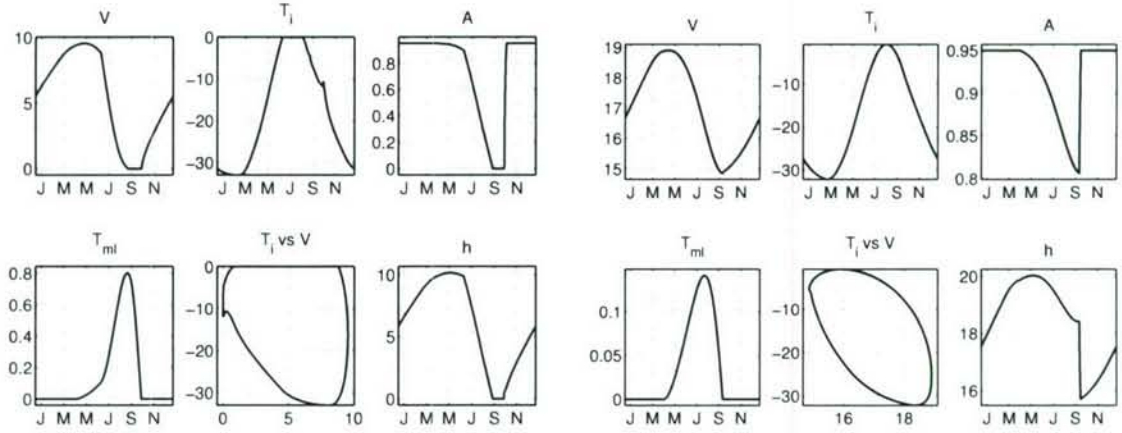


Figure 10: Multiple sea states under the same forcing. Plots represent evolution of the model variables during the seasonal cycle, as in Fig. 7, for the thin ice (left) and thick ice (right) states. Here $L^* = 10$ (i.e. sea ice latent heat of fusion is reduced $10\times$) and CO_2 has been increased to $1.5\times$ the present-day value. It should be emphasized that we are pushing the idealized model to the extremes in search of multiple summer ice states brought on by the ice–albedo effect: neither a $10\times$ diminished latent heat of fusion nor a simulated 19m ice thickness are purported here to be physically realistic.

enough to lead to multiple states. We experimented with allowing the ice albedo to depend on thickness following the parameterization of Maykut [16]. We tried varying the loosely constrained parameters. None of these approaches led to multiple summer ice cover states.

The stabilizing thickness–growth effect becomes less pronounced as ice gets thicker (i.e., very thick ice does not grow much slower than fairly thick ice), so we considered allowing excursions into state-space regions with large thickness. The most straightforward way to do this is to make it easier to grow ice by reducing the latent heat of fusion. Defining the original and observationally constrained sea ice latent heat to be L_{orig} , we scaled the latent heat according to

$$L = \frac{L_{orig}}{L^*}. \quad (49)$$

Letting $L^* = 10$ led to multiple summer ice cover states (Fig. 10).

Although the multiple states demonstrated in Fig. 10 are related to the ice–albedo effect, it should be noted that it is not the difference in albedo between open water and ice that is primarily responsible. Rather, it is the difference between the cold sea ice albedo (α_i) and the albedo used to account for the presence of melt ponds when $T_i = 0$ (α_{mp}). Both states have minimal temporal overlap between extended open water and intense sunlight, but the thin ice state has the ice surface at $T_i = 0$ for much of the peak of the summer, while in the thick ice state the surface temperature remains below the freezing temperature for the entire year.

Varying CO_2 with $L^* = 10$, we finally find the desired catastrophe (or “tipping point”) in summer ice cover. This is illustrated in Fig. 11.

Next, we vary both CO_2 and L^* to explore the parameter space and find the edge of the region associated with multiple summer ice states. To do this, we slowly increase and

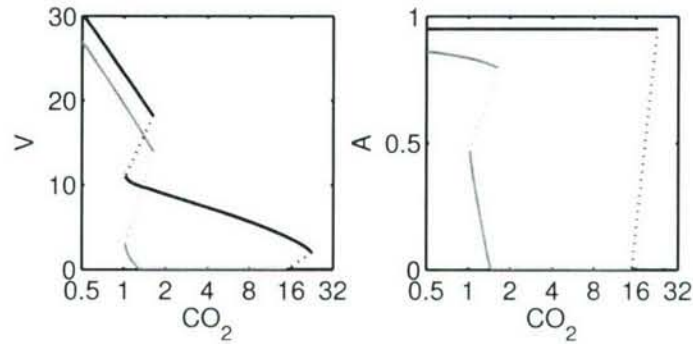


Figure 11: As in Fig. 8, but with $L^* = 10$. Now two regions exist with multiple sea ice states, and there is a catastrophe in summer ice cover (discontinuity in gray solid line).

then decrease CO_2 for an array of L^* values and look for hysteresis. The result is presented in Fig. 12. There are two regions of multiple states, each bounded by lines on which a saddle-node bifurcation of cycles occurs. These lines are associated with a cusp catastrophe: entering and then exiting either of these regions by slowly varying the parameters will lead to a catastrophe in which the current state suddenly disappears and the system rapidly approaches a new state.

Fig. 12 suggests that a catastrophe in summer ice cover would be possible if the latent heat of ice fusion were reduced from the observationally constrained value by a factor of at least $4\times$. The latent heat of sea ice can change depending on salinity, and observed sea ice has a salinity of roughly 0–8ppt (varying both vertically and seasonally). Theoretical and empirical formulas suggest that the latent heat of melting sea ice is about 25% lower for ice with 8ppt salinity than for pure ice (e.g., Bitz and Lipscomb [1]). The dominant variability in global mean ocean salinity over the past million years is associated with glacial cycles, during which salinity varies about the mean value of 35ppt by about 1ppt because of the reduction in ocean volume caused by the presence of large ice sheets on land. If the mean ocean salinity change associated with glacial cycles were carried into a change in mean sea ice salinity, it would lower the latent heat of fusion by 3%. This implies that a reduction in the latent heat of fusion of sea ice by $4\times$ (i.e., 75%) would be quite significant, and it is unlikely that it could be physically realized in the foreseeable future.

5 Conclusions

We have extended Thorndike’s [31] idealized Arctic sea ice model to allow for partial ice cover, adding an active ocean mixed layer and scalable CO_2 . This model simulates an accelerating approach to an ice-free Arctic summer as CO_2 concentrations exponentially rise, suggesting that the approach may be fairly abrupt. We find two regions in the parameter space where multiple states are possible because of the ice–albedo effect. One region has multiple winter ice cover states (with both states ice-free in summer); the other has multiple summer ice cover states (with both states ice-covered in winter). Catastrophes are associated with exiting either region, but the actual Arctic appears to be far from the region in

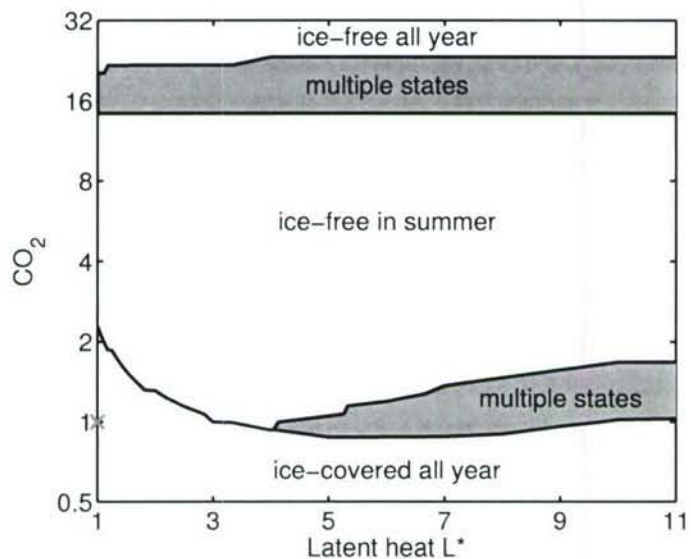


Figure 12: Regions where multiple states are possible in CO_2 versus latent heat parameter space. A saddle-node bifurcation of cycles associated with a cusp catastrophe occurs at the edge of each shaded region. Inside each shaded region there are three possible solutions: two stable periodic orbits and one unstable periodic orbit. The gray “x” marks the present-day physical world. This implies that for a “tipping point” in summer ice cover to be possible, the latent heat of sea ice fusion would have to be $4\times$ smaller than it is in the present-day physical world ($L^* = 4$). This model does find a “tipping point” in the distant but physically realizable parameter space ($L^* = 1$, $CO_2 = 20\times$ present-day) associated with the transition from seasonal ice cover to a state which is ice-free all year.

parameter space where CO₂ changes could cause a catastrophe in summer ice cover.

This research suggests that a “tipping point” in summer Arctic sea ice cover brought on by the ice–albedo affect, which has been conjectured to be likely for the 21st century, does not occur in a physically realistic region of the parameter space. In light of the fact that the seasonal minimum in ice cover occurs several months after the time of maximum Arctic sunlight, the destabilizing ice–albedo effect is not sufficient to outweigh the stabilizing thickness–growth effect and produce multiple summer sea ice states.

This model is a significantly idealized representation of the physical world. Similar to Thorndike [31], the model does not include ridging, snow, sensible and latent heat exchange, salinity, or cloud feedbacks. It is possible that other bifurcations would be introduced by adding more realistic physics to the model. For example, a wide variety of parameterizations of sea ice albedo variations have been presented in previous studies (e.g., Maykut [16], Flato and Brown [8]) and may affect these results. Furthermore, despite our fairly thorough investigations, other bifurcations may be hiding nearby in the ~ 20 -dimensional parameter space.

Nonetheless, all the physics in the standard argument for a “tipping point” brought on by ice albedo has been faithfully represented in this model. This result suggests that the popular heuristic may not hold up when properly quantified.

Acknowledgments

This work benefited significantly from discussions with many visitors and staff at the GFD summer program. I am particularly grateful to John Wettlaufer who supervised the summer project, as well as Norbert Untersteiner, John Walsh, Jamie Morison, Dick Moritz, Danny Feltham, Göran Björk, Bert Rudels, Doug Martinson, Andrew Fowler, George Veronis, and Victor Tsai. I would also like to thank Alan Thorndike, who’s 1992 paper formed the foundation for this model, for a helpful phone meeting in August. This work drew upon research carried out during the spring with Eli Tziperman, and I am grateful for his advising and also for helpful conversations with Cecilia Bitz during that time. Lastly, I would like to thank the other GFD fellows and staff for a great summer.

The IPCC AR4 data was downloaded from <https://esg.llnl.gov:8443>. I appreciate the 16 modeling groups for making their data available and the Program for Climate Model Diagnostics and Intercomparison at Lawrence Livermore National Laboratory for compiling the data and allowing me access to it for this project. NCEP-NCAR Reanalysis data was provided by the NOAA/OAR/ESRL PSD website.

References

- [1] C. M. BITZ AND W. H. LIPSCOMB, *An energy-conserving thermodynamic model of sea ice*, Journal of Geophysical Research-oceans, 104 (1999), pp. 15669–15677.
- [2] G. BJORK AND J. SODERKVIST, *Dependence of the Arctic Ocean ice thickness distribution on the poleward energy flux in the atmosphere*, Journal of Geophysical Research-oceans, 107 (2002).

- [3] D. CAVALIERI, C. PARKINSON, P. GLOERSON, AND H. ZWALLY, *Sea ice concentrations from Nimbus-7 SSMR and DMSP SSM/I passive microwave data*, Boulder, CO, USA: National Snow and Ice Data Center, (1997, updated 2005).
- [4] D. CHEN, R. GERDES, AND G. LOHMANN, *A 1-D atmospheric energy-balance model developed for ocean modeling*, *Theoretical and Applied Climatology*, 51 (1995), pp. 25–38.
- [5] M. EWING AND W. L. DONN, *A theory of ice ages*, *Science*, 123 (1956), pp. 1061–1066.
- [6] D. L. FELTHAM, N. UNTERSTEINER, J. S. WETTLAUFER, AND M. G. WORSTER, *Sea ice is a mushy layer*, *Geophysical Research Letters*, 33 (2006).
- [7] F. FETTERER AND N. UNTERSTEINER, *Observations of melt ponds on Arctic sea ice*, *Journal of Geophysical Research-oceans*, 103 (1998), pp. 24821–24835.
- [8] G. M. FLATO AND R. D. BROWN, *Variability and climate sensitivity of landfast Arctic sea ice*, *Journal of Geophysical Research-oceans*, 101 (1996), pp. 25767–25777.
- [9] R. GOODY AND Y. YUNG, *Atmospheric Radiation: Theoretical Basis*, Oxford University Press, 2 ed., 1989.
- [10] W. D. HIBLER, *A dynamic thermodynamic sea ice model*, *J. Phys. Oceanogr.*, 9 (1979), pp. 815–846.
- [11] J. T. HOUGHTON, Y. DING, D. GRIGGS, M. NOGUER, P. J. VAN DER LINDEN, AND D. XIAOSU, eds., *IPCC third assessment report: Climate change 2001: The scientific basis*, Cambridge University Press, Cambridge, UK, 944pp, 2001.
- [12] E. KALNAY, M. KANAMITSU, R. KISTLER, W. COLLINS, D. DEAVEN, L. GANDIN, M. IREDELL, S. SAHA, G. WHITE, J. WOOLLEN, Y. ZHU, M. CHELLIAH, W. EBISUZAKI, W. HIGGINS, J. JANOWIAK, K. C. MO, C. ROPELEWSKI, J. WANG, A. LEETMAA, R. REYNOLDS, R. JENNE, AND D. JOSEPH, *The NCEP/NCAR 40-year reanalysis project*, *Bulletin of the American Meteorological Society*, 77 (1996), pp. 437–471.
- [13] R. KWOK, G. F. CUNNINGHAM, AND S. S. PANG, *Fram strait sea ice outflow*, *Journal of Geophysical Research-oceans*, 109 (2004).
- [14] R. W. LINDSAY AND J. ZHANG, *The thinning of Arctic sea ice, 1988-2003: Have we passed a tipping point?*, *Journal of Climate*, 18 (2005), pp. 4879–4894.
- [15] S. MANABE AND R. J. STOUFFER, *Co₂-climate sensitivity study with a mathematical-model of the global climate*, *Nature*, 282 (1979), pp. 491–493.
- [16] G. A. MAYKUT, *Large-scale heat-exchange and ice production in the central Arctic*, *Journal of Geophysical Research-oceans and Atmospheres*, 87 (1982), pp. 7971–7984.
- [17] G. A. MAYKUT AND P. E. CHURCH, *Radiation climate of Barrow, Alaska, 1962-66*, *Journal of Applied Meteorology*, 12 (1973), pp. 620–628.

- [18] G. A. MAYKUT AND M. G. MCPHEE, *Solar heating of the Arctic mixed layer*, Journal of Geophysical Research-oceans, 100 (1995), pp. 24691–24703.
- [19] G. A. MAYKUT AND N. UNTERSTEINER, *Some results from a time-dependent thermodynamic model of sea ice*, J. Geophys. Res., 76 (1971), pp. 1550–1575.
- [20] M. G. MCPHEE, *Turbulent heat-flux in the upper ocean under sea ice*, Journal of Geophysical Research-oceans, 97 (1992), pp. 5365–5379.
- [21] K. MORAN, J. BACKMAN, H. BRINKHUIS, S. C. CLEMENS, T. CRONIN, G. R. DICKENS, F. EYNAUD, J. GATTACCECA, M. JAKOBSSON, R. W. JORDAN, M. KAMINSKI, J. KING, N. KOC, A. KRYLOV, N. MARTINEZ, J. MATTHIessen, D. MCINROY, T. C. MOORE, J. ONODERA, M. O'REGAN, H. PALIKE, B. REA, D. RIO, T. SAKAMOTO, D. C. SMITH, R. STEIN, K. ST JOHN, I. SUTO, N. SUZUKI, K. TAKAHASHI, M. WATANABE, M. YAMAMOTO, J. FARRELL, M. FRANK, P. KUBIK, W. JOKAT, AND Y. KRISTOFFERSEN, *The Cenozoic palaeoenvironment of the Arctic ocean*, Nature, 441 (2006), pp. 601–605.
- [22] J. MORISON AND J. D. SMITH, *Seasonal-variations in the upper Arctic ocean as observed at T-3*, Geophysical Research Letters, 8 (1981), pp. 753–756.
- [23] N. NAKAMURA AND A. H. OORT, *Atmospheric heat budgets of the polar-regions*, Journal of Geophysical Research-atmospheres, 93 (1988), pp. 9510–9524.
- [24] N. ONO, *Physics of Snow and Ice*, vol. 1, Inst. of Low Temp. Sci., Hokkaido, Japan, 1967, ch. Specific heat and heat of fusion of sea ice, pp. 599–610.
- [25] J. OVERPECK, M. STURM, J. A. FRANCIS, D. K. PEROVICH, M. C. SERREZE, R. BENNER, E. C. CARMACK, F. S. C. III, S. C. GERLACH, L. C. HAMILTON, L. D. HINZMAN, M. HOLLAND, H. P. HUNTINGTON, J. R. KEY, A. H. LLOYD, G. M. MACDONALD, J. MCFADDEN, D. NOONE, T. D. PROWSE, P. SCHLOSSER, AND C. VVRVSMARTY, *Arctic system on trajectory to new, seasonally ice-free state*, EOS, 86 (2005), pp. 309–313.
- [26] C. L. PARKINSON, K. Y. VINNIKOV, AND D. J. CAVALIERI, *Evaluation of the simulation of the annual cycle of Arctic and Antarctic sea ice coverages by 11 major global climate models*, Journal of Geophysical Research-oceans, 111 (2006).
- [27] P. SCHWERDTFEGER, *The thermal properties of sea ice*, J. Glaciol., 4 (1963), pp. 789–807.
- [28] M. C. SERREZE AND J. A. FRANCIS, *The Arctic amplification debate*, Climatic Change, 76 (2006), pp. 241–264.
- [29] J. C. STROEVE, M. C. SERREZE, F. FETTERER, T. ARBETTER, W. MEIER, J. MASLANIK, AND K. KNOWLES, *Tracking the Arctic's shrinking ice cover: Another extreme September minimum in 2004*, Geophysical Research Letters, 32 (2005).

- [30] A. THORNDIKE, *A minimal model of sea ice and climate*, in *Ice Physics and the Natural Environment*, N. U. J.S. Wettlaufer, J.G. Dash, ed., Springer-Verlag, 1999, pp. 169–183.
- [31] A. S. THORNDIKE, *A toy model linking atmospheric thermal radiation and sea ice growth*, *J. Geophys. Res.*, 97 (1992), pp. 9401–9410.
- [32] N. UNTERSTEINER, *On the mass and heat budget of Arctic sea ice*, *Arch. Meteorol. Geophys. Bioklimatol., Ser. A*, 12 (1961), pp. 151–181.
- [33] ———, *Ice budget of the Arctic ocean*, in *Proceedings of the Arctic Basin Symposium*, 1963, pp. 219–230.
- [34] G. WALKER, *The tipping point of the iceberg*, *Nature*, 441 (2006), pp. 802–805.
- [35] J. E. WALSH, *Climate change: The Arctic as a bellwether*, *Nature*, 352 (1991), pp. 19–20.
- [36] M. WORSTER, *Perspectives in Fluid Dynamics*, Cambridge University Press, 2000, ch. Solidification of fluids, pp. 393–446.

Breaking moraine dams by catastrophic erosional incision

Rachel Zammett

March 15, 2007

1 Introduction

Glacial lakes occur in many mountainous areas of the world, such as the European Alps or the Cordillera Blanca mountain range in north-central Peru. Here we consider those glacial lakes that were formed during the period of glacier retreat that followed the end of the Little Ice Age (figure 1). Such lakes are typically up to a kilometre long, hundreds of metres wide and up to a hundred metres deep and are often dammed on at least one side by moraine (sediment deposited by a glacier).

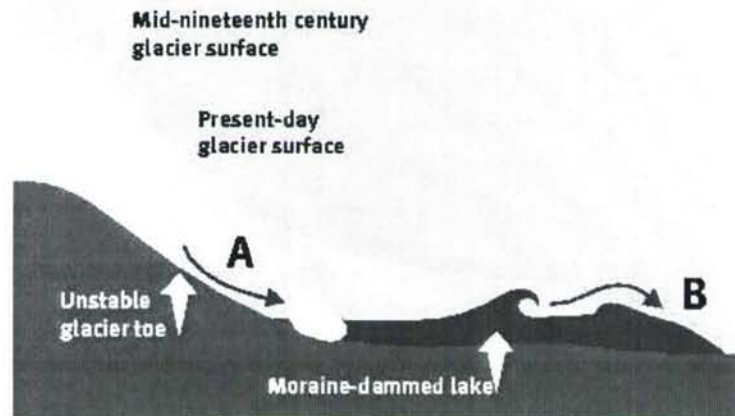


Figure 1: Schematic diagram of a glacial lake, taken from Clague and Evans [2]. The upper (grey) glacier surface is that of a long, thick glacier that would have advanced during the Little Ice Age. When this period of cool climate ended, glaciers retreated rapidly and substantially; such a thin, retreating glacier is labelled 'modern day glacier'. It is during a period of glacier retreat that a glacial lake is typically formed. The moraine dam is shown at the right of the picture. If the toe of the retreating glacier (which is often unstable and heavily crevassed) suddenly deposits a large amount of ice into the lake, a displacement wave which can overtop the dam is initiated.

Moraine dams fail in two main ways. As glacial lakes are often located in steep alpine

valleys (where avalanches and rockfalls are common), or beneath the unstable toe of a retreating glacier, there is the possibility that a large amount of ice or rock may suddenly fall into the lake. This initiates a displacement wave: one such rock avalanche in Peru deposited $O(10^6)$ m³ of rock in glacial lake Safuna Alta, and initiated a displacement wave estimated to be over 100 m high [8]; more generally, it is estimated that avalanches typically create displacement waves up to 10 m high [4]. Such a displacement wave can overtop the moraine dam and erode its downstream face.

In general, however, we have seen experimentally that one such overtopping wave does not cause the dam to fail. Instead, we observed that some of the initial wave is reflected back into the lake, leading to the formation of a seiche wave (a standing wave in an enclosed, or partially enclosed, body of water). Such waves are often observed to occur naturally in harbours due to tidal influence, for example [13].

The subsequent reflected waves can also overtop the dam, and it is these repeated overtopping events and associated erosion of the dam that lead to the incision of a channel on the downstream face of the dam. If such a channel is eroded to a sufficient depth quickly enough, it becomes a conduit through which the lake can drain; it is this mechanism of lake drainage that we term 'catastrophic erosional incision'.

Evidence for more than one overtopping event has been seen in several such drainage floods [9], and the possibility of a 'series' of waves was identified by Costa and Schuster [4]. The only mention in the literature of a seiche wave in connection with dam failure is found in Hubbard et al. [8], where examination of a moraine dam after a rockfall-initiated displacement wave indicated at least ten reflected waves. We show here how the reflected waves play a crucial role in the failure of the dam.

The other mechanism by which a moraine dam can break is that of gradual overtopping, whereby the lake water level slowly increases until the water overtops and then breaches the dam. Such a water level rise can be caused by excessive snowmelt or rainfall: the moraine which dammed Lake Tempanos in Argentina failed in the 1940s due to meltwater accompanying a 350 m glacier retreat [16].

Drainage of a glacial lake can release $O(10^6)$ m³ of water and have a peak discharge of 10^3-10^4 m³ s⁻¹ [2]. As the subsequent floodwater moves down valley, it entrains sediment and can form a debris flow. One such debris flow, initiated by a glacial lake flood in Peru in 1941, devastated the city of Huaraz, killing over 6000 people [5]. While the majority of such floods occur in remote, uninhabited valleys, these locations are now often considered for recreation, tourism and as sites for hydro-electric power stations, for example. Thus understanding the hazards associated with such a flood is of prime importance.

In this project, there are two main issues we will address. Firstly, we shall consider the threshold behaviour of the phenomenon - why didn't the moraine dam break in the case of Laguna Safuna Alta, despite an initial wave 100 m high and at least ten subsequent seiche waves? We also consider how to estimate the peak discharge from such a catastrophic drainage event, as this can be used as a measure of how destructive the resulting flood will be.

2 Experiments

We performed a series of experiments over the summer, both as a qualitative exploration of the phenomenon and to quantify some of the theoretical results outlined in Section 3 below. In all cases we used the experimental setup shown in figure 2: a rectangular glass tank with length 125 cm, width 20 cm and depth 30 cm. This was open at one end (the right hand end in figure 2), so that sediment and water could drain from the tank. At the open end, we built a sediment dam. This dam was approximately 10 cm high and 40 cm wide at the base and was made using a mould to endeavour to keep the dams uniform in shape. The tank was then filled with water, and the experiment was left until water had seeped through the entire dam. A single wave was then initiated at the left hand end of the tank; this was to simulate the displacement wave initiated by a rockfall or avalanche.

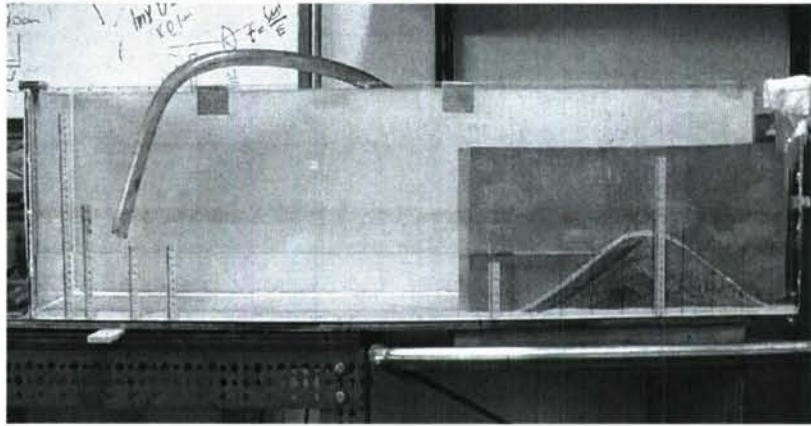


Figure 2: Experimental setup.

Sediment properties

We used four different sediments in the dambreak experiments. These were grit and three types of sand with different particle size distributions. The properties of these sediments (when dry) are summarised in Table 1.

Glacial moraine is characterized by a wide range of particle sizes, from fine clays to large boulders. This sediment is poorly sorted and loosely consolidated; lake drainage typically occurs by seepage through the dam. Clarke [3] shows an example of moraine from Trapridge glacier with a bimodal particle size distribution; this is a feature of many moraines. In order to reproduce such a bimodal particle size distribution, we therefore made two mixtures of sand and grit. The properties of these mixtures (when dry) are summarised in Table 2.

The sediments and their properties will also be discussed in Section 3 below, where we consider the erosion of the dam.

Sediment	ρ (10^3 kg m^{-3})	Porosity	Repose	Modal particle size (μm)
Caribbean Sand	N/A	N/A	N/A	250
Florida Sand	2.34	0.38	$39^\circ/34^\circ$	310
Beach Sand	2.34	0.35	$40^\circ/33.5^\circ$	950
Grit	2.42	0.42	$37^\circ/28^\circ$	1150

Table 1: Properties of individual sediments when dry. Sediment density was calculated from the weight of a given sediment volume once the sediment porosity was determined. Sediment porosity was measured by measuring how much water was absorbed by a given volume of sediment. The column headed ‘Repose’ shows the angles of repose of the dry sediment; the first value is the angle of repose associated with tilting a pile of sediment, the second that associated with creating a conical pile of the sediment. The differing values are due to the bistability of the system [11]. Modal particle size was estimated from particle size distributions which were obtained by laser diffraction. Some of the properties of the Caribbean sand were not determined.

Mixture	Composition	ρ (10^3 kg m^{-3})	Porosity	Repose
1	Caribbean Sand/Grit	2.38	0.32	$38.5^\circ/33^\circ$
2	Florida Sand/Grit	2.36	0.37	$44^\circ/34^\circ$

Table 2: Properties of sediment mixtures, determined as in Table 1. As the mixtures are bimodal by design, we have omitted the modal particle size column.

2.1 Results

Here we consider results from qualitative experiments. We first consider the results of experiments using the individual sediments, some of which are shown in Table 3. We see that grit alone makes a poor dam - its high porosity means that the lake drains out rapidly, and thus makes the dam unstable. It is also difficult to incise a channel in the downstream face because overtopping water simply seeps into the dam rather than eroding it. In contrast, the sands are, in general, better in terms of ease of channel incision. However, they are also prone to slumping when wet, indicating that they would make a poor dam; sand dams were occasionally observed to break before a wave was initiated.

Some of the results for the sediment mixtures are shown in Table 4. Although it is not clear from this table that dams constructed from the sediment mixtures were easier to break by catastrophic incision than those made from the individual sediments, they were qualitatively observed to be better in terms of both initial dam stability and ease of channel incision. These observations lead to the conclusion that it is perhaps the composition of moraine that leads such dams to fail via catastrophic erosional incision - the distribution of particle sizes both increases the dam stability, making the existence of a lake possible, and allows for easier channel incision. This may explain why the phenomenon is not seen in other natural dams, such as landslide dams for example.

Sediment	1	2	3	4
Play Sand	1/9	1/14	2/19	1/12
Beach Sand	2/16	1/19	2/14	2/16
Grit	X	1/6	X	X

Table 3: Experimental results for the individual sediments. The columns show different experimental runs. The first number in each column is the number of waves that needed to be initiated for dambreak. The second number is the total number of waves that overtopped the dam before incision occurred. The onset of incision is taken to be the point at which the lake drains independently of the action of the seiche wave. A cross denotes a dam which did not break.

Mixture	1	2	3	4
1	X	2/28	1/15	1/8
2	1/13	1/5	2/24	1/13

Table 4: Experimental results for the sediment mixtures. The table is laid out as Table 3 above.

3 Theory

In this section, we split the problem in two. Firstly, we model the seiche wave in the lake using shallow water theory in one dimension. We then use a hydraulic model for the dambreak itself, before considering a unified theory to explain the interaction between the seiche wave and the dam.

3.1 Describing the seiche wave

We work in two dimensions, x and z . Water of velocity $\mathbf{u} = (u(x, z, t), w(x, z, t))$ and depth $h(x, t)$ flows over an erodible bed with elevation $\zeta(x, t)$. We assume that the horizontal extent of the flow is much greater than its depth; the lake is much longer than it is deep. In this case, we have that $\frac{\partial}{\partial z} \gg \frac{\partial}{\partial x}$, and thus the continuity equation implies that $u \gg w$. Conservation of vertical momentum then implies that the pressure is hydrostatic to leading order, and irrotationality that u is independent of z .

We therefore write conservation of mass and horizontal momentum in the following form

$$h_t + (hu)_x = 0, \quad (1)$$

$$u_t + uu_x = -g(h + \zeta)_x - D(u, h) + \nu u_{xx}, \quad (2)$$

where u is the depth averaged velocity, given by

$$u = \frac{1}{h} \int_{\zeta}^{h+\zeta} u dz, \quad (3)$$

and $D(u, h)$ is a drag term which represents frictional effects, with the properties that

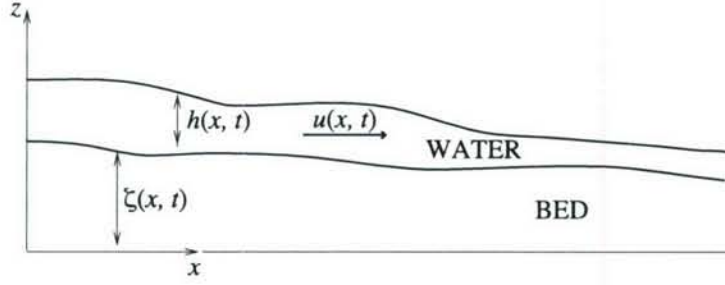


Figure 3: The co-ordinate system used in the shallow water theory.

$\frac{\partial D}{\partial u} > 0$ and $\frac{\partial D}{\partial h} < 0$; drag increases with velocity and decreases with depth. A full derivation of the shallow water equations may be found in Stoker [18], for example.

In fluvial systems, it is common to use the Chèzy drag law, given by

$$D(u, h) = c_f \frac{u|u|}{h}, \quad (4)$$

where c_f is the dimensionless Chèzy drag coefficient. Typically, for a smooth watercourse such as a glass tank, $c_f = O(10^{-3})$ [1], while for a rough watercourse, such as a rocky alpine stream, it may be as large as 0.1 [6].

However, this formula is not appropriate to use in the context of our experiments, where the flow was observed to be laminar. In 1959, Keulegan determined that for a standing wave in a glass rectangular tank, the drag is primarily accounted for by laminar viscous boundary layers on the tank walls and base [10]. This theory was later modified to account for the effects of surface tension and surface contamination [12], but we shall consider these to be small corrections.

To modify Keulegan's linear theory for our purposes, we note that shallow water theory can also be used in the boundary layers near the tank walls. Using the same arguments as above, we write conservation of momentum as

$$u_t = -\frac{1}{\rho} p_x + \nu u_{zz}, \quad (5)$$

and then, given that $p_z \approx 0$, we eliminate the hydrostatic pressure to obtain

$$u_{zt} = \nu u_{zzz}. \quad (6)$$

We then pose a time periodic solution of the form $u = f(z)e^{i\omega t}$ (and consider only the real part of this solution) to obtain

$$f = C + A_{\pm} e^{\pm Kz}, \quad (7)$$

where A_{\pm} and C are constants of integration, and $K = \sqrt{\frac{\omega}{2\nu}}(1 + i)$. The boundary conditions are

$$u_z \rightarrow 0, \quad \text{as } z \rightarrow \infty, \quad (8)$$

$$u \rightarrow u_0, \quad \text{as } z \rightarrow \infty, \quad (9)$$

$$u = 0, \quad z = 0, \quad (10)$$

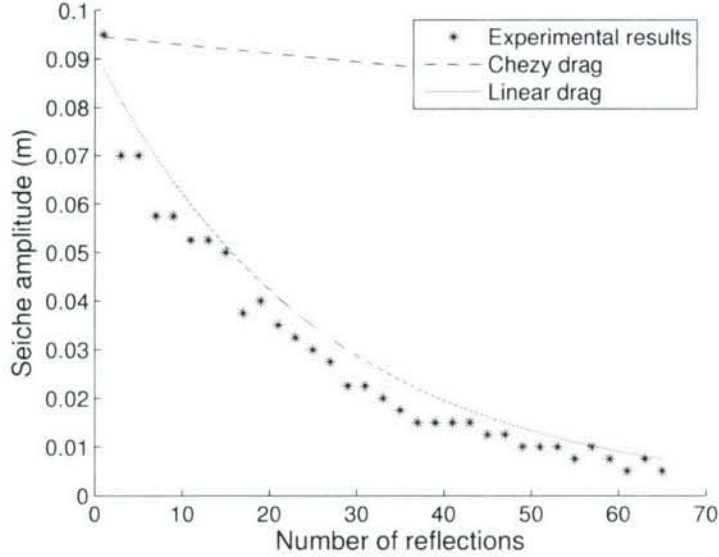


Figure 4: Comparison of the Chèzy and linear drag laws with experiment, where a seiche (standing) wave was initiated in a rectangular tank. The values used were $c_f = 0.001$, $\nu = 1 \times 10^{-6}$. We see that the linear drag theory (solid magenta line) is a much better fit to the data than the nonlinear Chèzy drag law (dashed line). Stars denote the experimental data.

where u_0 is the flow velocity in the main body of fluid outside the boundary layer. The solution is therefore

$$u = u_0 e^{i\omega t} (1 - e^{-Kz}), \quad (11)$$

and the vertical velocity gradient at the base is given by

$$u_z|_{z=0} = K u_0. \quad (12)$$

In the shallow water equations for the main flow, we therefore have

$$u_t + uu_x = -g(h + \zeta)_x - \sqrt{\frac{\nu\omega}{2}} \frac{u}{h} + \nu u_{xx}, \quad (13)$$

where the drag term is now $D(u, h) = \sqrt{\frac{\nu\omega}{2}} \frac{u}{h}$. We set $\alpha = \sqrt{\frac{\nu\omega}{2}}$; thus α has units of velocity.

We illustrate the difference between the drag laws by comparing them with the results from a simple laboratory experiment (figure 4), where a standing wave was initiated in a closed, rectangular glass tank. Figure 4 shows that that the linear drag is a much better fit to the data than the Chèzy drag; we therefore use linear drag in the theory that is to follow. However, we note that in a glacial lake where the Reynolds numbers are much higher, it is likely that the Chèzy formula will be more appropriate.

We consider a lake with mean depth $H(x)$, on which there is a seiche wave of amplitude $\eta(x, t)$, such that the total water depth is given by $h(x, t) = H(x) + \eta(x, t)$. Equations (1)

and (2) then become

$$\eta_t + [(H + \eta)u]_x = 0, \quad (14)$$

$$u_t + uu_x = -g(H + \eta + \zeta)_x - \alpha \frac{u}{h} + \nu u_{xx}. \quad (15)$$

We now nondimensionalise using the following scales

$$t \sim \frac{1}{\omega}, \quad u \sim U, \quad \eta \sim N, \quad H \sim H_0, \quad h \sim H_0, \quad \zeta \sim H_0, \quad x \sim L, \quad (16)$$

where ω is the frequency of the seiche wave. Equations (14) and (15) become

$$\omega N \eta_t + \frac{UH_0}{L} [(H + \varepsilon\eta)u]_x = 0, \quad (17)$$

$$\omega U u_t + \frac{U^2}{L} uu_x = -\frac{gH_0}{L} (H + \varepsilon\eta + \zeta)_x - \alpha \frac{U}{H_0} \frac{u}{H + \varepsilon\eta} + \nu \frac{U}{L^2} u_{xx}, \quad (18)$$

where $\varepsilon = \frac{N}{H_0} \ll 1$. To retain a balance in equation (17), we choose $U = \varepsilon\omega L$, and we assume that $(H + \zeta)_x = 0$, i. e. the undisturbed free surface is flat, to obtain,

$$\eta_t + (Hu)_x = -\varepsilon(\eta u)_x, \quad (19)$$

$$u_t + \beta\eta_x = -\varepsilon uu_x - \varepsilon \hat{\alpha} \frac{u}{H + \varepsilon\eta} + \varepsilon \hat{\nu} u_{xx}, \quad (20)$$

where the dimensionless parameters are given by

$$\beta = \frac{gH_0}{\omega^2 L^2}, \quad \hat{\alpha} = \frac{\alpha}{\omega H_0}, \quad \hat{\nu} = \frac{\nu}{\omega L^2}, \quad (21)$$

and we have rescaled the drag and viscosity terms with ε ; i. e. we have assumed that they are small.

We now assume that there are a fast and a slow timescale in the problem, such that $\frac{\partial}{\partial t} = \frac{\partial}{\partial t} + \varepsilon \frac{\partial}{\partial T}$. On dropping the $\hat{\cdot}$, equations (19) and (20) become

$$\eta_t + (Hu)_x = -\varepsilon(\eta u)_x - \varepsilon\eta_T, \quad (22)$$

$$u_t + \beta\eta_x = -\varepsilon uu_x - \varepsilon \frac{\alpha u}{H + \varepsilon\eta} + \varepsilon\nu u_{xx} - \varepsilon u_T. \quad (23)$$

We now pose expansions in the form $u \sim u_0 + \varepsilon u_1 + \dots$ and $\eta \sim \eta_0 + \varepsilon\eta_1 + \dots$. To leading order, equations (22) and (23) are

$$\eta_{0t} + (Hu_0)_x = 0, \quad (24)$$

$$u_{0t} + \beta\eta_{0x} = 0. \quad (25)$$

Differentiating equation (24) with respect to time and using equation (25), we obtain the single equation for the wave height, η :

$$\eta_{0tt} = \beta(H\eta_{0x})_x. \quad (26)$$

In the simple case of a rectangular tank of constant depth H_0 and width L , such that the scaled boundaries are at $x = 0$ and $x = 1$, (where we require the velocity to vanish, so $\eta_x = 0$ if we assume time periodic solutions), there are solutions of the form

$$\eta = Ae^{it} \cos\left(\frac{x}{\sqrt{\beta}}\right), \quad (27)$$

where we require $\pi = \sqrt{\beta}$, i. e. $\omega = \frac{\pi\sqrt{gH_0}}{L}$. In dimensional terms, the solution for η is

$$\eta = Ae^{i\omega t} \cos\left(\frac{\pi x}{L}\right). \quad (28)$$

This first approximation to the behaviour of the seiche wave will be used in Section 3.3 below.

Numerical solutions for a given basal topography

It is possible to solve equation (26) numerically for a given basal topography, if we again assume time periodic solutions. We replace the right hand boundary, previously a vertical tank wall, by a non-erodible dam of prescribed shape, so that dimensionlessly $H = 0$ at $x = 1$. As this is an eigenvalue problem, we require three boundary conditions. On the left boundary, $x = 0$, we require that $u = 0$. At $x = 1$ (where $H = 0$) we require that the solution is regular. For the case of a uniformly sloping base, an analytic solution may be found in terms of Bessel functions, such that $\eta \sim J_0(x^{1/2})$ [19]. This analytic solution is shown in figure 5. We set $y = 1 - x$, such that close to $x = 1$,

$$\eta \sim J_0[(1 - y)^{1/2}] \sim 1 + O(1 - y). \quad (29)$$

To ensure we obtain a regular solution, we therefore require that $\eta = 1$ at $x = 1$. We note that near $x = 1$, $H \sim -(1 - x)H'_*$, where $H'_* = H'|_{x=1}$. Again setting $y = 1 - x$, we use equation (26) to write

$$-\omega^2\eta = \beta H'_*(y\eta)'. \quad (30)$$

which gives, to leading order,

$$\omega^2\eta = \beta H'_*\eta'. \quad (31)$$

The three boundary conditions are therefore

$$\eta = 0 \quad \text{on } x = 0, \quad (32)$$

$$\eta = 1 \quad \text{on } x = 1, \quad (33)$$

$$\omega^2\eta = \beta H'_*\eta' \quad \text{on } x = 1. \quad (34)$$

Note that if $H'_* = 0$, the problem is ill-posed, as boundary conditions (33) and (34) then imply both $\eta = 0$ and $\eta = 1$ at $x = 1$. A numerical solution of equation (26) with boundary conditions (32) – (34) for a dam of Gaussian shape is shown in figure 6.

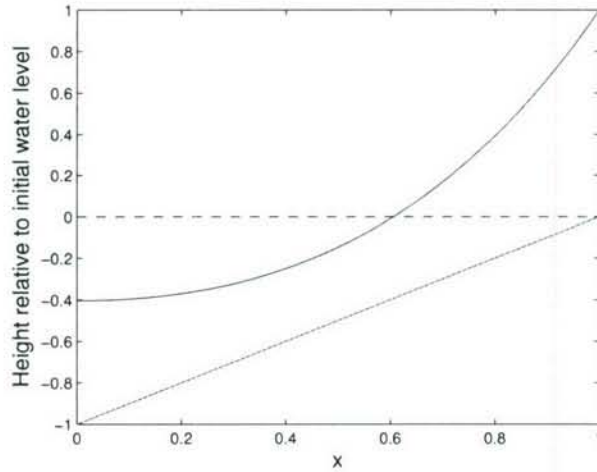


Figure 5: Numerical result for a uniformly sloping bed, with initial water depth given by $H(x) = 1 - x$. The upper solid line is the water surface, the lower line the basal topography. The dashed line indicates the initial water level.

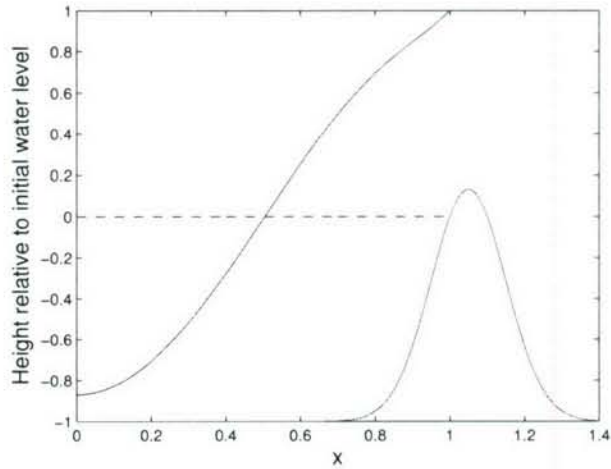


Figure 6: Numerical result for a uniformly sloping bed, with initial water depth given by $H(x) = 1 - 1.1 \exp(-(x - 1.05)^2 / (2 \times 0.1^2))$. The upper solid line is the water surface, the lower line the basal topography. The dashed line indicates the initial water level.

Higher order terms

We consider solutions of equation (26) of the form

$$(\eta_0, u_0) = (N, iU)A(T)e^{i\omega t} + \text{c.c.}, \quad (35)$$

thus N, U are real. Equations (24), (25) and (26) then become

$$\omega N = -(HU)_x, \quad (36)$$

$$U = \beta N_x, \quad (37)$$

$$-\omega^2 N = \beta(HN_x)_x, \quad (38)$$

with solutions as above. To the next order in ε , we then have

$$\eta_{1t} + (Hu_1)_x = -(\eta_0 u_0)_x - \eta_{0T}, \quad (39)$$

$$u_{1t} + \beta\eta_{1x} = -u_0 u_{0x} - \frac{\alpha u_0}{H} + \nu u_{0xx} - u_{0T}. \quad (40)$$

We now use equation (35) to write equations (39) and (40) in terms of N and U ;

$$\eta_{1t} + (Hu_1)_x = -iA^2 NU e^{2i\omega t} - A_T N e^{i\omega t} + \text{c.c.} \quad (41)$$

$$u_{1t} + \beta\eta_{1x} = A^2 U U_x e^{2i\omega t} - 2AA^* U U_x - \frac{\alpha i AU e^{i\omega t}}{H} + i\nu AU_{xx} e^{i\omega t} - iA_T U e^{i\omega t} + \text{c.c.} \quad (42)$$

We can find particular solutions to remove any terms on the right hand sides of equations (41) and (42) which are not multiples of $e^{i\omega t}$. The remaining parts which are proportional to $e^{i\omega t}$ are potentially secular in time, and must therefore be removed in order to find a uniform asymptotic approximation over the fast time t . Discarding the non-secular inhomogeneous terms, and assuming that $\eta_1 = \eta_1(x)e^{i\omega t}$ and $u_1 = u_1(x)e^{i\omega t}$, the system we therefore look to solve is

$$i\omega\eta_1 + (Hu_1)_x = -A_T N e^{i\omega t} \quad (43)$$

$$i\omega u_1 + \beta\eta_{1x} = -\frac{\alpha i AU e^{i\omega t}}{H} + i\nu AU_{xx} e^{i\omega t} - iA_T U e^{i\omega t}. \quad (44)$$

Equations (43) and (44) may be rewritten as

$$i\omega\eta_1 + (Hu_1)_x = I_1, \quad (45)$$

$$i\omega u_1 + \beta\eta_{1x} = I_2, \quad (46)$$

where

$$I_1 = -A_T N, \quad (47)$$

$$I_2 = -\frac{\alpha i AU}{H} + i\nu AU_{xx} - iA_T U. \quad (48)$$

We combine equations (45) and (46) to obtain

$$\omega^2 \eta_1 + \beta(H\eta_{1x}) = -i\omega I_1 + (HI_2)_x, \quad (49)$$

and then integrate equation (49) with respect to x . After integrating by parts and using the seiche equations (36) and (37), we obtain

$$\int_0^1 N [-i\omega I_1 + (HI_2)_x] dx = 0, \quad (50)$$

which can be simplified using equations (47) and (48) to give

$$-2A_T \int_0^1 \omega N^2 dx + \alpha A \int_0^1 NU_x dx + \nu A \int_0^1 N(HU_{xx})_x dx = 0. \quad (51)$$

This then gives a solution of the form $A = A_0 e^{-\gamma T}$, where γ is evaluated numerically using equation (51). The calculation can be repeated for dissipative terms given by Chèzy drag and viscosity, yielding

$$A_T \int_0^1 \omega N^2 dx = -\nu A \int_0^1 N(HU_{xx})_x dx + \frac{4A|A|c_f}{\pi} \int_0^1 N(U|U|)_x dx. \quad (52)$$

Again, the integrals in equation (52) may be evaluated numerically for any given basal topography $H(x)$, and this allows the relative importance of the dissipative terms to be quantified.

3.2 Modelling the dambreak

Erosion

The flux of sediment is governed by a (dimensionless) critical value of the Shields stress, defined by

$$\tau_* = \frac{u_*^2}{RgD}, \quad (53)$$

where $R = \frac{\rho_s - \rho_l}{\rho_l}$ is the specific gravity, D is a typical particle diameter and u_* is the threshold velocity, which is particular to the sediment and is determined empirically. The idea is that the fluid flow needs to exceed the threshold velocity in order to exert enough shear stress at the base to lift particles into suspension and thereby erode the bed.

We follow Parker [20], [21] and use the following empirical, dimensionless erosion law

$$E(u) = \begin{cases} \left(\frac{u^2}{u_*^2} - 1 \right)^{1.5} & \text{for } u > u_*, \\ 0 & \text{for } u < u_*. \end{cases} \quad (54)$$

A law of this type captures the two important features of any erosion law: below a certain threshold, there is no erosion, and for large values of the Shields stress (or velocity, in this case), erosion has a power law behaviour. The exponent in equation (54) is again empirically determined and, while not universally agreed upon, it is common to use the value 1.5 [14].

In fluvial systems, the Exner equation (conservation of sediment) is commonly used to model the erosion of the dam (which has elevation $\zeta(x, t)$),

$$(1 - \lambda_p) \frac{\partial \zeta}{\partial t} + \frac{\partial q_s}{\partial x} = 0, \quad (55)$$

where λ_p is the sediment porosity and q_s is the sediment flux, which is again determined empirically as a function of the Shields stress.

However, it is also possible to consider the evolution of the dam height to be the net effect of erosion and deposition,

$$\frac{\partial \zeta}{\partial t} = -wE(u) + w_s C, \quad (56)$$

where the first term on the right hand side of equation (56) represents erosion and the second represents deposition. w is a sediment-dependent constant with units of velocity, w_s is a particle settling velocity, and C is a depth-averaged volumetric sediment concentration. Equation (56) must then be supplemented with an equation to describe the evolution of C , and it is usual to use an advection-diffusion equation, moderated by erosion and deposition, thus

$$h(C_t + uC_x) = \kappa hC_{xx} + wE(u) - w_s C, \quad (57)$$

where κ is the sediment diffusivity. As a first approximation, we assume there is no deposition; thus we eliminate C and simply use

$$\frac{\partial \zeta}{\partial t} = -wE(u). \quad (58)$$

We calculated w experimentally using equation (58), and performing erosion experiments where we measured the dam height, ζ (at a fixed point in space as a function of time), and the flow velocity u . We followed Parker [14] and calculated u_* using the following empirical relationship for τ_*

$$\tau_* = 0.5 \left[0.22 Re_p^{-0.6} + 0.06 \times 10^{-7.7 Re_p^{-0.6}} \right], \quad (59)$$

where Re_p is the particle Reynolds number, defined as

$$Re_p = \frac{(RgD)^{1/2} D}{\nu}. \quad (60)$$

Equation (59) coupled with equation (53) allows estimation of u_* and thus w . Typical values for the sediments used experimentally are given in Table 5. It is much more complicated to estimate sediment parameters for a mixture of sediments, and so this was not attempted. For calculations involving particle diameter (such as estimation of the particle Reynolds number), the modal particle size was used.

Sediment	Re_p	τ_*	u_* (m s ⁻¹)	w (m s ⁻¹)
Play sand	20	0.0198	9×10^{-3}	9.6×10^{-9}
Beach sand	107	0.0169	1.5×10^{-2}	4.7×10^{-8}
Grit	147	0.0179	1.7×10^{-2}	4.9×10^{-8}

Table 5: Empirically and experimentally determined sediment properties.

Hydraulic Control

We now use a hydraulic model coupled with erosion to describe the dambreak. Hydraulic models are commonly used to describe stratified flows over sills in the ocean, see Pratt [15], for example. The benefit of using such a model is that at one or more locations in the system the flow adjusts to a well-defined state; i. e. it is in some sense ‘controlled’ by this critical point. Here, the location of hydraulic control will be the point at which the dam height is a maximum.

Hydraulic control theory also assumes steady flow. From equation (58), we have that the timescale over which erosion occurs is $t_E \sim \frac{H}{wE_0}$. Using typical values from Table 5, $u_* = 1 \times 10^{-2} \text{ m s}^{-1}$ and $w = 5 \times 10^{-8} \text{ m s}^{-1}$, and a typical experimental value $H = 0.1 \text{ m}$, we estimate that $t_E \approx 100 \text{ s}$. This implies that for the dambreak $\frac{\partial}{\partial t} \ll 1$, and we can therefore neglect the time derivatives in the shallow water equations (1) and (2). As a first approximation, we also neglect drag and viscosity (although it is possible to include these in the description, see Pratt [15], Hogg and Hughes [7]).

We can therefore integrate the equations for conservation of mass and momentum with respect to x to obtain

$$q = hu, \quad (61)$$

$$\frac{1}{2}u^2 + g(h + \zeta) = B, \quad (62)$$

where q is the constant water flux (with units $\text{m}^2 \text{ s}^{-1}$) and B is the energy, sometimes referred to as the Bernoulli constant.

We consider the problem of a reservoir of depth H and length L , which must drain over a dam of maximum height ζ_m . Here, the subscript m will be used to denote evaluation of a function at this maximum of ζ ; thus u_m is the flow velocity at the highest point of the dam. We assume that the dam has finite width, and thus $\zeta = 0$ outside some finite region. We can therefore use equations (61) and (62) to write

$$B = \frac{1}{2} \frac{q^2}{H^2} + gH \approx gH, \quad (63)$$

if we assume that the depth of the reservoir is much greater than the depth of the water flowing over the dam, i. e. $H \gg h$. Using equation (61), we may write the non-integrated momentum equation in the form

$$u_x = \frac{-g\zeta_x u^2}{u^3 - gq}, \quad (64)$$

and thus for the velocity gradient to be defined at all points in the system, we require that $u^3 = gq$ at the point where $\zeta_x = 0$; i. e. where $\zeta = \zeta_m$. We therefore obtain

$$u_m = (gq)^{\frac{1}{3}}, \quad h_m = \frac{q}{u_m} = \left(\frac{q^2}{g}\right)^{\frac{1}{3}}. \quad (65)$$

Note that we can use the expressions in equation (65) to write the Bernoulli constant as

$$B = \frac{3}{2}u_m^2 + g\zeta_m. \quad (66)$$

Equations (63) and (66) allow us to relate upstream variables to those at the maximum height of the dam,

$$gH = \frac{3}{2}u_m^2 + g\zeta_m. \quad (67)$$

To complete the system, we couple equations (61) and (62) with equations describing the drainage of the lake,

$$L \frac{dH}{dt} = -q, \quad (68)$$

and the erosion of the dam,

$$\frac{\partial \zeta}{\partial t} = -wE(u). \quad (69)$$

Nondimensionalisation

We nondimensionalise the system of equations (61), (62), (68) and (69) using the following scales

$$u \sim u_0, \quad h \sim h_0, \quad H \sim H_0, \quad \zeta \sim H_0, \quad t \sim t_0, \quad q \sim q_0, \quad E \sim E_0. \quad (70)$$

and thus obtain

$$\left(\frac{q_0}{h_0 u_0}\right) q = hu, \quad (71)$$

$$\frac{1}{2} \frac{u_0^2}{gH_0} u^2 + \left(\frac{h_0}{H_0}\right) h + \zeta = B^*, \quad (72)$$

$$\left(\frac{LH_0}{q_0 t_0}\right) \frac{dH}{dt} = -q, \quad (73)$$

$$\left(\frac{H_0}{wt_0 E_0}\right) \frac{\partial \zeta}{\partial t} = -E(u), \quad (74)$$

where B^* is the dimensionless Bernoulli constant.

We make the choices $q_0 = h_0 u_0$, and as we are interested in the timescale over which erosion occurs, we choose $t_0 = \frac{H_0}{wE_0}$. Equations (71) – (74) then become

$$q = hu, \quad (75)$$

$$\frac{1}{2} F^2 \alpha^2 u^2 + \alpha h + \zeta = B^*, \quad (76)$$

$$\mu \frac{dH}{dt} = -q, \quad (77)$$

$$\frac{\partial \zeta}{\partial t} = -E(u^2), \quad (78)$$

where the dimensionless parameters are the Froude number, $F^2 = \frac{u_0^2}{gH_0}$, the ratio of the water height at the dam peak to the reservoir height, $\alpha = \frac{h_0}{H_0}$, and a measure of how quickly erosion occurs relative to lake drainage, $\mu = \frac{wLE_0}{q_0}$. We now make the further choices $h_0 = H_0$ and $u_0 = \sqrt{gH_0}$, such that $\alpha = F^2 = 1$.

The dimensionless form of the erosion law (equation (61)) is

$$E(u) = (u^2 - \delta^3)_+^{1.5}, \quad (79)$$

where $E_0 = \left(\frac{u_0}{u_*}\right)^3$, $\delta = \frac{u_*}{u_0}$ and the subscript $_+$ indicates that $E = 0$ when the quantity in the brackets is less than zero.

We take typical experimental values: $H_0 = 0.1$ m, $w = 5 \times 10^{-8}$ m s $^{-1}$, $L = 1$ m, $u_0 = 1$ m s $^{-1}$ and $u_* = 1 \times 10^{-2}$ m s $^{-1}$, to obtain

$$\mu = 0.5, \quad \delta = 10^{-2}, \quad E_0 = 1 \times 10^5. \quad (80)$$

Again, we estimate $t_0 = 100$ s, which should be both the timescale for erosion and for lake drainage in our experiments (as μ is $O(1)$).

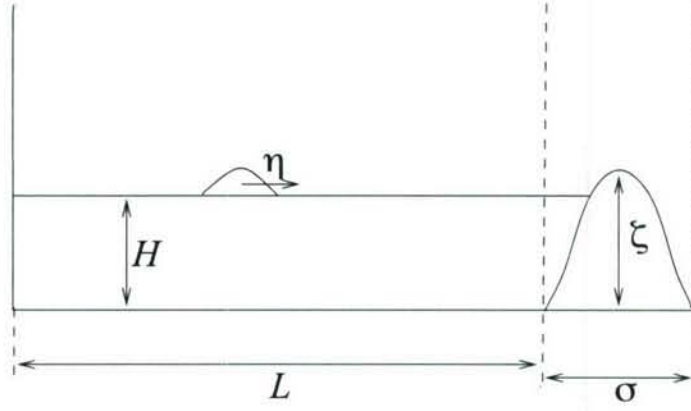


Figure 7: Schematic diagram of the two domains under consideration: a lake of length L and depth H adjacent to a dam of width σ and height ζ , such that $\sigma \ll L$ and, initially, $H \sim \zeta_m$.

3.3 Unified theory: spatially distributed dam

In order to combine the theory of the seiche wave (outlined in Section 3.1) with the hydraulic model, we consider the following configuration, shown in figure 7: a rectangular lake of length L and mean level $H(t)$, on which there is a seiche wave of amplitude $\eta(x, t)$. The lake is adjacent to a dam of height $\zeta(x, t)$ and width σ , where $\sigma \ll L$.

We now revisit the scalings used Sections 3.1 and 3.2. In the lake,

$$h = H + \varepsilon\eta, \quad t \sim \frac{1}{w} \sim \frac{\sqrt{gH_0}}{L}, \quad x \sim L, \quad u \sim \varepsilon\sqrt{gH_0}, \quad (81)$$

while over the dam,

$$t \sim \frac{H_0}{wE_0}, \quad x \sim \sigma, \quad u \sim \sqrt{gH_0}. \quad (82)$$

We impose the condition that the timescale in the lake must be of the same order as that over the dam. However, we note that velocities in the lake are $O(\varepsilon)$ smaller than those over the dam, which means that the dam ‘sees’ the seiche wave as a gradual change in water depth, to which it can adjust instantaneously. We also note that x derivatives are much larger over the dam than in the lake.

We assume that there is a right hand boundary of the lake which lies close to the edge of the dam, $x = x_{\sigma-}$, such that $\zeta(x_{\sigma-}, t) = 0$. We consider the water height at this fixed point, given dimensionally by $h(x_{\sigma-}, t) = H(x_{\sigma-}, t) + \eta(x_{\sigma-}, t)$, and we suppose that $\eta(x_{\sigma-}, t) = \eta(t)$ satisfies the ordinary differential equation

$$\ddot{\eta} + \gamma\dot{\eta} + \omega^2\eta = 0, \quad (83)$$

where $\gamma = \frac{\alpha}{H}$ is the damping coefficient calculated in Section 3.1, and $\omega(H)$ is the seiche frequency. As we assume that the lake is a rectangular basin, we have that $\omega = \frac{\pi\sqrt{gH}}{L}$ and thus $\gamma = \gamma(H)$.

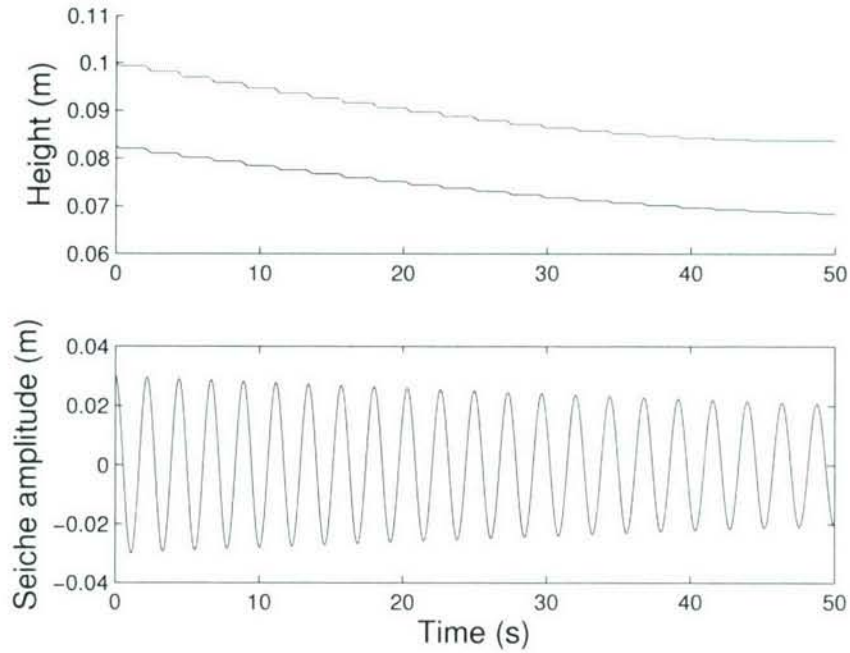


Figure 8: Solution of the spatially distributed system in the case of no dambreak, with initial conditions $\eta_0 = 0.03$ m, $H_0 = 0.0825$ m, $\zeta_0 = 0.01$ m. In the top plot, the upper (red) line shows the evolution of the maximum height of the dam, ζ_m , while the lower (blue) line shows the lake depth, H . We see that in this case there is no dambreak, as the lake level never exceeds the maximum height of the dam. The top plot shows that after approximately 42 s, erosion switches off while drainage continues; however, the velocities attained by the fluid are below the threshold and thus erosion cannot occur. The bottom graph shows the corresponding decay of the seiche amplitude.

We couple equation (83) with equations (62), (68) and (69); these are four equations for the four variables η , H , ζ and u . Numerical solutions to this system are shown in figures 8 – 10. We see that by changing the initial water depth, H_0 , (and thus the initial level of the lake below the dam), we change from a regime where dambreak is possible to one where it is not. This motivates the following attempt to identify the parameters in the system which govern this threshold behaviour.

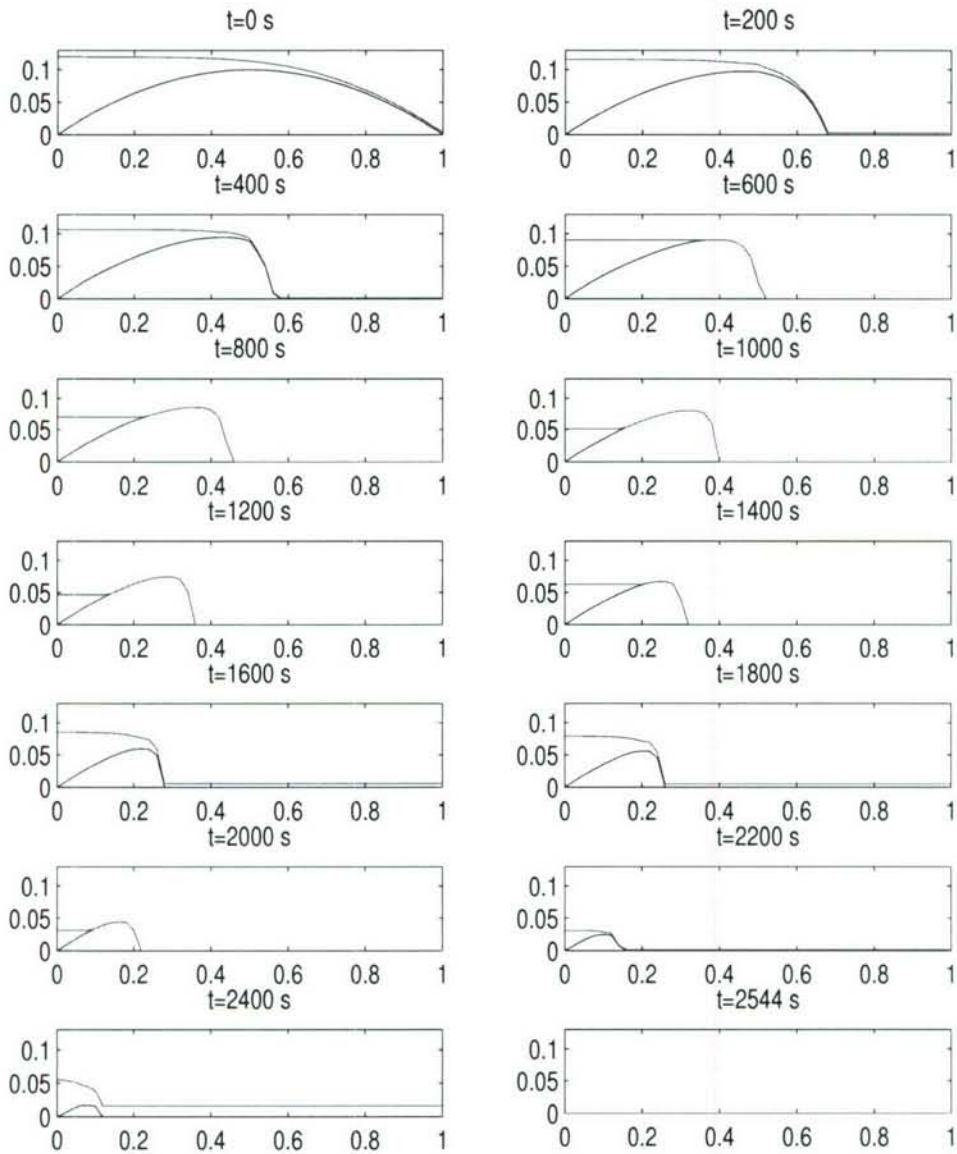


Figure 9: Snapshots of the solution in the case of dambreak, with initial conditions $\eta_0 = 0.03$ m, $H_0 = 0.09$ m, $\zeta_0 = 0.01$ m. The upper (red) line is the water level, h ; the lower (blue) line the dam surface, ζ . For all graphs, the x axis is position and the y axis height. The initial dam elevation is a parabola with endpoints at $x = 0$ and $x = 1$. The solution is shown at time intervals of 200 s, and then at the time when the dam has completely eroded away (2544 s). Note the steepening of the downstream face of the dam as erosion progresses. This solution has 50 evenly spaced gridpoints.

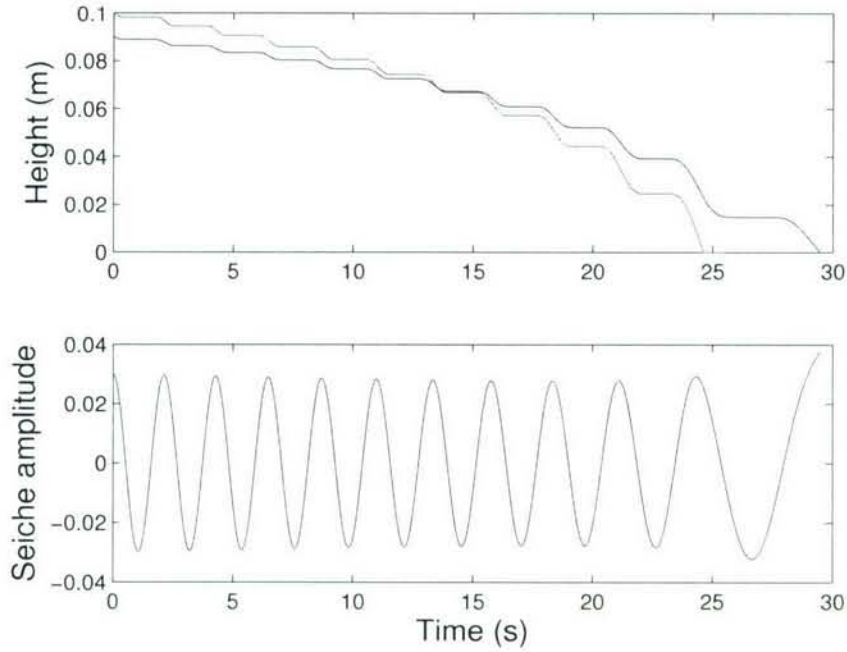


Figure 10: Solution in the case of a dambreak, for initial conditions $\eta_0 = 0.03$ m, $H_0 = 0.09$ m, $\zeta_0 = 0.01$ m (corresponding to figure 9). In the top plot, the (red) line, which is the line that is initially upper, shows the evolution of the maximum height of the dam, ζ_m , while the lower (blue) line shows the lake depth H . This plot shows erosion events, followed by periods of inactivity when the water level drops below the dam, and neither drainage nor erosion can occur. After seven such events $H > \zeta_m$, but drainage is still modulated by the seiche wave. The bottom graph shows the seiche amplitude. We note that as H becomes small so must ω , and to compensate for this, the amplitude of the seiche wave must increase.

3.4 Unified theory: point dam

To understand the governing parameters in the problem, we make a further simplification and assume that the dam can be approximated by a point, at which $\zeta = \zeta_m$. This reduces the model to the dimensional system

$$\ddot{\eta} + \gamma\dot{\eta} + \omega^2\eta = 0, \quad (84)$$

$$L \frac{dH}{dt} = -q = -\frac{u_m^3}{g}, \quad (85)$$

$$\frac{d\zeta_m}{dt} = -wE(u_m), \quad (86)$$

$$u_m = \left[\frac{2g}{3}(H + \eta - \zeta_m) \right]^{1/2}. \quad (87)$$

Equation (87) motivates the definition of a new variable, $\theta = H + \eta - \zeta_m$. Thus when $\theta > 0$ the height of the water in the lake is greater than the height of the dam, so the lake can drain over the dam. When $\theta > \theta_*$ (corresponding to the threshold velocity for erosion, u_*), erosion can occur. For $\theta < 0$, the water level is below the dam and neither drainage nor erosion can occur.

Using this definition of θ , we write equation (87) as

$$u_m = \left(\frac{2g}{3}\theta \right)^{1/2}, \quad (88)$$

and combine equations (84) and (85) to obtain a single ordinary differential equation for θ

$$\dot{\theta} = w\tilde{E}(\theta) - D\theta^{3/2} + \dot{\eta}, \quad (89)$$

where $D = \frac{1}{gL} \left(\frac{2g}{3} \right)^{3/2}$ is a drainage parameter (with units of velocity) and $\tilde{E}(\theta) = E \left[\left(\frac{2g}{3}\theta \right)^{1/2} \right]$. If we consider that H is approximately constant, then we can write the solution for the seiche wave in the form

$$\eta = \eta_0 e^{-\gamma t} \sin \omega t. \quad (90)$$

In this case, θ can be evaluated as a function of time, as shown in figure 11. We see that there are time intervals over which drainage can occur; i.e. where $\theta > 0$, and marginally shorter intervals where $\theta > \theta_*$ and erosion can occur. Erosion acts to increase these time intervals (by decreasing ζ_m and thus θ), while drainage and damping act to reduce these time intervals (by decreasing H and η respectively). We therefore see that there is a competition between erosion, which acts to increase θ , and lake drainage and seiche damping, which act to decrease θ .

This allows us to identify five parameters in the problem: the initial values θ_0 and η_0 , the drainage parameter D , the erosion parameter w and the parameter governing the damping of the seiche wave, γ . We see from figure 11 that decreasing θ_0 (the initial difference between the mean lake level and the dam height) and increasing the initial seiche amplitude η_0 will

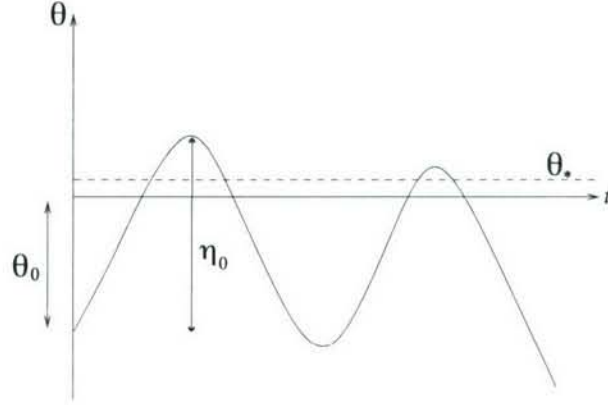


Figure 11: Schematic diagram of $\theta = H + \eta - \zeta_m$ as a function of time. When $\theta > 0$, drainage may occur, and when $\theta > \theta_*$, erosion switches on. Initially, $\eta = 0$ (from equation (90)), and thus θ_0 is simply $(H - \zeta_m)|_{t=0}$. At time $t \approx \frac{\pi}{\omega}$, $\theta \approx H + \eta_0 - \zeta_m$.

both act to increase the intervals over which erosion and drainage can occur, and thus increase the likelihood of a dam break - which is what one might intuitively expect. To investigate these parameters further, we use a difference method to crudely approximate the derivatives in equations (84) – (87). More specifically, if

$$\frac{dy}{dt} = f(y, t), \quad (91)$$

we use a difference scheme (essentially the forward Euler method) to write

$$y_n = y_{n-1} + \Delta t f(y_{n-1}, t_{n-1}), \quad (92)$$

where Δt is the time interval over which we consider the change in y . In terms of our model, we let n be the number of erosion ‘events’ i.e. time intervals over which $\theta > 0$. Then we set $\Delta t = T_{n-1}$, where T_{n-1} is the time interval over which the $(n - 1)$ th erosion event occurs.

Using figure 11, it can be estimated that

$$T_{n-1} = \frac{\pi}{\omega_{n-1}} - \frac{2}{\omega_{n-1}} \sin^{-1} \left(\frac{\zeta_{n-1} - H_{n-1}}{\eta_{n-1}} \right), \quad (93)$$

where $\omega_{n-1} = \frac{\pi \sqrt{gH_{n-1}}}{L}$. The system is now

$$\eta_n = \eta_{n-1} e^{-\frac{2\pi\gamma_n}{\omega_n}}, \quad (94)$$

$$H_n = H_{n-1} - T_{n-1} \frac{u_{n-1}^3}{gL}, \quad (95)$$

$$\zeta_n = \zeta_{n-1} - wT_{n-1} E(u_{n-1}), \quad (96)$$

$$u_n = \left[\frac{2g}{3} (H_n + \eta_n - \zeta_n) \right]^{1/2}. \quad (97)$$

Equations (93)–(97) may be solved numerically. Figure 12 shows a comparison between results from this model and those of the spatially distributed model outlined in Section 3.3 above. We see that there is agreement between the models, indicating that the simple discretised model may be sufficient to estimate the critical values of the governing parameters.

We have now answered the question posed initially regarding threshold behaviour of this system - in the context of this simple model, at least. Understanding such behaviour is useful in terms of hazard mitigation. For example, many moraine dams in the Cordillera Blanca are drained by artificial channels [8]. Figure 12 allows an estimate to be made of how low the lake level should be in order that no reasonably sized wave can break the dam.

We also wish to use our model to estimate the peak discharge of a drainage flood. The hydraulic model gives the ‘weir formula’ for the discharge,

$$q = \left(\frac{2}{3}\right)^{3/2} g^{1/2} (H - \zeta_m)^{3/2}, \quad (98)$$

which is simply obtained from equations (61) and (65). We compare this formulation with the experimentally determined flux. Figure 13 shows time series of water depth in a lake which drained by catastrophic erosional incision. The smaller tank width of 5 cm was chosen to prevent channelization occurring; channels formed in the 20 cm wide tank.

We used the data from figure 13 to estimate the maximum value of $\frac{dH}{dt}$. Using a value $L = 1$ m, we were then able to estimate the maximum value of q using equation (77). This value was then multiplied by the width of the lake. To use the weir formula, we estimated the maximum value of $H - \zeta_m$ during the experiment. We then multiplied this value by the width of the channel (5 cm in both cases, as the channel which formed in the 20 cm wide tank also had approximately this width).

Thus we obtain, for the narrow tank,

$$Q_{\text{data}} = 1 \times 10^{-4} \text{ m}^3\text{s}^{-1}, \quad Q_{\text{weir}} = 1 \times 10^{-4} \text{ m}^3\text{s}^{-1}.$$

while for the wide tank,

$$Q_{\text{data}} = 4 \times 10^{-4} \text{ m}^3\text{s}^{-1}, \quad Q_{\text{weir}} = 1 \times 10^{-3} \text{ m}^3\text{s}^{-1}.$$

We see that the predictions agree in the case of the narrow tank, but there is an overestimation of the peak discharge by the weir formula in the case of the wide tank. This may be due to our approximation of the channel as a breach of constant width.

We can compare the weir formula with empirically derived estimates of the peak discharge. Clague and Evans [2], for example, give

$$Q \sim Q_0(\lambda) (gd^5)^{1/2}, \quad \lambda = \frac{kV}{(gd^7)^{1/2}},$$

where d is the breach depth, k is the rate (speed) of breach growth and V is the lake volume. We see that, in the case of a square breach, the weir formula would also have a $d^{5/2}$ dependence, indicating that a simple hydraulic model may capture some elements of the flood well. However, the dynamics of the channel are missing from the model, and will undoubtedly play an important role.

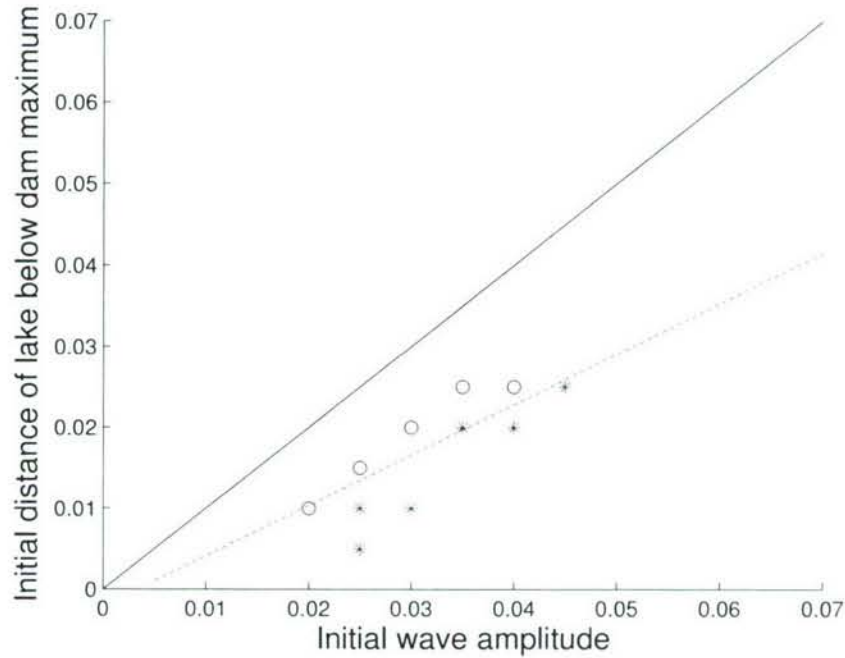


Figure 12: Comparison of the discretised point dam model with the spatially distributed model. We fix all parameters and vary only the initial wave amplitude η_0 and the initial distance between the mean water level in the lake and the dam, $(H - \zeta_m)|_{t=0}$. Above the upper (black) line we are in the physically unrealistic regime where η_0 is too small to overtop the dam: in this case, catastrophic incision will never occur. The lower (magenta) line indicates the results from the difference model: above this line, there is no dam break. This makes physical sense, as it implies that decreasing η_0 makes it more difficult to break the dam, while increasing the initial lake level makes it easier. On top of this are plotted results from the spatially distributed model: (red) stars indicate parameter values where incision occurred; (black) circles where it did not. We see that there is agreement between the models, although more numerical simulations using the spatially distributed model should be performed.

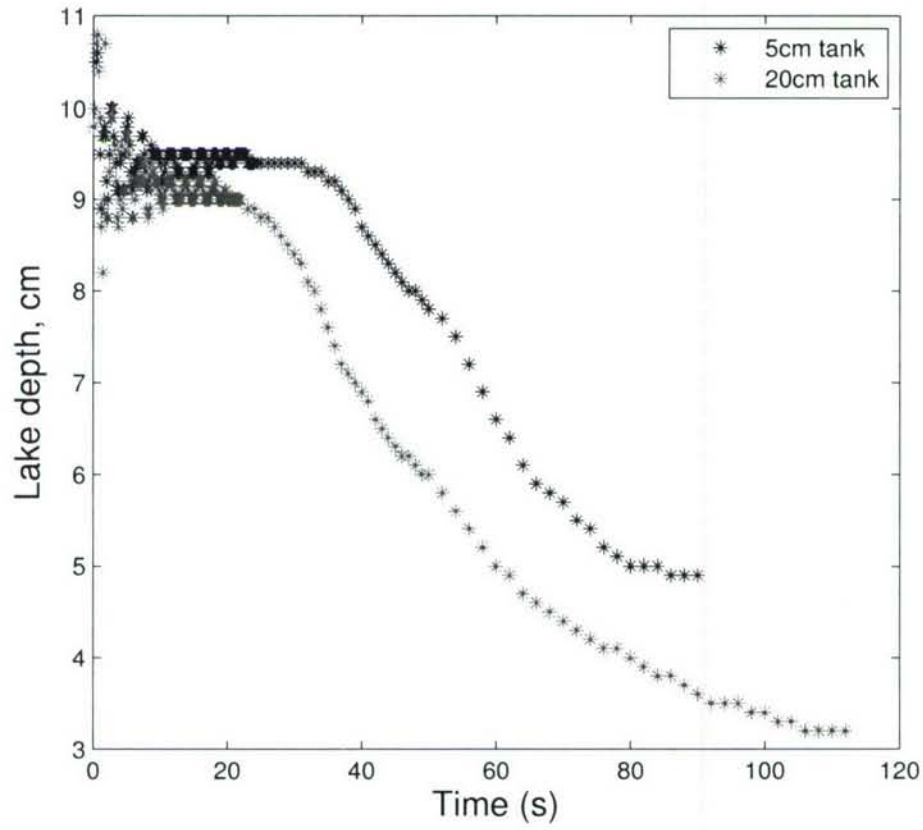


Figure 13: Time series of $H(t) + \eta(t)$ for experiments performed in a 5 cm wide tank (upper blue stars) and a 20 cm wide tank (lower magenta stars). The initial fluctuations in the data are due to the seiche wave.

4 Conclusions and future work

In this project, we have formulated and solved a one dimensional model to try and understand the breaking of a moraine dam by a mechanism which we term catastrophic erosional incision. We have seen that, experimentally, dissipation of the seiche is accounted for by linear drag and that the dambreak can be described using a hydraulic model. On joining these two simple theories together, we are able to make some rough estimates of the threshold behaviour of the phenomenon. These estimates agree qualitatively with experimental results.

Experimentally, we have confirmed the applicability of a linear damping law for the seiche wave. We have seen that the bimodal particle size distribution of moraine may explain why moraine dams are prone to fail in such a spectacular fashion: the combination of large boulders and fine sands makes the dam stable, but the loose consolidation means that it is also easily eroded. We have also compared a theoretical formulation of the peak discharge with experiment.

However, there is much future work to be done. The first step would be to include deposition in the model, as this is observed to occur experimentally. For example, as the dam erodes in the numerical simulation (figure 9), the downstream face of the dam steepens. However, experimentally the downstream face is much shallower, and the dam never erodes away completely: a dam of constant, shallow downstream slope (and approximately one quarter of the original height) remains. This final shape can perhaps be explained by the effects of deposition. Modelling this would involve either using the Exner formulation or incorporating the depth-averaged volumetric sediment into the model as described in Section 3.2.

Improvements could also be made in the description of the interaction between the seiche wave and the dam. We can use numerical methods, such as those described in Section 3.1, to allow for a more realistic basal topography. The seiche mode for such a topography, as shown in figure 6, can be coupled with a 'runup' law [19] to describe how far the seiche wave moves up the dam, and thus allow for a better coupling of the one dimensional seiche theory with the hydraulic model.

The next important step is to add an extra spatial dimension to the model in order to study the channelization instability and understand the channel dynamics. Even a basic understanding of the channel dynamics would allow for a better estimate of the peak discharge to be made. Figure 14 shows an experiment when four channels formed initially on the downstream face of the dam; two of these channels were incised to a sufficient depth to drain the lake, and did so simultaneously. It is therefore clear understanding the channelization process is key to understanding these catastrophic drainage events. Comparison can be made with the channelization instability of a flowing sheet over an erodible bed (Smith-Bretherton model, [17]), whereby a thicker layer of water acts to increase erosion, and thus deepen a channel. It should be noted, however, that in its original form such a model is mathematically ill-posed.

Finally, there is scope for more experimental exploration of some of the ideas here - a test of the results in figure 12, for example, where more accurate measurements than those obtained in our experiments would be required. Experiments could also be useful in helping to understand the channel dynamics.



Figure 14: Photograph from laboratory experiments, flow is from top to bottom. Here two channels (one on the far left, one on the far right) are draining the lake (located at the top of the picture) simultaneously. Four channels formed initially on the downstream face of the dam.

Acknowledgements

Firstly, I would like to thank Neil Balmforth for his help and patience this summer - I have certainly learned a lot! Thanks also to Keith Bradley for his 'amazing' work in the lab, and to both John and Neil for organising such an enjoyable and educational summer. Finally, thanks to the GFD staff and fellows for being so friendly (and patient on the softball field). A special thankyou must go to the monkey for the pep talks and last-minute computer wizardry.

References

- [1] BAINES P.G. AND WHITEHEAD J.A. *On multiple steady states in single-layer flows*, Physics of Fluids, 15(2) (2002), pp. 298-307.
- [2] CLAGUE J.J. AND EVANS S.G. *A review of catastrophic drainage of moraine-dammed lakes in British Columbia*, Quaternary Science Review, 19 (2000), pp. 1763-1783.
- [3] CLARKE G.K.C. *Subglacial Till: A Physical Framework for Its Properties and Processes*, Journal of Geophysical Research, 92(B9) (1987), pp. 9023-9036.
- [4] COSTA J.E. AND SCHUSTER R.L. *The formation and failure of natural dams*, Bulletin of the Geological Society of America, 100(7) (1988), pp. 1054-1068.
- [5] ERICKSEN G.E., PLAFKER G. AND CONCHA J.F., *Preliminary report on the geologic events associated with the May 31, 1970, Peru earthquake*, U.S. Geologic Survey Circular, 639 (1970), 25 pp.
- [6] FOWLER A.C., *Mathematics and the Environment*, Mathematical Institute (Oxford University), 2004, 264 pp.

- [7] HOGG, A.M. AND HUGHES G.O. *Shear flow and viscosity in single-layer hydraulics*, Journal of Fluid Mechanics, 548 (2006), pp. 431-443.
- [8] HUBBARD B. ET AL. *Impact of a rock avalanche on a moraine-dammed proglacial lake: Laguna Safuna Alta, Cordillera Blanca, Peru*, Earth Surface Processes and Landforms, 30 (2005), pp. 1251-1264.
- [9] KERSHAW J.A., CLAGUE J.J. AND EVANS S.G. *Geomorphic and sedimentological signature of a two-phase outburst flood from moraine-dammed Queen Bess Lake, British Columbia, Canada*, Earth Surface Processes and Landforms, 30 (2005), DOI: 10.1002/esp.1122.
- [10] KEULEGAN G.H. *Energy dissipation in standing waves in rectangular basins*, Journal of Fluid Mechanics, 6 (1959), pp. 33-50.
- [11] MEHTA A. AND BARKER G.C. *Bistability and hysteresis in tilted sandpiles*, Europhysics Letters, 56(5) (2001), pp. 626-632.
- [12] MILES J.W. *Surface-Wave Damping in Closed Basins*, Proceedings of the Royal Society of London A, 297 (1967), pp. 459-475.
- [13] MILES J. W. *Harbor Seiching*, Annual Review of Fluid Mechanics, 6 (1974), pp. 17-36.
- [14] PARKER G. *1D sediment transport morphodynamics with applications to rivers and turbidity currents*, last updated April 13 2006, http://cee.uiuc.edu/people/parkerg/morphodynamics_e-book.htm
- [15] PRATT, L.J. *Hydraulic Control of Sill Flow with Bottom Friction*, Journal of Physical Oceanography, 16 (1986), pp. 1970-1980.
- [16] RABASSA J. RUBULIS S. AND SUAREZ J. *Rate of formation and sedimentology of (1976-1978) push-moraines, Frias Glacier, Mount Tronadoz (41° 10' S; 71° 53' W), Argentina*, in Schluchter C. (ed.): *Moraines and varves: origins, genesis, classification*. Rotterdam, Balkema (1979).
- [17] SMITH T.R. AND BRETHERTON F.P. *Stability and the conservation of mass in drainage basin evolution*, Water Resources Research, 8(6) (1972), pp. 1506-1529.
- [18] STOKER J.J. *Water Waves*. Interscience Publishers, New York, 567 pp. Third Edition (1957).
- [19] SYNOLAKIS C.E. *The runup of solitary waves*, Journal of Fluid Mechanics, 185 (1987), pp. 523-545.
- [20] TAKI K. AND PARKER G. *Transportational cyclic steps created by flow over an erodible bed. Part 1. Experiments*, Journal of Hydraulic Research, 43(5) (2004), pp. 488-501.
- [21] TAKI K. AND PARKER G. *Transportational cyclic steps created by flow over an erodible bed. Part 2. Theory and numerical simulation*, Journal of Hydraulic Research, 43(5) (2004), pp. 502-514.

Patterns of convection in a mushy layer

S.R. Keating

March 15, 2007

Abstract

A solidification front advancing into a binary melt is often preceded by a mushy layer of fine dendritic crystals in thermodynamic equilibrium with solutal liquid in the interstices. One of the most striking features of such directional solidification — and most undesirable in industrial contexts — is the formation of vertical channels of zero solid fraction in the mushy layer. These “chimneys” are believed to form as a consequence of coupling between dissolution, solidification and compositional convection within the mush.

In this work, we extend the weakly nonlinear analysis of previous studies to the case of a continuous horizontal planform, in an effort to understand better the structure and spatial distribution of chimneys in a mushy layer. The relevant pattern equation is derived and has the form of a Swift-Hohenberg equation with an additional quadratic term. We show that this quadratic term is only present for the case of a hexagonal array of rolls and breaks the symmetry between up-flow and down-flow at the center of hexagons. Such symmetry-breaking is ultimately rooted in the non-Boussinesq solid-fraction dependence of the permeability within the mushy layer. Finally, we show that in a periodic domain the pattern equation exhibits localized structures which we interpret as nascent chimneys.

“Work is the curse of the drinking classes.” -Oscar Wilde

“One of us has to go.” -Oscar Wilde (last words, attrib.)

“Press On!” -EAS

1 Introduction

A mushy layer can be thought of as the means by which a solidification front adjusts to constitutional supercooling in a two-component melt. The mush itself is a forest of dendritic crystals — generated via morphological instability of the solid-liquid interface — in thermodynamic equilibrium with solutal liquid in the interstices. It can also be thought of as a reactive porous medium in which the solid fraction, and hence the permeability, is dynamically coupled to the flow. Mushy layers are found in a wide variety of situations in nature and industry: large alloy castings, sea ice, lava lakes and Earth’s inner-core boundary

are a few examples. For an overview of mushy layers and other issues in solidification theory, see Davis [1].

One of the most compelling features of mushy layers, and most undesirable in the context of industrial applications, is the formation of "chimneys" — quasi-vertical channels of zero solid fraction from which solute-poor residual liquid is expelled from the mush into the adjacent liquid region [2]. Such chimneys manifest themselves as "brine channels" in sea ice and are believed to give rise to "freckles" in alloy casting and geological formations.

Weakly nonlinear analysis of a simplified model of convection in a mushy layer was first carried out by Amberg & Homsy ([3]; hereafter AH93) and Anderson & Worster ([4]; hereafter AW95). In both of these treatments a discrete planform was assumed — three rolls of different amplitude were superimposed at 120 degrees to one another. In AW95 the relative stability of rolls (one non-zero amplitude), hexagons (three equal amplitudes) and mixed modes (three finite amplitudes, two equal) was calculated and it was concluded that there exists a transcritical bifurcation to hexagons.

AW95 also indicated the presence of a Hopf bifurcation, giving rise to an oscillatory instability examined in more detail in a later paper [5]. In contrast to an oscillatory instability detected earlier by Chen, Lu and Yang [6], and which owed its origin to double-diffusive convection in the liquid above, the instability of Anderson & Worster [5] is due to physical interactions internal to the mush itself. A number of authors have developed the theory of these oscillatory modes [7, 8, 9]. In this work, we shall focus attention on the direct mode, leaving its extension to the oscillatory case a subject for future research.

In this work we ask the following question: what determines the structure and spatial distribution of the chimneys? This article proceeds as follows: we briefly review the formulation of AH93 and AW95 in section 2 and the linear theory of Anderson & Worster [5] in section 3. In section 4 we extend the weakly nonlinear analysis of AW95 to the case of a continuous horizontal planform and derive the relevant pattern equation. In section 5, we calculate explicit expressions for the coefficients appearing in the pattern equation in terms of the physical parameters of the system for the near-marginal case of an infinitesimally thin band of wavenumbers centred on the critical value. We show in section 6 that the general, stationary pattern equation possesses solutions with localized structure and interpret these as nascent chimneys. Finally, in section 7 we discuss our results.

2 Formulation

We outline here the formulation of AH93 and subsequent studies [4, 5, 7, 8, 9, 10, 11], as depicted in fig.(1). The mush is modelled as a single porous layer sandwiched between liquid above and solid below. For mathematical expedience we prescribe a constant solidification speed V and assume that the mush is dynamically decoupled from both the liquid and the solid. These and subsequent assumptions are considered in detail in the references cited above and will not be discussed further here. It is sufficient to note that, while the assumptions simplify the analysis considerably, they preserve the essential physical interactions of interest.

It is assumed that, within the mushy layer, interstitial liquid is in thermodynamic equilibrium with fine-grained dendritic crystals, so that the temperature and solute fields are coupled via a liquidus relation

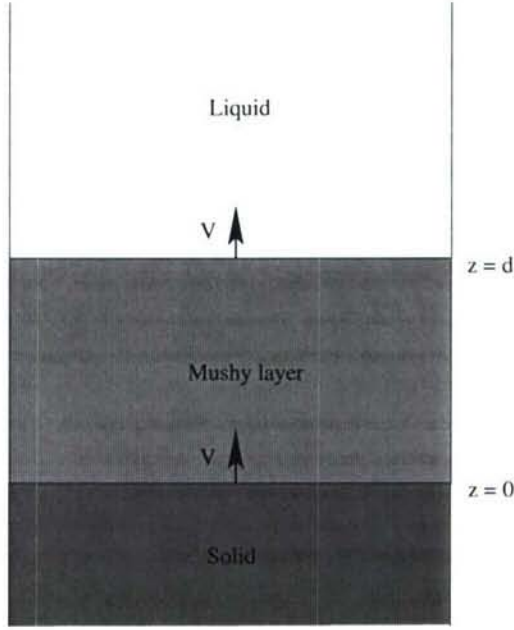


Figure 1: The model system. A solidification front advances into a binary alloy at a rate V . A mushy layer of thickness d is sandwiched between the two regions and advances with the front. The solid is at the eutectic temperature T_E and solid composition C_S ; the liquid region is at the far-field composition C_0 and associated liquidus temperature $T_L(C_0)$. See text and references for further discussion.

$$T = T_L(C). \quad (1)$$

The far-field composition C_0 and temperature T_∞ are taken to be above the eutectic composition ($C_0 > C_E$), and above the far-field liquidus temperature ($T_\infty > T_L(C_0)$), respectively. The temperature field T , solid fraction ϕ , fluid velocity \mathbf{u} and pressure p within the mushy layer are then governed by equations describing heat balance, solute balance, Darcy's law for flow in a porous medium, and mass continuity; the non-dimensional ideal mushy layer equations in a reference frame moving with the solidification front are given by Worster [12] as

$$(\partial_t - \partial_z)(\theta - \mathcal{S}\phi) + \mathbf{u} \cdot \nabla \theta = \nabla^2 \theta, \quad (2)$$

$$(\partial_t - \partial_z)((1 - \phi)\theta + \mathcal{C}\phi) + \mathbf{u} \cdot \nabla \theta = 0, \quad (3)$$

$$\mathcal{K}(\phi) \mathbf{u} = -\nabla p - Ra\theta \hat{\mathbf{z}}, \quad (4)$$

$$\nabla \cdot \mathbf{u} = 0. \quad (5)$$

The non-dimensional temperature field (or, via the liquidus relation (1), the compositional field) is

$$\theta = \frac{T - T_L(C_0)}{T_L(C_0) - T_E} = \frac{C - C_0}{C_0 - C_E}, \quad (6)$$

Symbol	Physical Quantity	Symbol	Physical Quantity
L	Latent heat	β	Expansion coefficient
c_l	Specific heat	g	Gravitational acceleration
T_E	Eutectic temperature	$\Pi(0)$	Permeability at zero solid-fraction
T_∞	Far-field temperature	κ	Thermal diffusivity
C_E	Eutectic composition	ν	Kinematic viscosity
C_0	Far-field composition	d	Mushy layer thickness
C_S	Solid composition	V	Speed of solidification front

Table 1: Physical quantities appearing in the dimensionless parameters \mathcal{S} , \mathcal{C} and Ra , and the mushy layer equations (2-5). For further details see cited references.

while lengths, times and velocities in (2-5) have been scaled with κ/V , κ/V^2 and V respectively, with κ as the thermal diffusivity. The function $\mathcal{K}(\phi)$ appearing in equation (4) measures the variation of permeability $\Pi(\phi)$ with solid fraction, with respect to some zero-solid-fraction permeability $\Pi(0)$, assumed finite:

$$\mathcal{K}(\phi) = \frac{\Pi(0)}{\Pi(\phi)}. \quad (7)$$

The dimensionless parameters appearing in (2-5) are the Stefan number

$$\mathcal{S} = \frac{L}{c_l (T_L(C_0) - T_E)}, \quad (8)$$

the concentration ratio

$$\mathcal{C} = \frac{C_S - C_0}{C_0 - C_E}, \quad (9)$$

and the Rayleigh number

$$Ra = \frac{\beta(C_0 - C_E) g \Pi(0) \kappa/V}{\nu \kappa}. \quad (10)$$

The various physical quantities appearing in (8-10) are listed in table (1). Further discussion of these parameters and their physical significance can be found in the references cited above.

A fourth dimensionless parameter, the dimensionless mush thickness $\delta = d/(\kappa/V)$, appears in the boundary conditions:

$$\theta = -1, w = 0 \quad \text{on } z = 0, \quad (11)$$

$$\theta = 0, w = 0, \phi = 0 \quad \text{on } z = \delta. \quad (12)$$

Boundary conditions (11) and (12) correspond to impermeable rigid plates co-moving with the upper and lower boundary of the mushy layer. The lower plate, between the solid and the mush, is maintained at the eutectic temperature T_E , while the upper boundary between the liquid and the mush (that is, at zero solid fraction ϕ), is maintained at the far-field liquidus temperature $T_L(C_0)$.

A more physically plausible kinematic upper boundary condition might be one of constant pressure p . Chung and Chen [10] considered a stress-free upper boundary condition and, while their analysis was much more involved than that of AH93 and AW95, no qualitatively new results were uncovered. We therefore proceed with confidence that the boundary conditions (11) and (12) preserve the interactions of interest without undue complication.

To isolate a parameter regime for which there is a physically interesting interplay between dissolution, solidification and convection we adopt the following additional scalings: we consider a thin mushy layer ($\delta \ll 1$) [3]; we assume a near-eutectic approximation ($C = \bar{C}/\delta = O(\delta^{-1})$) [13]; and we assume a large Stefan number ($S = \bar{S}/\delta = O(\delta^{-1})$) [4]. The reader may consult the cited references for further details on these scalings. We note in passing, however, that a key implication of the near-eutectic approximation ($C = O(\delta^{-1})$) is that the solid fraction is small, and hence the permeability is uniform to lowest order. As a consequence, we follow AH93 and expand the permeability in the small solid fraction:

$$\mathcal{K}(\phi) = 1 + \mathcal{K}_1\phi + \mathcal{K}_2\phi^2 + \dots \quad (13)$$

where, on physical grounds, we demand that $\mathcal{K}_1, \mathcal{K}_2$, etc. are non-negative.

3 Linear theory

We continue to follow AH93 and AW95 and rescale space and time as

$$\mathbf{x} \rightarrow \delta\mathbf{x}, \quad (14)$$

$$t \rightarrow \delta^2 t, \quad (15)$$

and introduce the effective Rayleigh number

$$R^2 = \delta Ra. \quad (16)$$

Note that, following the notation of AH93 and AW95, R is the *square root* of the effective Rayleigh number.

The dynamical fields θ , ϕ , \mathbf{u} and p are separated into a stationary basic state and a perturbation:

$$\begin{aligned} \theta &\rightarrow \theta_B(z) + \epsilon\theta(\mathbf{x}, t), \\ \phi &\rightarrow \phi_B(z) + \epsilon\phi(\mathbf{x}, t), \\ \mathbf{u} &\rightarrow \mathbf{0} + \epsilon\mathbf{u}(\mathbf{x}, t), \\ p &\rightarrow p_B(z) + \epsilon p(\mathbf{x}, t), \end{aligned} \quad (17)$$

where the subscript 'B' denotes the basic state and ϵ is the amplitude of the perturbations. Subtracting the basic states from the equations of motion and eliminating the pressure p via the incompressibility condition, we obtain the equations for the perturbations θ , ϕ and \mathbf{u} :

$$\begin{aligned}
(\delta\partial_z - \epsilon^2\partial_T) \left(\theta - \frac{\bar{S}}{\delta}\phi \right) - R'\theta'_B(z)w + \nabla^2\theta &= \epsilon R\mathbf{u} \cdot \nabla\theta, \\
(\delta\partial_z - \epsilon^2\partial_T) \left((1 - \delta\phi_B(z) - \epsilon\phi)\theta - \left(\theta_B - \frac{\bar{C}}{\delta} \right)\phi \right) - R\theta'_B(z)w &= \epsilon R\mathbf{u} \cdot \nabla\theta, \\
\nabla^2(\mathcal{K}u) - \partial_x(\mathbf{u} \cdot \nabla\mathcal{K}) - R\partial_x\partial_z\theta &= 0, \\
\nabla^2(\mathcal{K}v) - \partial_y(\mathbf{u} \cdot \nabla\mathcal{K}) - R\partial_y\partial_z\theta &= 0, \\
\nabla^2(\mathcal{K}w) - \partial_z(\mathbf{u} \cdot \nabla\mathcal{K}) + R\nabla_z^2\theta &= 0, \\
\nabla \cdot \mathbf{u} &= 0.
\end{aligned} \tag{18}$$

The equations of motion (18) can be written as

$$(\mathcal{L} - \mathcal{T}\partial_t)\mathbf{v} = \epsilon\mathbf{N}, \tag{19}$$

where $\mathbf{v} = \{\theta, \phi, \mathbf{u}\}$ is the vector of perturbed fields, $\mathcal{L} - \mathcal{T}\partial_t$ is the linear operator. We discard the nonlinearity \mathbf{N} by setting ϵ to zero, and look for solutions of the form $\mathbf{v}_{0k\sigma}(z) \exp(i\mathbf{k} \cdot \mathbf{x} + \sigma t)$ satisfying

$$(\mathcal{L}_{0k} - \sigma\mathcal{T}_{0k})\mathbf{v}_{0k\sigma} = 0. \tag{20}$$

Here, $\mathbf{k} = (k_x, k_y)$ and $\mathbf{x} = (x, y)$. Note that, as a consequence of the assumption that $\mathcal{K}_1 = O(\epsilon)$, variations in the permeability appear only at higher order.

The matrix operators \mathcal{L}_{0k} and \mathcal{T}_{0k} , the linear fields $\mathbf{v}_{0k\sigma}$, the growth rate σ and the basic states $\theta_B(z)$ and $\phi_B(z)$ can be expanded in powers of δ and the linear equation (20) solved perturbatively. Thus, we have

$$\mathcal{L}_{0k}(z) = \mathcal{L}_{00} + \delta\mathcal{L}_{01} + \dots \tag{21}$$

$$\mathbf{v}_{0k\sigma}(z) = \mathbf{v}_{00} + \delta\mathbf{v}_{01} + \dots \tag{22}$$

$$\sigma = \sigma_0 + \delta\sigma_1 + \dots \tag{23}$$

$$\phi_B(z) = -\delta\frac{z-1}{C} - \delta^2\left(\frac{(z-1)^2}{C^2} - \frac{z^2-z}{2C}\right) + \dots \tag{24}$$

$$\theta_B(z) = (z-1) - \delta\frac{z^2-z}{2} + \dots \tag{25}$$

We now substitute the expansions (21–25) into the linear equation (20) and at each order in δ obtain a linear ordinary differential equation for the linear fields $\mathbf{v}_{00}(z)$, $\mathbf{v}_{01}(z)$ \dots . At $O(\delta^{-1})$ we find

$$\sigma_0\phi_{00} = 0, \tag{26}$$

implying that $\sigma\phi_0 = O(\delta)$.

At $O(\delta^0)$, we find solutions

$$\theta_{00k} = -f_k \sin \pi z, \quad w_{00k} = f_k \frac{|\mathbf{k}|}{\sqrt{\Omega}} \sqrt{1 + \frac{\Omega \sigma_0}{\pi^2 + k^2}} \sin \pi z, \quad (27)$$

$$u_{00k} = \frac{ik_x}{k^2} w'_{00k}, \quad v_{00k} = \frac{ik_y}{k^2} w'_{00k}, \quad (28)$$

where, as a consequence of incompressibility, the planform f_k satisfies

$$\nabla_H^2 f_k = -k^2 f_k, \quad (29)$$

and we have introduced $\Omega = 1 + \bar{S}/\bar{C}$. The zeroth-order growth rate is given by

$$\sigma_0 = \frac{\pi^2 + k^2}{\Omega} \left(\frac{R^2}{R_{00}^2(k)} - 1 \right), \quad (30)$$

where $R_{00}^2(k)$ describes the neutral curve

$$R_{00}^2(k) = \frac{(\pi^2 + k^2)^2}{\Omega k^2}. \quad (31)$$

The neutral curve (31) has a minimum of $4\pi^2/\Omega$ at $k_c = \pi$.

In addition to the solutions (27) and (28), we require the linear perturbation to the solid fraction ϕ_0 . However, the condition (26) requires that we consider terms of higher order in δ . To lowest order,

$$\phi_{0k}(z) = -\frac{\pi^2 + k^2}{\Omega \bar{C}} \frac{\pi}{\pi^2 + (\sigma/\delta)^2} \left(\cos \pi z + \frac{\sigma}{\pi \delta} \sin \pi z + e^{-\sigma(1-z)/\delta} \right) f_k. \quad (32)$$

Notice that this expression is valid for the case of both $\sigma = O(1)$ and $\sigma = O(\delta)$. In the former, condition (26) demands that $\phi_0 = O(\delta)$, while the latter implies that $\phi_0 = O(1)$. Anderson & Worster [5] showed that, for the case of $\sigma = O(\delta)$, the dispersion relation admits complex solutions, indicating the presence of an oscillatory instability. As we will be performing weakly nonlinear analysis near the marginal stability curve ($R = R_{00}(k) + O(\epsilon)$) in the asymptotic limit $\epsilon \ll \delta \ll 1$, we will be considering only the case of $\sigma = O(\delta)$, in which case (32) reduces to

$$\phi_{00k}(z) = -\frac{\pi^2 + k^2}{\Omega \bar{C}} \frac{\pi}{\pi^2 + \sigma_1^2} \left(\cos \pi z + \frac{\sigma_1}{\pi} \sin \pi z + e^{-\sigma_1(1-z)} \right) f_k. \quad (33)$$

This is precisely the result of Anderson & Worster [5]. We shall employ this result for $\phi_{00k}(z)$ throughout our analysis.

4 Weakly nonlinear analysis

In this section, we perform a finite-amplitude perturbation expansion of the equations of motion in the spirit of AH93 and AW95. In contrast to these studies, and those of subsequent authors, we retain horizontal spatial information by considering a continuous horizontal

planform rather than prescribing a discrete superposition of rolls. Again, unlike previous authors, we shall not *a priori* assume that the critical wavenumber k_c is the only mode excited. Rather, we consider a continuous band of wavenumbers, centred on k_c . In section 5, we restrict our attention to an infinitesimally thin band of wavenumbers, thus reproducing the results of previous studies. What is different about this approach is that we retain information about horizontal gradients in the amplitude equation thus obtained, and hence need make no *a priori* assumptions about the pattern. Note that in this calculation we do not rely upon a separation of scales to retain some slow spatial dependence of the amplitudes, as in standard derivations of the Ginzburg-Landau equation for example. Rather, spatial dependence is preserved in the wavenumber k , which is allowed to vary.

We follow AW95 and perform an asymptotic expansion in the ordered limit $\epsilon \ll \delta \ll 1$. That is, we first expand $\mathbf{v} = \{\theta, \phi, \mathbf{u}\}$ and R in ϵ ; then, at each order, we expand in δ :

$$\begin{aligned} \mathbf{v} &= (\mathbf{v}_{00} + \delta \mathbf{v}_{01} + \cdots) + \epsilon (\mathbf{v}_{10} + \delta \mathbf{v}_{11} + \cdots) \\ &\quad + \epsilon^2 (\delta^{-1} \mathbf{v}_{2,-1} + \mathbf{v}_{20} + \delta \mathbf{v}_{21} + \cdots) + \cdots \end{aligned} \quad (34)$$

$$\begin{aligned} R &= (R_{00} + \delta R_{01} + \cdots) + \epsilon (R_{10} + \delta R_{11} + \cdots) \\ &\quad + \epsilon^2 (R_{20} + \delta R_{21} + \cdots) + \cdots \end{aligned} \quad (35)$$

Notice that, as a consequence of $\mathcal{S}, \mathcal{C} = O(\delta^{-1})$, we must include in the expansion the field $\mathbf{v}_{2,-1} = \{0, \phi_{2,-1}, \mathbf{0}\}$. It is also worthwhile noting that, because of the presence of a term of order $\epsilon^2 \delta^{-1}$, the expansion (34) is singular in the limit $\delta \ll \epsilon \ll 1$, when the order is reversed.

We now substitute expansions (34) and (35) into the equations of motion (19) and look for slow time dependence $\partial_t = \epsilon^2 \partial_T$. The perturbation expansion then proceeds as follows:

$$\begin{aligned} O(\epsilon^0 \delta^0) : \quad \mathcal{L}_{00} \cdot \mathbf{v}_{00} &= \mathbf{0}, \\ O(\epsilon^0 \delta^1) : \quad \mathcal{L}_{00} \cdot \mathbf{v}_{01} &= -\mathcal{L}_{01} \cdot \mathbf{v}_{00}, \\ &\quad \vdots \quad \quad \quad \vdots \\ O(\epsilon^1 \delta^0) : \quad \mathcal{L}_{00} \cdot \mathbf{v}_{10} &= -\mathcal{L}_{10} \cdot \mathbf{v}_{00} + \mathbf{N}_{10}, \\ O(\epsilon^1 \delta^1) : \quad \mathcal{L}_{00} \cdot \mathbf{v}_{11} &= -\mathcal{L}_{11} \cdot \mathbf{v}_{00} - \mathcal{L}_{10} \cdot \mathbf{v}_{01} + \mathbf{N}_{11}, \\ &\quad \vdots \quad \quad \quad \vdots \\ O(\epsilon^2 \delta^{-1}) : \quad \mathcal{L}_{00} \cdot \mathbf{v}_{2,-1} &= \mathcal{T}_{2,-1} \cdot \partial_T \mathbf{v}_{00}, \\ O(\epsilon^2 \delta^0) : \quad \mathcal{L}_{00} \cdot \mathbf{v}_{20} &= \mathcal{T}_{2,-1} \cdot \partial_T \mathbf{v}_{01} + \mathcal{T}_{20} \cdot \partial_T \mathbf{v}_{00} - \mathcal{L}_{20} \cdot \mathbf{v}_{00} \\ &\quad - \mathcal{L}_{10} \cdot \mathbf{v}_{10} - \mathcal{L}_{01} \cdot \mathbf{v}_{2,-1} + \mathbf{N}_{20}, \\ &\quad \vdots \quad \quad \quad \vdots \end{aligned}$$

At each step in the perturbation expansion, we obtain a system of linear, inhomogeneous ordinary differential equations of the form

$$\mathcal{L}_{00} \cdot \mathbf{v}_{mn} = \mathcal{I}_{mn}. \quad (36)$$

As is well-known (see, for instance, [14, 15, 16]) a solution to (36) exists if and only if the inhomogeneities \mathcal{I}_{mn} are orthogonal to the solutions $\tilde{\mathbf{v}}$ of the adjoint problem. That is,

$$\int_0^1 dz \tilde{\mathbf{v}} \cdot \mathcal{I}_{mn} = 0. \quad (37)$$

In the present problem, neither the differential operator nor the boundary conditions is self-adjoint.

The solvability condition at $O(\epsilon^1 \delta^0)$ gives:

$$R_{10} \equiv 0. \quad (38)$$

This is a direct consequence of the assumption that $\mathcal{K}_1 = O(\epsilon)$.

The solvability condition at $O(\epsilon^2 \delta^0)$ gives the pattern equation for the planform f_k :

$$\lambda_k \partial_T f_k = \frac{2}{\sqrt{\Omega}} R_{20} |\mathbf{k}| f_k + \mathcal{M}\{f^2\} + \mathcal{N}\{f^3\}, \quad (39)$$

where

$$\mathcal{M}\{f^2\} \equiv \int d\mathbf{p} d\mathbf{q} \delta^2(\mathbf{k} - \mathbf{p} - \mathbf{q}) \mathcal{M}_{kpq} f_p f_q, \quad (40)$$

$$\mathcal{N}\{f^3\} \equiv \int d\mathbf{l} d\mathbf{m} d\mathbf{n} \delta^2(\mathbf{k} - \mathbf{l} - \mathbf{m} - \mathbf{n}) \mathcal{N}_{klmn} f_l f_m f_n. \quad (41)$$

Here \mathcal{M}_{kpq} and \mathcal{N}_{klmn} , the kernels of the integrals (40) and (41) are complicated functions of the horizontal wavevectors \mathbf{k} , \mathbf{p} , \mathbf{q} , \mathbf{l} , \mathbf{m} , and \mathbf{n} .

Close to marginality, the coefficient of the linear term on the right-hand side of (39) can be expressed as

$$\frac{2}{\sqrt{\Omega}} R_{20} |\mathbf{k}| \approx \frac{\pi^2 + k^2}{\Omega \epsilon^2} \left(\frac{R^2}{R_{00}^2(k)} - 1 \right). \quad (42)$$

This is exactly the linear growth rate σ_0 . Expanding about the critical wavenumber $k_c = \pi$ we find

$$\sigma_0 \approx \frac{2\pi^2}{\Omega \epsilon^2} \left(\frac{R^2 - R_c^2}{R_c^2} - \frac{1}{4} \left(\frac{k^2}{\pi^2} - 1 \right)^2 \right), \quad (43)$$

so that in real space the pattern equation for the planform $f = f(x, y)$ becomes

$$\lambda \partial_T f = \rho f - (\nabla_H^2 + 1)^2 f + \mu f^2 - \nu f^3. \quad (44)$$

This has of the form of a Swift-Hohenberg equation [17] with an additional quadratic term. In (44), we have replaced the integrals $\mathcal{M}\{f^2\}$ and $\mathcal{N}\{f^3\}$ with numbers μf^2 and νf^3 ; we shall calculate explicit expressions for μ and ν in the following section.

5 Evaluation of the integrals

As discussed in section 4, the primary motivation for deriving a general pattern equation for a continuous planform f_k (or, in real space, $f(x, y)$) was to avoid making any *a priori* assumptions about the pattern. Rather, one can proscribe some arbitrary initial pattern (for instance, a random one) and, with the aid of a small computer, investigate its evolution. For Swift-Hohenberg-like pattern equations, one typically sees a number of patterns competing with one another until the planform settles into a fixed pattern and evolves no further. The final pattern generally falls into one of three categories: discrete rolls, hexagons (up or down), or labyrinths - which can be thought of as a planform frustrated between rolls and hexagons.

It is interesting to calculate explicit expressions for the coefficients μ and ν for discrete planforms. This is aided by the observation that, close to criticality the planforms f_p, f_q etc. are confined to a narrow band of wavenumbers centred on $k_c = \pi$, as depicted in fig. (2). Under these conditions it is possible to evaluate the integrals $\mathcal{M}\{f^2\}$ and $\mathcal{N}\{f^3\}$. That is, we assume that $f_p = f(\alpha)\delta(|\mathbf{p}| - \pi)$ where α is the angle \mathbf{p} makes with $\mathbf{k} = k\hat{\mathbf{x}}$, without loss of generality. Under this assumption, all wavevectors must be of the same length and so only certain tessellations will satisfy the delta functions present in the integrands.

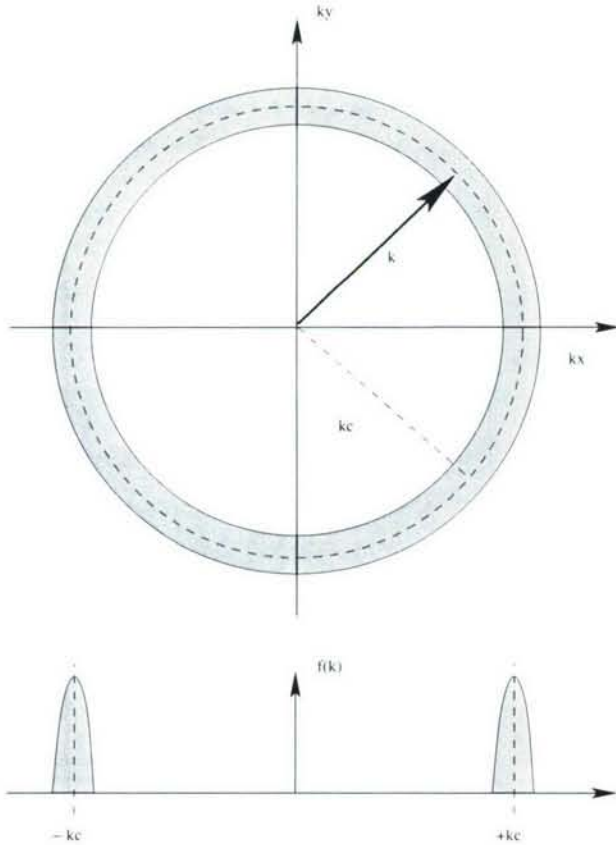


Figure 2: Support for f_k . We assume that f_k is confined to a narrow band of wavenumbers centred on $k_c = \pi$.

Concretely, the quadratic term $\mathcal{M}\{f^2\}$ in the pattern equation (44) is integrated over wavevector triads $\{\mathbf{k}, \mathbf{p}, \mathbf{q}\}$ satisfying the condition

$$\mathbf{k} = \mathbf{p} + \mathbf{q} \quad (45)$$

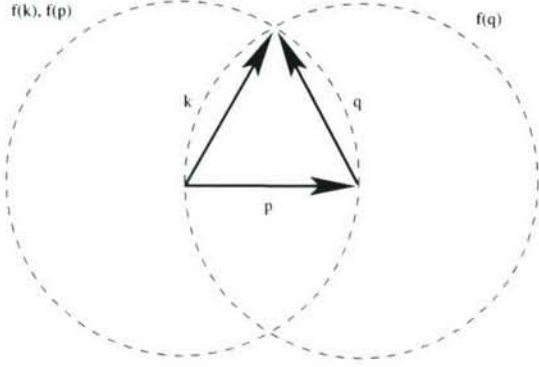


Figure 3: Allowed tessellations satisfying the condition $\mathbf{k} = \mathbf{p} + \mathbf{q}$. As \mathbf{k} , \mathbf{p} and \mathbf{q} are all of the same length ($k_c = \pi$), the triplet must form an equilateral triangle. Thus, the only planform possessing a quadratic term in its pattern equation is an "hexagonal array".

As all wavevectors are of the same length, the triad $\{\mathbf{k}, \mathbf{p}, \mathbf{q}\}$ must form an equilateral triangle. Consequently, the only planform possessing a quadratic term in its pattern equation is one with an equiangular array ("hexagonal array") of three superposed rolls, as depicted in fig. (3). This is the discrete case considered by AH93 and AW95. It is interesting to note that the appearance of a quadratic term is a special case of the more general pattern equation for a continuous planform.

We summarize this result as follows:

$$\begin{aligned} \mu f^2 &= \pi^3 (\bar{\mathcal{K}}_1 / \Omega \bar{C}) f\left(\frac{\pi}{3}\right) f^*\left(\frac{2\pi}{3}\right) && \text{for a hexagonal array,} \\ &= 0 && \text{otherwise,} \end{aligned} \quad (46)$$

where $f^*(\alpha) = f(\alpha + \pi)$.

In the case of the cubic term, the 4-tuple $\{\mathbf{k}, \mathbf{l}, \mathbf{m}, \mathbf{n}\}$ must satisfy

$$\mathbf{k} = \mathbf{l} + \mathbf{m} + \mathbf{n}, \quad (47)$$

so that $\{\mathbf{k}, \mathbf{l}, \mathbf{m}, \mathbf{n}\}$ form an equilateral parallelogram (fig. (4)). For general angle α between \mathbf{k} and \mathbf{l} (say), we find that

$$\begin{aligned} \nu f^3 &= \frac{8\pi^5}{9} \int_0^{2\pi} d\alpha \left\{ \frac{8}{5} + \frac{3 - \cos\alpha}{9 - 4\cos\alpha} (1 + \cos\alpha)^2 + \frac{3 + \cos\alpha}{9 + 4\cos\alpha} (1 - \cos\alpha)^2 \right\} f(0) |f(\alpha)|^2 \\ &+ \frac{22\pi^5}{3} \frac{\mathcal{K}_2}{\Omega^2 \bar{C}^2} \int_0^{2\pi} d\alpha f(0) |f(\alpha)|^2. \end{aligned} \quad (48)$$

As both rolls ($\alpha \equiv 0$) and hexagons ($\alpha \in \{0, \pi/3, 2\pi/3\}$) are special cases of (47), we expect the cubic term to appear in pattern equations for both planforms, with the coefficients

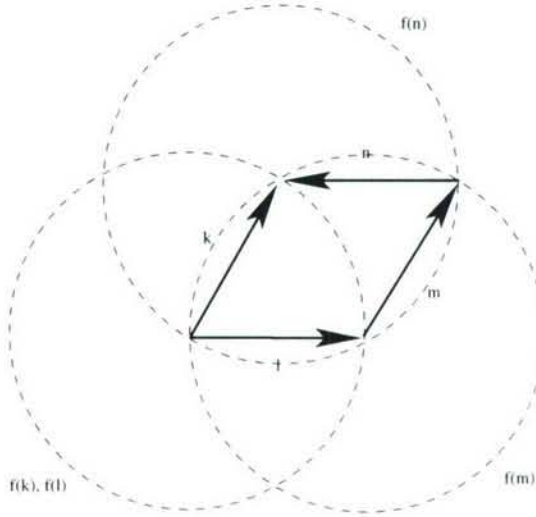


Figure 4: Allowed tessellations satisfying the condition $\mathbf{k} = \mathbf{l} + \mathbf{m} + \mathbf{n}$. The 4-tuple $\{\mathbf{k}, \mathbf{l}, \mathbf{m}, \mathbf{n}\}$ forms an equilateral parallelogram. If all four wavevectors lie along the same axis, this corresponds to the case of three interacting 1D rolls.

$$\begin{aligned}
 \nu f^3 &= \pi^5 \left(2.36 + 7.34 \frac{\mathcal{K}_2}{\Omega^2 \bar{C}^2} \right) f(0) \left(\left| f\left(\frac{\pi}{3}\right) \right|^2 + \left| f\left(\frac{2\pi}{3}\right) \right|^2 \right) \\
 &\quad + \pi^5 \left(2.84 + 7.34 \frac{\mathcal{K}_2}{\Omega^2 \bar{C}^2} \right) f(0) |f(0)|^2 \quad \text{for a hexagonal array,} \\
 &= \pi^5 \left(2.84 + 7.34 \frac{\mathcal{K}_2}{\Omega^2 \bar{C}^2} \right) f(0) |f(0)|^2 \quad \text{for rolls.}
 \end{aligned} \tag{49}$$

Note that (48) is positive definite, indicating that, in the absence of a quadratic term in the pattern equation, the bifurcation is supercritical.

Finally, we note that the coefficient in front of the time derivative in the pattern equation (44) is sign-altering:

$$\lambda = \Omega - 2 \frac{\bar{S}}{\Omega \bar{C}^2}. \tag{50}$$

Thus, for a particular parameter regime λ may be negative or even vanish. As AW95 noted, this indicates the presence of a Hopf bifurcation. In this work, we do not consider this regime of parameter values and consider the direct mode only. A derivation of the full pattern equation in the presence of a Hopf bifurcation remains a topic for further research; in the meantime, our analysis is valid away from $\lambda = O(\delta)$ in parameter space.

6 Nascent chimney solutions to the pattern equation

For a stationary planform, the pattern equation (44) reduces to a non-linear inhomogenous ordinary differential boundary value problem and is easily handled by numerical mathe-

mathematical tools such as MATLAB. Figure (5) depicts the solution in a periodic domain with representative values of $\rho = 3.9$, $\mu = 0.1$ and $\nu = 1.0$. See caption for details.

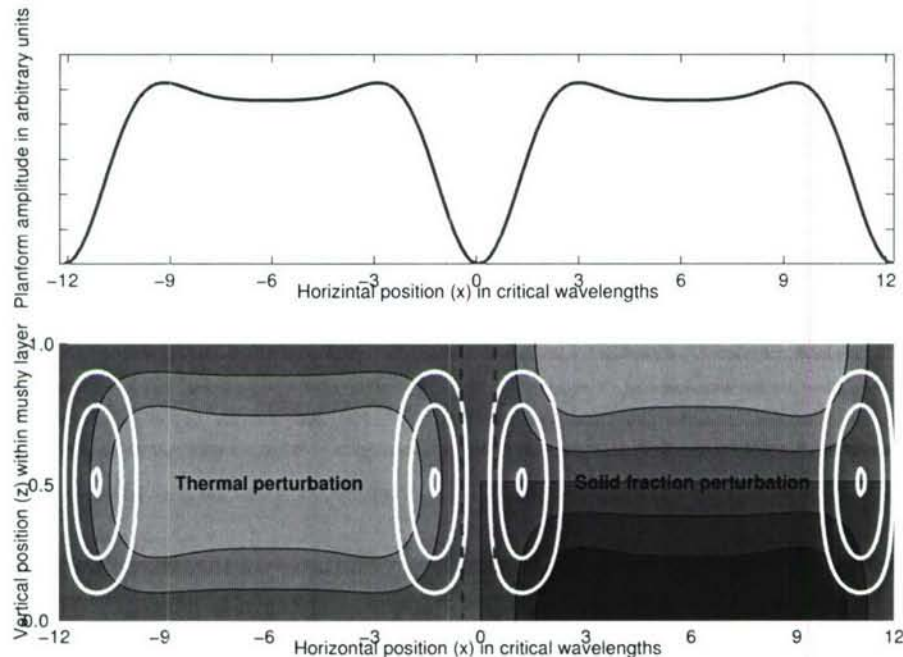


Figure 5: Stationary solutions for the planform (*top*) and perturbed fields (*bottom*). Horizontal position in each is measured in units of the critical wavelength. In the upper figure, the planform amplitude is plotted in arbitrary units. In the lower figure, the streamfunction is plotted in the x - z plane. Moving from left to right, the direction of rotation of the rolls is alternately clockwise and counter-clockwise. The region indicated by the vertical hatched lines represents a nascent chimney. In the background of the lower diagram, the temperature perturbation (*left*) and solid fraction perturbation (*right*) are indicated by contours. The units of these perturbations are arbitrary.

7 Discussion

As we have noted, the pattern equation derived in section (4) has the form of a Swift-Hohenberg equation with an additional quadratic term. The Swift-Hohenberg equation arises in a wide variety of physical, chemical and biological contexts and has a substantial literature associated with it (see Cross & Hohenberg [17] and references therein for a comprehensive review of this topic).

The quadratic term appearing in the pattern equation (44) breaks the symmetry between up and down. As we have noted, this quadratic term appears only for planforms made up of three rolls superposed at 120° to one another. If all three rolls have an equal amplitude, the unit cell is a hexagon. Thus, we recover the result of AH93 that the transition to three-dimensional hexagons is transcritical. The sign of the quadratic term determines whether there is up-flow or down-flow at the center of the hexagons.

We also note that the expression for the quadratic term (46) is proportional to \bar{K}_1 . Thus, symmetry-breaking between up-flow and down-flow at the center of hexagons is ultimately rooted in the non-Boussinesq effect of permeability variation with solid fraction. As \bar{K}_1 is strictly positive on physical grounds, the overall sign of the quadratic term is determined by the planform $f(\alpha)$ itself, at least in this pared-down model.

Finally, it is amusing to note that while hexagons may determine which way is up by looking at the flow direction in their centre, rolls and all other planforms have no such method of distinguishing up from down. Translation of rolls and parallelograms by a half-cell merely exchanges the two directions. In this way, the hexagonal planform is fundamentally different from all other patterns: it is manifestly asymmetric.

Acknowledgements:

Thanks to the GFD Staff for an unforgettable experience, in particular: Neil B and John W for their constant encouragement; the Worster family for being so entertained and entertaining; Joe K and Louis H for permitting me to pick their esteemed brains; George V for introducing me to the national pastime, and his own; and Andrew Folwer (sic) for that beer I bought him. Thanks to Grae W for capturing my imagination in lectures, papers, and conversations. Special thanks to all of my fellow Fellows for their fellowship. Profound thanks to EAS for his guidance, supervision, and good company all summer. Finally, the author thanks SLK for permitting him to spend ten weeks away from her.

References

- [1] Stephen H. Davis. *Theory of Solidification*. Cambridge University Press, 2001.
- [2] M.G. Worster. Convection in mushy layers. *Ann. Rev. Fluid Mech.*, 29:91–122, 1997.
- [3] Gustav Amberg and G.M. Homsy. Nonlinear analysis of bouyant convection in binary solidification with applications to channel formation. *J. Fluid Mech.*, 252:79–98, 1993.
- [4] D.M. Anderson and M. Grae Worster. Weakly nonlinear analysis of convection in mushy layers during the solidification of binary alloys. *J. Fluid Mech.*, 302:307–331, 1995.
- [5] D.M. Anderson and M. Grae Worster. A new oscillatory instability in a mushy layer during the solidification of binary alloys. *J. Fluid Mech.*, 307:245–267, 1996.
- [6] F. Chen, J.W. Lu, and T.L. Yang. Convective instability in ammonium chloride solution directionally solidified from below. *J. Fluid Mech.*, 276:163–187, 1994.
- [7] D.N. Riahi. On nonlinear convection in mushy layers part 1. oscillatory modes of convection. *J. Fluid Mech.*, 467:331–359, 2002.
- [8] D.N. Riahi. On nonlinear convection in mushy layers. part 2. mixed oscillatory and stationary modes of convection. *J. Fluid Mech.*, 517:71–101, 2004.

- [9] Peter Guba and M. Grae Worster. Nonlinear oscillatory convection in mushy layers. *J. Fluid Mech.*, 553:419–443, 2006.
- [10] C.A. Chung and Falin Chen. Onset of plume convection in mushy layers. *J. Fluid Mech.*, 408:53–82, 2000.
- [11] Peter Guba. On the finite-amplitude steady convection in rotating mushy layers. *J. Fluid Mech.*, 437:337–365, 2001.
- [12] M.G. Worster. Instabilities of the liquid and mushy regions during solidification of alloys. *J. Fluid Mech.*, 237:649–669, 1992.
- [13] A.C. Fowler. The formation of freckles in binary alloys. *IMA J. App. Maths*, 35(2):159–174, 1985.
- [14] E.L. Ince. *Ordinary Differential Equations*. Dover Publications, Inc., 1926.
- [15] W.V.R. Malkus and G. Veronis. Finite amplitude cellular convection. *J. Fluid Mech.*, 4:225–260, 1958.
- [16] F.H. Busse. The stability of finite amplitude cellular convection and its relation to an extremum principle. *J. Fluid Mech.*, 30:625–649, 1967.
- [17] M.C. Cross and P.C. Hohenberg. Pattern formation outside of equilibrium. *Rev. Mod. Phys.*, 65(3):851–1112, 1993.

The evaporation of a salty film

Rob Style

March 15, 2007

1 Introduction

Evaporation of water is an important phase transformation that appears in many guises throughout everyday life. Its effects range from processes intrinsically involved in the atmospheric water cycle, to the regulation of body temperature in hot environments, the production of coffee ring stains beneath a spilt coffee droplet and to important processes underlying microfluidics.

Although evaporation as a pure bulk phase transformation is well understood, when one adds solutes to the liquid, or brings the liquid into contact with a substrate, we obtain a new and rich variety of possible behaviours that we can access experimentally and analyse theoretically.

A well known example of is the effect of combining a solute with evaporation is given by the ‘tears of wine’ phenomenon [1],[2]. When one swills a glass of wine, a liquid film is produced up the side of the glass above the bulk liquid. Alcohol evaporates more rapidly in the film away from the bulk wine, and the film becomes depleted of alcohol. This depletion decreases the surface concentration of the film relative to that of the bulk wine, leading to a gradient in surface energy. This gradient causes a marangoni flow, drawing liquid up into the film above the bulk wine. Eventually, enough liquid is drawn up into the film that it becomes unstable to gravity and falls—like a tear of wine. Any gradient in surface temperature or concentration will cause Marangoni flows, and thus marangoni flows can be extremely important in the presence of phase transitions, particularly evaporation.

A second complexity is introduced by the addition of a substrate into the problem [3]. Although the wetting of substrates has been well studied [4], there are still many interesting phenomena associated with the evaporation of films that have only recently received attention, such as the investigation of coffee ring formation by a sessile, particle-laden droplet [5], the observations of a finite contact angle in an evaporating wetting film [6], and of particular interest, the experiments of Du and Stone on evaporatively grown salt trees [7].

Neufeld has recently performed a series of experiments observing the evaporation of a sessile, salty droplet (private communication). Although simple in nature, the experiments show several key features that we wish to understand (see Fig. 1). Namely:

- Overturning of liquid in the bulk

- Salt crystal deposition in the bulk, initiating at the outer edge
- Formation of a thin, rough salt crystal film beyond the edge of the bulk droplet
- Continual growth of the outer limit of this thin salt film

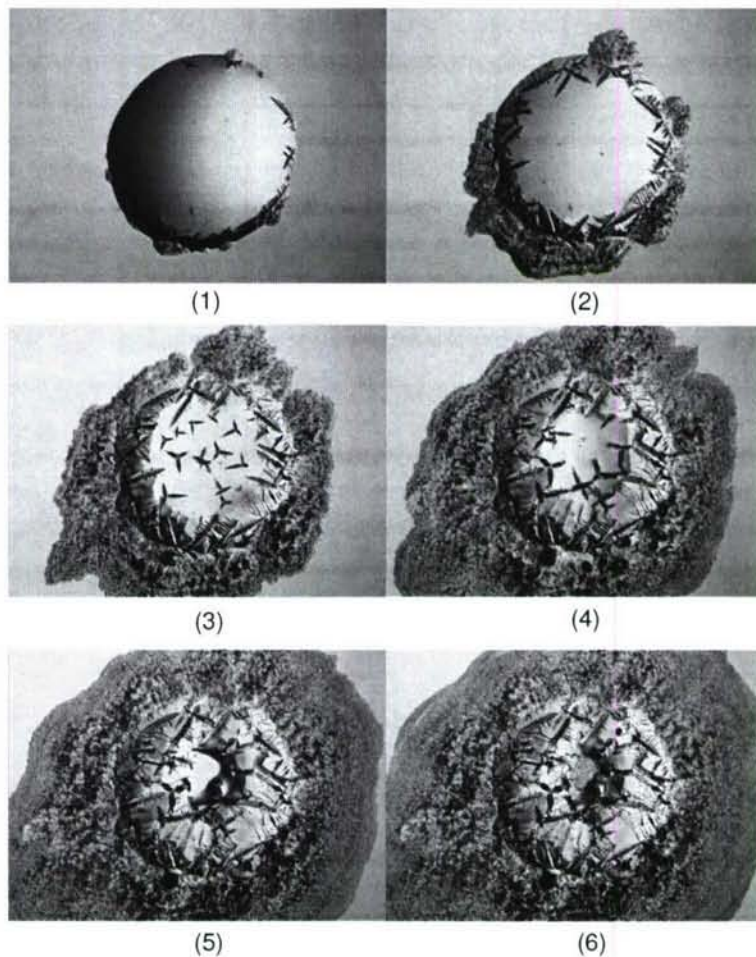


Figure 1: Plan view of the evaporation of a $5\mu\text{l}$ droplet of saturated NH_4Cl solution. Room temperature is 22°C and relative humidity is 42%. The images are shown at approximately six minute intervals. (1) Just post commencement of the experiment: some salt is observed at the edge of the droplet when evaporation is highest. (2) Precursor film growth observed around droplet. (3) Some dendritic growth observed in the bulk droplet: these crystals are effected by flow in the droplet. (4) Bulk liquid reduces in radius while precursor film continues to spread. (5) Dewetting occurs at the centre of the droplet and hence bulk liquid is no longer exposed to air. (6) Precursor film continues to grow and dewetted area covered in growth similar in appearance to outlying precursor growth.

In this work, we will demonstrate the basic processes at work in the evaporation of a salty droplet by way of simplified models and show that the above observations stem from

the combined action of these processes. In this way, we will be able to understand the processes important for the growth of evaporatively grown salt trees which we aim to study in later work. For the current study, of most interest is the creation of the salt crystal under and beyond the edge of the bulk droplet. Vapour transport of salt cannot account for the deposition beyond the confines of the bulk droplet, so we ascribe the presence of the salt to the evaporation of a thin film of liquid fed by Marangoni flow from the bulk droplet. We will see that the growth of the salt–crystal from this film is subject to a new instability associated with the development of supersaturation at the liquid–vapour boundary.

We describe the mechanism for this new instability as follows. A thin film of constant salt concentration sits atop a planar salt crystal with which it is in equilibrium. The vapour pressure in the surrounding atmosphere is reduced so that evaporation occurs from the surface of the film and so that salt previously dissolved in the evaporated portion of liquid is rejected into the surface layer of the film (salt having effectively zero partial pressure in the vapour phase). This causes supersaturation at the liquid–vapour interface that diffuses towards the solid–liquid interface. In this manner, salt will be transported from the liquid–vapour interface to deposit upon the salt crystal. However, as the salt crystal will be growing into an increasing supersaturation, the interface will be unstable to small perturbations.

In many aspects, this salt precipitation is similar to the unstable solidification front of a salt freezing from a binary alloy [8]. For comparison, we briefly review the theory of constitutional supercooling.

Imagine a pure, planar salt crystal, growing from a binary alloy (water and salt). We set the far field composition and temperature of the alloy to be c_∞ and T_∞ respectively, and assume that the liquidus relationship between concentration c and temperature T is approximately linear so that

$$T_L(c) = mc + T_0. \quad (1)$$

Then $T_L(c_\infty) < T_\infty$ so that the far field liquid is not supercooled. Also, the temperature at the solid–liquid interface $T_i < T_\infty$ is such that the solid is in equilibrium with the surrounding liquid so that we must have $T_i = T_L(c_i)$.

Now, in front of the advancing salt front, water must be being rejected so that $c_i < c_\infty$. Thus we will see solutal and thermal boundary layers in front of the advancing front, across which the salt and temperature respectively will vary between their interface and far field values. The diffusivity of heat κ is much larger than the diffusivity of salt in water D_s , and so the thermal boundary layer will be thicker than the solutal boundary layer. If we translate the solutal concentration into the equilibrium liquidus temperature in the liquid from Eq.(1), we then see (Fig. 2) that this implies that there will be a region directly ahead of the advancing solid front where the liquid is at a temperature below the liquidus if

$$\left. \frac{\partial T}{\partial z} \right|_{\text{sl}} < m \left. \frac{\partial c}{\partial z} \right|_{\text{sl}}. \quad (2)$$

This ‘constitutional supercooling’ is produced by rejection of solvent in front of the solidification front, and it is well known that the front is unstable to small perturbations [9] leading to dendritic growth as has been observed experimentally, for example in the case of ammonium chloride, by Huppert [10].

Therefore in both situations, we produce salt from a binary alloy of salt and water. Also in both cases, there is a local increase of the free energy of the system above the

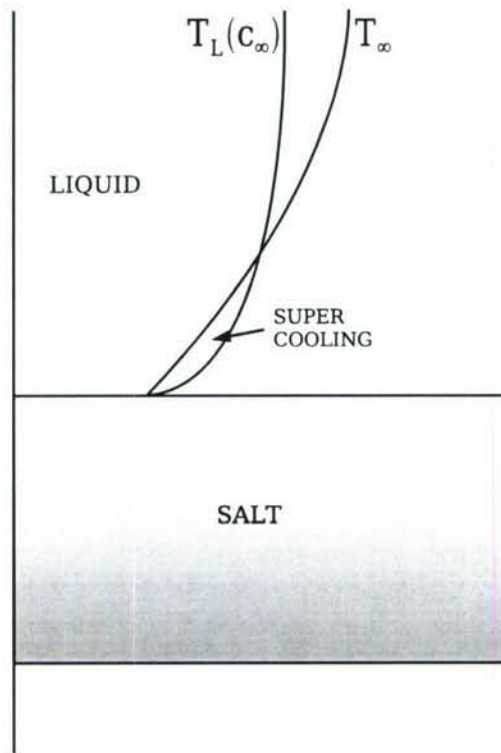


Figure 2: Diagram demonstrating the origin of constitutional supercooling at the salt–liquid interface (cf principle lectures by MGW for added details).

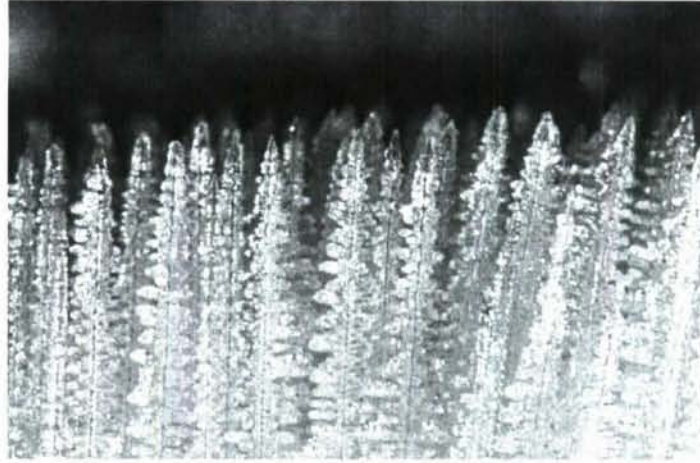


Figure 3: Close up of salt dendrites at the surface of a mushy layer advancing into ammonium chloride solution [10].

equilibrium value (supersaturation/supercooling) which drives the salt–liquid interface to become unstable. One final similarity is that in both situations convection can occur due to density differences associated with gradients in temperature and concentration. However, the key difference lies in the fact that constitutional supercooling is caused by water rejection at the salt crystal boundary, and is always immediately relieved by immediate solidification upon the salt crystal. However in the evaporative case, supersaturation is produced at some distance, namely the film thickness, away from the deposited salt crystal and therefore leads to differing growth behaviour and the possibility of homogeneous nucleation of salt at the liquid–vapour interface for rapid enough evaporation rates. The simple observation that the crystal forms produced by both processes vary significantly (Fig. 3) tells us that this difference is important in determining growth characteristics, and thus worthy of study.

2 Model of an evaporating film

In order to wade through the mire of competing processes involved in producing the complex patterns seen experimentally, we begin by considering a simple model consisting of a planar salt interface, covered with a film of uniform thickness d . In this manner we can systematically study the most important physical mechanisms at play. We can control the water vapour pressure P_∞ in the surrounding atmosphere and so initially we choose a vapour pressure such that the water in the film is in equilibrium with the water vapour and the film has uniform concentration c_L in equilibrium with the underlying salt crystal. We then reduce P_∞ so evaporation occurs at the liquid–vapour interface at a rate E where E is measured in volume per second per unit area of surface.

At this point it is useful to make explicit the assumptions that we make in order that we may justify them later:

- Because of the disparity between solutal and thermal diffusivities, thermal effects are neglected in the dynamics of the system.

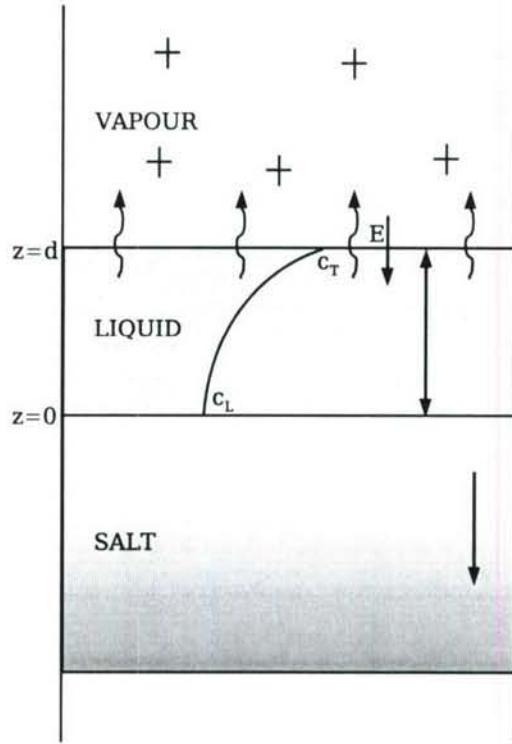


Figure 4: Schematic diagram for the evaporation of a film of salty liquid

- The film is of uniform thickness, and vapour pressure over the film is constant so that there is no marangoni flow feeding the film,
- The salt concentration is sufficiently low that the advection–diffusion equations hold,
- The addition of salt to a volume of liquid does not change the volume: $\rho_l(c) = \text{const.}$

Therefore we have a film as shown in Fig.(4), in the frame of reference of the liquid–vapour interface. In the liquid, the concentration of the salt satisfies the diffusion–advection equation, so that we have

$$\frac{\partial c}{\partial t} - E \frac{\partial c}{\partial z} = D_s \nabla^2 c, \quad (3)$$

which we can nondimensionalise by scaling times with d_0/E and lengths with d_0 , where d_0 is the initial thickness of the quasi–stationary film, to give

$$\text{Pe} \left[\frac{\partial c}{\partial \tilde{t}} - \frac{\partial c}{\partial \tilde{z}} \right] = \tilde{\nabla}^2 c, \quad (4)$$

where nondimensional variables are denoted by a tilde, and the effective Peclet number $\text{Pe} = d_0 E / D_s$ is the ratio of evaporation to diffusion rates. A natural starting point in the analysis of the phenomenon is therefore to select a small Peclet number by choosing a slow evaporation rate (or sufficiently small film). We will then use a quasi–stationary approximation so that $d \approx d_0$ throughout the analysis.

As boundary conditions for the problem, there are several natural conditions arising from the formulation. These consist of equilibrium at the solid–liquid interface

$$c|_{sl} = c_L + \mathcal{C}\mathcal{K}_{sl}, \quad (5)$$

conservation of salt at the solid–liquid interface

$$D_s \frac{\partial c}{\partial z} \Big|_{sl} = (V + \dot{h})c_{salt}, \quad (6)$$

thinning of the film

$$\dot{d} = -E, \quad (7)$$

and conservation of salt at the liquid–vapour interface

$$D_s \frac{\partial c}{\partial z} \Big|_{lv} = Ec_T, \quad (8)$$

where we define \mathcal{K}_{sl} to be the curvature of the solid–liquid interface, \mathcal{C} to be the Gibbs–Thomson coefficient for the equilibrium salt concentration (see Appendix A), V is the growth velocity of the salt crystal, h is the height of the crystal surface, and c_T and c_{salt} are the salt concentrations at the liquid–vapour interface and in the salt crystal respectively.

We will require one more boundary condition to complete the set of equations, and this will come from the relationship between the evaporation rate E , the concentration at the liquid–vapour interface c_T and far field vapour pressure P_∞ . The evaporation rate will depend upon the dynamics of the vapour, in that the transport of water vapour from the interface will be determined by the water vapour gradient at the liquid–vapour interface

$$D_w \frac{\partial P_{wv}}{\partial z} \Big|_{lv} = E, \quad (9)$$

where D_w is the diffusivity of water vapour in air and P_{wv} is the local water vapour pressure. Therefore to obtain the water vapour pressure profile for a steady diffusion of vapour in a background of air, we must solve Laplace’s equation in the vapour with boundary conditions $p(\infty) = P_\infty$ and

$$P_{lv} = P_0(1 - c_T), \quad (10)$$

where P_0 is the vapour pressure at pure equilibrium, and c_T is the concentration of salt at the film surface (see Appendix B). For pure evaporation, these boundary conditions reduce to constant values at the surface of the droplet and in the far field, and so good approximations to the evaporation rate can be made by assuming simple geometries for the droplet [5],[11]. For fast evaporation rates, there is a jump in vapour pressure from the equilibrium vapour pressure, given by Eq.(10) that will be controlled by the Hertz–Knudsen relationship, which written as the boundary conditions will add some detail to the form of the flow. However in this paper, since E is an experimentally controllable parameter, we will assume constant evaporation rate.

For small Peclet number, the diffusion–advection equation reduces to Laplace’s equation, and so the solutal field in the film for planar growth is given by

$$c \approx (c_T - c_L) \frac{z}{d} + c_L. \quad (11)$$

Applying boundary condition (8) gives

$$c_T = \frac{c_L}{1 - \text{Pe}} \quad (12)$$

and so the rate of growth of the solid is given by

$$V = E \frac{c_T}{c_{\text{salt}}}. \quad (13)$$

This agrees with our intuition, because for the small Peclet number limit, information is diffused rapidly across the film, and so we expect evaporation to occur simultaneously with salt precipitation. Equation (13) demonstrates that if we evaporate a layer of water of thickness δd , simultaneously an amount of salt equivalent to the salt dissolved in δd is precipitated corresponding to instantaneous diffusion.

We are now in a position to conduct a quasi-stationary linear stability analysis of the film. In the film, there is a slow time dependence of the basic state given by $O(\dot{c}/c_L) \sim \text{Pe}E/d$. We will impose a perturbation upon the solid-liquid interface which will grow on a faster timescale (that we can check *a posteriori*). Therefore we designate slow and fast timescales as $(\text{Pe}E/d)t = t^*$ and $(E/d)t = \tau$ respectively so that

$$\frac{\partial}{\partial t} = \frac{\partial}{\partial t^*} + \frac{\partial}{\partial \tau}.$$

We label the linear, quasi-stationary state given by Equation (11) as $c_0(z, t^*)$, and impose a dimensionless perturbation with a fast timescale upon the solid-liquid interface

$$h = \tilde{h} e^{ik\tilde{x} + \sigma\tau}. \quad (14)$$

We assume a form

$$c(\tilde{z}, \tau, t^*) = c_0(z, t^*) + \tilde{c}(\tilde{z}, t^*) e^{ik\tilde{x} + \sigma\tau}. \quad (15)$$

Then the diffusion advection equation (3) in the frame of reference of the solid-liquid interface becomes

$$\text{Pe}^2 \frac{\partial}{\partial t^*} \left(c_0 + \tilde{c} e^{ik\tilde{x} + \sigma\tau} \right) + \text{Pe} \sigma \tilde{c} e^{ik\tilde{x} + \sigma\tau} = \frac{\partial^2 c_0}{\partial \tilde{z}^2} + \left[\frac{\partial^2 \tilde{c}}{\partial \tilde{z}^2} - k^2 \tilde{c} \right] e^{ik\tilde{x} + \sigma\tau}, \quad (16)$$

which in the small Peclet number limit, reduces to

$$\frac{\partial^2 \tilde{c}}{\partial \tilde{z}^2} - k^2 \tilde{c} = 0, \quad (17)$$

and has solution

$$\tilde{c} = A \sinh k\tilde{z} + B \cosh k\tilde{z}. \quad (18)$$

Applying boundary conditions in the small Peclet number limit, we obtain

$$A = -\tilde{h} \tanh kd \left[\frac{\mathcal{C}}{d} k^2 + \text{Pe} \frac{c_L}{1 - \text{Pe}} \right]$$

and

$$B = \tilde{h} \left[\frac{\mathcal{C}}{d} k^2 + \text{Pe} \frac{c_L}{1 - \text{Pe}} \right],$$

Table 1: Table of typical values for the ammonium chloride/water system at $T = 20^\circ\text{C}$

Constant	Value	Units
c_L	27.2	wt%
γ_{sl}	5×10^{-2}	J m^{-2}
μ	1.787×10^{-3}	$\text{kg m}^{-1} \text{s}^{-1}$
R	8.314	$\text{J K}^{-1} \text{mol}^{-1}$
m	4.79	$\text{K wt}\%^{-1}$
D_s	10^{-9}	$\text{m}^2 \text{s}^{-1}$
$\frac{\partial \gamma}{\partial c}$	4×10^{-4}	$\text{kg s}^{-2} \text{wt}\%^{-1}$
ρ_s	5.6×10^4	mol m^{-3}
\mathcal{C}	-7×10^{-9}	$\text{wt}\% \text{m}$
E	10^{-7}	m s^{-1}

so that applying the Equation (6) for the conservation of salt at the solid–liquid interface, we find the dimensional dispersion relationship

$$\sigma = \frac{1}{c_{\text{salt}}} k \tanh kd [Ec_L + D_s C k^2]. \quad (19)$$

For relatively short wavelengths, we can approximate this as

$$\sigma = \frac{k}{100} [Ec_L + D_s C k^2], \quad (20)$$

as is plotted in Fig.(5).

Using typical values from Table (1), we find from Eq.(20) that the cutoff wavenumber $k_c = 6.2 \times 10^5 \text{m}^{-1}$, so that the small wavelength approximation is justified. The maximum growth rate can also be derived from Eq.(20), and we find that $k_{\text{max}} = 3.57 \times 10^5 \text{m}^{-1}$ and $\sigma_{\text{max}} = 6.4 \times 10^{-3} \text{s}^{-1}$ corresponding to a time period of around 3 hours. For this instability to be relevant, we require that the growth rate be faster than the rate of thinning of the film, so that $E/d < \sigma_{\text{max}}$ and we find that $d > 1.5 \times 10^{-5} \text{m}$. Therefore we expect that in the precursor film (typically around a micron thick), with these conditions, the instability will not have time to develop, unless there is a flow of liquid in to replace evaporated material. We must also remember that for a sufficiently thin film such as the precursor film, electrostatic forces will retard the evaporation rate of the film, and so for a full treatment, we will need to include these effects.

We note that for $E \sim 10^{-7} \text{m s}^{-1}$, the Peclet number is $d \times 10^2$, and so for most natural situations, the Peclet number will be reasonably small. We also note that when the film is sufficiently thick, convection of the film will set in due to the increase in density at the surface of the film, and the stationary approximation of the liquid in the film will no longer be valid.

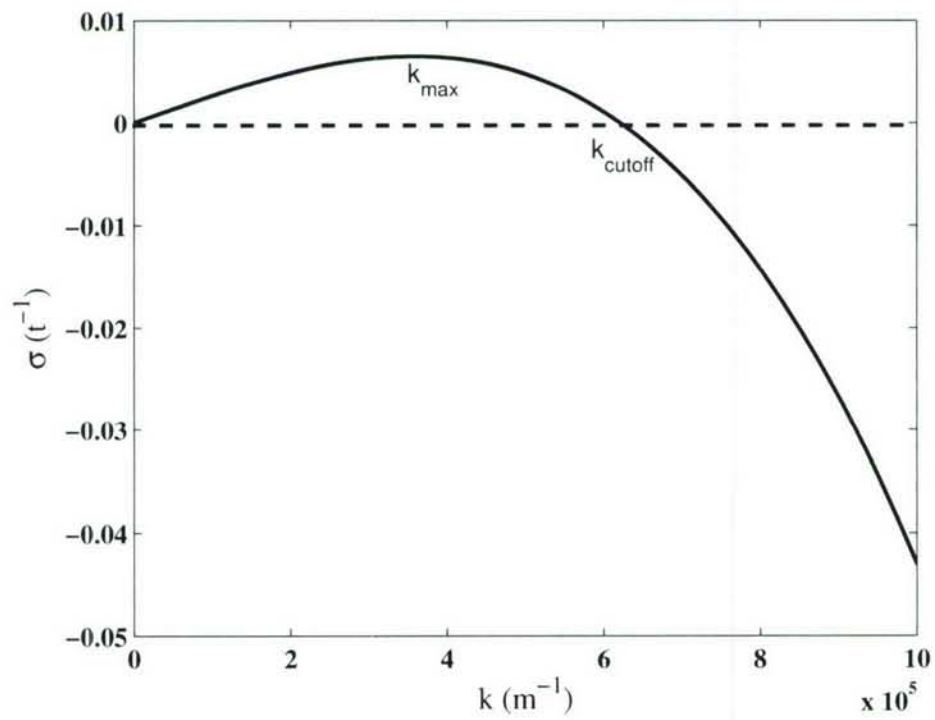


Figure 5: Plot of growth rate against wavenumber for small Peclet number.

3 Large Peclet number

When the evaporation rate is sufficiently high, or the film is sufficiently thick, the rate of diffusion of salt across the film becomes small relative to the thinning rate of the film. This means that there will be a solutal boundary layer at the liquid–vapour interface with on some time scale, the salt–liquid interface unaware of the presence of evaporation at the upper surface.

Therefore, in the frame of reference of the liquid–vapour interface, the diffusion–advection equation for salt concentration becomes

$$\frac{\partial c}{\partial t} - E \frac{\partial c}{\partial z} = d \frac{\partial^2 c}{\partial z^2}, \quad (21)$$

so that before the diffusive information reaches the salt–liquid interface, the profile will satisfy the time independent form of Eq.(21) so that

$$c = c_L + (c_T - c_L) \left[\frac{e^{\frac{E(z+d)}{D_s}} - 1}{e^{\frac{dE}{D_s}} - 1} \right]. \quad (22)$$

Applying Eq.(6) for the conservation of mass at the liquid–vapour interface, we find that

$$c_T = c_L e^{\text{Pe}} \quad (23)$$

which, we note gives the same result as for the small Peclet number case (Eq.(12)) when we take the small Peclet number limit of this expression. From this expression, we notice that the surface value of the salt concentration in the film will increase very rapidly with Peclet number. Therefore, there will be some value of the Peclet number above which the concentration at the liquid–vapour interface is sufficiently high to cause homogeneous nucleation.

In order to estimate the critical Peclet number above which homogeneous nucleation will occur, we need to calculate the energy required to create a critical nucleus of salt from solution.

The free energy change associated with creating a nucleus of radius r of salt from salt solution is

$$\Delta G = \gamma_{sl} 4\pi r^2 + [\mu_s(T, P_s) - \mu_l(T, P_l, c)] \frac{4}{3} \pi r^3, \quad (24)$$

where the first term on the right hand side stems from the energy change required to create a solid–liquid surface between the two phases, and the second term is the change in free energy associated with the change of phase.

Expanding the chemical potentials of the two phases about equilibrium, we have

$$\mu_s(T, P_s) - \mu_l(T, P_l, c) = -RT \ln(c/c_L), \quad (25)$$

and therefore

$$\Delta G = \gamma_{sl} 4\pi r^2 - RT \ln(c/c_L) \frac{4}{3} \pi r^3. \quad (26)$$

As can be seen, this free energy change has a maximum at $r = r^*$, so that if $r < r^*$, the nucleus will shrink to zero and if $r > r^*$, the nucleus will diverge and homogeneous nucleation occurs. The critical energy is therefore

$$\Delta G(r^*) = \frac{16\pi\gamma_{sl}^3}{\rho^2 R^2 T^2 \ln(c/c_L)}. \quad (27)$$

For homogeneous nucleation to occur, the thermal fluctuations in the film must be large relative to the critical free energy of nucleation. This means that the Gibbs number $g = \Delta G(r^*)/kT$ must be smaller than $O(100)$ for nucleation to occur [12] (note that this estimate will depend upon the nature of the system). Approximating $c/c_L = e^{\text{Pe}}$ from Eq.(23), we thus obtain that

$$\text{Pe} \leq 1 \quad (28)$$

for no homogeneous nucleation, and so the large Peclet number case is unviable.

We note that for intermediate Peclet number, we cannot treat the profile as quasi-stationary, and so a full treatment of the instability will require a numerical evaluation of the instability from the initial conditions, or otherwise a modified model. One possibility would be to assume a flow perpendicular to the plane of the instability that maintains the film at constant thickness. This model may be applicable to the case of the precursor film.

Finally, we note that for a thick enough film, there is the possibility of convection in the the film due to the salty cold liquid overlying hot, fresh liquid. As previously mentioned, we expect the thermal effect to be small relative to the solutal effect due to the high thermal diffusivity relative to solutal diffusivity in the system. In order to estimate the film thickness at which Rayleigh–Benard convection sets in, we approximate the system by Rayleigh–Benard convection with a solid base and an open top. Letting the critical Rayleigh number be $Ra_c \approx 1000$, and taking the small Peclet number limit (which holds up to films of the order of 1mm thick), we find that [13]

$$Ra_c = \frac{\beta g d^3 (c_T - c_L)}{D_s \nu} \approx 1100 \quad (29)$$

where all the symbols take their standard meanings. Thus we expect Rayleigh Benard convection to set in when $d \approx 2mm$.

4 Flow in a thin film

Consider a droplet of salt solution evaporating on an infinite planar substrate. Evaporation is driven by the far-field vapour pressure below the equilibrium vapour pressure of the film. Towards the edge of the droplet, the liquid film is exposed to the drier air above the adjacent dry substrate, while in the centre of the droplet, the ambient air is more moist due to the homogeneity of the environment more than a diffusion length from the edge. This means that the evaporation rate will change from the centre to the edge of the film, and hence there will be a gradient in salinity along the surface of the film and an associated marangoni flow.

The Marangoni effect is a well known process whereby gradients in surfactant concentration in liquids cause associated gradients in surface tension. These gradients then drive

a flow from regions of low surface tension to regions of high surface tension. Unlike for most solutes, where the Marangoni coefficient, or gradient in surface tension associated with a change in solute is negative, for ionic salts such as ammonium chloride and sodium chloride, the surface tension gradient,

$$\frac{\partial\gamma_{lv}}{\partial c} \approx 4 \times 10^{-4} \text{J m}^{-2} \text{wt}\%^{-1} \quad (30)$$

is positive [14]. This means that as the evaporation rate, and hence the salinity, increases towards the edge of the film, we will see an outwards marangoni flow associated with the salinity gradient. We can analyse the flow in order to determine the volume flow rate, and the possibility of this flow as a volume source for precursor film growth.

Assuming that the film is thin enough that we can use lubrication theory, when we incorporate the marangoni flow, the equation of conservation of solute (3) becomes

$$\frac{\partial c}{\partial t} - V \frac{\partial c}{\partial z} + z \frac{\tau}{\mu} \frac{\partial c}{\partial x} = D_s \frac{\partial^2 c}{\partial z^2} + D_s \frac{\partial^2 c}{\partial x^2}, \quad (31)$$

where μ is the dynamic viscosity of water and

$$\tau = \frac{\partial\gamma_{lv}}{\partial c} \frac{\partial c}{\partial x} \quad (32)$$

is the surface stress, and in order to simplify the model, we will assume that the the liquid is a planar film of constant thickness d , and that the surface concentration is linear in x [15], which is equivalent to the assumption that the vapour pressure is linear in x (Fig. 6).

We would like to investigate whether adding a linear surface concentration gradient will significantly vary the concentration profile in the film. Therefore, we will consider the small Peclet number case in the instance that the surface concentration is given by

$$c_T = c_0 + Gx. \quad (33)$$

By imposing this concentration profile, we have also imposed a horizontal lengthscale upon the problem given by $(c_0 - c_L)/G$, which we will assume is large relative to d so that we can reduce equation (31) to

$$z \frac{\tau}{\mu} \frac{\partial c}{\partial x} = D_s \frac{\partial^2 c}{\partial z^2},$$

and so upon non-dimensionalisation of lengths with d , and concentrations such that $c = (c_0 - c_L)\tilde{c} + c_L$, the governing equations become

$$\tilde{z} F \frac{\partial \tilde{c}}{\partial \tilde{x}} = \frac{\partial^2 \tilde{c}}{\partial \tilde{z}^2}, \quad (34)$$

with

$$\tilde{c}(0) = 0, \quad (35)$$

and

$$\tilde{c}(d) = 1 + \delta \tilde{x}, \quad (36)$$

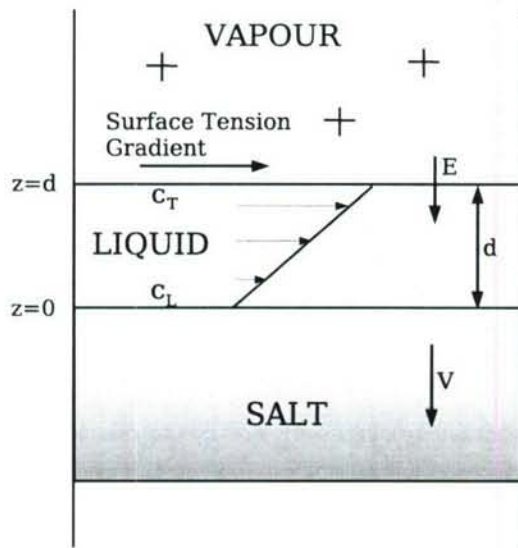


Figure 6: Schematic diagram for a marangoni film in a thin film.

where $F = \tau d^2 / \mu D_s$ is the ratio of the diffusive response time to the viscous response time over the film and we have required $\delta = Gd / (c_0 - c_L) \approx GD_s$ to be small as previously mentioned. Estimating $c_0 - c_L = p$ from the small Peclet number, this implies that for typical evaporation rates, $G \ll 2700 \text{ wt}\% \text{m}^{-1}$, which will be satisfied over all but the very edges of the droplet (see Appendix C).

We proceed by seeking a separable solution to the equations, by setting (dropping tildes) $c(x, z) = X(x)Z(z)$ so that

$$F \frac{X'}{X} = \lambda = \frac{Z''}{Zz}, \quad (37)$$

where λ is a constant. Thus we see that

$$X = Ae^{\frac{\lambda x}{F}},$$

which for small values of the exponent becomes

$$X = A \left(1 + \frac{\lambda x}{F} \right)$$

which is of the right form to match Eq. (36) if we set $\lambda/F = \delta$, so that our assumption of a small exponent value is appropriate for $\delta x \ll 1$.

Thus we see that

$$Z'' - \frac{d^3 \tau G}{\mu D_s (c_0 - c_L)} z Z,$$

and by letting $z = \alpha \zeta$, with

$$\alpha = \left(\frac{\mu D_s (c_0 - c_L)}{d^3 \tau G} \right)^{\frac{1}{3}},$$

the Z equation reduces to Airy's Equation

$$Z''(\zeta) - Z(\zeta)\zeta = 0. \quad (38)$$

Therefore we find the dimensional solution to the concentration profile to be

$$\begin{aligned} c &= c_I + (c_0 - c_I) \left[\frac{\text{Bi}\left(\frac{z}{\alpha d}\right) \text{Ai}(0) - \text{Ai}\left(\frac{z}{\alpha d}\right) \text{Bi}(0)}{\text{Bi}\left(\frac{1}{\alpha}\right) \text{Ai}(0) - \text{Ai}\left(\frac{1}{\alpha}\right) \text{Bi}(0)} \right] e^{\frac{Gx}{(c_0 - c_L)}} \\ &= c_I + (c_0 - c_I) f(z) e^{\frac{Gx}{(c_0 - c_L)}} \end{aligned} \quad (39)$$

Thus we see that the relative importance of the Marangoni flow is given by the size of the parameter α : when α is large, we can Taylor expand Eq. (39) to see that

$$c \approx c_I + (c_0 - c_I) \frac{z}{d} e^{\frac{Gx}{(c_0 - c_L)}} \approx c_I + (c_0 - c_I + Gx) \frac{z}{d}$$

so that we may effectively ignore the horizontal flow, and treat the concentration profile as linear. However, when α is sufficiently small, the solution can deviate from the linear solution.

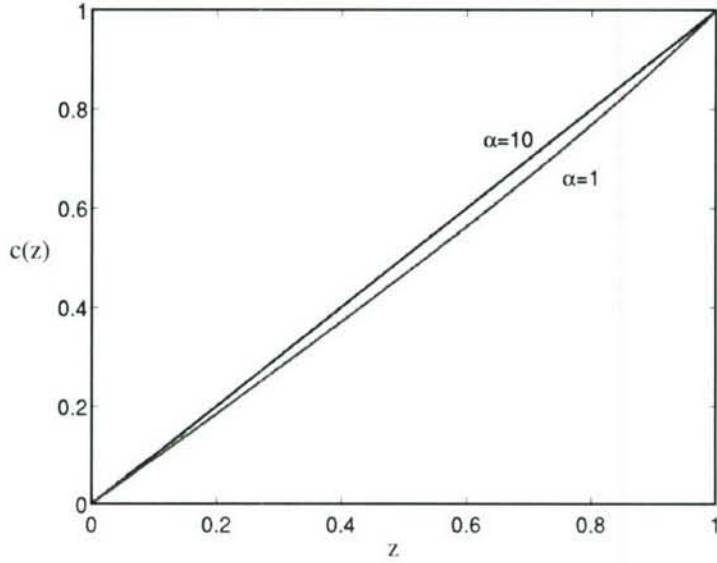


Figure 7: $f(x)$ calculated for $\alpha = 1, 10$. To good approximation $c = z/d$ for $\alpha > 1$.

In Appendix C, we treat the question of the value of G for an evaporating droplet, from which we obtain a reasonable upper estimate for G near the edge of the droplet of $2.7 \times 10^3 \text{wt}\% \text{m}^{-1}$. For films in the small Peclet number limit, this implies $\alpha \gg 1$ except within $2d$ of the edge of the droplet where geometry dependent factors will be important. Therefore there will be no significant alteration to the linear profile across the bulk of the film (cf Fig. 7).

5 Linear stability of a film including marangoni flow

In the previous section, we investigated the concentration profile for a film with a concentration gradient applied to the upper surface giving rise to a Marangoni flow. As has been seen previously, the underlying salt-crystal growth is diffusively unstable, and so the solid-liquid boundary will become corrugated. When we include a Marangoni flow with the perturbation, we expect the perturbation to move upstream because the flow will compress the solutal boundary layer on the upstream side, and thus promote growth in that direction. We can analyse this effect as follows.

From the previous section we saw that the steady state solutal profile for small Peclet number can be closely approximated by

$$c = c_L + (c_0 - c_L) \frac{z}{d} e^{\frac{Gx}{(c_0 - c_L)}}, \quad (40)$$

for $Gx/(c_0 - c_L) \ll 1$. Hence we will use the linear approximation throughout.

Assuming that we are in the lubrication limit and that any perturbations are long wavelength, the non-dimensional governing equations are the same as previously (Eqns. 34-36). Therefore the steady state can be taken as that given in Eqn. (40).

If we apply a perturbation of the form

$$z = \tilde{h} e^{ik\tilde{x} + \sigma t}$$

to the solid–liquid interface (where we do not expect σ to be real), then $\tilde{c} = c_0(\tilde{x}, \tilde{z}) + \tilde{c}(\tilde{z}) \exp(ik\tilde{x} + \sigma t)$, where c_0 is the steady state solution. Neglecting the Gibbs–Thomson effect, and dropping tildes we find that

$$ikF\tilde{c} = \tilde{c}'', \quad (41)$$

and we can convert this to Airy's equation by transforming

$$z = i \left(\frac{1}{kF} \right)^{\frac{1}{3}} \zeta \equiv i\beta\zeta.$$

Thus

$$\tilde{c} = -\tilde{h} \left[\frac{\text{Ai} \left(\frac{\zeta}{i\beta} \right) \text{Bi} \left(\frac{1}{i\beta} \right) - \text{Ai} \left(\frac{1}{i\beta} \right) \text{Bi} \left(\frac{\zeta}{i\beta} \right)}{\text{Ai}(0)\text{Bi} \left(\frac{1}{i\beta} \right) - \text{Ai} \left(\frac{1}{i\beta} \right) \text{Bi}(0)} \right], \quad (42)$$

and by applying the boundary condition for conservation of salt (Eqn. 6), we obtain the dispersion relation for the system

$$\sigma = \frac{iD_s}{\beta d^2} \left(\frac{c_L - c_0}{1 - c_L} \right) \left[\frac{\text{Ai}'(0)\text{Bi} \left(\frac{1}{i\beta} \right) - \text{Ai} \left(\frac{1}{i\beta} \right) \text{Bi}'(0)}{\text{Ai}(0)\text{Bi} \left(\frac{1}{i\beta} \right) - \text{Ai} \left(\frac{1}{i\beta} \right) \text{Bi}(0)} \right]. \quad (43)$$

Figure 8 shows the imaginary part of σ , as a function of β . As expected, the velocity of the travelling waves disappears for small k (large β), and we see that σ is significant relative to the timescale V/d associated with the growth of the salt for $\beta < 1$. From the previous linear stability analysis, we found that the most unstable wavenumber was $k_{max} \approx 3.57 \times 10^5 d$, which corresponds to $\beta = (1.2 \times 10^{-14} / d^3 G)^{1/3}$ and therefore we see from the appendix estimates of G that the travelling velocity of the waves may be significant for sufficiently thick films.

It should be mentioned that this is only a longwave analysis of the problem, and for k small, the entire Laplacian must be considered in Eq. (34). This will also reintroduce the instability considered in the first linear stability analysis. However this analysis should give a good indication of the relative size of the travelling wave velocity.

6 Volume flow rate due to Marangoni flows

We are interested in whether the gradient in surface concentration across a droplet is sufficient to act as a source for precursor film growth. From the Appendix, we have that

$$\frac{\partial c_T}{\partial r} = \frac{2c_I d D_v (P_I - P_\infty)}{\pi D P_a} \frac{r}{(R^2 - r^2)^{\frac{3}{2}}}.$$

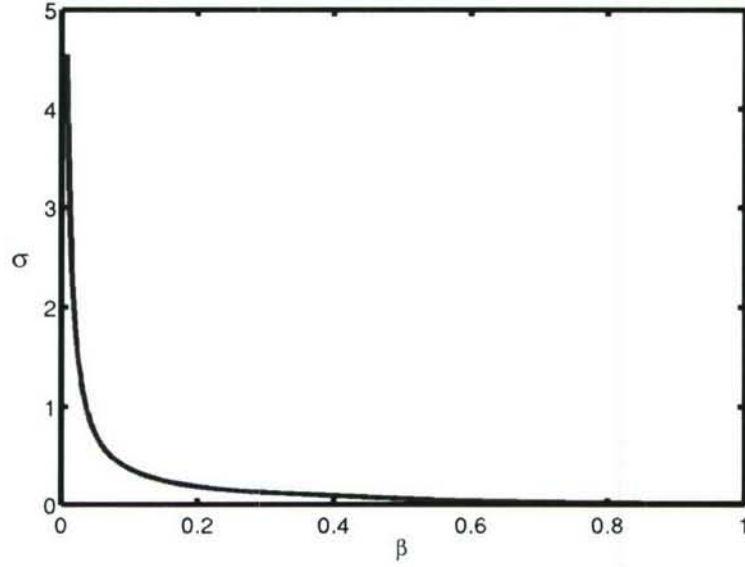


Figure 8: $\text{Im}(\sigma)$ from the dispersion relation for the travelling wave instability in terms of β .

and from lubrication theory, the volumetric flow rate is

$$\int_0^d z \frac{\partial \gamma}{\partial c} \frac{\partial c}{\partial r} \frac{1}{\mu} dz = \frac{d^2}{2\mu} \frac{\partial \gamma}{\partial c} \frac{\partial c}{\partial r}.$$

so that the flow rate is given by

$$q = \frac{c_I d^3 D_v (P_I - P_\infty)}{\pi \mu D P_a} \frac{\partial \gamma}{\partial c} \frac{r}{(R^2 - r^2)^{\frac{3}{2}}}. \quad (44)$$

As discussed in the Appendix, we will ignore the region at the edge of the droplet, as there will be local shape complications there that will effect the expression for c_T . In order to avoid this, we calculate q at a distance d from the edge of the droplet, to find that for $R = 1\text{cm}$, $d = 10^{-6}$ that $q(R - d) \approx 3.4d$ or 1.2cm hr^{-1} which is in line with typical growth rates of the film.

It should be noted that there are only sufficiently large concentration gradients to maintain this flow rate near to the edge of the film. However away from the edge, decreases in curvature associated with the Marangoni flow should draw fluid outwards to help maintain the source of liquid to the edge.

7 Conclusions

In this work, we have considered the processes involved with the growth of salt from an sessile, salty, evaporating droplet. The chief result is that we have demonstrated the existence of a new instability of the growing salt crystal due to evaporation at the liquid–vapour

interface. The instability stems from the creation of supersaturation at the evaporating interface, which diffuses through the film to the growing salt crystal. Hence the salt crystal grows into an increasing supersaturation and the interface will be unstable. The instability differs from the morphological instability of a binary alloy [8] in that in the new instability, the creation of supersaturation is created at some distance *away* from the advancing salt front. Whereas with morphological instability, the supersaturation is caused by rejection of solvent immediately adjacent to the salt front.

We find that for typical evaporation rates, the instability will be important for films of thickness $d > 1.5 \times 10^{-5}$ m. For sufficiently thick films ($d \sim O(1\text{mm})$), convection will set in and the formulation becomes invalid. Marangoni convection may also be important, as well as thermal effects, however these are expected to be small relative to the solutal effects.

For a growing droplet, there will exist gradients in surface tension associated with the gradient in evaporation rate across the liquid–vapour interface. Associated with these gradients in surface tension there will be a Marangoni flow that drives liquid outwards, feeding the precursor film observed in experiments. We have analysed the effect of the Marangoni flow on solutal profile in the small Peclet number regime (relevant for typical film thicknesses), and find that there will be no significant alteration to the solutal profile across the film except in the tip region, where geometry effects are expected to be important.

We have also analysed the effect of the Marangoni flow upon corrugation of the salt surface. We find that the flow induced compression of the upstream boundary layer of the surface roughness causes increased solid growth thereby creating an upstream travelling solid/liquid wave. The calculated travelling wave velocity suggests that the process will be operative in sufficiently thick films. Finally an estimate of the overall flow rate due to Marangoni flow in a precursor film shows that the flow is sufficient to cause observed spreading rates of the precursor film.

As noted in the text, numerical work is necessary to properly analyse the intermediate Peclet number case and solutal convection, and we hope to achieve these in further studies. For the future, we aim to produce a more complete model of the precursor film including electrostatic double layer forces and van der Waals forces and to extend the results from the current work to produce a more complete model of the processes involved in salty droplet evaporation and salt tree formation.

8 Acknowledgements

But of course, there are many thanks to be given for helping make such a fun and productive summer. I am indebted to all the staff and fellows for many useful discussions on the porch and for keeping me amused throughout. In particular, I would like to thank Grae for helping me find that last boundary condition, Alan for helping me delve into some of the murkier depths of thermodynamics, Jerome for performing the experiments at incredibly short notice, Victor and Devin for teaching me how to throw properly and Rachel for the amusing episode with the lobster. Finally, I owe a huge debt of gratitude to my supervisor John Wettlaufer who has patiently guided and encouraged me throughout the summer.

9 Appendix A: Derivation of the Gibbs–Thomson co-efficient C

In order to obtain an approximation for C , the dependence of the equilibrium salt concentration at an interface upon curvature, we start with the liquidus relationship at a curved surface including solute:

$$T = T_m - m(1 - c) + \frac{\gamma_{sl}T_m}{\mathcal{L}_f}\mathcal{K} \quad (45)$$

where T_m is the melting temperature of a pure liquid salt, m is the slope of the liquidus, γ_{sl} is the surface energy of the liquid–salt interface and \mathcal{L}_f is the heat of solution of the salt. We note that we have assumed that the curvature term is independent of solution concentration, so the resulting expression will not be exact.

Rearranging, we obtain

$$c = 1 - \frac{T_m - T}{m} - \frac{\gamma_{sl}T_m}{m\mathcal{L}_f}\mathcal{K} \quad (46)$$

we we recognise as

$$c = c_L(T) + \mathcal{C}\mathcal{K} \quad (47)$$

where $c_L(T)$ is the liquidus concentration, so that we find

$$\mathcal{C} = -\frac{\gamma_{sl}T_m}{m\mathcal{L}_f}. \quad (48)$$

Taking typical values of the constants, $\mathcal{L}_f = 4 \times 10^8 \text{J m}^{-3}$, $T_m = 273\text{K}$ and $\gamma_{sl} = 5 \times 10^{-2} \text{J m}^{-2}$, we find that $\mathcal{C} \sim -7 \times 10^{-9} \text{wt}\%$.

10 Appendix B: Equilibrium vapour pressure and surface concentration

We consider the effect upon equilibrium vapour pressure of adding salt to a liquid. In equilibrium, the chemical potentials of the two phases are equal:

$$\mu_l(T, P, c) = \mu_v(T, P), \quad (49)$$

where the subscripts correspond to liquid and vapour respectively and we have assumed the vapour pressure of salt to be zero.

Expanding the chemical potentials about pure equilibrium at temperature T and vapour pressure P_0 , and using the Gibbs–Duhem equation [Wood Battino],

$$\mu_l(T, P_0) + v_l(P - P_0) - kTc = \mu_v(T, P_0) + v_v(P - P_0), \quad (50)$$

where $v_l \ll v_v$ are the volumes per mole of each phase, so that using

$$\mu_l(T, P_0) = \mu_v(T, P_0), \quad (51)$$

we obtain

$$P - P_0 = -\frac{kT}{v_v}c, \quad (52)$$

which for an ideal gas becomes

$$P = P_0(1 - c). \quad (53)$$

11 Appendix C: Estimating the magnitude of G

For a realistic experiment, the controllable factors are the temperature T , the initial salinity of the droplet, the initial volume of the droplet and the far field water vapour pressure P_∞ . Therefore there will be a variation in local vapour pressure at the surface of the droplet which is determined by local equilibrium with the droplet and diffusion in the vapour.

Assuming that the vapour is stagnant above the droplet so that vapour transport occurs by diffusion alone, then the vapour pressure will satisfy Laplace's equation

$$\nabla^2 P = 0. \quad (54)$$

A number of studies [11],[5] have modelled the evaporation rates of a pure droplet by treating the vapour diffusion problem identically to an electrostatic problem. Poulard et al. assumed that the droplet is effectively a flat disc, which is appropriate for fluids with small contact angles to the substrate, while Deegan et al achieved a more accurate result by considering the electrostatic field associated with a lens. As we require an estimate only, we will assume the evaporation rate matches that for a disc held at constant surface vapour pressure so that the evaporation rate is approximately

$$E \approx \frac{2D_v(P_l - P_\infty)}{\pi P_a} \frac{1}{\sqrt{R^2 - r^2}} \quad (55)$$

where D_v is the diffusion rate of water vapour in the air, P_a is atmospheric pressure, P_l is the vapour pressure for a droplet in equilibrium with the vapour, r is the radial coordinate for the disc, and R is the radius of the disc.

Although in deriving the evaporation rate, we have assumed a constant vapour pressure (and hence constant surface concentration which is only an approximation), this should provide us with a reasonable approximation for the local surface vapour pressure.

We will now convert the local evaporation rate into the surface concentration c_{surf} as follows. Using the boundary condition for conservation of mass at the liquid–vapour interface,

$$D_s \left. \frac{\partial c}{\partial z} \right|_{z=d} = Ec_T, \quad (56)$$

and using the approximations

$$c_T = c_L \quad \text{and} \quad \frac{\partial c}{\partial z} = \frac{c_T - c_L}{d}, \quad (57)$$

we find that

$$E = \frac{D_s}{d} \left(\frac{c_T - c_L}{c_L} \right) \quad (58)$$

and so

$$c_T - c_L = \frac{2c_L d D_v (P_l - P_\infty)}{\pi D_s P_a} \frac{1}{\sqrt{R^2 - r^2}}$$

so that

$$\frac{\partial c_T}{\partial r} = \frac{2c_L d D_v (P_l - P_\infty)}{\pi D_s P_a} \frac{r}{(R^2 - r^2)^{\frac{3}{2}}}.$$

As we expect there to be shape determined complications at the edge of the droplet we take $r = R - d$ to obtain an upper limit upon \mathcal{C} , and $r = 0$ for a lower limit. Therefore, for a 6% difference in relative humidity so that $(P_I - P_\infty)/P_a \approx 1.8 \times 10^{-3}$, and letting $d = 10^{-6}\text{m}$, we find that a reasonable approximation for G is that it will vary from 0 to $2.7 \times 10^3 \text{wt\% m}^{-1}$ across the droplet.

References

- [1] J. M. Fournier and A. M. Cazabat. Tears of wine. *Europhys. Lett.*, 20:517–522, 1992.
- [2] A. E. Hosoi and J. W. M. Bush. Evaporative instabilities in climbing films. *J. Fluid Mech.*, 442:217–239, 2001.
- [3] A. Oron, S. H. Davis, and S. G. Bankoff. Long-scale evolution of thin liquid films. *Rev. Mod. Phys.*, 69(3):931–980, 1997.
- [4] P. G. de Gennes. Wetting: statics and dynamics. *Rev. Mod. Phys.*, 57(3):827–863, 1985.
- [5] R. D. Deegan, O. Bakajin, T. F. Dupont, Greg Huber, S. R. Nagel, and T. A. Witten. Contact line deposits in an evaporating drop. *Phys. Rev. E*, 62(1):756–765, 2000.
- [6] S. G. Lipson. Pattern formation in drying water films. *Physica Scripta*, T67:63–66, 1996.
- [7] Rose Du and H. A. Stone. Evaporatively controlled growth of salt trees. *Phys. Rev. E*, 53(2):1994, 1996.
- [8] M. G. Worster. Solidification of fluids. In G. K. Batchelor, H. K. Moffat, and M. G. Worster, editors, *Perspectives in Fluid Dynamics*. Cambridge University Press, 2000.
- [9] W. W. Mullins and R. F. Sekerka. Stability of a planar interface during solidification of a dilute binary alloy. *J. Appl. Phys.*, 35(2):444, 1964.
- [10] H. E. Huppert. The fluid mechanics of solidification. *J. Fluid Mech.*, 212:209, 1990.
- [11] C. Poulard, G. Guena, and A. M. Cazabat. Diffusion-driven evaporation of sessile drops. *J. Phys. Condens. Matt.*, 17(49):S4213–S4227, 2005.
- [12] V. P. Skripov and M. Z. Faizullin. *Crystal-Liquid-Gas Phase Transitions and Thermodynamic Similarity*. Wiley, 2006.
- [13] J. S. Turner. *Buoyancy Effects in Fluids*. Cambridge University Press, 1973.
- [14] S. A. Lowry, M. H. McCay, T. D. McCay, and P. A. Gray. Surface-tension measurements of aqueous ammonium chloride (NH_4Cl) in air. *J. Cryst. Growth*, 96(4):774–776, 1989.

- [15] J. S. Wettlaufer, M. Elbaum, H. A. Stone, and M. G. Worster. Molecular diffusion in nonequilibrium alloy films and molecular motion in polymeric networks. In D. C. Gillies and D. E. McCauley, editors, *Proceedings of the NASA Microgravity Materials Science Conference, Huntsville, Alabama, 14-16 July*, pages 679–684. NASA/CP-1999-209092, 1999.

A particle-simulation method to study mixing efficiencies

Takahide Okabe

March 15, 2007

1 Introduction

Mixing by fluid flows is a ubiquitous natural phenomenon that plays a central role in many of the applied sciences and engineering. A geophysical example is the mixing of aerosols (e.g., CO₂ supplied by a volcano, say, or by human activity) in the atmosphere. Aerosols are dispersed by molecular diffusion on the smallest scales but are more effectively spread globally by atmospheric flows. The density—and density fluctuations—of some aerosols influence the albedo of the earth and thus have an environmental impact. Hence it is important to understand fundamental properties of dispersion, mixing, and the suppression of concentration fluctuations by stirring flow fields.

At the most basic level, the mixing of a passive scalar can be modeled by an advection-diffusion equation for the scalar concentration field with a specified stirring flow field. In this work we will focus on problems where fluctuations in the scalar field are generated and sustained by temporally steady but spatially inhomogeneous sources. The question of interest here is this: for a given source distribution, how well can a specified stirring flow mix the scalar field? Mixing can be measured by the scalar variance over the domain. A well-mixed scalar field will have a relatively uniform density with “small” variance while increased fluctuations in the scalar density will be reflected in a “larger” variance. We put quotes around the quantifiers small and large because the variance is a dimensional quantity whose magnitude depend on the choice of units employed. A dimensionless measure of the scalar fluctuations is necessary to give precise meaning to these characterizations.

Several years ago Thiffeault *et al* [1] introduced the notion of “mixing efficiency” for a velocity field stirring a steadily sustained scalar by comparing the bulk (space-time) averaged density variance with and without advecting flow. In the absence of stirring the mixing is accomplished by molecular diffusion alone, which can be very effective on small scales but is not generally very good at breaking up and disbursing large scale fluctuations quickly. Stirring can greatly enhance the transport of the scalar from regions of excess density to regions of depletion, however, suppressing the variance far below its diffusion-only value. The magnitude of this variance suppression by the stirring, i.e., the ratio of the variance without stirring to the variance in the presence of stirring, is a dimensionless quantity that provides a sensible gauge of the mixing efficiency of the flow. Different advection fields will have different efficiencies stirring scalars supplied by different sources.

It is then of obvious interest both to determine theoretical limits on mixing efficiencies for various source configurations and to explore whether those limits may be achieved.

In this project we develop a computational scheme that is easy to implement and applicable to the study of mixing by any advection field and with any source distribution. The idea is to develop a method that accurately simulates advection and diffusion of large numbers of passively advecting particles introduced by a steady source, and to measure density fluctuations by “binning” the particles to produce an approximation of the “hydrodynamic” concentration field. Unlike a numerical PDE code, a particle code does not prefer specific forms of advection or source (PDE methods generally work best with smooth fields). There is, however, no free lunch: the accuracy of the particle code is ultimately limited by the finite number of particles that can be tracked. The limitation to finite numbers of particles inevitably introduces statistical errors due to discrete fluctuations in the local density and systematic errors in the variance measurements due to binning. But these problems can be addressed and as will be shown in this report, for some applications the method proves to be computationally efficient and quantitatively accurate.

The most significant upside of a particle code—and one of the most significant motivations for this work—is that it can easily handle (i.e., resolve) small scales in sources and, subsequently, in the concentration field. It is even applicable to delta-function sources whose resolution requirements would strain standard PDE methods. Delta-function scalar sources are the most singular physically relevant distributions, and at the same time the simplest to implement in a particle tracking scheme: just introduce the particles at the same point in space. A delta-function source could serve, for example, as a model of a smoke stack supplying an aerosol into the atmosphere when the smallest scales in the flow are larger than the radius of the outlet.

The remainder of this report is organized as follows. In section 2 the mathematical model is presented, basic quantities characterizing mixing phenomena are defined, and some general results about mixing efficiencies are reviewed. In section 3 the particle simulation scheme is explained in detail. The problems inherent to a discrete particle method, and solutions to these problems, are also discussed. The particle code as implemented is numerically validated in section 4. There, the variance from the particle code is compared with exact solutions and the results of a PDE code for some benchmark problems. In section 5 the particle method is used to measure the mixing efficiency of a particular statistically homogeneous flow stirring ever smaller-scale sources (down to a delta-function source). This is a new result, and it is qualitatively and quantitatively compared to previous analysis of upper bounds on the mixing efficiency for such sources. We close this report with conclusive remarks and provide appendices containing details of the computer code used to implement the scheme.

2 Basic facts about the mixing efficiency problem

In this section we review basic facts about the mixing efficiency problem as formulated by Thiffeault, Doering & Gibbon *et al* [1] and further developed by Plasting & Young [2], Doering & Thiffeault [3], and Shaw *et al* [4]. The dynamics is given by the advection-diffusion equation for the concentration of a passive scalar $\rho(t, \mathbf{x})$ with time-independent

but spatially inhomogeneous source field $S(\mathbf{x})$:

$$\frac{\partial \rho}{\partial t} + \mathbf{u} \cdot \nabla \rho = \kappa \Delta \rho + S(\mathbf{x}), \quad (1)$$

where κ is the molecular diffusivity and $\mathbf{u}(t, \mathbf{x})$ is a specified advection field that satisfies (at each instant of time) the incompressibility condition

$$\nabla \cdot \mathbf{u} = 0. \quad (2)$$

For simplicity, the domain is the d -torus, i.e., $[0, L]^d$ with periodic boundary conditions. We will limit attention in this report to stirring fields that satisfy the properties of statistical homogeneity and isotropy defined by

$$\overline{u_i(\mathbf{x}, \cdot)} = 0 \quad (3)$$

$$\overline{u_i(\mathbf{x}, \cdot) u_j(\mathbf{x}, \cdot)} = \frac{U^2}{d} \delta_{ij} \quad (4)$$

where the overbar is time average and U is the root mean square speed of the velocity field, a natural indicator of the intensity of the stirring (recall that d is the spatial dimension). These statistical properties are shared by homogeneous isotropic turbulence on the torus.

We are interested in fluctuations in the concentration ρ so the spatially averaged background density is irrelevant. It is easy to see from (1) that the spatial average of ρ grows linearly with time at the rate given by the spatial average of S . Hence we may change variables to spatially mean-zero quantities

$$\theta(t, \mathbf{x}) = \rho(t, \mathbf{x}) - \frac{1}{L^d} \int d^d x' \rho(t, \mathbf{x}') \quad (5)$$

and

$$s(\mathbf{x}) = S(\mathbf{x}) - \frac{1}{L^d} \int d^d x' S(\mathbf{x}') \quad (6)$$

that satisfy

$$\frac{\partial \theta}{\partial t} + \mathbf{u} \cdot \nabla \theta = \kappa \Delta \theta + s(\mathbf{x}). \quad (7)$$

(We must also supply initial conditions for ρ and/or θ but they play no role in the long-time statistically steady statistics that we are interested in.)

The “mixedness” of the scalar may be characterized by, among other quantities, the long-time averaged variance of ρ , proportional to the long-time averaged L^2 norm of θ ,

$$\langle \theta^2 \rangle := \lim_{T \rightarrow \infty} \frac{1}{T} \int_0^T dt \frac{1}{L^d} \int d^d x \theta^2(t, \mathbf{x}) \quad (8)$$

The smaller $\langle \theta^2 \rangle$ is, the more uniform the distribution is. The “mixing efficiency” of a stirring field is naturally evaluated by comparing the scalar variance to the variance with

the same source but in the absence of stirring. To be perfectly precise, we compare $\langle \theta^2 \rangle$ to $\langle \theta_0^2 \rangle$ where θ_0 is the solution to

$$\frac{\partial \theta_0}{\partial t} = \kappa \Delta \theta_0 + s(\mathbf{x}) \quad (9)$$

(with, say, the same initial data although these will not affect the long-time averaged fluctuations). Formally, then, the dimensionless *mixing efficiency* is defined

$$\mathcal{E}_0 := \sqrt{\frac{\langle \theta_0^2 \rangle}{\langle \theta^2 \rangle}}. \quad (10)$$

This efficiency carries the subscript 0 because we can also define *multiscale mixing efficiencies* by weighting large/small wavenumber components of the scalar fluctuations:

$$\mathcal{E}_p := \sqrt{\frac{\langle |\nabla^p \theta_0|^2 \rangle}{\langle |\nabla^p \theta|^2 \rangle}} \quad (p = -1, 0, 1). \quad (11)$$

As discussed in Doering & Thiffeault [3], Shaw *et al* [4] and Shaw [5], $\mathcal{E}_{\pm 1}$ provide a gauge of the mixing efficiencies of the flow as measured by scalar fluctuations on relatively small and large length scales respectively. In this project, however, we will focus exclusively on the mixing efficiency at “moderate” length scales, \mathcal{E}_0 .

There is a theoretical upper bound on \mathcal{E}_0 valid for any statistically stationary homogeneous and isotropic stirring field [3, 5, 4]:

$$\mathcal{E}_0 \leq \sqrt{\frac{\sum_{\mathbf{k} \neq 0} |\hat{s}(\mathbf{k})|^2 / k^4}{\sum_{\mathbf{k} \neq 0} |\hat{s}(\mathbf{k})|^2 / (k^4 + \frac{\text{Pe}^2}{L^{2d}} k^2)}} \quad (12)$$

where $\hat{s}(\mathbf{k})$ are the Fourier coefficients of the source and the Péclet number

$$\text{Pe} := \frac{UL}{\kappa}. \quad (13)$$

is a dimensionless measure of the intensity of the stirring. Generally we anticipate that \mathcal{E}_0 is an increasing function of Pe and the estimate in (12) guarantees that $\mathcal{E}_0(\text{Pe}) \lesssim \text{Pe}$ as $\text{Pe} \rightarrow \infty$, the scaling expected if there is any residual variance suppression in the singular vanishing diffusion limit (i.e., $\kappa \rightarrow 0$ with all other parameters held fixed).

The upper limit to the mixing efficiency in (12) depends on the stirring field only through U via Pe, but it depends on all the details of the source distribution. As studied in depth in references [3, 4, 5], the structure of the scalar source can have profound effects on the behavior, i.e., the high Pe scaling, of \mathcal{E}_0 . It is precisely this source-dependence of the qualitative behavior of $\mathcal{E}_0(\text{Pe})$ that motivates this development of a computational method that can handle singular source distributions.

In the remainder of this report we focus on the two-dimensional torus ($d = 2$) and for computational simplicity and efficiency we take as the stirring field the “random sine flow” defined for all time by

$$\mathbf{u}(t, \mathbf{x}) = \begin{cases} w \sin(\frac{2\pi y}{L} + \phi_n) \hat{\mathbf{i}} & \text{for } nT < t \leq nT + T/2 \\ w \sin(\frac{2\pi x}{L} + \phi'_n) \hat{\mathbf{j}} & \text{for } nT + T/2 < t \leq (n+1)T \end{cases} \quad (14)$$

where T is the period, $n = 0, 1, 2, \dots$, and ϕ_n and ϕ'_n are random phases chosen independently and uniformly on $[0, 2\pi)$ in each half cycle. Then $U = w/\sqrt{2}$.

3 A particle code

In a particle code to solve the advection-diffusion equation, the concentration field ρ is represented by a distribution of particles. Particles introduced by generating random locations using the properly normalized source $S(\mathbf{x})$ as a probability distribution function, and advecting them with the flow. Given a particle distribution, $\rho(t, \mathbf{x})$ is measured by covering the domain with bins counting the number of particles per bin.

A particle code is employed because it can deal with a small-scale source. It is easily applicable for any source fields and advection fields, while the spectral method prefers fields whose Fourier expansion is simple. The downside of a particle code is that it necessarily introduces statistical errors: the number density of particles calculated by dividing the domain into bins is only resolved down to the lengthscale of bin size, and the measurement of ρ always includes error due to the use of finite number of particles.

In this section the numerical scheme based on a particle code is explained. The code mainly consists of three parts: 1) Time evolution, 2) calculation of variance, and 3) a particle subtraction scheme. The time evolution is realized by displacing each particle with appropriate advection and diffusion, and by adding new particles in accordance with a source term. We calculate spatial variance at a random instant once each half cycle in order to take its time average. A subtraction scheme removes group of particles that are well-mixed and this not participating in time evolution any longer. The subtraction scheme is necessary and crucial to prevent a calculation from slowing down due to an ever increasing number of particles in the system. Details of the code are presented in the appendix.

3.1 Variance calculation

The variance $\langle \theta^2 \rangle$ is measured by monitoring the fluctuations in the number of particles per bin and time averaging. In two dimensions the domain is divided into l^2 bins and the code calculates $\langle n^2 \rangle$ where n is the number of particles in a bin and $\langle \theta^2 \rangle$ is initially approximated by

$$\langle n^2 \rangle - \langle n \rangle^2 = \left(\frac{L}{l} \right)^2 \langle \theta^2 \rangle. \quad (15)$$

We say “initially” because the expression above includes both the hydrodynamic fluctuations of interest *and* discreteness fluctuations resulting solely from the fact that each bin contains a finite number of particles. We will discuss corrections to this expression for the variance to account for this effect below in Section 3.3. Beyond these inevitable fluctuations due to discreteness, because of the binning density fluctuations are observed only down to the length scales $\sim \frac{L}{l}$, which is one of the sources of error in this procedure.

The variance is calculated once per each half period, and the instant when it is calculated is determined randomly in order to obtain an unbiased time average. Thus each half period is divided into two parts, before and after variance calculation, and the particle transport and source processes are appropriately adapted.



Figure 1: Gaussian due to diffusion only. Figure 2: Distorted Gaussian due to shear.

3.2 Time evolution: particle transport

At each time step, the system is evolved by advection and diffusion, and by the source terms. First we focus on particle motion, and then on the particle input.

An advection-only equation would be solved by evolving particles along characteristics, and a diffusion-only equation would be solved by adding Gaussian random noise to each particle. With both advection and diffusion we need to solve a stochastic differential equations to determine the proper displacement of the particles during a time step. The stochastic differential equation is

$$d\mathbf{X} = \mathbf{u}(t, \mathbf{X})dt + \sqrt{2\kappa} d\mathbf{W} \quad (16)$$

where $\mathbf{W}(t)$ is a standard vector-valued Wiener process.

In order to solve (16) we will assume that the displacement due to the noise in a half-period $T/2$ is much smaller than the wavelength of the random sine flow. Then during each half period the drift field $\mathbf{u}(t, \mathbf{X})$ experienced by each particle can be approximated by a constant flow with a linear shear superposed. For the first half of the period for a particle starting at $(x_0, y_0) = (X(t=0), Y(t=0))$ we approximate (16) by

$$\begin{cases} dX = w \sin(\frac{2\pi y_0}{L} + \phi)dt + w \cos(\frac{2\pi y_0}{L} + \phi)\frac{2\pi}{L}(Y - y_0)dt + \sqrt{2\kappa} dW_1 \\ dY = \sqrt{2\kappa} dW_2 \end{cases} \quad (17)$$

and for the second half of the period, starting from $(x'_0, y'_0) = (X(t=T/2), Y(t=T/2))$,

$$\begin{cases} dX = \sqrt{2\kappa} dW_1 \\ dY = w \sin(\frac{2\pi x'_0}{L} + \phi')dt + w \cos(\frac{2\pi x'_0}{L} + \phi')\frac{2\pi}{L}(X - x'_0)dt + \sqrt{2\kappa} dW_2. \end{cases} \quad (18)$$

Therefore, during the first half period we evolve the position of a particle through a time interval Δt (where $\Delta t \leq T/2$ need *not* be small) by the map

$$x \rightarrow x_0 + w \sin(\frac{2\pi y_0}{L} + \phi) \Delta t + \sqrt{\frac{1}{6}S^2\kappa\Delta t^3 + 2\kappa\Delta t} \times N_1 + \sqrt{\frac{1}{2}S^2\kappa\Delta t^3} \times N_2 \quad (19)$$

$$y \rightarrow y_0 + \sqrt{2\kappa\Delta t} \times N_2 \quad (20)$$

where N_1 and N_2 are independent $N(0, 1)$ random variables. A similar map is employed during the second half of the period. These stochastic maps include the shear—in the approximation that the shear remains constant for each particle during each half cycle—that causes a “distortion” of a Gaussian cloud of particles; see Figures 1 and 2.

3.3 Time evolution: particle input

The steady scalar source is realized by introducing new particle one by one using normalized $S(\mathbf{x})$ as a probability distribution function. Numerically, such probability distribution function can be realized by mapping uniform random numbers with an inverse of cumulative probability distribution function in question. In Figures 3, 4 and 5, sample source terms are visualized by putting many (in these examples 10^4) particles at once. The monochromatic source in Figure 3 is $S(\mathbf{x}) = A[1 + \sin(2\pi(x + y)/L)]$.

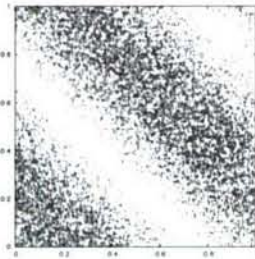


Figure 3: Monochromatic

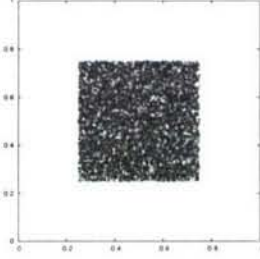


Figure 4: Square ($a = \frac{L}{2}$)

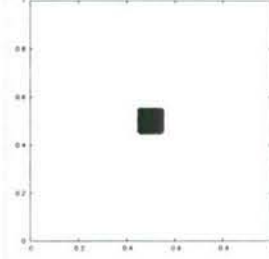


Figure 5: Square ($a = \frac{L}{10}$)

In the actual time evolution of the system, however, new particles are added one by one. Since new particles are put in constantly, the total number of particles increases which makes computation slow down. To cope with increasing particles, we will implement a particle subtraction scheme as described in the next section.

3.4 Background noise and subtraction scheme

Particles eventually get well mixed, and the “older” particles do not contribute the value of the hydrodynamic variance. There is no added value in keeping track of those particles, and we can simply remove them from the system after a sufficiently long time. In fact it is necessary to implement such a particle subtraction scheme so that computation goes on without slowing down.

A subtraction scheme eliminates particles which are “well-mixed”, but we need to be careful about the well-mixedness in a particle code. If the system is completely mixed, the hydrodynamic variance $\langle \theta^2 \rangle = 0$. But since $\theta(t, \mathbf{x})$ is represented with a finite number of particles and bin of a finite size, $\langle \theta^2 \rangle_{\text{measured}}$ is nonzero even when the particles are uniformly distributed: $\langle n^2 \rangle$ has the same amount of fluctuations as the error we might have when N_{all} particles are randomly thrown in l^2 bins. Thus when the particles are uniformly distributed $\langle n^2 \rangle - \langle n \rangle^2$ is the order of N_{all}/l^2 as illustrated in Figures 6 and 7. There $\overline{\theta^2}_{\text{measured}}(t)$ —where the overline now represents the volume average—is plotted in the diffusion-only case with the monochromatic initial condition. Instead of approaching 0, $\overline{\theta^2}_{\text{measured}}(t)$ goes to N_{all}/l^2 . We call this departure from 0 a *background fluctuation*, and we refer to the error

due to the use of the finite number of particles and finite size of a bin as error due to *discreteness*.

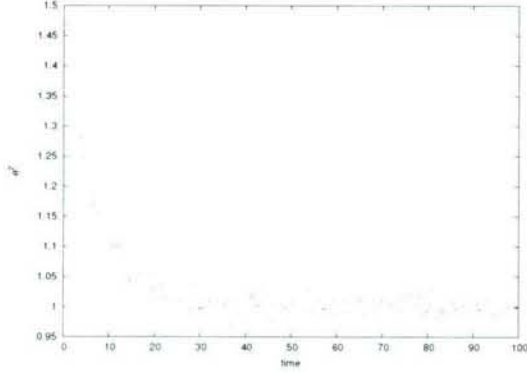


Figure 6: $\kappa = 10^{-3}$, $N_{\text{all}} = 10^4$, 10^4 bins

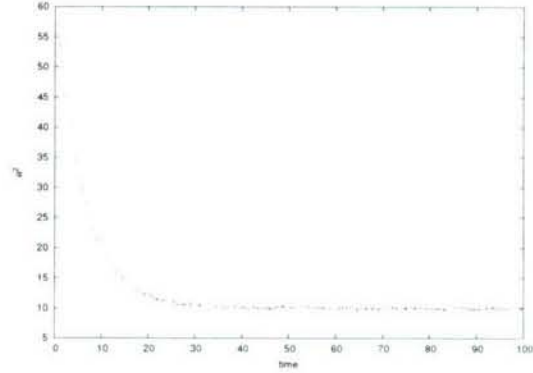


Figure 7: $\kappa = 10^{-3}$, $N_{\text{all}} = 10^5$, 10^4 bins

These background fluctuations must be removed to obtain hydrodynamic variance that we are interested in. The effect of this subtraction is illustrated in Figures 8 and 9. When the initial density is $\rho(0, \mathbf{x}) = A[1 + \sin(2\pi(x + y)/L)]$,

$$\rho(t, \mathbf{x}) = A \left[1 + e^{-\frac{8\pi^2}{L^2}\kappa t} \sin\left(\frac{2\pi}{L}(x + y)\right) \right], \quad (21)$$

the instantaneous hydrodynamic variance, i.e., $\overline{\theta^2} = \overline{(\rho - \bar{\rho})^2}$, is

$$\overline{\theta^2}(t) = \frac{A^2}{2} e^{-\frac{16\pi^2}{L^2}\kappa t}. \quad (22)$$

As illustrated in Figure 9, after background fluctuations are subtracted off we obtain the correct behavior, i.e., exponential decay. In Figure 8 it might be difficult to tell the difference, but in the log-linear plot in Figure 9 it is obvious that θ^2 shows exponential decay only after background noise is removed. From this point on, this background noise is always removed when $\langle \theta^2 \rangle$ is calculated.

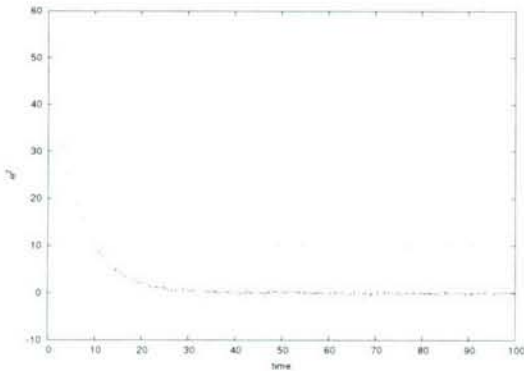


Figure 8: Normal plots

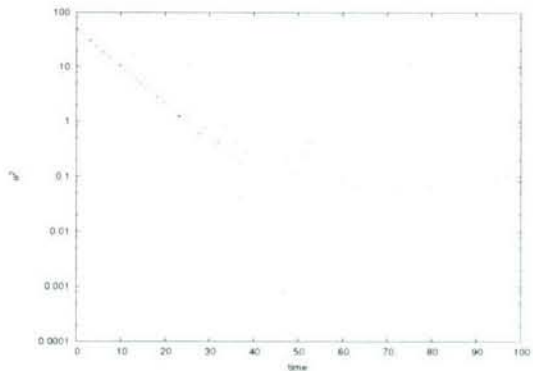


Figure 9: Log-normal plots

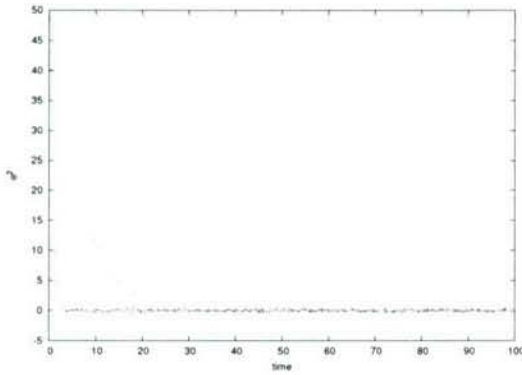


Figure 10: Normal plots

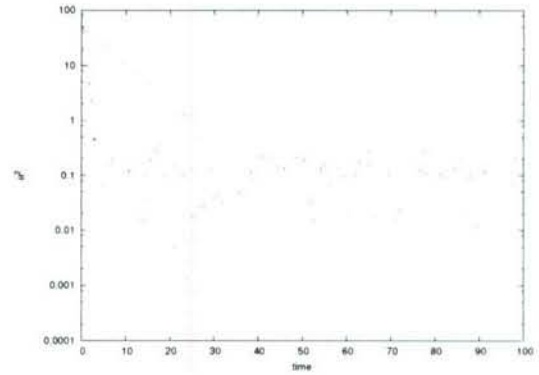


Figure 11: Log-normal plot.

A group of particles can be discounted, removed from further consideration, once their variance reaches the level of background fluctuation. In the actual code, we keep track the Δn particles put in a half period as a group and they are removed after they participate in the time evolution for a time t_* , where t_* is a typical time scale for Δn particles to reach the background fluctuation level. The “lifetime” t_* depends on the number of particles in the cohort we are regarding as “old”, the form of the source field, the advection field, and of course the diffusion coefficient κ . This lifetime is estimated by plotting a transient behavior of the variance of Δn particles under the particular advection and/or diffusion conditions of interest. In Figures 10 and 11, 10^5 particles, initially distributed as for the monochromatic source, are mixed by diffusion or advection-diffusion. Eventually both cases end up in a well-mixed state (in the figures, background fluctuations are already removed) and t_* is estimated to be ~ 10 in the case of advection-diffusion and ~ 45 in the case of only diffusion. These values of t_* would then be used for long time average measurements for these particular source, stirring and diffusion conditions. For each source, stirring or amplitude of diffusion, such a transient calibration simulation must be repeated to determine the appropriate value of t_* .

3.5 Benchmark Tests

In this section we report the results of specific simulation where the particle code results can be compared to either exact solutions or numerical solutions of the inhomogeneous advection-diffusion partial differential equation. These benchmark tests serve as a check of the code and give some quantitative information about our particle tracking scheme’s accuracy.

3.5.1 Simulation parameter independence

First of all, the measures of hydrodynamic variances should be independent of Δn (the number of particles introduced each half-cycle of the stirring) or the bin size that is used to estimate $\rho(t, \mathbf{x})$. The parameter independence can be checked by changing the value of Δn or l with other conditions fixed. Here, we illustrate Δn independence by showing the exponential decays of transient variance for several values of Δn . κ is 0.01, 0.001,

0.0001, respectively, and $\Delta n = 10^4$ (red), 10^5 (green) and 10^6 (blue) (Figures 12, 13 and 14). The plots show exponential decay until the particles are well-mixed, as expected, and

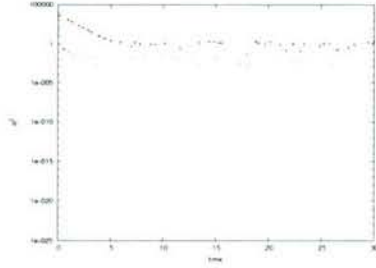


Figure 12: $\kappa=0.01$

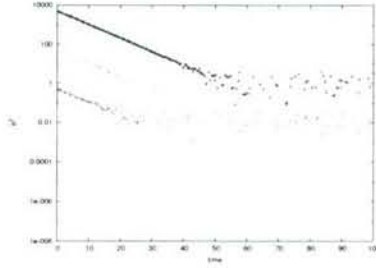


Figure 13: $\kappa=0.001$

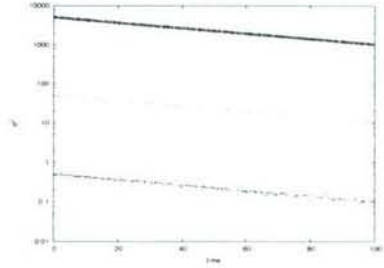


Figure 14: $\kappa=0.0001$

the exponential decay rates are independent of Δn (at least in the range $[10^4, 10^6]$ tested). The straight lines fit to the data here are the exact theoretical values with no adjustable parameters.

3.5.2 Diffusion-only with steady source

Secondly we consider diffusion-only with a steady source since $\langle \theta_0^2 \rangle$ can be calculated exactly for these cases. It is possible to solve Eq. (9) analytically by Fourier expansion:

$$\theta_0(t, \mathbf{x}) = \sum_{\mathbf{k} \neq 0} \hat{\theta}_0(t, \mathbf{k}) e^{i\mathbf{k} \cdot \mathbf{x}} \quad (23)$$

$$s(\mathbf{x}) = \sum_{\mathbf{k} \neq 0} \hat{s}(\mathbf{k}) e^{i\mathbf{k} \cdot \mathbf{x}} \quad (24)$$

Note that $\hat{\theta}_0(t, \mathbf{k} = \mathbf{0}) = 0$ and that $\hat{s}(t, \mathbf{k} = \mathbf{0}) = 0$, because $\theta(t, \mathbf{x})$ and $s(\mathbf{x})$ have zero spatial means. The inhomogeneous diffusion equation is

$$\frac{\partial \hat{\theta}_0}{\partial t} = -\kappa k^2 \hat{\theta}_0(t, \mathbf{k}) + \hat{s}(\mathbf{k}) \quad (25)$$

so that

$$\hat{\theta}_0(t, \mathbf{k}) = \frac{\hat{s}(\mathbf{k})}{\kappa k^2} + \left(\hat{\theta}_0(0, \mathbf{k}) - \frac{\hat{s}(\mathbf{k})}{\kappa k^2} \right) e^{-\kappa k^2 t} \quad (26)$$

Plugging this expression into the definition of $\langle \theta_0^2 \rangle$,

$$\langle \theta_0^2 \rangle = \lim_{T \rightarrow \infty} \frac{1}{T} \int_0^T dt \frac{1}{L^d} \int d^d x \sum_{\mathbf{k}, \mathbf{k}' \neq 0} \hat{\theta}_0(t, \mathbf{k}) \hat{\theta}_0(t, \mathbf{k}') e^{i(\mathbf{k} + \mathbf{k}') \cdot \mathbf{x}} \quad (27)$$

$$= \lim_{T \rightarrow \infty} \frac{1}{T} \int_0^T dt \sum_{\mathbf{k} \neq 0} |\hat{\theta}_0(t, \mathbf{k})|^2 \quad (28)$$

$$= \frac{1}{\kappa^2} \sum_{\mathbf{k} \neq 0} \frac{|\hat{s}(\mathbf{k})|^2}{k^4} \quad (29)$$

We now check if the particle simulation code produces this value with three kinds of sources: (1) a monochromatic source, (2) a square source and (3) a delta-function source.

For the monochromatic source,

$$\langle \theta_0^2 \rangle = \frac{S^2 L^4}{128\pi^4 \kappa^2} \quad (30)$$

$$\langle n_0^2 \rangle = \langle \theta_0^2 \rangle \cdot (\text{bin vol.}) = \frac{\left(\frac{\Delta n}{\Delta t}\right)^2 L^4}{128\pi^4 \kappa^2} \quad (31)$$

and the comparison of theory and simulation is presented in tabular form:

κ	$\langle \theta_0^2 \rangle_{\text{calculated}}$	theoretical values
0.05	0.1290±0.0076	0.128324
0.02	0.7914±0.0032	0.802029
0.01	3.215±0.010	3.208119
0.005	12.370±0.014	12.8324
0.002	78.836±0.052	80.2029
0.001	312.82±0.13	320.8119
0.0005	1236.39±0.29	1283.24

For the square sources

$$s(\mathbf{x}) = \begin{cases} S & \mathbf{x} \in \left[-\frac{a}{2} + \frac{L}{2}, \frac{a}{2} + \frac{L}{2}\right] \\ 0 & \text{otherwise} \end{cases} \quad (32)$$

the variances are

$$\langle \theta_0^2 \rangle = \frac{1}{\kappa^2} \frac{16S^2}{L^4} \sum_{\mathbf{k} \neq \mathbf{0}} \frac{1}{(k_1^2 + k_2^2)^2} \left(\frac{\sin(k_1 \frac{a}{2})}{k_1} \right)^2 \left(\frac{\sin(k_2 \frac{a}{2})}{k_2} \right)^2 \quad (33)$$

$$\langle n_0^2 \rangle = \frac{1}{\kappa^2} \frac{16}{a^4} \left(\frac{\Delta n}{\Delta t} \right)^2 \sum_{\mathbf{k} \neq \mathbf{0}} \frac{1}{(k_1^2 + k_2^2)^2} \left(\frac{\sin(k_1 \frac{a}{2})}{k_1} \right)^2 \left(\frac{\sin(k_2 \frac{a}{2})}{k_2} \right)^2 \quad (34)$$

and the simulations yield

$a = \frac{L}{2}$		
κ	$\langle \theta_0^2 \rangle_{\text{calculated}}$	theoretical values
0.01	45.593±0.041	45.862
0.005	177.750±0.092	183.448

$a = \frac{L}{10}$		
κ	$\langle \theta_0^2 \rangle_{\text{calculated}}$	theoretical values
0.01	141.593±0.075	142.092
0.005	565.99±0.19	568.37

$a = \frac{L}{20}$		
κ	$\langle \theta_0^2 \rangle_{\text{calculated}}$	theoretical values
0.01	150.502±0.086	150.615
0.005	599.79±0.20	602.46

Finally, for the delta-function source

$$s(\mathbf{x}) = S\delta\left(x - \frac{L}{2}\right)\delta\left(y - \frac{L}{2}\right), \quad (35)$$

we have

$$\langle\theta_0^2\rangle = \frac{1}{\kappa^2} \frac{S^2}{L^4} \sum_{\mathbf{k}\neq\mathbf{0}} \frac{1}{(k_1^2 + k_2^2)^2} \quad (36)$$

$$\langle n_0^2 \rangle = \frac{1}{\kappa^2} \left(\frac{\Delta n}{\Delta t}\right)^2 \sum_{\mathbf{k}\neq\mathbf{0}} \frac{1}{(k_1^2 + k_2^2)^2} = \frac{1}{\kappa^2} \left(\frac{\Delta n}{\Delta t}\right)^2 L^4 \cdot 3.8669 \times 10^{-3}. \quad (37)$$

(Note that (37) can be obtained by letting $a \rightarrow 0$ in (34).) We can check if the code outputs the same value:

κ	l	$\langle\theta_0^2\rangle_{\text{measured}}$	theoretical values
0.02	100	37.772±0.023	38.669
0.01	100	142.673±0.064	154.678
0.02	200	2.4127±0.0025	2.4168
0.01	200	9.4448±0.0044	9.6674
0.02	400	0.15116±0.00024	0.15105
0.01	400	0.59042±0.00034	0.60421
0.005	400	2.36000±0.00085	2.41684

In those results, $\langle\theta_0^2\rangle_{\text{measured}}$ tends to be smaller than the theoretical values because variance calculation is based on bins of a finite size and the contribution from smaller scales is not included. If $\langle\theta_0^2\rangle_{\text{measured}}$ is compared with, say,

$$\frac{1}{\kappa^2} \sum_{\substack{|\mathbf{k}|\leq\frac{2\pi}{\Delta l} \\ \mathbf{k}\neq\mathbf{0}}} \frac{|\hat{s}(\mathbf{k})|^2}{k^4}, \quad (38)$$

the discrepancies would be smaller. Also, note that in the case of a delta function source, the bin size needs to be very small—at least in the neighborhood of the source—in order to obtain accurate values.

3.5.3 Advection, diffusion and a steady source

Finally, we compare the full advection-diffusion-source code with the results of a spectral method applied to the inhomogeneous advection-diffusion partial differential equation. In Figure 15, the mixing efficiency is plotted against Pe for the case of the monochromatic source stirred by the random sine flow. The green curve shows the theoretical upper bound and the red curve is calculated by spectral method [4, 5]. The blue points are from the particle code. This comparison shows that the code accurately calculates mixing efficiencies and that it can be effectively as accurate as spectral method even with Δn is as small as 10^4 .

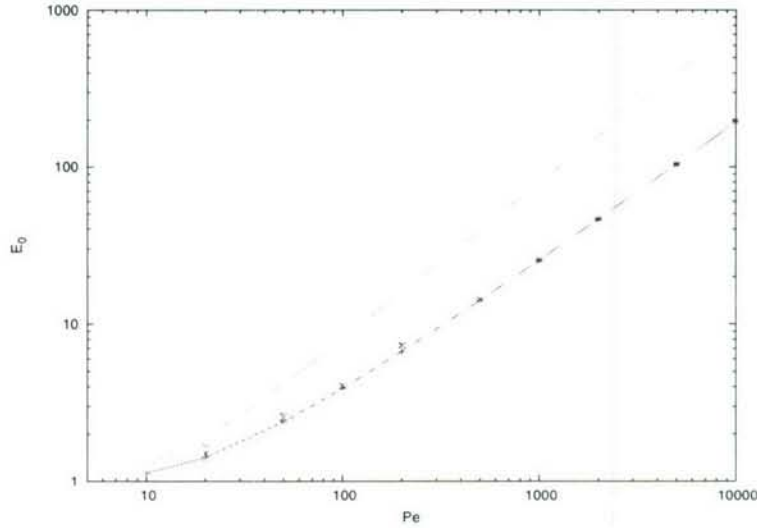


Figure 15: Benchmark test for the mixing efficiency with a monochromatic source.

4 New applications

The particle code is applicable for small-scale sources, as shown in the diffusion-only case in the previous section. Figures 16, 17 show, respectively, the upper bounds on the mixing efficiencies and the measured values of the mixing efficiencies for square and delta function sources. The theoretical upper bounds and data plots are for source sizes $L/2, L/10, L/50$ and a delta function source (from top to bottom in each plot). The upper bound analysis predicted that as the source gets smaller, the $\mathcal{E}_0(\text{Pe})$ curves are lowered. While the upper bound for any finite-size source is asymptotically $\sim \text{Pe}$, the delta function source behaves $\sim \frac{\text{Pe}}{\sqrt{\ln \text{Pe}}}$ in the large Pe limit.

As the source gets smaller, the measured mixing efficiencies get smaller in a way that is qualitatively remarkably similar to that shown by the bounds. That is, Figures 16 and 17 show that the observed mixing efficiencies qualitatively display the same features as that of upper bounds as far as source-size is concerned. The bounds and simulation data are plotted together for comparison in Figure 18.

5 Future Works and Conclusions

We have confirmed that we can use a particle code to study hydrodynamic mixing efficiencies. The particle method reproduces theoretical values and previous numerical simulation correctly. As we saw, the outputs may be as accurate as a PDE code. Moreover, the number of particles used to represent the passive scalar field can be as small as 10^4 . The particle method is particularly useful for simulations at high Péclet number and with a wide variety, including singular measure-valued source distributions. In this project, the same code was used effectively for a monochromatic source, square sources and a delta-function source. The code efficiently produced reliable results for all these cases.

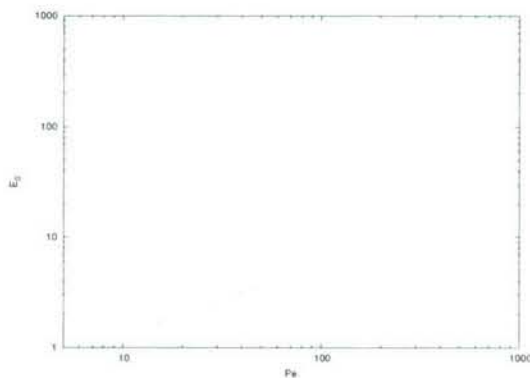


Figure 16: Upper bounds

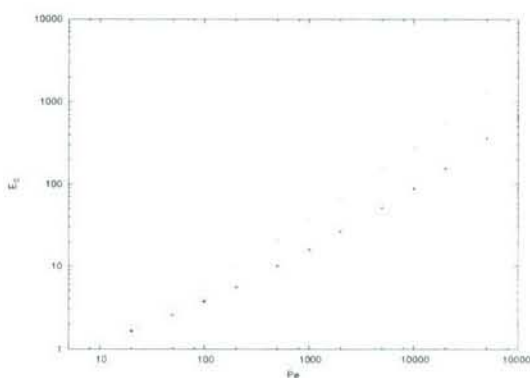


Figure 17: The plot of mixing efficiencies

What we have done here is just the very beginning of investigations exploiting the particle code. There are lots of problems to be explored. Firstly, we can adapt the method to other stirring fields. In this paper only the random sine flow was used, but it is possible to extend this approach to other advection fields such as sine flows with a variety of wave numbers or turbulent flows. Secondly, simulations in three dimensions important. The distinction between mixing efficiencies for the finite-size square sources and a delta function source is predicted to be much more apparent in 3D. The extension of the particle method to 3D is straightforward although simulations will require much more computation power (more particles and more bins will be necessary). Thirdly, the mixing efficiency on large length scales, \mathcal{E}_{-1} , can be calculated in principle even though only \mathcal{E}_0 was calculated in this project. Fourthly, we would like to see the results of the small-scale sources reported here reproduced by another numerical scheme. Then the results presented in this report can serve as a benchmark test for new codes.

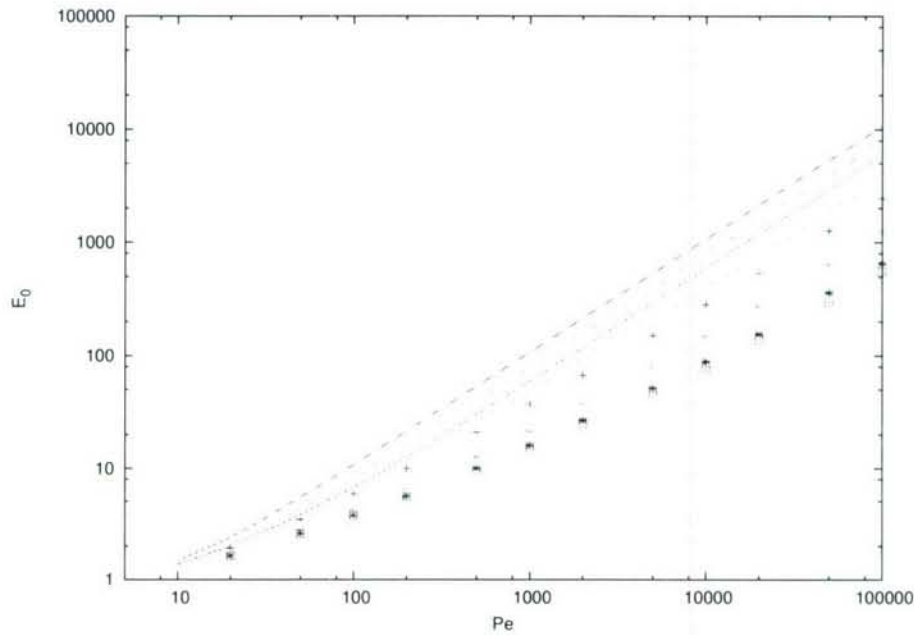


Figure 18: Upper bounds (solid lines) and simulation data (points). The different colors represent the different source sizes.

6 Acknowledgements

The author is grateful for the wonderful summer. I learned much by studying with the intelligent fellow Fellows. The principal lecture by Dr. Worster was full of intellectual excitement even though I knew nothing about the theory of sea ice before. The author sincerely appreciates my advisor, Dr. Doering. He taught me the mixing efficiency problem from scratch, and when I was having difficulties with the code, he helped me by suggesting possible solutions. I could not have accomplished the project without his patient guidance and encouragement. It has been one of my greatest honors to complete research under the supervision of Dr. Doering.

References

- [1] J. -L. Thiffeault, C. R. Doering, and J. D. Gibbon, *J. Fluid Mech.* **521** (2004), 105-114.
- [2] S. Plasting and W. R. Young, *J. Fluid Mech.* **552** (2006), 289-298.
- [3] Charles R. Doering and Jean-Luc Thiffeault, *Phys. Rev. E* Vol. 74, 025301(R) (2006).
- [4] T. A. Shaw, J. -L. Thiffeault and C. R. Doering, Stirring up trouble, *Physica D* (submitted, 2006).

- [5] T. A. Shaw, Bounds on Multiscale Mixing Efficiencies. *Proc. 2005 Summer Program in Geophysical Fluid Dynamics*. Woods Hole Oceanographic Institution, Woods Hole, MA, USA. <http://gfd.who.edu/proceedings/2005/PDFvol2005.html>.

Appendices

In these appendices we explain the detail of the code, including the actual implementation.

A Calculation of Variance

The domain is divided into $l \times l$ bins (i.e. bin size is $\text{deltal}=L/l$) in order to calculate instantaneous variances. Given positions of all the particles, ($p[n].x$ and $p[n].y$ ($n=1, 2, \dots, N_{\text{all}}$), the number of particles in each bin ($\text{bin}[c]$, $c=1, 2, \dots, l \times l$) is counted as follows.

```
for(n=1; n<=N_all; n++){
  u=(int)(p[n].x/deltal);
  v=(int)(p[n].y/deltal);
  bin[v*l+u+1]=bin[v*l+u+1]+1;
}
```

u and v are horizontal and vertical positions of a bin. Bins are labeled from bottom left to top right, and if a bin is located at (u, v) , the label is $v \times l + u + 1$. Variance calculation follows.

```
nbar=(double)N_all/(double)(l*l);
a=0;
for(c=1; c<=l*l; c++){
  {
  a=a+(bin[c]-nbar)*(bin[c]-nbar)/((double)l*(double)l);
  }
}
var=a-nbar;
```

In the last line, background fluctuation is removed.

B Miscellaneous components on time evolution

B.1 Periodic boundary condition

```
for(n=1; n<=N_all; n++) {
  while(p[n].x>L){p[n].x=p[n].x-L;}
  while(p[n].x<0.0){p[n].x=p[n].x+L;}
  while(p[n].y>L){p[n].y=p[n].y-L;}
  while(p[n].y<0.0){p[n].y=p[n].y+L;}
}
```

B.2 Source term

Source term is realized by adding a new particle one by one in accordance with $S(\mathbf{x})$. In the case of a square source, a new particle is generated every $\Delta n/\Delta t$, using a probability distribution function

$$p(x, y) = \begin{cases} \frac{1}{a^2} & \mathbf{x} \in \left[-\frac{a}{2} + \frac{L}{2}, \frac{a}{2} + \frac{L}{2}\right]^2 \\ 0 & \text{otherwise} \end{cases} \quad (39)$$

The corresponding code is

```
void source(double a, double *xo, double *yo){
double x1,x2;
x1=a*(double)rand()/(double)RAND_MAX+0.5-0.5*a;
x2=a*(double)rand()/(double)RAND_MAX+0.5-0.5*a;
*xo=x1;
*y0=x2;
}
```

A monochromatic source is a little bit difficult. We need to generate a pair of random numbers which follow

$$p(x, y) = 1 + \sin\left(\frac{2\pi}{L}(x + y)\right) \quad \mathbf{x} \in [0, L]^2 \quad (40)$$

Because this probability distribution function is tilted, let us consider it in the new coordinates $(\xi, \eta) = \left(\frac{1}{\sqrt{2}}(x + y), \frac{1}{\sqrt{2}}(-x + y)\right)$. Then, the probability distribution function becomes

$$p(\xi) = \frac{1}{\sqrt{2}} \left(1 + \sin\left(\frac{2\pi}{L}\sqrt{2}\xi\right)\right) \quad \xi \in [0, \sqrt{2}], \eta \in [0, \sqrt{2}]. \quad (41)$$

η is given by uniform random numbers, and ξ is given by mapping uniform random numbers by the inverse of the cumulative distribution function of (41):

$$\frac{\xi}{\sqrt{2}} + \frac{L}{4\pi} - \frac{L}{4\pi} \cos\left(\frac{4\pi}{\sqrt{2}L}\xi\right) \quad (42)$$

The subroutine `inv` maps a uniform random number `y` with the function above by using bisection method up to the accuracy of `0.01*deltal`. Then `source` subroutine rotates the frame by $\frac{\pi}{4}$ and imposes periodic boundary conditions.

```
void source(double deltal, double *xo, double *yo){
double x1,x2,y,z1,z2;
y=(double)rand()/(double)RAND_MAX;
x1=inv(y,deltal);
x2=sqrt(2.0)*(double)rand()/(double)RAND_MAX;
```



```

z1=(x1-x2)/sqrt(2.0)+0.5;
z2=(x1+x2)/sqrt(2.0)-0.5;
while(z1>1.0){z1=z1-1.0;}
while(z1<0.0){z1=z1+1.0;}
while(z2>1.0){z2=z2-1.0;}
while(z2<0.0){z2=z2+1.0;}
*xo=z1;
*y0=z2;
}

double inv(double y, double deltal)
{
double small, mid, large;
int i;
small=0.0;
large=sqrt(2.0);
while(large-small>0.01*deltal)
{
mid=0.5*(large+small);
if(func(large,y)*func(mid,y)<0.0){small=mid;}
else{large=mid;}
}
return(mid);
}

double func(double x,double y)
{
double z;
z=-y+x/sqrt(2.0)+1.0/(4.0*pi)-cos(4.0*pi*x/sqrt(2.0))/(4.0*pi);
return(z);
}

```

B.3 distorted Gaussian profile: (noise) subroutine

The following code is just the noise parts of (19) and (20). Normal Gaussian noises (y1, y2) are generated by using Box-Muller method.

```

void noise(double kappa, double S, double dt, double *rand1, double
*rand2) {

double x1,x2,y1,y2, a,b,c;
x1=((double)rand()+0.01)/((double)RAND_MAX+0.01);
x2=((double)rand()+0.01)/((double)RAND_MAX+0.01);

```

```

y1=sqrt(-2.0*log(x1))*cos(2.0*pi*x2);
y2=sqrt(-2.0*log(x1))*sin(2.0*pi*x2);
a=S*sqrt(0.5*kappa)*dt*sqrt(dt);
b=sqrt(kappa*S*S*dt*dt*dt/6.0+2.0*kappa*dt);
c=sqrt(2.0*kappa*dt);
*rand1=a*y1+b*y2;
*rand2=c*y1;
}

```

B.4 Subtraction scheme

It is easy to implement subtraction scheme. Subtraction of N_{old} older particles is done by re-labeling particles. $(N_{\text{old}} + i)$ th particle becomes i th particle, and the number of all the particles gets smaller by N_{old} . In this code, $N_{\text{old}} = \Delta n$.

```

if(j>=cutoff){
N_all=N_all-deltan;
for(n=1;n<=N_all;n++){
p[n].x=p[n+deltan].x;
p[n].y=p[n+deltan].y;
}
}

```

C Time evolution

The following code is time evolution from the beginning of the period to variance calculation.

```

phi=2.0*pi*rand()/(double)RAND_MAX;
randt=(double)rand()/(double)RAND_MAX;
for(c=1;c<=l*1;c++)
{
bin[c]=0;
}
a=0.0;
t_obs=deltat*randt;
N_obs=(int)(deltan*randt);
for(n=1;n<=N_all;n++)
{
noise(kappa, -w*2.0*pi*cos(2.0*pi*p[n].y/L+phi)/L, t_obs, &rand1,
&rand2);
p[n].x=p[n].x-t_obs*w*sin(2.0*pi*p[n].y/L+phi)+rand1;
p[n].y=p[n].y+rand2;
while(p[n].x>L){p[n].x=p[n].x-L;}
}

```

```

while(p[n].x<0.0){p[n].x=p[n].x+L;}
while(p[n].y>L){p[n].y=p[n].y-L;}
while(p[n].y<0.0){p[n].y=p[n].y+L;}
u=(int)(p[n].x/deltal);
v=(int)(p[n].y/deltal);
bin[v*1+u+1]=bin[v*1+u+1]+1;
}
for(n=1;n<=N_obs;n++)
{
dt=t_obs-deltat*(double)n/(double)deltan;
source(deltal, &xo, &yo);
noise(kappa, -w*2.0*pi*cos(2.0*pi*yo/L+phi)/L, dt, &rand1, &rand2);
p[n+N_all].x=xo-dt*w*sin(2.0*pi*yo/L+phi)+rand1;
p[n+N_all].y=yo+rand2;
while(p[n+N_all].x>L){p[n+N_all].x=p[n+N_all].x-L;}
while(p[n+N_all].x<0.0){p[n+N_all].x=p[n+N_all].x+L;}
while(p[n+N_all].y>L){p[n+N_all].y=p[n+N_all].y-L;}
while(p[n+N_all].y<0.0){p[n+N_all].y=p[n+N_all].y+L;}
u=(int)(p[n+N_all].x/deltal);
v=(int)(p[n+N_all].y/deltal);
bin[v*1+u+1]=bin[v*1+u+1]+1;
}
N_all=N_all+N_obs;
nbar=(double)N_all/(double)(1*1);

```

First, random phase (ϕ), the time to calculate variance (t_{obs}) and the number of particles added into the domain from the beginning of the period to the variance calculation (N_{obs}) are calculated. In the first `for`-loop, the particles which already existed at the beginning of the period are evolved based on (19) and (20), boundary conditions are imposed and (coarse-grained) concentration field is recovered by binning. In the following `for`-loop, new particles from a source term are added with `source` subroutine. `dt` is a time from particle creation to the variance calculation, which is different from particle to particle. Those new particles are evolved in the same way as existing particles. The time evolution after the variance calculation is implemented in the same way. The time evolution of the second half of the period is similar except that the random sine flow is vertical.

On Thin Ice: The Mechanics of Failure in Sea Ice

Dominic Vella

March 15, 2007

1 Introduction

Sheets of floating ice are rarely at rest or found in isolation. They are driven by wind and water stresses and hence collisions with other sheets are unavoidable. The focus of this report is on the mechanical aspects of slow collisions between thin sheets of floating ice. Such interactions underlie the mosaic of patterns found in the world's most extensive bodies of floating ice — sea ice — and hence are of geophysical importance. However, we are drawn to the topic by the simple fact that the patterns resulting from collisional interactions are visually arresting and may have mechanical implications that extend beyond the system that motivates our work. We begin with a description of some of the phenomenology that we aim to understand.

In sea ice, where the “sheets” of relevance are called “floes”, collisions are observed to create three families of patterns. The creation of each family, which can be characterized by a post-collision pattern or morphology, can be envisioned either as the result of the compression of a single sheet, or floe, of ice that fails and forms two floes which continue to collide, or the collision between two pre-existing floes. Often, due to the inhomogeneities of the floes involved, or the forcing that drives them together, some combination of these three patterns is observed in the field.

The most destructive of these families of ice patterns is the pressure ridge in which the two ice floes break up as they collide thereby forming a “sail” and a “keel” of highly fractured ice blocks. Less destructive are the two types of rafting illustrated in figure 1: simple rafting and finger rafting. In simple rafting, one ice floe rides over the adjoining floe without the creation of a large amount of rubble. Finger rafting is similar to simple rafting in the sense that the two floes alternately ride over and under one another forming a series of interlocking fingers. Generically, these fingers have very sharp linear features that are particularly striking — as is the well-defined spacing of the fingers.

For those interested in geophysical scale modelling of the interaction of sea ice with the atmosphere and the ocean, these deformation processes are particularly important. For example, the ridging and rafting of ice alters the albedo of the ice cover significantly (in rafting, the ice doubles in thickness and so appears much whiter than surrounding ice) and plays a major role in the mechanical redistribution of sea ice thickness [2]. Rothrock [15] also provides reasons for studying these deformation phenomena:

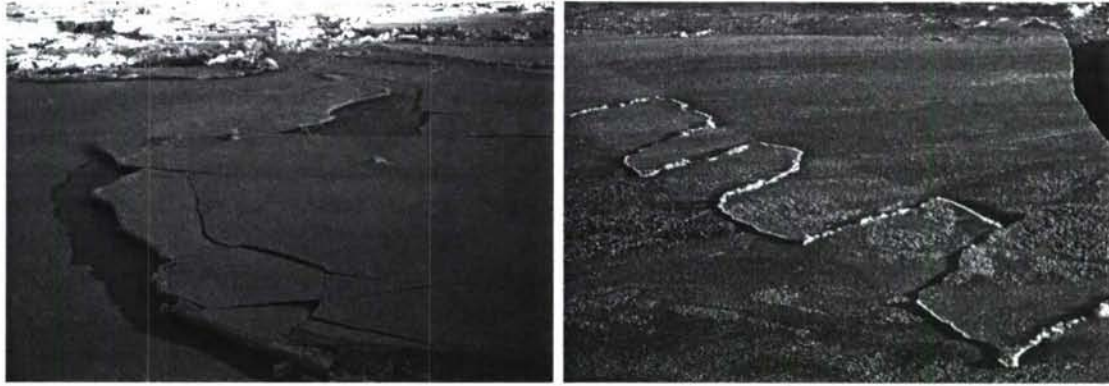


Figure 1: Rafting of thin sea ice. Left: ‘simple’ rafting of one floe over another in the Beaufort Sea. Note the crack formation parallel to the free edge of the ice. Right: ‘finger’ rafting in the Amundsen Sea. Photographs courtesy of Wilford Weeks [21].

“If we knew what the constitutive equation for pack ice should be, we would not need to pay attention to the mechanisms of floe interaction. But the simple fact is that we are not at all sure about the constitutive equation . . . we have turned to the study of these mechanisms — rafting, ridging, shearing, and opening — to deduce what we can about the large-scale mechanical behavior of pack ice.”

Because the families of deformation patterns are intrinsically interesting, our outlook on the value of this study is one of optimism. We would like to understand the formation of finger structures in finger rafting and determine what the characteristic width of the resulting fingers is. We would also like to characterize the precise conditions under which each of the three deformation patterns is observed.

2 Governing equations

Throughout this report, we shall model an ice floe as a thin elastic sheet floating on a denser liquid: water. In this section we describe the governing equations for a thin plate, including the effects of in-plane forces. Some detail on the origin of these equations is given by Mansfield [12].

The midplane displacement, $w(x, y)$, of a thin elastic plate subject to a pressure p is determined by a balance of forces on the plate. If we introduce a force function φ to ensure that forces are balanced in the plane of the plate, then the normal force balance leads to the governing partial differential equation

$$B\nabla^4 w = p + [w, \varphi] \quad (1)$$

where B is the bending stiffness, or flexural rigidity, of the plate and

$$[a, b] \equiv \frac{\partial^2 a}{\partial x^2} \frac{\partial^2 b}{\partial y^2} - 2 \frac{\partial^2 a}{\partial x \partial y} \frac{\partial^2 b}{\partial x \partial y} + \frac{\partial^2 a}{\partial y^2} \frac{\partial^2 b}{\partial x^2}. \quad (2)$$

B is related to the plate thickness, h , as well as the elastic properties of the material (the Young's modulus, E , and Poisson ratio, ν) by

$$B = \frac{Eh^3}{12(1 - \nu^2)}. \quad (3)$$

For an elastic sheet (of density ρ_s) floating on a liquid (of density ρ) the pressure p is simply the hydrostatic pressure in the liquid. With no forces other than gravity acting, the sheet will float with $w = w_\infty \equiv h(1/2 - \rho_s/\rho)$. For simplicity, therefore, we shall measure all vertical displacements relative to this equilibrium level. The pressure p is then given by $p = -\rho gw$ from which it immediately follows that

$$B\nabla^4 w + \rho gw = [w, \varphi]. \quad (4)$$

For a displacement (u, v, w) , the in-plane strains, ϵ_{ij} , are given by

$$\epsilon_{xx} = u_{,x} + \frac{1}{2}w_{,x}^2, \quad \epsilon_{yy} = v_{,y} + \frac{1}{2}w_{,y}^2, \quad \epsilon_{xy} = \frac{1}{2}(u_{,y} + v_{,x} + w_{,x}w_{,y}), \quad (5)$$

where $w_{,x}$ denotes the partial derivative of w with respect to x and so on (hopefully avoiding confusion with the various components of tensors). The displacements u and v may be eliminated from these relationships using the condition of compatibility (e.g., [12], pg. 13). Relating the strains to the in-plane forces and hence to the derivatives of the force function φ , it is possible to show that

$$\nabla^4 \varphi = -\frac{1}{2}Eh[w, w]. \quad (6)$$

Equations (4) and (6) may be non-dimensionalized by rescaling lengths with $\ell_* \equiv (B/\rho g)^{1/4}$ and the force function φ with the bending stiffness. In this analysis, ℓ_* , the length scale over which vertical deflections of the floe decay, plays a central role. We use uppercase letters to denote dimensionless quantities so that $X = x/\ell_*$, $\Phi = \varphi/B$ and so on. Equations (4) and (6) may then be rewritten as

$$\nabla^4 W + W = [\Phi, W], \quad (7)$$

and

$$\nabla^4 \Phi = -\frac{1}{2}\mathcal{S}[W, W] \quad (8)$$

respectively. Equations (7) and (8) are commonly attributed to one or both of Föppl and von Kármán (e.g., [12]).

In (8) we have introduced the dimensionless stretching stiffness

$$\mathcal{S} \equiv \frac{Eh}{(B\rho g)^{1/2}}, \quad (9)$$

which measures the relative ease with which the ice floe stretches and bends to accommodate deformation. Note that because $B \sim h^3$, $\mathcal{S} \sim h^{-1/2}$, and hence for the thin ice floes that are of interest here, we expect to find that $\mathcal{S} \gg 1$ so that deformation can be accommodated more easily by bending than stretching. This expectation is vindicated by substituting some typical values for the material properties of ice, as is shown by the data collected in table 1. This table also gives typical values for the characteristic length ℓ_* based on these material properties.

Ice type	Material Properties			Values for $h = 0.1$ m		Reference
	E (GPa)	ν	σ_m (MPa)	ℓ_* (m)	\mathcal{S}	
Fresh	0.3 – 12	0.33	1 – 3	3.1 ± 0.1	10^4	[8, 17]
Sea	0.1 – 0.9	—	0.1 – 0.4	1 – 1.7	$1 - 3 \times 10^3$	[22]
Sea	1	0.29	0.4	1.75	3.4×10^3	[5]

Table 1: Typical values from the literature for the mechanical properties of ice. Here, σ_m is the yield strength, to be introduced later. Also shown are the implied values of the characteristic length ℓ_* and the non-dimensional stretching stiffness, \mathcal{S} .

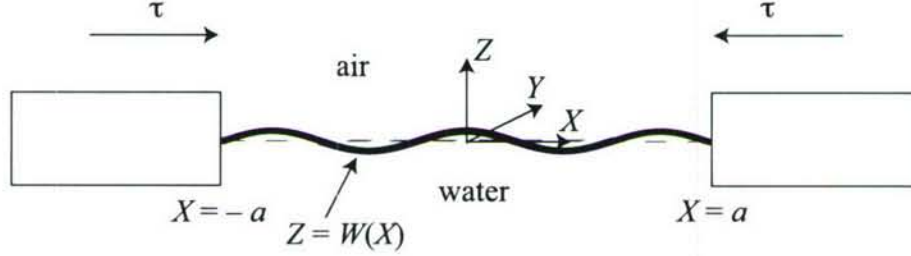


Figure 2: Schematic diagram showing a floating thin elastic sheet buckling under a compressive load τ .

3 The buckling failure of an ice floe

The most striking deformation patterns in sea ice are observed when two ice floes collide. This commonly occurs when a lead opens in thick ice and a thin layer of ice is formed by the freezing of ocean water in the lead. The movement of the thicker ice subjects the thin ice growing over the lead to large forces, which cause it to buckle and ultimately to fracture forming two or more floes. In this section we consider the buckling and subsequent failure of this thin ice.

In the two-dimensional buckling problem (illustrated in figure 2) there are no variations in the Y direction (i.e. into the page). The displacement of the ice plate, W , is therefore independent of Y and the Föppl-von Kármán equations (7)-(8) simplify to the system

$$W_{,4X} + W = \Phi_{,2Y}W_{,2X}, \quad \nabla^4\Phi = 0. \quad (10)$$

Since $W = W(X)$, $\Phi_{,2Y} = f(X)$ and so $\Phi_{,XY} = A(X) + Yf'(X)$. However, $\Phi_{,XY}$ is just the traction exerted on the ice in the Y -direction, i.e. into the page. This traction is zero for compression purely in the X -direction and so we have $f'(X) = 0$ and $f(X)$ is a constant. Since the traction in the X direction is τ at the boundary $X = a$, we have $\Phi_{,2Y}(a) = -\tau$ and so $f(X) = -\tau$. Equation (10) therefore reduces to the ordinary differential equation

$$W_{,4X} + \tau W_{,2X} + W = 0. \quad (11)$$

The relevant boundary conditions to accompany (11) deserve some discussion. The thin layer of ice covering a lead is normally frozen into the thicker ice at the edge of the lead. We therefore take the boundaries of the thin ice at $X = \pm a$ to be clamped so that $W_{,X}(\pm a) =$

$W(\pm a) = 0$. The symmetry conditions about $X = 0$ suggest that a solution is the form $W(X) = A \cos kX$, where the wavenumber k satisfies

$$k^4 - \tau k^2 + 1 = 0. \quad (12)$$

There are, therefore, two possible wavenumbers, k_{\pm} , given by

$$k_{\pm}^2 = \frac{1}{2}(\tau \pm \sqrt{\tau^2 - 4}). \quad (13)$$

In general $W(X)$ will contain both of the wavenumbers given in (13). The condition of zero vertical displacement at $X = \pm a$ is satisfied by

$$W(X) = A \left(\frac{\cos k_+ X}{\cos k_+ a} - \frac{\cos k_- X}{\cos k_- a} \right), \quad (14)$$

where A is some (as yet undetermined) constant. The remaining boundary condition that $W_X(\pm a) = 0$ leads to a condition relating k_+ and k_- , namely the dispersion relation

$$k_+ \tan k_+ a = k_- \tan k_- a. \quad (15)$$

Since $k_{\pm} = k_{\pm}(\tau)$, the solutions of (15) determine the compressive force τ required to produce this displacement. For a given value of a , (15) has an infinite number of solutions, the smallest of which is $\tau = 2$. This corresponds to the smallest value of τ for which k_+ and k_- are real; it is shown in Appendix A that there are no solutions of (15) for complex k_{\pm} . When $\tau = 2$, $k_+ = k_-$ and (14) shows that $W \equiv 0$. Each value of $\tau > 2$ that solves (15) corresponds to a different mode of buckling in the ice floe. We shall consider only the lowest mode of buckling, which corresponds to the smallest value of $\tau > 2$ that solves (15).

Having determined τ by solving (15) the solution for the shape of the buckled ice floe is given by (14) up to the multiplicative constant A . The value of A is determined by the natural length, L , of the ice floe in its undeformed state. Neglecting any stretching of the ice floe and assuming small deformations, the contour length of the deformed floe must be equal to its natural length, i.e.

$$L = \int_{-a}^a (1 + W_{,X}^2)^{1/2} dX \approx 2a + \frac{1}{2} \int_{-a}^a W_{,X}^2 dX. \quad (16)$$

In general, the ice floe may accommodate some of the imposed deformation by compressing (negative stretching). To account for this, we recall the expression for the strain ϵ_{XX} given in (5) and express the strain in terms of the force function Φ

$$U_{,X} + \frac{1}{2}W_{,X}^2 = \epsilon_{XX} = \frac{1}{S}(\Phi_{,2Y} - \nu\Phi_{,2X}) = -\frac{\tau}{S}. \quad (17)$$

Integrating this expression between $X = -a$ and a and using symmetry about $X = 0$, we find that

$$\int_0^a W_{,X}^2 dX = L - 2a(1 + \tau/S). \quad (18)$$

Substituting the form of $W(X)$ from (14), we find that

$$\int_0^a W_{,X}^2 dX = A^2 \left[\frac{a}{2}(k_+^2 + k_-^2) + ak_+^2 \tan^2 k_+ a + k_+ \tan k_+ a \right], \quad (19)$$

which can be substituted into (18) to give A . Since k_+ and τ are determined by the numerical solution of (15), they depend only on the value of a . The shape of the ice floe can, therefore, be completely determined numerically for given values of a and L .

Beyond some critical compression, the stresses within the ice floe become so large that a crack is initiated within the ice and the ice fails, forming multiple floes. We now quantify this expectation using the results just obtained for the buckled shape of the floe. Throughout this report we shall assume that failure occurs when the maximum stress throughout the thickness of the ice floe reaches some critical failure stress, denoted by σ_m . For elastic plates, the stress varies linearly with the perpendicular distance, z , from the mid-plane. In particular, from [12] p. 5 we have

$$\sigma_{ij} = \frac{Ez}{(1-\nu^2)B} M_{ij}, \quad (20)$$

where M is the bending moment. The maximum stress is then achieved at the plate surface ($|z| = h/2$) and the ice will fail if

$$\sigma_m \leq \frac{Eh}{2(1-\nu^2)B} |M_{\max}| = \frac{6|M_{\max}|}{h^2}. \quad (21)$$

Implicit in the derivation of the failure criterion in (21) are two assumptions. The first is that ice behaves like a brittle material on the timescales of interest to us here. The second assumption is that strains vary linearly throughout the thickness of the floe. While these two assumptions are not always appropriate for floating ice, they are extremely convenient and are in good agreement with experiments to determine the maximum load that can be borne by an ice floe [9].

In the buckled state considered here,

$$|M_{\max}| = \frac{B}{\ell_*} \|W_{,XX}\|_{\infty}, \quad (22)$$

and so the ice will fail when

$$\|W_{,XX}\|_{\infty} = \frac{2\ell_*(1-\nu^2)\sigma_m}{h} \frac{1}{E}. \quad (23)$$

Note that this relation suggests that for ice of given material properties, thin ice floes can support relatively large curvatures without breaking. By fixing L and calculating $\|W_{,XX}\|_{\infty}$ numerically for different degrees of compression, we find that typical ice floes fail while the ice deformation is small. In particular, figure 3 shows that the maximum slope of the interface is small at failure even for very thin ice floes. The linear theory presented here is, therefore, self-consistent and we may continue to make use of the linearized equations for the remainder of this report.

We note also from figure 3 that ice is very fragile and breaks readily under compression. To emphasize this point further, figure 4 shows the dimensional amplitude of the floe deflection at failure as a function of ice thickness. This shows that we can only expect to see very small amplitude buckles in unbroken ice. This is in accordance with the observation of Weeks [21] that it is very difficult to observe these buckles in the field unless there is drifting snow to highlight them.

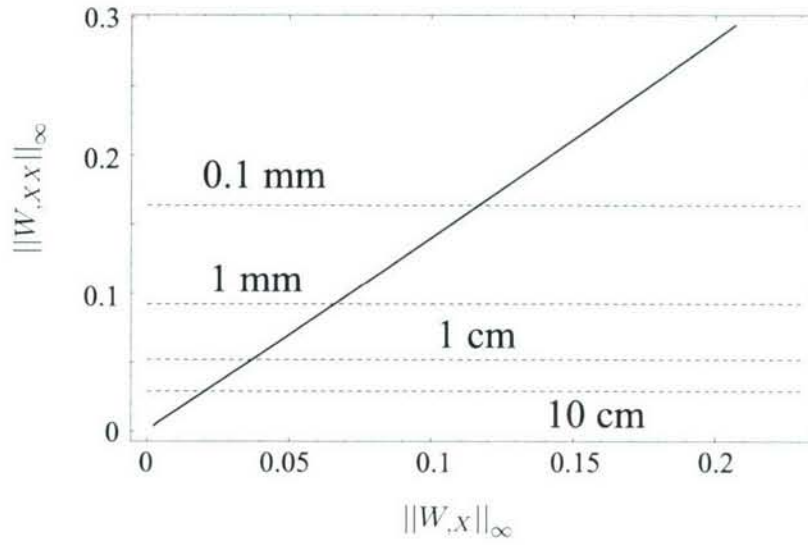


Figure 3: The magnitude of the maximum sheet curvature, $\|W_{,XX}\|_{\infty}$, as a function of the largest gradient of the buckling mode, $\|W_{,X}\|_{\infty}$. Here $S = 10^3$, $L = 50$ and we have taken $\sigma_m = 2 \times 10^5$ Pa, $E = 3 \times 10^8$ Pa and $\nu = 0.3$ to plot horizontal dashed lines corresponding to the maximum curvature possible before failure for four different ice thicknesses.

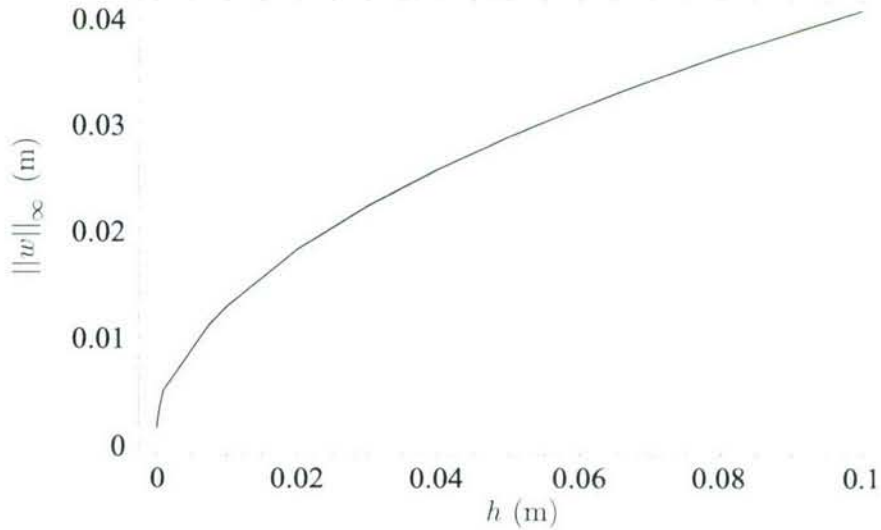


Figure 4: The maximum dimensional deflection of a buckled ice floe as a function of ice thickness, h . Here $S = 10^3$, $L = 50$ and we have taken $\sigma_m = 2 \times 10^5$ Pa, $E = 3 \times 10^8$ Pa and $\nu = 0.3$ as typical values [14].



Figure 5: Photograph showing an end-on view of simple rafting. The overriding floe has failed in places, suggesting a close link between simple rafting and pressure ridging. Courtesy of John Wettlaufer.

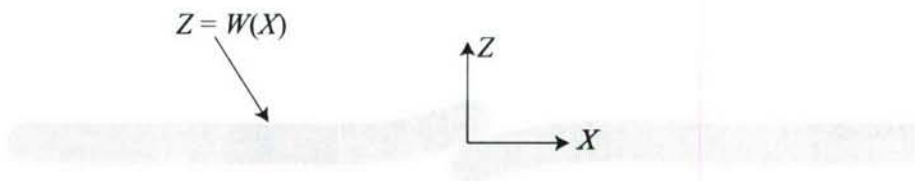


Figure 6: Schematic of two ice floes on the brink of rafting.

4 Rafting versus ridging

Having explored how a thin ice floe can buckle and then break under compression, we now move on to consider what happens once the ice has broken but the compression has not ceased. For simplicity, we shall consider two ice floes colliding, although the analysis in the previous section shows that two or more breaks may occur in general. Two outcomes of this collision seem plausible: either one ice floe may ride over the top of the other ('simple' rafting) or both ice floes may break as they come into contact causing an accumulation of rubble in a ridge. The photograph in figure 5 shows that these two possibilities are very closely related. Here, we show that there is a critical thickness above which ridging, rather than rafting, should occur. This is a result first derived by Parmeter [14], though we develop a much simplified model that leads to essentially the same result. This simplified analysis highlights the important physical principles that determine when rafting can occur.

Consider two ice floes in the configuration shown in figure 6 — the two floes are on the brink of rafting. In this scenario, any tension within the floes can only be balanced by friction in the very small overlapping region. We shall neglect this friction and hence neglect the tension within the floes. This means that the shape of each floe is governed by

(11) simplified by the assertion that $\tau = 0$, i.e.

$$W_{,4X} + W = 0. \quad (24)$$

Solving this equation subject to the jump in plate height at $X = 0$:

$$W(0^-) - W(0^+) = H \equiv h/\ell_*,$$

and the continuity of the first three derivatives of W at $X = 0$, we find that

$$W(X) = \begin{cases} \frac{H}{2} \exp(X/\sqrt{2}) \cos(X/\sqrt{2}), & X < 0 \\ -\frac{H}{2} \exp(-X/\sqrt{2}) \cos(X/\sqrt{2}), & X > 0. \end{cases} \quad (25)$$

From this expression, it is a simple matter to show that the maximum bending moment in the two plates occurs at $X = \pm\pi/2\sqrt{2}$ and has a value

$$|M_{\max}| = \frac{Bh \exp(-\pi/4)}{\ell_*^2 \frac{2\sqrt{2}}{2\sqrt{2}}}. \quad (26)$$

For rafting to be possible we require that this bending moment be less than the maximum allowed by the failure criterion (21). In dimensionless terms, we require that the thickness satisfy

$$H < H_c \equiv 2^{5/4} e^{\pi/8} (1 - \nu^2)^{1/2} \left(\frac{\sigma_m}{E} \right)^{1/2} \quad (27)$$

for rafting to be possible. Note that dimensional analysis leads us to expect that $H_c = f(\sigma_m/E)$. The functional form of f cannot be determined without this detailed calculation, however. In dimensional terms, (27) reads

$$h < h_c = \frac{8}{3} e^{\pi/2} \frac{1 - \nu^2}{\rho g} \frac{\sigma_m^2}{E}, \quad (28)$$

which has the same dependence on material properties as the result given by Parmeter [14] but with a prefactor ≈ 12.8 rather than 14.2. Our approach has the advantage of being analytic, rather than numerical, and arises from a much simpler model of the rafting process.

We can use the typical values given in table 1 for the material properties of ice to give an estimate for h_c . Because these properties are sensitive functions of temperature and salinity, we must be careful to use estimates of σ_m and E observed in the same sample — mixing values from a weak sample (small σ_m) with those of a stiff sample (large E) can confuse the issue. We find that $12 \text{ cm} \leq h_c \leq 19 \text{ cm}$, which brackets the transition thickness of 15 cm described in the context of field observations [24].

Above the critical thickness given in (28) we expect that the ice floes will break before rafting can occur and a pressure ridge will be formed. In particular, the maximum bending moment occurs a dimensional distance $\pi\ell_*/2\sqrt{2}$ away from the contact region and so we expect that a crack will form here and will be parallel to the edge of the floe. The simple rafting shown in figure 1 shows just such a crack forming. We expect also that the blocks within the resulting pressure ridge should have this typical size. Weeks and Kovacs [24]

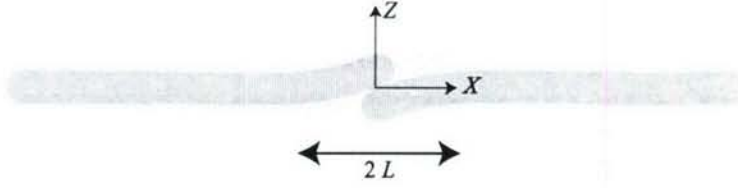


Figure 7: Schematic of two ice floes preloaded by rubble formed during failed rafting.

report that in one particular pressure ridge they found ice of thickness 30 cm and thickness/length ratio in the range 0.1–0.2. This compares well with the calculated ratio, which should lie in the range 0.07–1.2 based on the typical material properties of ice.

On occasion, ice has been reported to raft even though it was well above the critical thickness given in (28); rafting has been reported in ice up to 2 m thick. In these instances, it is also reported that the region where rafting occurs is covered with rubble formed by previously broken ice. Babko *et al.* [2] suggested that the presence of this rubble could lift one floe above the other, thereby facilitating rafting. In particular, consider two floes on the brink of rafting, as shown in figure 7. If these floes are too thick to raft in the configuration shown in figure 6, pieces will break off of them. The weight of overlying rubble formed from the overlying floe will depress the subducting floe further while the buoyancy of submerged ice blocks from the subducted floe will lift the overlying floe further. Here, we present a simple model to quantify how much of an effect this preloading could have and whether it can significantly alter the critical thickness at which rafting occurs.

We imagine that the region $-L < X < L$ is covered in rubble: this weighs down the ice floe with $X > 0$ and lifts the ice floe with $X < 0$. The shape of the two floes is obtained by solving (24) modified to incorporate the loading produced by the rubble. The appropriate boundary conditions are the same as in the earlier calculation leading to (25). This yields the floe displacement

$$W(X) = \begin{cases} \frac{H(1-r)}{2} \exp(\eta) \cos \eta + \frac{Hr}{2} \exp(\xi) \cos \xi, & X < -L \\ H(1-r) - \frac{H(1-r)}{2} \exp(-\eta) \cos \eta + \frac{Hr}{2} \exp(\xi) \cos \xi, & -L < X < 0 \\ -Hr - \frac{H(1-r)}{2} \exp(-\eta) \cos \eta + \frac{Hr}{2} \exp(\xi) \cos \xi, & 0 < X < L \\ -\frac{H(1-r)}{2} \exp(-\eta) \cos \eta - \frac{Hr}{2} \exp(-\xi) \cos \xi, & X > L, \end{cases} \quad (29)$$

where $r \equiv \rho_s/\rho$ is the non-dimensional density of the ice and

$$\xi \equiv \frac{X+L}{\sqrt{2}}, \quad \eta \equiv \frac{X-L}{\sqrt{2}}. \quad (30)$$

The maximum bending moment in either floe may then be determined numerically using the solution in (29) for given values of r and L . The results in figure 8 show the maximum curvature as a function of the extent of rubble, L , for three different values of the density ratio r . These curves show that as $L \rightarrow \infty$ the maximum curvature tends to a constant value. Considering the asymptotic limit $L \gg 1$, we find that the maximum value of $\|W_{,XX}\|_\infty$ occurs at $X \sim \pm\pi/2^{3/2} \pm L$ from which it immediately follows that the maximum curvature throughout the system is

$$\|W_{,XX}\|_\infty \sim \frac{Hr}{2\sqrt{2}} e^{-\pi/4}. \quad (31)$$

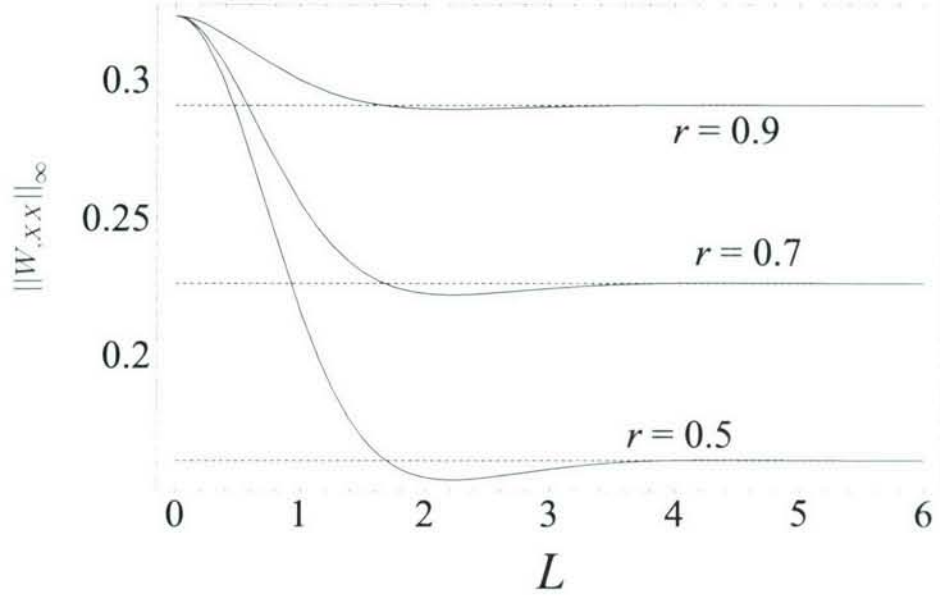


Figure 8: The maximum curvature in ice floes loaded/supported with rubble over a horizontal extent of L for three different values of $r = \rho_s/\rho$. The dashed lines show the asymptotic result (31), which is valid for $L \gg 1$.

Following the same procedure that led to (27), we find that the maximum non-dimensional thickness, H_c^* , for which rafting can occur is

$$H_c^* = \frac{2^{5/4} e^{\pi/8} (1 - \nu^2)^{1/2}}{r^{1/2}} \left(\frac{\sigma_m}{E} \right)^{1/2}, \quad (32)$$

which is precisely the same result as presented in (27) modified by a factor $r^{-1/2}$, i.e. $H_c^* = r^{-1/2} H_c$.

For ice, $r \approx 0.9$ and so in dimensional terms this mechanism can account for an increase of about 25% in the maximum thickness for which rafting can occur ($h_c^* = r^{-2} h_c \approx 1.23 h_c$). It seems that this mechanism could explain rafting in slightly thicker ice (up to $h \approx 25$ cm, say) but does not explain rafting in much thicker ice. We therefore conclude that the large discrepancy must instead be attributed to variations in the mechanical properties of the ice, as well as the complex rheology and geometry [16] of sea ice. In this regard, note that the data presented by Weeks and Anderson [22] shows that σ_m is a very sensitive function of salinity while E is more sensitive to temperature.

5 Finger rafting

In the remainder of this report, we shall be concerned with understanding a more exotic form of rafting between two ice floes: the formation of interlocking fingers that ride over and under one another. This is commonly called finger rafting because of the striking finger patterns that form (see figure 1).

5.1 Field observations

Several authors have written about the phenomenology of finger rafting from their observations in the field. These include not only observations in sea ice (starting with Weeks and Anderson [23]) but also observations in fresh water ice by Weber [20] and Green [7]. Tuhkuri and Lensu [19] have also observed some evidence of finger rafting in their ice-tank experiments using a mixture of ethanol and water. With the exception of the field observations of Mahoney and others [11], all observations of finger rafting have been limited to very thin ice; typically $h < 10$ cm.

As well as being the thickest ice for which finger rafting has been reported, the wavelength of the fingering pattern observed by Mahoney is also large. Does the thickness of the ice influence the wavelength of the finger rafts that are formed? We have collated the reported estimates of ice thickness and the wavelength of the fingering pattern (reported and measured from published photographs). Table 2 shows this collection of data, and seems to suggest that the narrowest fingers occur in the thinnest ice. This correlation between ice thickness and wavelength was suggested by Green [7] although Weeks and Anderson [23] believed that there was no such correlation.

5.2 Finger rafting in wax

To the best of our knowledge, finger rafting has been reported only in ice floating on water. This might lead the reader to think that the appearance of fingers is reliant on some property of ice that is not common in solids. To investigate whether this is in fact the case, and hence determine the extent to which the phenomenon is of a general mechanical nature, we have conducted experiments using very thin layers of solid sealing wax floating on water to mimic ice floes. The sheets of wax were manufactured by pouring molten wax onto a solid substrate covered with a flexible film of polyvinylidene chloride (a.k.a. saran wrap). After the wax has cooled, the polyvinylidene chloride film may be peeled away leaving a thin wax sheet. It is difficult to ensure that the thickness is uniform, but this seems not to matter a great deal.

The mechanical properties of the same sealing wax were kindly characterized by Larry Wilen of Unilever using an ultrasonic apparatus. His experiments showed that for frequen-

Thickness	Wavelength	Ice type	Reference	Symbol
2 – 3 mm	6 – 20 cm	Fresh ice	[7]	■
3 – 8 mm	2 m	Fresh ice	[7]	■
1 – 2 cm	10 m	Fresh ice	[7]	■
2 – 6 cm	2 – 8 m	Sea ice	[23]	▲
2.5 – 6.9 cm	4 – 6 m	Ethanol-water	[19]	★
3.5 – 4.5 cm	7 – 9 m	Sea ice	[6]	○
1.3 – 1.5 m	20 – 100 m	Sea ice	[11]	◆

Table 2: Field observations of ice thicknesses in which finger rafting has been reported and the wavelength of the resulting fingering pattern. The symbols indicated are used to plot these data in figure 11.

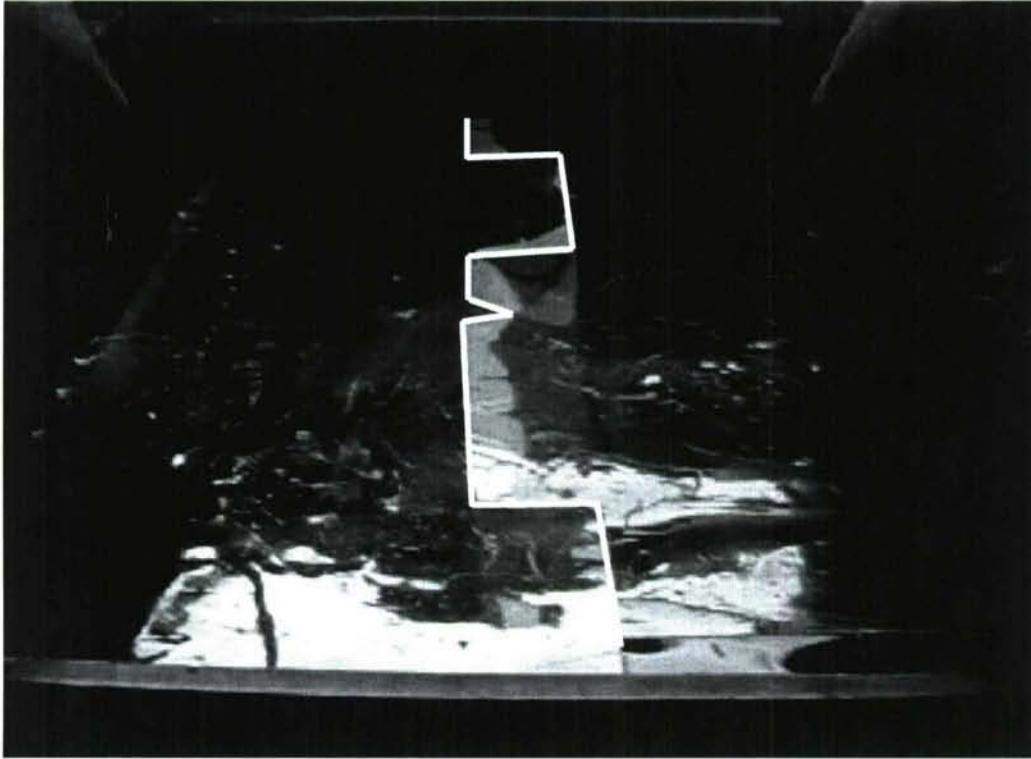


Figure 9: Experimental realization of finger rafting in thin wax sheets floating on water. Here the thickness of the wax sheets is in the range $150 - 500 \mu\text{m}$ and the length of the sheets is around 40 cm. For clarity, the edge of the fingered wax sheets has been highlighted with a white line.

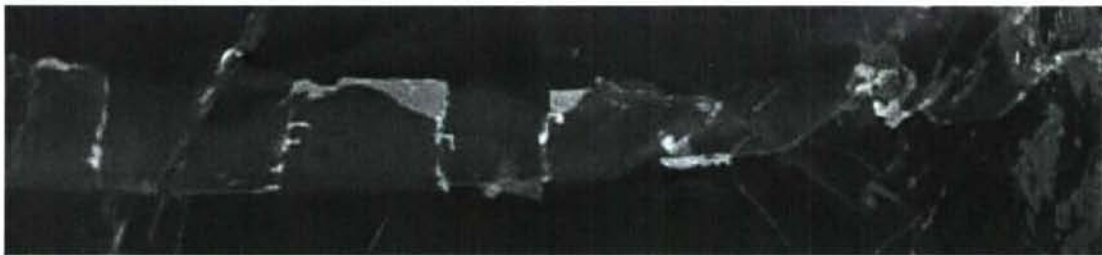


Figure 10: Plan view of finger rafting as observed in thin wax sheets of thickness in the range $170 - 380 \mu\text{m}$. The total field of view here is around 30 cm.

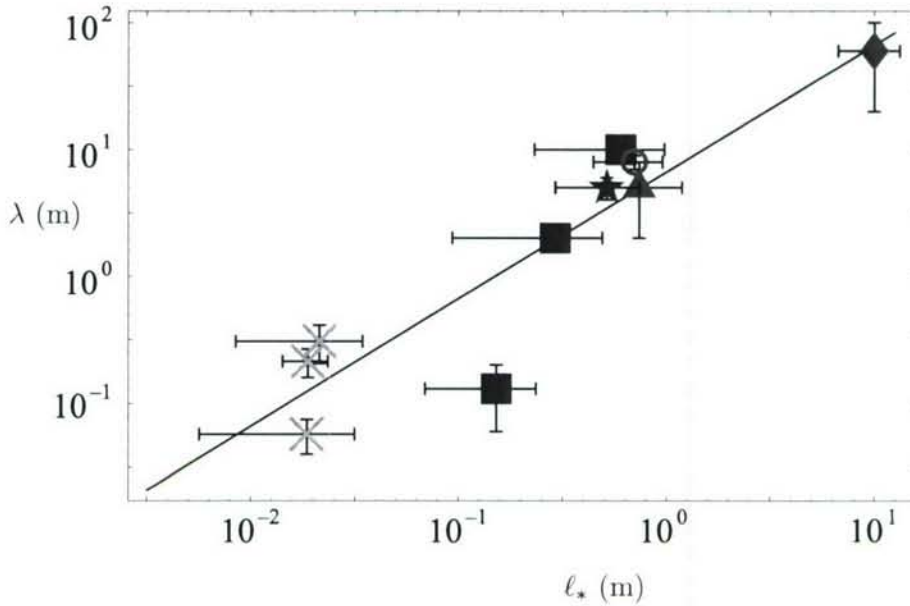


Figure 11: Wavelength of fingering pattern, λ , for floating sheets with differing characteristic lengthscales, ℓ_* . The data plotted here are a combination of those in table 2 (obtained from the field observations of others) and our own experiments with thin sheets of wax floating on water (denoted by \times). The colouring of points signifies the type of solid in which the finger rafting was observed — sea ice, fresh ice and sealing wax. The line shows the theoretical prediction (40).

cies in the range $10^{-2} - 10^2$ Hz the Young's modulus lies in the range $1.57 \times 10^8 - 1.16 \times 10^9$ Pa, assuming a Poisson ratio $\nu = 0.3$. These experiments also demonstrated a solid-solid phase transition in the wax at a temperature close to 35°C . Above this temperature the wax becomes ductile and does not fail under loading. Rather, it deforms plastically. We therefore ensured that the wax was allowed to cool to room temperature before performing the experiments reported here.

The thin wax sheets were floated on water with their long edges in contact and then pushed together by hand. As shown in figures 9 and 10, we observed finger rafting. Experimental constraints, the most important of which were the ability to accurately control the thickness of the wax and to avoid edge effects in the transverse direction, limited the number of fingers observed. However, the fingers shown in figures 9 and 10 have the strong rectilinear features reported of finger rafting ice. Moreover, plotting the typical wavelength of this fingering pattern (λ) as a function of the characteristic length ℓ_* seems to show reasonable collapse with field observations of finger rafting in ice, as shown in figure 11. Note that $\ell_* \sim h^{3/4}$ and so there is some correlation between λ and h .

5.3 A physical mechanism

Several authors have suggested that finger rafting occurs because of wave action [3, 4, 23]. Although their mechanisms differ in terms of details, the essential ingredients are the same

and may be paraphrased as follows. Finger rafting is initiated when a small portion of one ice floe is deposited on top of another ice floe by an advancing wave crest. This leaves a portion of the ice out of water and not supported by another ice floe. A tear forms in this area (since sea ice is not strong enough to support its own weight) and a first finger is formed. As the wave crest passes on, the other ice floe protrudes onto the first, tears and forms a finger pointing in the opposite direction to the first. As more waves are incident on the ice, a series of prototype interlocking fingers is formed which grow as the ice floes are compressed and the ice floes plough through one another.

While this explanation may be correct in many circumstances, it cannot form the basis of a general theory of finger rafting. Firstly, in nature finger rafting occurs when there is wind but no open water for the generation of a swell [7]. Secondly, the mechanism above relies on the fact that sea ice cannot support its own weight and so will fail if not supported by either water or other regions of ice. This is certainly not the case for the thin sheets of wax used in our laboratory experiments, and is also unlikely to be the case in the fresh water situations for which finger rafting has been observed.

An alternative explanation relies on some small overlap between the two ice floes (see figure 12): if a small portion of ice floe A overrides ice floe B at a point C, floe A is lifted slightly at the point C by the additional buoyancy provided by the presence of floe B. Conversely, floe B is depressed at the point C by the additional load provided by the presence of floe A. As we have seen many times already in this report, the characteristic response of an ice floe to such perturbations is not monotonic decay in the far field but rather an oscillatory deflection modulated by an exponential decay. We therefore expect that away from the point C both floes A and B will have an oscillatory vertical deflection, shown schematically in figure 12. In particular, the free edges of the two floes should have an oscillatory vertical deflection. Moreover, because the initial perturbations to each of the floes are of opposite sign, these oscillations remain out of phase along the length of the free edge: crests of floe A correspond to troughs of floe B and vice versa. The free edges of the two floes are displaced vertically relative to one another. Thus, these out of phase oscillations cause the two floes to form interlocking thrusts during subsequent compression.

Because the displacement of the floe decays exponentially away from the protrusion, we do not expect an overlap at one place to be sufficient for finger rafting everywhere; the vertical displacement must be a reasonable fraction of the thickness for the oscillations we describe to give rise to floes running over one another. Instead, we propose that the rafting propagates along the edge rather like a zipper: when rafting occurs in one place the displacements nearby are sufficient to cause finger rafting there too and so on. This wave of rafting should travel at the speed of gravity waves in water covered with an elastic sheet. The phase speed, c , of these waves [18] depends on their wavenumber, k , and is given by

$$c^2 = \frac{Bk^4 + \rho g}{\rho_s h k^2 + \rho k}. \quad (33)$$

In our wax experiments, the speed of the waves with wavenumber ℓ_*^{-1} is typically around 0.5 ms^{-1} , making this zippering unobservable within the scope of the technology we employed. For ice of thickness 10 cm, this wave speed is on the order of 5 ms^{-1} .

The mechanism we have described does not rely on any material properties that are peculiar to ice, though we do require the solid material to be able to tear to form fingers as

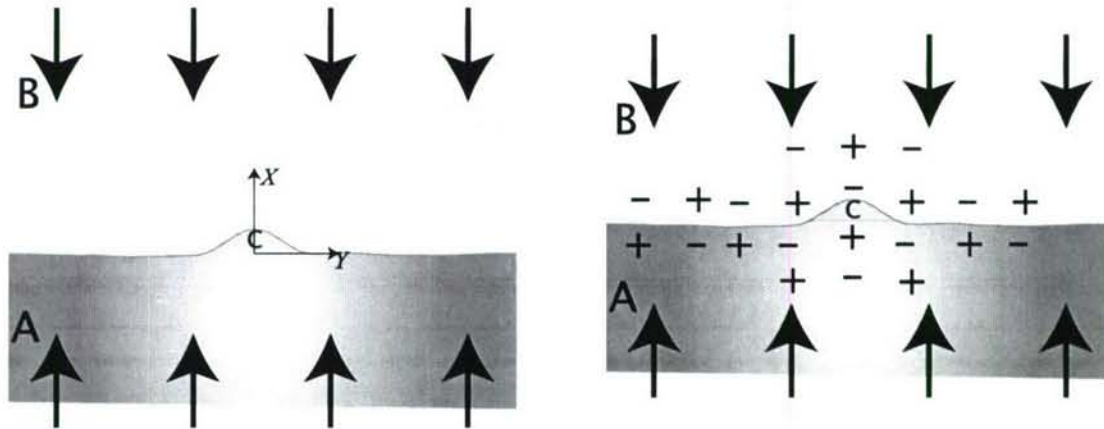


Figure 12: Plan view of two ice floes A and B colliding. A small protrusion in floes A leads to an overlap of the floes in a small region, C. This overlap causes oscillations in the vertical position of the floes, which decay away from C. The sign of these displacements is indicated by the $+/-$ symbols in the figure. Notice that the oscillations along the free edge are exactly out of phase in the two floes causing the two floes to alternately ride over and under each other under compression (arrows).

the two floe edges are pushed past one another. This condition seems also to be satisfied by wax whereas other materials, such as aluminium foil, do not tear sufficiently easily and so cannot form these fingers.

5.4 The deflection of a semi-infinite elastic plate

A mechanism resembling that presented above seems to have been outlined briefly by Fukutomi and Kusunoki [6]. They discuss finger rafting only cursorily and give a very vague presentation of a model of a point force acting on an infinite elastic sheet to give some idea of the scale of fingers formed. However, they give no details of their calculations nor of the equations solved. Here, we rectify this situation by presenting a thorough analysis of the problem.

We modify the earlier analysis of rafting to incorporate the effect of a vertical load, F , on a semi-infinite ice floe. Again neglecting the in-plane forces, we find that the deflection of the floe satisfies

$$\nabla^4 W + W = F(X, Y) \quad (34)$$

The Green's function for the deflection of an semi-infinite elastic plate on an elastic foundation was given by Kerr and Kwak [10] as well as Nevel [13]. Because an elastic foundation is exactly analogous mathematically to a floating sheet, we shall make extensive use of their result in what follows. In particular, if a concentrated force of dimensional magnitude f is applied at the point (X_0, Y_0) , as shown schematically in figure 13, then the

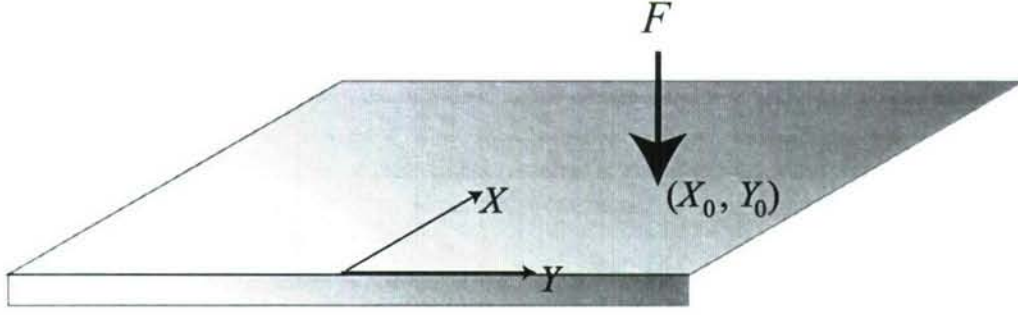


Figure 13: A point force F acting at the point (X_0, Y_0) on a semi-infinite floating elastic sheet.

vertical displacement at a point (X, Y) is given by

$$\begin{aligned} \pi \frac{\rho g \ell_*^3}{f} W(X, Y; X_0, Y_0) &= -\frac{1}{2} [\text{Kei}(R_0^-) + \text{Kei}(R_0^+)] + \int_0^\infty A(X_0, \alpha) e^{-k_+ X} \left\{ \cos k_- X \right. \\ &\quad \left. - \frac{k_+ [2k_-^2 + (1-\nu)\alpha^2]}{k_- [2k_+^2 - (1-\nu)\alpha^2]} \sin k_- X \right\} \cos \alpha(Y - Y_0) d\alpha. \end{aligned} \quad (35)$$

Here Kei is the Kelvin function of zeroth order [1], R_0^\pm is given by

$$R_0^\pm = [(X \pm X_0)^2 + (Y - Y_0)^2]^{1/2}, \quad (36)$$

k_\pm is given by

$$k_\pm = \left(\frac{1}{2} [\sqrt{\alpha^4 + 1} \pm 1] \right)^{1/2}, \quad (37)$$

and

$$\begin{aligned} A(X_0, \alpha) &= \frac{\exp(-k_+ X_0)}{\sqrt{\alpha^4 + 1}} \frac{2k_+^2 - (1-\nu)\alpha^2}{4k_+^2 [k_-^2 + (1-\nu)\alpha^2] - (1-\nu)^2 \alpha^4} \\ &\quad \times [k_- (k_-^2 + k_+^2 + \nu\alpha^2) \cos k_- X_0 - k_+ (k_-^2 + k_+^2 - \nu\alpha^2) \sin k_- X_0]. \end{aligned} \quad (38)$$

This expression simplifies considerably if we look at the case of a point mass acting at the origin (i.e. $X_0 = Y_0 = 0$). In particular, the profile of the plate along the free edge ($X = 0$) takes the form

$$W(0, Y) = \frac{F}{\pi} \left(-\text{Kei}(|Y|) + \int_0^\infty A(0, \alpha) \cos \alpha Y d\alpha \right), \quad (39)$$

where $F \equiv f/\rho g \ell_*^3$. This function can be plotted numerically but what is of most interest here is the position of the zeros of $W(0, Y)$, since these determine the regions in which the two ice floes can most easily ride over one another. The smallest Y_* satisfying $W(0, Y_*) = 0$ is $Y_* \approx 4.507$ with the next root occurring at $Y_* \approx 7.827$. Since the vertical displacement decays exponentially with increasing Y , we take the distance between these first two roots to be that determining the wavelength of the finger rafting pattern with the position of

subsequent fingers determined once the initial fingers are in place. We therefore expect that

$$\lambda \approx 2(7.827 - 4.507)\ell_* = 6.64\ell_*, \quad (40)$$

which agrees well with the results presented in figure 11.

While the case of a point mass acting on an elastic sheet is a convenient abstraction, our actual interest lies in determining how an ice floe responds to having a finger from another ice floe pressed on top of it. We therefore consider a finger of width $2a$ protruding a distance $2b$ onto another ice floe. Each infinitesimal element of the protruding finger contributes to the displacement of the overridden floe. Since the equation governing the displacement of the ice is linear, we can sum these displacements to give the displacement field due to the presence of the finger. An element of width δY_0 and length δX_0 has a weight $f = -\rho_s g h \ell_*^2 \delta X_0 \delta Y_0$. Summing the displacement due to all of these elements, we find that

$$\begin{aligned} W(X, Y) &= \int_0^{2b} \int_{-a}^a W(X, Y; X_0, Y_0) dY_0 dX_0 \\ &\equiv \frac{\rho_s h}{\rho \ell_*} \omega(a, b, X, Y). \end{aligned} \quad (41)$$

We are particularly interested in determining whether we need a large perturbation to initiate finger rafting. For the mechanism of finger rafting proposed here to be reasonable, we need the edge displacement induced by the overlap to be comparable to the ice thickness near the position where the load is being applied. To investigate whether this is the case, we calculated the rescaled displacement at the origin, $\omega(a, b, 0, 0)$, as a function of finger size for a square finger (i.e. $a = b$). Because of the definition of ω , the displacement becomes of the same order as the thickness when $\omega = \mathcal{O}(1)$.

The numerically determined dependence of ω on a is shown in figure 14. These results show that as a finger gets larger the vertical displacement at the origin grows quickly. Indeed, upon expanding the integrals in the definition of ω for $a, b \ll 1$, we find that

$$\omega(a, b, 0, 0) \sim \frac{4ab}{\pi} \left[\int_0^\infty A(0, \alpha) d\alpha - \text{Kei}(0) \right] \approx 1.848ab, \quad (42)$$

which agrees with the numerically computed values shown in figure 14 when $b = a \ll 1$. This asymptotic result is useful because it shows that the displacement grows quadratically as the finger size increases — this ensures that increasing the size of the perturbation makes a large difference to the displacement field, since the size of the force applied by the finger increases greatly. In particular, the displacement does become $\mathcal{O}(1)$ even for relatively small finger sizes (i.e., values of a).

We also note that for $a \gg 1$, $\omega(a, a, 0, 0) \sim 1$. This is to be expected since in the limit that an ice floe is overlain by another floe, it must sink a vertical distance $\rho_s h / \rho \ell_*$ to increase its Archimedes buoyancy enough to balance the overlying weight.

5.5 A threshold thickness

Just as there was a critical thickness above which simple rafting is not possible, we expect that there might also be a critical ice thickness above which simple rafting, rather than

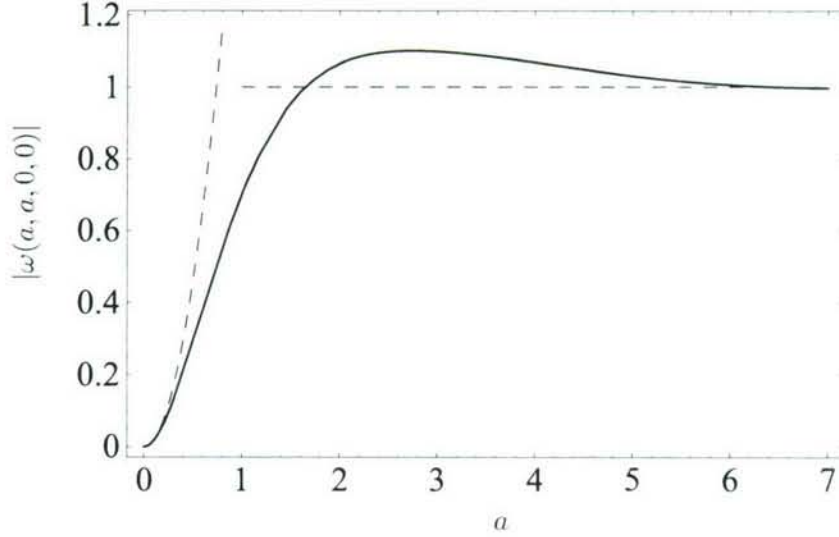


Figure 14: Plot of $\omega(a, a, 0, 0)$ for various values of finger size a (solid line). The dashed lines indicate the asymptotic expression (42) valid in the limit $a \ll 1$ and the limit $\omega \sim 1$ valid for $a \gg 1$.

finger rafting, will take place. Based on intuition gleaned from many field observations Weeks [21] suggests that for ice thicker than around 10 cm, finger rafting becomes rarer, presumably resulting instead in simple rafting.

As we found with the rafting/ridging transition discussed earlier, we expect that the generation of large moments within the ice may cause the stresses within the ice to exceed the maximum value that the ice can support, σ_m . For simplicity, we will consider the moments generated in a plate when a rectangular finger of width $2a$ and length $2b$ from another floe sits above it. (The finger is imagined to occupy the region $0 \leq X \leq 2b$, $|Y| \leq a$.) Explicit formulae for the moments generated by a point force are given by Kerr and Kwak [10], but are not reproduced here. After integrating these expressions over the square $0 \leq X_0 \leq 2b$, $|Y_0| \leq a$ (as for displacements in the last section), the moments in the X and Y directions may be written

$$M_{xx}(X, Y) = -\frac{B}{\ell_*} (W_{,XX} + \nu W_{,YY}) \equiv \frac{\rho_s Bh}{\rho \ell_*^2} \mu_x(a, b, X, Y)$$

$$M_{yy}(X, Y) = -\frac{B}{\ell_*} (\nu W_{,XX} + W_{,YY}) \equiv \frac{\rho_s Bh}{\rho \ell_*^2} \mu_y(a, b, X, Y),$$

respectively.

The functions μ_x and μ_y may be evaluated by numerical quadrature. Our numerical results are in perfect agreement with those tabulated by Nevel [13], over his limited range of values of a and b . We find that the largest moments generated are in $\mu_y(a, b, 0, 0)$ so that the failure of the ice floe should be manifested in a crack perpendicular to the floe edge. This is contrary to the failure of simple rafting in which a crack formed parallel to the free edge of the ice floe.

To find a critical thickness above which finger rafting can no longer occur, we look

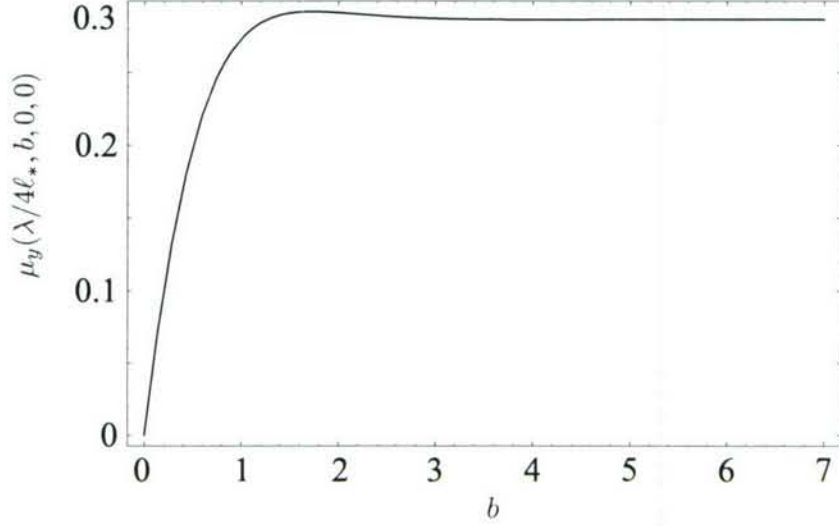


Figure 15: Plot of $\mu_y(\lambda/4\ell_*, b, 0, 0)$ as a function of the finger length b .

for the maximum value, μ_∞ , of $\mu_y(a, b, 0, 0)$. Since we expect individual fingers to have a dimensional width of $\lambda/2$, where λ is given by (40), we choose $a = \lambda/4\ell_*$ and calculate $\mu_y(a, b, 0, 0)$ for this value of a .

Figure 15 shows the numerically computed values of $\mu_y(\lambda/4\ell_*, b, 0, 0)$. This demonstrates that there is indeed a maximum value, $\mu_\infty \approx 0.292$. Given this maximum moment we require that

$$\sigma_m > \frac{6}{h^2} \frac{\rho_s B h}{\rho \ell_*^2} \mu_\infty, \quad (43)$$

for the finger to be able to grow indefinitely without the ice beneath it breaking. This condition is satisfied provided that

$$H < \left[\frac{\rho}{\rho_s} \frac{2(1-\nu^2)}{\mu_\infty} \right]^{1/2} \left(\frac{\sigma_m}{E} \right)^{1/2} \approx 2.6 \left(\frac{\sigma_m}{E} \right)^{1/2}. \quad (44)$$

The critical thickness at which finger rafting cannot happen scales with σ_m/E in precisely the same way as the critical thickness at which simple rafting gives way to ridging. However, the prefactor is different (and smaller!) suggesting that for a given value of σ_m/E we may be able to transition between finger rafting, simple rafting and ridging just by varying the ice thickness. The condition in (44) may be recast in dimensional terms as

$$h < \frac{\rho}{\rho_s} \frac{1-\nu^2}{3\rho_s g \mu_\infty^2} \frac{\sigma_m^2}{E}. \quad (45)$$

Taking typical values for the material properties of sea ice, we find that this transition thickness lies in the interval

$$4 \text{ cm} \leq h \leq 8 \text{ cm}. \quad (46)$$

This estimate is in reasonable agreement with the suggestion of Weeks [21] for a transition thickness on the order of 10 cm and is consistent with most of the field observations collected

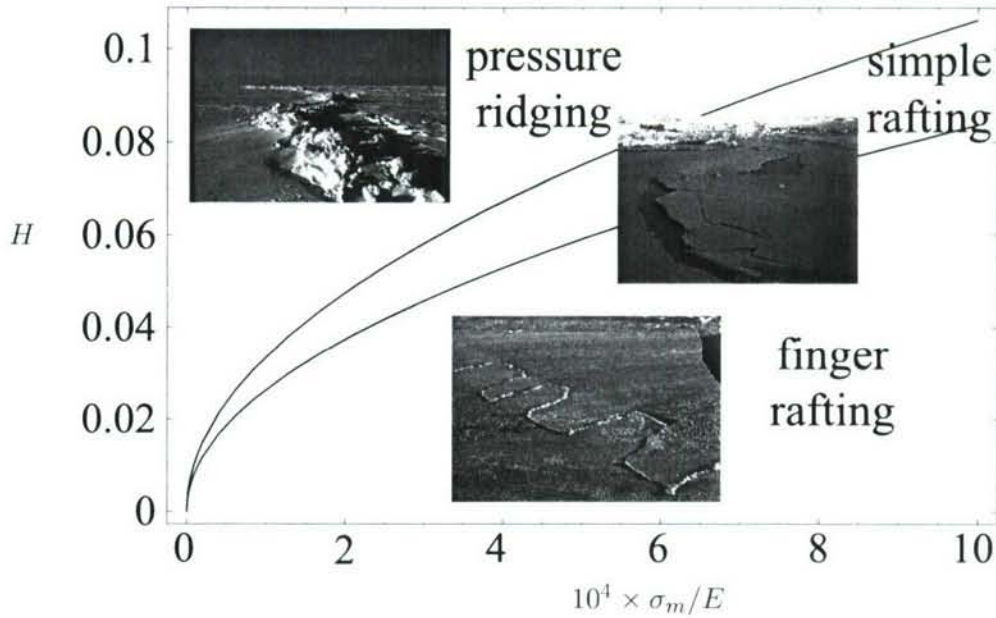


Figure 16: Regime diagram showing the values of σ_m/E and H for which we expect to observe each of the deformation types observed. Photographs courtesy of Wilford Weeks [21].

in table 2, for which finger rafting is observed in ice of thickness up to around 6 cm. This also provides some quantitative support for the statement of Weeks and Kovacs [24] that:

“Although less striking when observed from the air, simple rafting of thin ice. . . is actually more common than finger rafting.”

Because the maximum bending moment in the floe is $\mu_y(a, b, 0, 0)$, we expect that a crack will form perpendicular to its edge. Perhaps this means that the finger breaks through the floe and is subducted beneath along with the remainder of the raft in simple rafting? We expect that above the critical thickness a finger might start to grow but will fall through the underlying ice once it reached a length of at most $4\ell_*$. However, we are unaware of observations wherein finger rafting metamorphoses into simple rafting against which to check this picture.

6 Conclusions

We have studied the mechanics of ice floe failure using ideas from thin plate theory. Because ice is so weak ($\sigma_m/E \ll 1$), thin plate theory allows us to study the buckling instability of an ice floe compressed by the motion of much thicker flanking floes up to the point at which the ice fails. We then focused on the three main types of deformation that result from the subsequent collision of two floes. By considering the forces induced by these different deformations we determined quantitative conditions on the different ice thicknesses for which each of these deformation patterns is observed. In particular, by plotting the dimensionless conditions (27) and (44) on the same graph, we obtain a regime diagram showing the

values of σ_m/E and H for which finger rafting, simple rafting and pressure ridging should be observed. Such a regime diagram is shown in figure 16. Although our main interest lies in the applicability of these results to floating ice, our experiments with wax sheets demonstrate that finger rafting may also be observed in systems other than ice. However, we do not expect the regime diagram shown in figure 16 to be quantitatively valid for other materials: ice typically has $\sigma_m/E < 10^{-3}$ so that the transitions between different regimes always have $H \ll 1$, and thus thin plate theory is valid. This is not generally the case for other materials.

Appendix A: The wavenumber in buckling is real

In section 3 we assumed that the wavenumber k observed in buckling is purely real so that there are no exponentially decaying modes. Here, we prove this assertion by supposing instead that there is a complex pair of wavenumbers k_{\pm} satisfying (12). Since the tension τ is real, k_{\pm} must be complex conjugates of one another and we may write $k_{\pm} = k_r \pm ik_i$. The dispersion relation (15) then reads

$$(k_r + ik_i) \tan(k_r + ik_i)a = (k_r - ik_i) \tan(k_r - ik_i)a. \quad (47)$$

Expanding this equation and equating imaginary parts gives

$$f(ak_i) \equiv \frac{ak_i \cos^2 ak_i}{\cosh^2 ak_i} = -\frac{ak_r}{\tanh ak_r} \equiv g(ak_r). \quad (48)$$

A plot of the functions f and g reveals that their ranges do not overlap and so there cannot be any solution of (48) — our assumption that k was imaginary is incorrect and we have shown that k is, in fact, real.

Acknowledgments My experiments in wax would not have been possible without Keith Bradley's tolerance of my burning wax in the lab, the use of Neil Balmforth's camcorder, Lary Wilen's careful measurements of the Young's modulus of sealing wax and Rachel's impromptu (and uncalled for) karaoke sessions. I am grateful to Marcus Roper, L. Mahadevan and Neil Balmforth for discussions about the theoretical side of this work. Two people deserve special thanks. Firstly, Wilford Weeks has been incredibly forthcoming with all of the information that he has on these phenomena; he provided photographs from his upcoming book, his own translation of the Fukutomi and Kusunoki paper and has replied to what must seem like a deluge of emails. Secondly, for introducing me to this topic, helping in the lab, numerous conversations and maintaining his enthusiasm throughout the summer, cheers jsw!

References

- [1] M. ABRAMOWITZ AND I. A. STEGUN, *Handbook of Mathematical Functions with Formulas, Graphs, and Mathematical Tables*, Dover, New York, 1964.
- [2] O. BABKO, D. A. ROTHROCK, AND G. A. MAYKUT, *Role of rafting in the mechanical redistribution of sea ice*, J. Geophys. Res., 107 (2002). doi: 10.1029/1999JC000190.

- [3] M. DUNBAR, *Thrust structures in young sea ice*, J. Glaciol., 3 (1960), pp. 724–732.
- [4] ———, *Note on the formation process of thrust structures in young sea ice*, J. Glaciol., 4 (1962), pp. 147–150.
- [5] R. J. EVANS AND N. UNTERSTEINER, *Thermal cracks in floating ice sheets*, J. Geophys. Res., 76 (1971), pp. 694–703.
- [6] T. FUKUTOMI AND K. KUSUNOKI, *On the form and formation of hummocky ice ranges*, Low. Temp. Sci., 8 (1951), pp. 59–88. In Japanese (free translation by S. Takagi and W. F. Weeks).
- [7] J. C. GREEN, *Finger-rafting in fresh-water ice: Observations in Lake Superior*, J. Glaciol., 9 (1970), pp. 401–404.
- [8] P. V. HOBBS, *Ice Physics*, Oxford University Press, 1974.
- [9] A. D. KERR, *The bearing capacity of floating ice plates subjected to static or quasi-static loads*, J. Glaciol., 17 (1976), pp. 229–268.
- [10] A. D. KERR AND S. S. KWAK, *The semi-infinite plate on a winkler base, free along the edge, and subjected to a vertical force*, Arch. Appl. Mech., 63 (1993), pp. 210–218.
- [11] A. MAHONEY, H. EICKEN, L. SHAPIRO, AND T. C. GRENFELL, *Ice motion and driving forces during a spring ice shove on the Alaskan Chukchi coast*, J. Glaciol., 50 (2004), pp. 195–207.
- [12] E. H. MANSFIELD, *The Bending and Stretching of Plates*, Cambridge University Press, 1989.
- [13] D. E. NEVEL, *A semi-infinite plate on an elastic foundation*, Tech. Rep. 136, Cold Regions Research and Engineering Laboratory, 1965.
- [14] R. R. PARMETER, *A model of simple rafting in sea ice*, J. Geophys. Res., 80 (1975), pp. 1948–1952.
- [15] D. A. ROTHROCK, *The mechanical behaviour of pack ice*, Annu. Rev. Earth Planet. Sci., 3 (1975), pp. 317–342.
- [16] D. A. ROTHROCK AND A. S. THORNDIKE, *Measuring the sea ice-floe size distribution*, J. Geophys. Res., 89 (1984), pp. 6477–6486.
- [17] E. M. SCHULSON, *The structure and mechanical behaviour of ice*, JOM, 51 (1999), pp. 21–27.
- [18] V. A. SQUIRE, W. H. ROBINSON, P. J. LANGHORNE, AND T. G. HASKELL, *Vehicles and aircraft on floating ice*, Nature, 333 (1988), pp. 159–161.
- [19] J. TUHKURI AND M. LENSU, *Laboratory tests on ridging and rafting of ice sheets*, J. Geophys. Res., 107 (2002), p. 3125.

- [20] J. N. WEBER, *Ice thrust structures*, J. Glaciol., 3 (1958), p. 291.
- [21] W. F. WEEKS, *On Sea Ice*, University of Alaska Fairbanks Press, 2006. In Preparation.
- [22] W. F. WEEKS AND D. L. ANDERSON, *An experimental study of strength of young sea ice*, Trans. Am. Geophys. Un., 39 (1958), pp. 641–647.
- [23] ———, *Sea ice thrust structures*, J. Glaciol., 3 (1958), pp. 173–175.
- [24] W. F. WEEKS AND A. KOVACS, *On pressure ridges*, Tech. Rep. IR505, Cold Regions Research and Engineering Laboratory, 1970.

The Formation of Star Patterns on Lake Ice

Victor C. Tsai

March 15, 2007

1 Abstract

Star-like patterns have been found on many lakes that have a snow cover on top of a thin ice layer. A number of workers have described these ‘lake stars’ but there have been no attempts at constructing a mathematical model of the formation process. Here we put forth a mathematical model that describes the formation of radial fingers emanating from a central source. Performing linear stability analysis on the steady state solution, we are able to accurately predict the formation of fingers but the number of fingers is very sensitive to input parameters. We also carry out scaled experiments. At small times and to first order, the results of these experiments agree with our linear theory.

2 Introduction

It is a common occurrence that snow falls on lakes that already have a thinly ice covered surface. Holes often form in the thin ice (for reasons not well understood [3]), after which warm lake water flows through the hole and through the snow layer. This warm water melts the snow and leaves dark regions where the snow has melted away. The pattern left by this process looks star-like (see Figure 1) and we call this pattern a ‘lake star.’ Lake stars have been described a number of times (e.g. [3, 2, 5]) but very little work has been done to understand the formation process. Knight [3] outlines a physical idea that is meant to describe the process, but no attempt is made at determining whether this idea can be translated into a physical model that produces results consistent with field observation. The main idea of Knight is that locations with faster flow rates melt preferentially, leading to even faster flow rates and therefore to an instability that results in fingers. This idea is qualitatively similar to many other geomorphologic instability such as the ones discussed by Schorghofer et al. [4]. We take this idea as the starting point for our model.

3 Mathematical Model

3.1 Mathematical Formulation

In order to model the physics of lake star formation, we make a number of assumptions. Many of these assumptions are not strictly true but are reasonable approximations that

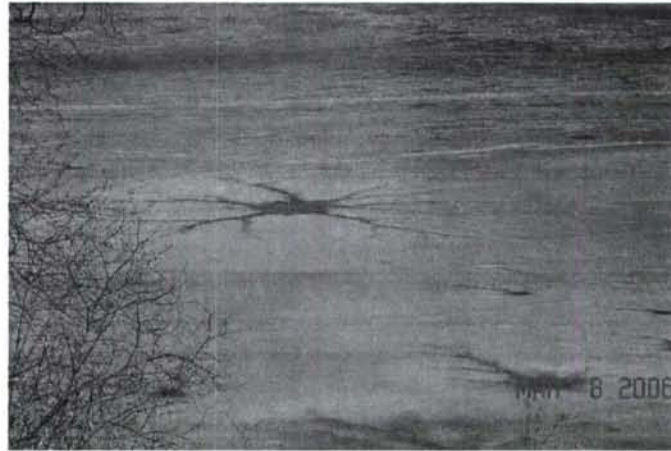


Figure 1: Typical lake star pattern. The branched arms are approximately 1 m in length.

facilitate the attainment of a simple solution that can be easily compared with observations. We shall discuss each assumption when it is made.

We begin our analysis by supposing that there exists a central hole through which warm lake water can seep. Both Katsaros [2] and Woodcock [5] attribute these holes as well as the associated lake star patterns to convection patterns within the lake. However, at least in some circumstances the holes seem to be formed from protrusions (e.g. sticks that poke through the ice surface) [3] thus casting doubt on the convection idea. Lake stars are observed in all of these circumstances so we treat the hole formation as independent of, but necessary for, lake star formation. As discussed by Knight [3], the hole results in a water level that extends above the thin ice and into a slush (wet snow) layer. We therefore treat this (warm) water region as having a constant height above the ice or equivalently a constant pressure head. This pressure head drives flow of water through the slush layer, subject to a melting condition (Stefan condition) at the water-slush interface. We treat flow within the slush as a Darcy flow of water at 0°C . Temperature within the liquid region is assumed to obey the (advection-diffusion) heat equation. The water in both the liquid and slush regions is treated as incompressible. In order to fully specify the mathematical problem, we require an outer boundary at which the pressure head is also known. While pressure measurements have not been made in the field, circular water-saturated regions (a few meters in radius) typically surround the lake stars. It therefore seems reasonable to assume that the differential pressure head falls to zero somewhere in the vicinity of this circular boundary. The actual boundary at which the differential pressure head is zero likely is not completely uniform (as in Figure 4 of Knight [3]) but is at least a good approximation especially before strong finger formation (i.e. in the linear regime in which we perform our analysis). Finally, we treat the system as a two-dimensional flow. This cannot be strictly true for two reasons. First, the water in contact with ice must be at 0°C whereas we treat this water as having an average temperature above freezing. However, perhaps this assumption is reasonable in a depth averaged sense. Second, the decreasing pressure head in the radial direction must be accompanied by a corresponding drop in water level, thus

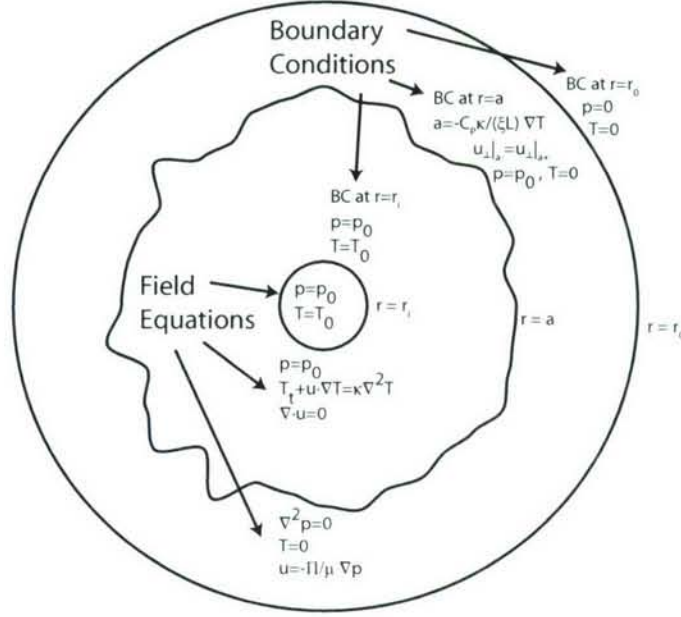


Figure 2: Schematic of the geometry of the model. The perspective is looking down on a nascent star. The equations are shown in the domains of the system and described in more detail below.

making the vertical dimension non-uniform. Therefore, the driving force is more accurately described as deriving from an axisymmetric gravity current. Regardless, the front whose stability we assess is controlled by the same essential physical processes that we model herein. For the purposes of the simple analysis presented here, we shall ignore these two second order effects but note that the analysis could be extended to account for them.

Translating the description in the previous paragraph into mathematical language, we have the following system of equations (see also Figure 2):

$$\frac{\partial T}{\partial t} + \mathbf{u} \cdot \nabla T = \kappa \nabla^2 T \quad r_i < r < a(\phi, t), \quad (1)$$

$$T = 0 \quad a(\phi, t) < r < r_0, \quad (2)$$

$$p = p_0 \quad r_i < r < a(\phi, t), \quad (3)$$

$$\nabla^2 p = 0 \quad a(\phi, t) < r < r_0, \quad (4)$$

$$\nabla \cdot \mathbf{u} = 0 \quad r_i < r < a(\phi, t), \quad (5)$$

$$\mathbf{u}|_{a^-} = \mathbf{u}|_{a^+} \quad r = a(\phi, t), \quad (6)$$

$$\mathbf{u} = -\frac{\Pi}{\mu} \nabla p \quad a(\phi, t) < r < r_0, \quad (7)$$

with boundary conditions

$$\dot{a} = -\frac{C_P \kappa}{\xi L} \nabla T \quad r = a(\phi, t), \quad (8)$$

$$T = \begin{cases} T_0 & r = r_i \\ 0 & r = a(\phi, t) \\ 0 & r = r_0 \end{cases}, \quad (9)$$

$$p = \begin{cases} p_0 & r = r_i \\ p_0 & r = a(\phi, t) \\ 0 & r = r_0 \end{cases}, \quad (10)$$

where (1) describes advection-diffusion in the liquid, (4) and (5) describe mass conservation with a Darcy flow (7) in the slush, (8) is the Stefan condition, and (9) and (10) are the temperature and pressure boundary conditions, respectively. Note that (3) and (5) can both be satisfied since the liquid region has an effectively infinite permeability. T is temperature, \mathbf{u} is Darcy fluid velocity, p is pressure, and a denotes the liquid-slush interface. Liquid properties are κ (thermal diffusivity), C_P (specific heat) and μ (dynamic viscosity). Slush properties are Π (permeability), ξ (solid fraction) and L (latent heat).

Non-dimensionalizing the equations yields

$$\frac{\partial \theta}{\partial t} + \mathbf{u} \cdot \nabla \theta = \epsilon \nabla^2 \theta \quad r_0 < r < a(\phi, t), \quad (11)$$

$$\theta = 0 \quad a(\phi, t) < r < 1, \quad (12)$$

$$p = 1 \quad r_i < r < a(\phi, t), \quad (13)$$

$$\nabla^2 p = 0 \quad a(\phi, t) < r < 1, \quad (14)$$

$$\nabla \cdot \mathbf{u} = 0 \quad r_i < r < a(\phi, t), \quad (15)$$

$$\mathbf{u}|_{a_-} = \mathbf{u}|_{a_+} \quad r = a(\phi, t), \quad (16)$$

$$\mathbf{u} = -\nabla p \quad a(\phi, t) < r < 1, \quad (17)$$

with boundary conditions

$$\dot{a} = -\frac{\epsilon}{S} \nabla \theta \quad r = a(\phi, t), \quad (18)$$

$$\theta = \begin{cases} 1 & r = r_i \\ 0 & r = a(\phi, t) \\ 0 & r = 1 \end{cases}, \quad (19)$$

$$p = \begin{cases} 1 & r = r_i \\ 1 & r = a(\phi, t) \\ 0 & r = 1 \end{cases}, \quad (20)$$

where all variables are now non-dimensional with length, velocity, pressure and temperature scaled (respectively) by

$$l \sim r_0, \quad (21)$$

$$U \equiv u_0 \sim \frac{\Pi p_0}{\mu r_0}, \quad (22)$$

$$P \sim p_0, \quad (23)$$

$$T \sim T_0 \quad T = T_0 \theta, \quad (24)$$

and non-dimensional parameters ϵ and S are given by

$$\epsilon \equiv \frac{\kappa}{u_0 r_0}, \quad (25)$$

$$S \equiv \frac{\xi L}{C_P T_0}. \quad (26)$$

In the lake star system, liquid temperatures must be less than or equal to 4°C since the lake is frozen at the top. Making conservative estimates, $T_0 < 4^\circ\text{C}$, $\xi > 0.3$ and $L/C_P \approx 80^\circ\text{C}$ then $S > 6 \gg 1$. Estimating u_0 ($1\text{cm/hr} < u_0 < 10\text{cm/hr}$) and r_0 ($0.3\text{m} < r_0 < 3\text{m}$) from the field observations of Knight [3] and using $\kappa \approx 10^{-7}\text{m}^2\text{s}^{-1}$ yields $\epsilon < 0.1 \ll 1$. Assuming $S \gg 1$ (quasi-stationary approximation, which we adopt henceforth) and $\epsilon \ll 1$, equations (11) - (20) are easily solved for a purely radial flow with cylindrical symmetry (no ϕ dependence) and circular liquid-slush interface. This (boundary layer) solution is

$$\mathbf{u} = u\hat{r} = -\frac{1}{\log(a_0)} \frac{1}{r} \hat{r} \quad r_i < r < 1, \quad (27)$$

$$p_b = \frac{\log(r)}{\log(a_0)} \quad r > a_0, \quad (28)$$

$$\theta_0 = 1 - \left(\frac{r}{a_0}\right)^{\frac{1}{\epsilon}(-1/\log(a_0)+2\epsilon)} \quad r < a_0, \quad (29)$$

$$\frac{S a_0 \dot{a}_0}{-1/\log(a_0) + 2\epsilon} = 1, \quad (30)$$

where equation (30) has an approximate implicit solution for a_0 given by

$$\frac{a_0^2}{4} - \frac{1}{2} a_0^2 \log(a_0) = \frac{t}{S}. \quad (31)$$

3.2 Linear Stability Analysis

In order to study the growth of perturbations from steady state, we perform a linear stability analysis around this cylindrically symmetrical flow. In this linear approximation, we still have a purely radial flow since the azimuthal component of flow enters quadratically with perturbations from steady state. Setting

$$r = a_0 + \epsilon r', \quad (32)$$

$$\phi = \epsilon\phi', \quad (33)$$

$$\theta = \theta_0 + f(r')e^{ik'\phi'+\sigma t}, \quad (34)$$

$$a = a_0 + \epsilon g e^{ik'\phi'+\sigma t}, \quad (35)$$

we first solve (14) subject to (20). For $g \ll 1$ and $\epsilon \ll k'$ then

$$p = \frac{\log(r)}{\log(a_0)} + \frac{g \exp(ik'\phi' + \sigma t)}{-a_0 \log(a_0)} \left(\frac{r}{a_0}\right)^{-k'/\epsilon} \quad r > a_0, \quad (36)$$

so that

$$u = \frac{1}{-\log(a_0)} \cdot \frac{1}{r} + \frac{k'}{\epsilon} \cdot \frac{g \exp(ik'\phi' + \sigma t)}{-a_0 \log(a_0)} \left(\frac{r}{a_0}\right)^{-k'/\epsilon-1} \quad r > a_0. \quad (37)$$

Substituting (37) into (16) and satisfying (15) yields

$$u = \frac{1}{-\log(a_0)} \cdot \frac{1}{r} + \frac{k'}{\epsilon} \cdot \frac{g}{-r \log(a_0)} \exp(ik'\phi' + \sigma t) \quad r < a_0. \quad (38)$$

Substituting (38) into (11), and dropping terms of $O(\epsilon)$ gives

$$f'' - \frac{1}{-a_0 \log(a_0)} \zeta^{-1} f' - \frac{k'^2}{a_0^2} f = \frac{k'g}{-a_0 \log(a_0)} \zeta^{-1} \frac{\partial \theta_0}{\partial r'} \quad (39)$$

where $\zeta \equiv r/a_0 = 1 + \epsilon r'/a_0$, with boundary conditions given by

$$f(r' = -\infty) = 0, \quad (40)$$

$$f(r' = g e^{ik'\phi'+\sigma t}) = 0. \quad (41)$$

To first order in g , (41) is equivalent to

$$f(r' = g) = -g \frac{\partial \theta_0}{\partial r'}. \quad (42)$$

Solving (39) subject to (40) and (42) gives

$$f(r') = \frac{g}{-a_0 \log(a_0)} \left(1 - \frac{a_0}{-k' \log(a_0)}\right) e^{\lambda^+ r'} + \frac{g}{k' \log^2(a_0)} e^{r'/(-a_0 \log(a_0))}, \quad (43)$$

with

$$\begin{aligned} \lambda^+ &\equiv \frac{1}{2a_0} \left(\frac{1}{-\log(a_0)} + \epsilon + \sqrt{\left(\frac{1}{-\log(a_0)} + \epsilon\right)^2 + 4k'^2} \right) \\ &\approx \frac{1}{-2a_0 \log(a_0)} \left(\sqrt{1 + \frac{4k'^2}{\log^2(a_0)}} + 1 \right) \end{aligned} \quad (44)$$

Equation (18) can be rewritten as

$$\dot{a} = \frac{1}{S} \frac{\partial \theta}{\partial r'} \Big|_{r'=g \exp(ik'\phi'+\sigma t)}, \quad (45)$$

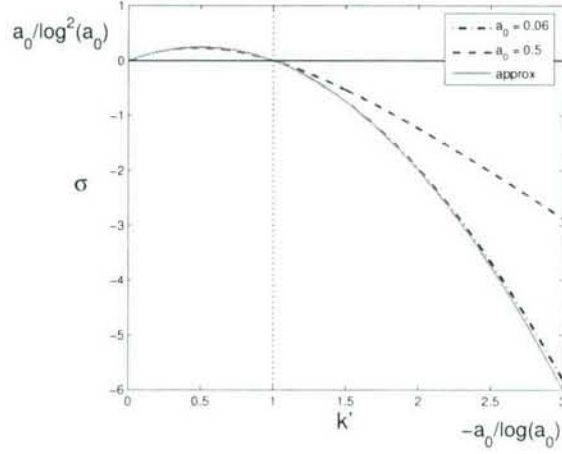


Figure 3: Stability curve: Nondimensional growth rate σ versus nondimensional wavenumber k' . Scales for the axes are given at the upper left (σ axis) and the lower right corners (k' axis). σ is plotted for the range of plausible a_0 (blue and red curves) and for the approximation (47) (green curve).

so that substituting (43) into (45) gives the nondimensional growth rate (σ) as a function of wave number (k'):

$$\sigma = \frac{1}{2a_0 \log^2(a_0)S} \left(\sqrt{1 + 4k'^2 \log^2(a_0)} - 1 \right) \left(\frac{a_0}{-k' \log(a_0)} - 1 \right). \quad (46)$$

Equation (46) can be approximated in $0 \leq x \lesssim 1$ as

$$\sigma \approx \frac{a_0}{\log^2(a_0)S} x(1-x), \quad (47)$$

where $x \equiv -k' \log(a_0)/a_0$.

The stability curve (46) and the approximation (47) are plotted in Figure 3. The essential features of (46) are a maximum in the range $0 < k' < a_0/\log(a_0)$, zero growth rate at $k' = a_0/\log(a_0)$ and a linear increase in stability with k' for large k' . The maximum growth rate occurs at approximately

$$k'_{max} \approx \frac{a_0}{-2 \log(a_0)}, \quad (48)$$

with (nondimensional) growth rate

$$\sigma_{max} \approx \frac{a_0}{4S \log^2(a_0)}. \quad (49)$$

Translating (48) and (49) back into dimensional quantities, we find that the most unstable mode has angular size given by

$$\phi_{degrees} = \frac{720^\circ \kappa}{u_0 r_0} \left(\frac{r_0}{a_0} \right) \log \left(\frac{r_0}{a_0} \right), \quad (50)$$

and has growth rate given by

$$\sigma_{dim} = \frac{u_0}{4Sr_0 \log^2(r_0/a_0)} \left(\frac{a_0}{r_0} \right). \quad (51)$$

3.3 Numerical Results

For observed lake stars, some of the relevant parameters are not well constrained. A plausible guess for r_0 is the radius of the wetted (snow) region around the lake stars since it is a reasonable estimate that if there were significant excess pressure at this point then the wetting front would have advanced further. Field observations [3, 5, 2] constrain this wetted radius to be $1.5\text{m} \lesssim r_0 \lesssim 4\text{m}$. However, it is also possible that the effective value of r_0 (r_0^{eff}) is less than this either because the wetted radius is smaller earlier in the star formation process or because the ambient pressure level is reached prior to reaching the wetting front. The most logical interpretation of a_0 is either as the radius of the lake star ($r_{lakestar}$) or as the radius of the roughly circular liquid-filled region at the center of the lake star (r_{liquid}) (see Figure 4). From field observations [3, 5, 2] $1\text{m} \lesssim r_{lakestar} \lesssim 2\text{m}$ and $0.1\text{m} \lesssim r_{liquid} \lesssim 0.5\text{m}$. Although r_0 , $r_{lakestar}$ and r_{liquid} each have a substantial range, the ratios $r_{lakestar}/r_0$ and r_{liquid}/r_0 are observed to have a somewhat smaller range of values: $0.3 \lesssim r_{lakestar}/r_0 \lesssim 0.6$ and $0.07 \lesssim r_{liquid}/r_0 \lesssim 0.15$. These constraints are useful since equations (50) and (51) are more sensitive to a_0/r_0 than a_0 or r_0 independently. Here we take $a_0 \approx r_{liquid}$ as the appropriate value of a_0 during the initial stages of star formation, although perhaps r_0^{eff} is sufficiently less than r_0 that $r_{lakestar}/r_0$ is a better approximation to a_0/r_0^{eff} than r_{liquid}/r_0 . Knight [3] estimates the rate of advance of the wetting front to be somewhat less than 10cm/hr . If the interpretation of r_0 above is correct then this rate gives a reasonable estimate of u_0 as $1.4 \cdot 10^{-5}\text{m/s} \lesssim u_0 \lesssim 2.8 \cdot 10^{-5}\text{m/s}$. κ is well constrained by measurements to be $\kappa \approx 10^{-7}\text{m}^2\text{s}^{-1}$.

Using these parameter values, our linear theory predicts the most unstable mode to have wavelength between 8° and 130° . Letting N equal the number of branches, then $N = 360^\circ/\phi_{deg}$ so that we expect between three and 45 branches (initially). These values of N encompass the observed values for lake stars ($4 < N < 15$), although the largest values ($15 < N < 45$) are never observed. Despite the dearth of field observations, we are encouraged by many qualitative features such as the fact that stars with larger values of a_0/r_0 seem to have a larger number of branches. Additionally, our analysis predicts that (given constant a_0/r_0) larger values of r_0 and u_0 would result in more branches. Larger p_0 (higher water height within the slush layer) and larger Π (less well-packed snow) would result in larger values of u_0 . Thus, some of the variability among field observations is likely to be due to variations in these quantities (for which we have no direct observations).

At this point, it is worth restating the fact that the theory presented here is only a linear one and the phenomenon of lake stars is highly non-linear since the dendritic arms are far from small perturbations to a radially symmetric pattern. Since the non-linear growth phase is likely different from the linear one, it should not be surprising that our model results only approximately agree with observations. In order to more accurately predict observations, one could perform a weakly non-linear pattern formation analysis (e.g. as in Cross and Hohenberg [1]) (which may result in a Landau-type equation) or one could solve the system numerically. Both of these approaches would likely yield improved results.

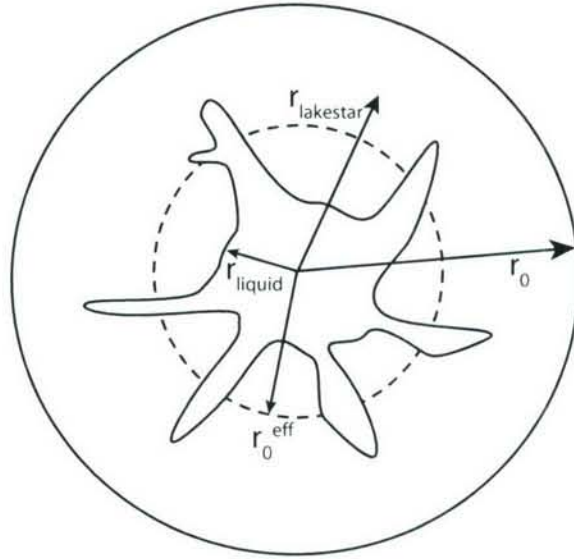


Figure 4: Schematic showing r_0 , r_0^{eff} , $r_{lakestar}$ and r_{liquid} .

However, while it is true that a more complex physical model may provide more detailed predictions than the model developed here, the state of the field observations does not at this time warrant that level of detail.

4 Experimental Setup

To check the validity of our analysis, we perform laboratory experiments. The goal of these experiments is more to test the conceptual ideas in our simple mathematical model than to make a quantitative connection with the observed lake stars. In these experiments, we cool a circular plate to slightly below freezing ($\approx -0.5^\circ\text{C}$); place a 0.5 to 1-cm high, roughly circular layer of slush on top; and flow 1°C water through the slush (see Figure 5).

To simulate wet snow we place ice in a high-power blender until the slush is visually uniform, although there is inevitably a range of grain sizes. To form the circular layer of slush we hand-pack the slush directly on the cold circular plate. We attempt to form a constant thickness, roughly circular layer simply by molding the slush and removing excess slush until the correct geometry remains. During this process air bubbles are sometimes incorporated which causes the slush permeability to be variable. This variable permeability likely affects our quantitative results.

We perform the experiment 14 times. The parameters that we vary are the initial size of the water-filled central hole (a_0), the initial size of the circular slush layer (r_0), and the flow rate (Q) (which determines u_0). In each run an attempt is made to manually vary the flow rate so that the water level (h_0) in the central hole remains roughly constant. In many of the runs, we begin the experiment without the central hole. In practice, however, the first few drops of warm water create a circular hole with radius one to three times the radius of the nozzle that delivers the water ($0.5\text{cm} < a_0 < 1.0\text{cm}$). It is significantly more



Figure 5: Experimental Setup: A 30 cm diameter plate with a built in manifold is connected to a cooling reservoir and maintained within a degree of freezing. A separate reservoir of fresh water 1° above freezing delivers fresh water at 1°C to the center.

difficult to prepare a uniform (permeability) sample with a circular hole initially present. These runs are therefore more difficult to interpret.

We observe fingering of some type in every experimental run. From this we can conclude that fingers are a robust feature under the conditions provided. However, there seem to be two distinct types of fingering: small-scale fingering (see Figure 6) that forms soon after the start of the experiment, and larger channel-like fingers (see Figure 7) that are ubiquitous at later times of the experiment and often extend from the central hole to the outer edge of the slush. Since the channel-like fingers provide a direct path for water to flow (without Darcy flow within the slush), these are likely not directly analogous with lake star fingers. The initial small-scale fingering, on the other hand, have characteristics more like the lake stars. We therefore assume that these small-scale features are the ones of interest. One should note, however, that the larger channel-like fingers seem to form out of small-scale fingers, so there may be a continuum of finger-like features and it is likely that the channels represent a very non-linear growth of the small-scale figures. In each experiment we measure a_0 , r_0 , h_0 , Q , and distance between fingers (d_f), which we tabulate in Table 1. From these quantities, we can calculate $u_0 = Q/(2\pi r_0 h_0)$, $\phi_{calc} \equiv \phi_{degrees}$ [from equation (50)] and $\phi_{obs} = 180^\circ d_f/(\pi a_0)$, and therefore compare scaled experiments both with the model and field observations.

5 Comparison of Theory, Experiment and Field Observations

In Figure 8 we plot ϕ_{obs} versus ϕ_{calc} for the various field observations for which we have estimates of parameters, the laboratory experiments described above, and the model [equation

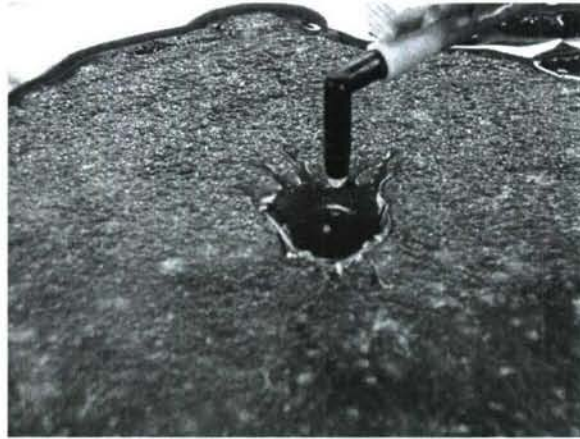


Figure 6: Typical experimental run where small-scale fingers are present. For scale, the nozzle head has diameter of 5 mm.

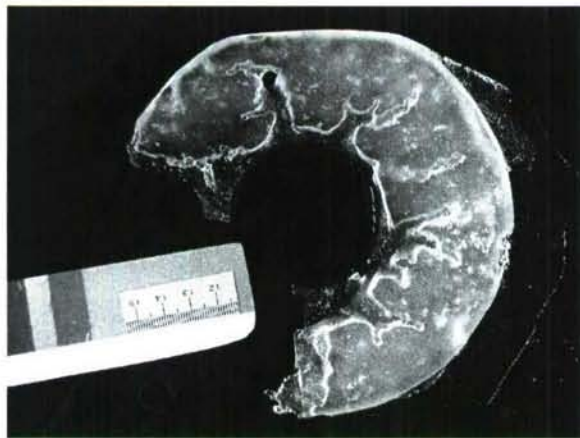


Figure 7: Typical run where channels form. This picture is taken from the underside. Note: part of the slush broke off when it was flipped to image it. The numbers on the ruler are in cm.

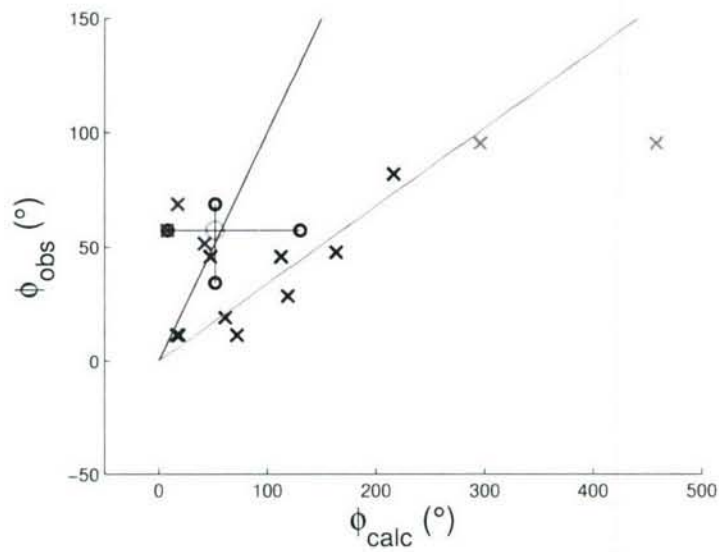


Figure 8: Comparison of theory, experiment and field observations. Circles are field observations (cyan = best constrained field observation, black = range of plausible field observations), crosses are experimental results (red: flag = 1, green: flag = 2, see Table 1), red line is theory, green line is best-fit line of unflagged (blue) experimental results. Note: all experimental results have error bars of at least a factor of two in the x-coordinate and 30% in the y-coordinate (see Table 1).

Expt #	a_0 (cm)	r_0 (cm)	h_0 (mm)	Q (ml/min)	d_f (cm)	flag
1	1.0	8	3	29	0.8	0
2	1.0	8	3	11	0.5	0
3	0.5	10	2	9	1.0	2
4	1.5	10	3	14	0.3	0
5	1.5	9	3	14	0.5	0
6	2.5	8.5	10	143	2.5	1
7	2.5	10	10	86	3.0	1
8	0.7	10	3	14	1.0	0
9	0.5	4.5	3	14	0.4	0
10	1.0	9	10	128	0.9	1
11	2.0	10.5	10	128	0.4	0
12	1.0	3.5	10	71	0.2	0
13	0.3	7.5	3	14	0.5	2
14	0.6	7	3	14	0.5	0

Table 1: Experimental Results: Runs with flag = 1 seem to have channels but show no clear small-scale fingers. In these cases, channel spacing is taken for d_f . Runs with flag = 2 were not well documented (blurry photos) and therefore difficult to interpret. Errors are approximately 0.3 cm, 0.5 cm, 2 mm, 5 ml/min and 0.2 cm (respectively) for the five measured quantities.

(50)]. The most obvious feature of Figure 8 is the large amount of scatter in both the experimental and observational data. Moreover, the data does not lie on the one-to-one curve predicted by the model. However, the data are not orders of magnitude off from the model predictions, and the experimental results even trend in the right direction, having a best-fit slope of 0.34. We also attempt to find trends in the experimental data not represented by the model by comparing $y \equiv \phi_{obs}/\phi_{calc}$ vs. various combinations of control parameters ($\equiv x$) including r_0 , a_0 , r_0/a_0 , r_0u_0 , $r_0/a_0 \log(r_0/a_0)$ and $\log(r_0/a_0)/(a_0u_0)$. For all plots of y vs. x , our model predicts a zero slope (and y-intercept of 1). A non-random dependence of y on x would point to failure of some part of our model. Thus, to test the validity of our model, we perform significance tests on all non-flagged data with the null hypothesis being a non-zero slope. In all cases, the null hypothesis is accepted (not rejected) at the 95% confidence level. Thus, although the agreement is far from perfect, the simple model captures all of the significant trends in the experimental data.

6 Conclusions

By quantifying and extending the qualitative ideas of Knight [3], we have constructed a mathematical model that is able to explain the radiating finger-like patterns on lake ice that we call the lake stars. The model yields a prediction for the wavelength of the most unstable mode as a function of various physical parameters [equation (50)] that agrees decently with field observations. We also perform experiments in which we observe a similar fingering pattern. To first order, the experimental results also agree with the model, although there

is substantial scatter in the data. The disagreement between field observations, model, and experiment can be attributed to poor measurements and the limitations of the simple theory, as discussed in more detail in Sections 3.3 and 4. We expect that adding complexity to the model should yield better quantitative results but that the general idea of the model and the qualitative predictions that result from it should remain valid.

7 Acknowledgements

Thanks to John Wettlaufer for guidance, Keith Bradley for help in the lab, the GFD staff for helpful conversations, and all the GFD fellows for a wonderful summer.

References

- [1] M. C. CROSS AND P. C. HOHENBERG, *Pattern-formation outside of equilibrium*, Rev. Modern Phys., 65 (1993), pp. 851–1112.
- [2] K. B. KATSAROS, *Convection patterns in a pond*, Bull. Amer. Meteor. Soc., 64 (1983), pp. 277–279.
- [3] C. A. KNIGHT, *Slush on lakes*, in Structure and dynamics of partially solidified systems, D. E. Loper, ed., Martinus Nijhoff, Dordrecht, 1987, pp. 453–465.
- [4] N. SCHÖRGHOFER, B. JENSEN, A. KUDROLLI, AND D. H. ROTHMAN, *Spontaneous channelization in permeable ground: theory, experiment, and observation*, J. Fluid Mech., 503 (2004), pp. 357–374.
- [5] A. H. WOODCOCK, *Melt patterns in ice over shallow waters*, Limnol. Oceanogr., 10 (1965), pp. R290–R297.

REPORT DOCUMENTATION PAGE	1. REPORT NO. 2007-02	2.	3. Recipient's Accession No.
4. Title and Subtitle 2006 Program of Studies: Ice		5. Report Date March 2007	
7. Author(s) Neil Balmforth and John Wettlaufer, Co-Directors; Grae Worster, Principal Lecturer		6.	
9. Performing Organization Name and Address Woods Hole Oceanographic Institution Woods Hole, Massachusetts 02543		8. Performing Organization Rept. No.	
12. Sponsoring Organization Name and Address National Science Foundation		10. Project/Task/Work Unit No.	
		11. Contract(C) or Grant(G) No. (C) OCE 03-25296 (G)	
		13. Type of Report & Period Covered Technical Report	
		14.	
15. Supplementary Notes This report should be cited as: Woods Hole Oceanog. Inst. Tech. Rept., 2007-02.			
16. Abstract (Limit: 200 words) Ice was the topic under discussion at Walsh Cottage during the 2006 Geophysical Fluid Dynamics Summer Study Program. Professor Grae Worster (University of Cambridge) was the principal lecturer, and navigated our path through the fluid dynamics of icy processes in GFD. Towards the end of Grae's lectures, we also held the 2006 GFD Public Lecture. This was given by Greg Dash of the University of Washington, on matters of ice physics and a well-known popularization: "Nine Ices, Cloud Seeding and a Brother's Farewell; how Kurt Vonnegut learned the science for Cat's Cradle (but conveniently left some out)." We again held the talk at Redfield Auditorium, and relaxed in the evening sunshine at the reception afterwards. As usual, the principal lectures were followed by a variety of seminars on topics icy and otherwise. We had focused sessions on sea ice, the impact of ice on climate, and glaciology. This year was a good summer for softball, with the Fellows enjoying some notable successes on the field (against both the other WHOI teams and the staff team at the summer's close). Some important acknowledgements: Young-Jin Kim helped out with the computers during the first few weeks, and Keith Bradley worked his usual magic in the Lab throughout the summer. The program continues to be indebted to W.H.O.I. Academic Programs, who once more provided a perfect atmosphere. Most unlike the '65 Dodge, Jeanne Fleming, Penny Foster and Janet Fields all contributed importantly to the smooth running of the program.			
17. Document Analysis a. Descriptors ice ice sheets sea ice b. Identifiers/Open-Ended Terms c. COSATI Field/Group			
18. Availability Statement Approved for public release; distribution unlimited.		19. Security Class (This Report) UNCLASSIFIED	21. No. of Pages 301
		20. Security Class (This Page)	22. Price